Advanced metabolite mapping at ultra-high field using ^{1}H-MRS, ^{1}H-MRSI and macromolecules: applications in a rat model of type C hepatic encephalopathy

Dunja ŠIMIČIĆ

Acknowledgments

During my time as a PhD student at EPFL I had the opportunity to work with many people who guided me and helped me on this journey. Without them my PhD years wouldn't have been the same and this thesis would not have been possible.

Cristina, from the first day you took me on, you taught me with patience. I learnt that not knowing something is a blessing that gives us the opportunity to improve and understand. You showed me your passion for science and resilience. Moreover, you were more than just a supervisor. Your friendship and support in difficult moments were crucial: without them, this thesis would certainly not be the same. Thank you for all the joy and positivity you try to bring every day, even when it is difficult, and for pushing me to live up to my potential, to appreciate myself and always strive for more. It was a pleasure being a part of your team and to continue to do so.

I would like to express my gratitude to Professor Rolf Grutter, for accepting me in his lab as a PhD student. Your vast knowledge of the MR field is remarkable and inspiring. Thank you for giving me the opportunity to work in such an amazing environment.

I would also like to acknowledge Prof. Carmen Sandi, Prof. Roland Kreis, Prof. Wolfgang Bogner and Prof. Laurent Villard for accepting to be members of my thesis committee and for all their constructive comments and discussions.

I would like to also thank our collaborators and all the people who provided additional help and guidance during the years of my PhD. Thank you, Bernard, for all the constructive discussions which were always fun and educational, for always being ready to help with my questions and for constructive feedback whenever I needed it. I learnt a great deal from you during the years. Thank you, Valerie and Olivier for all the meetings, time you took to give input and exchange knowledge. A special thank you to Katarzyna, for your precious contribution to my work and this thesis. You were always ready to help and perform every experiment that was needed. You taught me many things that were out of my field of expertise and helped me widen my knowledge. Thank you, Ileana, for always being ready to help, explain and teach.

I owe a big thanks to our veterinary team. Thank you, Analina and Mario, for your precious help with animal follow up during experiments. A special thanks to Stefan and Dario. Stefan, you were a great help and a friend from the start. You taught me a lot about animal handling and helped me overcome my fears. Thank you, Dario, for taking care of the animals with such dedication. My experiments wouldn't be a success without you.

Thank you, Dimitri and Pina, for your support and appreciation. Thank you, Lillian and Sarah, for your administrative support and help every time it was needed.

However, my journey in Lausanne started long before the start of my PhD and for that I owe a special thank you to Prof. László Forró. When you accepted me in your group for my master project, it wasn't only my first step in science, but you also showed me that a research group is, not only about work but also friendship and family. While being a part of your lab I learnt that I could be a part of a new family in Lausanne and gained friendships that will hopefully last for a lifetime. Thank you for your continuous support and guidance that lead me to accept this PhD position in the first place. A big thanks to Dr. Andrzej Sienkiewicz. Your constant presence, support and enthusiasm for science and research were a great inspiration and motivation for my future scientific work. I owe you a lot for who I am today.

As a PhD student you learn that the scientific collaborations are important, but the biggest gift you keep are the friendships and love of the people that made this journey even more special, important and fun.

Hello, Jessie, my special French friend. Your brilliance and love for research are amazing, I loved every discussion we ever had and learnt a lot by your side. But, what's even more amazing is your positivity, character, humor and friendship. Your constant support in every situation was immensely important. Thank you for being the best officemate I could ever imagine and for making every day at work fun. If we continue with officemates, I couldn't have had better ones. Songi, thank you for being a great friend and support from the start of my PhD. Thank you for making me dress business casual and do yoga and many other fun things. A special thanks goes to Veronika. Thank you for being patient, teaching and supporting me every step of the way in the beginning of my PhD and being a great friend at the same time. I big thank you goes also to the rest of the group, for making my PhD time easier and more fun every day. Thank you, Thanh, for always having all the answers and an emergency stash of chocolate. Emma for being the best gym buddy and friend. Mark, the best teaching buddy and evening support. Florian, the best IT guy in the world. Thank you, Brayan, for your help and contribution to this thesis. Many thanks also to the rest of the lab: Radek, Emma, Alice, Claudia, Antoine, Guillaume, Fred, Yujian, Yves, Mor, Masumeh, Hikari.

Some things start with an easy beer and end with some of the greatest memories for life. It is hard to decide with who to start, but it will have to be the "easy beer" creator Dr. Xavier Mettan. Thank you, Xavier, for teaching me about swiss traditions raclette and wine but also for being a great friend and support. My favorite Italian people, Andrea and Alessia. Andrea, thank you for being so positive, amazing, and fun. Alessia, you are so beautiful, and kind and the girl's dinners will always continue. My good friend Edo, for the best dancing moves and some Instagram fun. Thank you, Luka, for always being a great friend and support and Marton for your constant smile and positivity. Lidia, I enjoyed every coffee/lunch break with you and hope for many more to come. Endre, one of the most intelligent people I know and a great goulash/barbeque organizer. Iness, my first ever officemate and great murder mistery party organizer. And also many others: Elina, Sam, Konstantins x2, Peti, Trpimir, Josipa, Bruno, Michele, Mathieu, Eva, Juan, Jonas, Yanfei, Xiangwei, Gaetan, Arnaud, Iva, Jana.

Mojoj mami i tati

Abstract

Magnetic Resonance Spectroscopy (MRS) is the only technique capable of measuring a large number of metabolites simultaneously in vivo. Ultra-high magnetic fields (UHF) combined with ultra-short echo time (TE) sequences allow the detection of high-quality ^1H MR spectra and the quantification of 20 different metabolites in the brain (markers of energy metabolism, osmoregulation etc.).

In vivo brain localized ^1H MR spectra at short TEs contain the contribution of mobile macromolecules (MM). Reliable detection and fitting of MM are crucial for accurate quantification Higher spectral resolution at UHF led to increased interest in using a parametrized MM spectrum and flexible spline baselines to address unpredicted spectroscopic components.

In this thesis the MM spectra (from the rat brain at 9.4T) were characterized using an improved methodological approach for their post-processing, fitting and quantification. This method provided an efficient tool for parametrization of the MM spectrum into individual components and estimation of their T_2^{app} relaxation times. An extensive assessment on how the MM spectrum and spline baseline stiffness affect the metabolite and MM quantification is also reported

Type C hepatic encephalopathy (HE) is a complication of chronic liver disease (CLD). Children and adults respond differently to CLD and its related toxic accumulation of molecules (i.e. ammonium (NH_4^+), glutamine (Gln)). Children with CLD may grow up with significant neurocognitive deficits even after liver transplantation. Despite considerable advances in understanding the pathogenesis of type C HE, the exact metabolic mechanisms and their regional variations are not fully understood.

The advantages of UHF short TE ^1H MRS were used herein to describe the regional distribution of metabolites in the developing and adult brain using the bile duct ligated model (BDL) of type C HE (adult and postnatal day 21 rats). Three brain regions were assessed (hippocampus, cerebellum and striatum) pointing towards cerebellum as a region with the heaviest burden of Gln and unique metabolic response. Changes in cell morphology were followed longitudinally and related to the metabolic alterations. Elevated oxidative stress is reported using electron paramagnetic resonance, together with the decreased antioxidants (^1H MRS) emphasizing its important role in HE. The brain regional measurements confirmed the higher susceptibility of developing brain to the disease and the increased vulnerability of cerebellum. Finally, the beneficial effect of Cr supplementation on the neurometabolic profile is described using ^1H MRS and ^{31}P MRS in CLD pups (BDL at postnatal day 15) suggesting that an appropriate treatment may have significant public health impact.

MRSI is a powerful tool to non-invasively and spatially map the brain regional distribution of metabolites in vivo. While MRSI in the human brain is increasingly used, preclinical MRSI is not widely applied mainly due to the small rodent brain, long acquisition times and low signal to noise ratio.

The implementation of a novel approach: free induction decay (FID) MRSI on the 14.1T preclinical scanner is described herein. This method offers a fast and robust data acquisition with high spatial resolution resulting in high quality spectroscopic maps. Finally, preliminary assessment of the effect of two noise reduction techniques (MP-PCA and TGV reconstruction) on the spectra from preclinical MRSI datasets is briefly presented.

Keywords: Magnetic resonance spectroscopy (MRS), mobile macromolecules (MM), ^{1}H MRS, ^{31}P MRS, type C hepatic encephalopathy (type C HE), bile duct ligated (BDL) rats, magnetic resonance spectroscopic imaging (MRSI), free induction decay MRSI (FID-MRSI).

Résumé

La spectroscopie par résonance magnétique (SRM) est la seule technique capable de mesurer simultanément un grand nombre de métabolites *in vivo*. De très hauts champs (THC) magnétiques et des temps d'écho (TE) courts permettent la détection de spectres par RM du proton (^{1}H) de haute qualité et l'identification de 20 métabolites cérébraux différents (marqueurs du métabolisme énergétique, de l'osmorégulation, etc.).

Ces spectres contiennent la contribution de macromolécules mobiles (MM), dont la détection et la modélisation sont cruciales pour une quantification précise. Une résolution spectrale plus élevée à THC a accru l'intérêt pour la paramétrisation des spectres des MM et les splines flexibles pour la ligne de base afin de capturer les composantes spectroscopiques imprévisibles.

Dans cette thèse, une méthodologie améliorée pour le traitement, la modélisation et la quantification du spectre des MM (cerveau de rat à 9.4T) est développée, permettant leur paramétrisation en composantes individuelles et l'estimation de leurs temps de relaxation. L'influence du spectre des MM et de la rigidité de la spline sur la quantification des métabolites et des MM est également évaluée.

L'encéphalopathie hépatique (EH) de type C est une complication de la maladie hépatique chronique (MHC). L'accumulation de molécules toxiques (ammonium, glutamine (Gln)) durant la MHC impacte différemment les adultes et les enfants, ces derniers pouvant grandir avec des déficits neurocognitifs importants même après une transplantation hépatique. Malgré une meilleure compréhension de la pathogenèse de l'EH, les mécanismes métaboliques exacts et leurs variations locales restent partiellement incompris.

Les avantages de la SRM ^{1}H à THC et courts TE ont été utilisés ici pour décrire la distribution régionale des métabolites dans le cerveau adulte et en développement, à l'aide du modèle de ligature de la voie biliaire (LVB) de l'EH de type C (rats adultes et au jour 21 post-natal). Trois régions du cerveau ont été évaluées (hippocampe, cervelet et striatum), identifiant une réponse métabolique unique du cervelet, le plus touché par l'accumulation de Gln, ainsi qu'un impact plus important de l'EH sur le cerveau en développement. Des changements longitudinaux de morphologie cellulaire ont aussi été associés aux altérations métaboliques et un stress oxydatif élevé a été observé par résonance

paramagnétique électronique (RPE), ainsi qu'une diminution des antioxydants (SRM ^{1}H), soulignant son rôle important dans l'EH. Enfin, l'effet bénéfique de la supplémentation en Cr sur le profil neu-rométabolique est décrit à l'aide de la SRM ^{1}H et ^{31}P chez les jeunes rats avec la MHC (LVB au jour 15 post-natal), offrant des perspectives en santé publique.

L'imagerie spectroscopique par RM (ISRM) est un outil puissant pour cartographier la distribution régionale des métabolites cérébraux *in vivo*. Alors que le l'ISRM gagne de l'intérêt en clinique, les petits cerveaux des rongeurs, les temps d'acquisition longs et le faible rapport signal sur bruit limitent son utilisation préclinique.

La mise en œuvre d'une nouvelle approche, le FID-ISRM (de l'anglais *free induction decay*), sur un scanner préclinique 14.1T est décrite ici. Elle permet une acquisition rapide et robuste de cartes spectroscopiques avec une grande résolution spatiale. Enfin, une évaluation préliminaire de deux techniques de réduction du bruit (MP-ACP et reconstruction VTG) sur les spectres ISRM précliniques est brièvement présentée.

Mots-clés : Spectroscopie par résonance magnétique (SRM), macromolécules mobiles (MM), SRM ^{1}H, SRM ^{31}P, encéphalopathie hépatique de type C (EH de type C), rats ligaturés de la voie biliaire (LVB), imagerie spectroscopique par résonance magnétique (ISRM), *free induction decay*-ISRM

Contents

List of figures

List of Tables

List of abbreviations

Ala	alanine
ALT/GPT	alanine aminotransferase
AMARES	advanced method for accurate, robust, and efficient spectral fitting
Asc	ascorbate
Asp	aspartate
AST/GOT	aspartate aminotransferase
ATP	adenosine triphosphate
BBB	blood-brain barrier
BDL	bile duct ligation
bHB	β-hydroxybutyrate
CHESS	chemical shift selective
CLD	chronic liver disease
CNS	central nervous system
Cr	creatine
CRLB	Cramer-Rao lower bounds
EPR	electron paramagnetic resonance
FASTMAP	fast automatic shimming technique by mapping along the projections
FID	free induction decay
FOV	field of view
FT	Fourier transformation
FWHM	full width at half maximum
GABA	gamma-aminobutyric acid
GAMT	guanidinoacetate N-methyltransferase
GFAP	glial fibrillary acidic protein
Glc	glucose
Gln	glutamine
Glu	glutamate
Glx	glutamine+glutamate
GPC	glycerophosphocholine
GPE	glycerophosphoethanolamine
GS	glutamine synthetase
GSH	glutathione
HE	hepatic encephalopathy
Ins	myo-inositol
IHC	Immunohistochemistry
ISIS	image-selected in vivo spectroscopy
jMRUI	java based magnetic resonance user interface
Lac	lactate
LASER	Localization by Adiabatic Selective Refocusing
LCModel	linear combination of model spectra of metabolites
MM	mobile macromolecules
MRI	magnetic resonance imaging
MRS	magnetic resonance spectroscopy
MRSI	magnetic resonance spectroscopic imaging
NAA	N-acetyl aspartate

NAAG	N-acetylaspartylglutamate
NAD	nicotinamide adenine dinucleotide
NMR	nuclear magnetic resonance
NOE	nuclear Overhauser effect
OVS	outer volume suppression
PCho	phosphocholine
PCr	phosphocreatine
PDE	phosphodiester
PE	phosphorylethanolamine
PME	phosphomonoester
ppm	parts per million
PRESS	point resolved spectroscopy
RF	radiofrequency
RNS	reactive nitrogen species
ROS	reactive oxygen species
Scyllo	scyllo-inositol
SD	standard deviation
SNR	signal-to-noise ratio
SPECIAL	spin echo, full intensity aquired localized spectroscopy
STEAM	stimulated echo pulse sequence
Tau	taurine
tCho	total choline
tCr	total creatine
TE	echo time
TMS	tetramethyl silane
TR	repetition time
VAPOR	variable pulse power and optimized relaxation delay
VOI	volume of interest
WS	water suppression

Outline of the thesis

This thesis focused on developing a tool for efficient post processing and parametrization of the MM spectra to fully characterize the MM in a rat brain at 9.4T together with assessment of the effect that the spline baseline stiffness has on metabolite and MM quantification. Moreover, the purpose was to characterize brain regional vulnerability in type C HE by studying metabolic changes (^{1}H MRS) in adult and developing brain (recognized animal model of type C HE – bile duct ligated rats) and to put them in context of the morphological alterations (immunohistochemistry) and oxidative stress (EPR). Finally, it aimed to implement fast FID MRSI approach to a preclinical 14.1 T scanner.

Chapter 1 describes the basic principles of NMR phenomenon, starting from the spin system followed by the definition of macroscopic magnetization and how its manipulation leads to NMR signal. The principles of MRI and MRS are also described. Moreover, the main techniques used for single volume MRS, the characteristics of ^{1}H MR spectrum and its quantification as well as ^{31}P MR spectrum are reviewed presenting all the relevant properties for the measurements performed in this thesis. This chapter also provides an introduction to MRSI and an explanation of its basic principles.

Chapter 2 presents the work achieved on measurement and processing of macromolecules at 9.4T in the healthy rat brain. It provides details on acquisition, post-processing, fitting and parametrization of 10 MM components from in vivo spectra. Additionally, the estimation of T_2^{app} of the individual MM peaks, basis sets created for metabolite quantifications and the results achieved using the described methodology are presented. The chapter ends with a study assessing the influence of the MM model (parametrized or single MM spectrum) and spline baseline stiffness on the metabolite and MM quantification.

Chapter 3 starts with a general introduction and background on Type C HE as a consequence of chronic liver disease, especially highlighting deleterious mechanisms/molecules involved in the disease pathogenesis (ammonium, inflammation and oxidative stress). Followed by an extensive study describing the longitudinal metabolic changes during type C HE (^{1}H MRS, bile duct ligated rat model) in three brain regions (cerebellum, hippocampus and striatum) in parallel with astrocytic and neuronal morphological changes (immunohistochemistry) and the direct measurements of brain and systemic oxidative stress (EPR). Moreover, the brain regional vulnerability in the developing brain

model of type C HE (^{1}H MRS, bile duct ligation performed at postnatal day 21) is also presented. The chapter ends with a description of the beneficial effect of Cr supplementation on the neurometabolic profile using ^{1}H MRS and ^{31}P MRS in a developing brain model (bile duct ligation performed at postnatal day 15).

Chapter 4 starts with a brief description of the challenges of MRSI and the main sequences used for the preclinical MRSI acquisitions followed by the advantages of fast FID MRSI technique at ultrahigh filed. This chapter is focused on the first implementation of ^{1}H FID MRSI sequence in the preclinical setting (14.1 T) with all the optimization steps, basis set and quantifications. Moreover, the first results obtained using ^{1}H FID MRSI are presented in terms of metabolic maps. In addition, preliminary tests of two noise reduction techniques (MP-PCA and low-rank TGV reconstruction) as a potential processing step in the preclinical MRSI post-processing pipeline are presented. The chapter finishes with the prospective steps for future improvement and acceleration.

Chapter 1 Introduction to Nuclear Magnetic Resonance

Matter is made of atoms, which are built up from electrons and nuclei. The atomic nucleus has important physical properties: mass, electric charge, and spin. Here we will focus on the spin of the nucleus and its magnetism, as they are the key properties to explain the nuclear magnetic resonance (NMR) phenomenon. These two properties enable us to investigate matter without disturbing it (non-invasively). The basic principles of the NMR phenomenon and the main in vivo techniques that are based on it are described in this chapter.

*This chapter is structured into seven sub chapters. The first four sub chapters describe the basic principles of nuclear magnetism, define macroscopic magnetization and explain how its manipulation leads to the NMR signal. In addition, some basic NMR experiments (spin echo and inversion recovery) are described as well as the structure of the NMR spectrum (chemical shift and scalar coupling). The titles of the first four subchapters are: "**Quantum mechanical description – Spin in the magnetic field**" (1.1), "**Macroscopic magnetization**" (1.2), "**Excitation**"(1.3), "**Relaxation**"(1.4) and they are written with the help of: Keeler 2005[1], De Graaf 2019[2], Lauterbur 2000[3], Webb 2003[4] and Logan 2005[5]. The basic principles of the magnetic resonance imaging (MRI) acquisition are described in the fifth chapter titled "**MRI principles**" (1.5) and its written with the help of De Graaf 2019[2] and ,Webb 2003[4]. The sixth chapter titled "**Single volume magnetic resonance spectroscopy (MRS)**" (1.6) presents the main techniques used for in vivo single volume MRS. In addition, it describes the main properties of the ^{1}H MR spectrum and its quantification as well as the ^{31}P MR spectrum. Finally, principles of MR spectroscopic imaging are described in the last (seventh) chapter titled "**MRSI basic principles**"(1.7) written with the help of De Graaf 2019[2].*

1.1   Quantum mechanical description—Spin in a magnetic field

Every rotating object possesses a quantity called angular momentum. Described classically, the angular momentum is a vector quantity, having both magnitude and direction and it is defined as:

$$\vec{L} = \vec{r} \times \vec{p}, \qquad \vec{p} = m\vec{v}$$

Equation 1:1

If the rotating object carries an electrical charge, the resulting current creates a magnetic field which is characterized by the magnetic dipole moment $\vec{\mu}$. Considering the charge q, its position $\vec{r}$ and velocity $\vec{v}$ the general magnetic moment is given by:

$$\vec{\mu} = \frac{q(\vec{r} \times \vec{v})}{2}$$

Equation 1:2

Using the equation 1:1 we obtain: $\vec{\mu} = \frac{q}{2m}\vec{L}$; and assuming a single spin we can substitute $\vec{L}$ by $\vec{S}$ to express:

$$\vec{\mu} = g_N \frac{q}{2m_N}\vec{S} = g_N\beta_N\vec{S} = \gamma\vec{S}$$

Equation 1:3

where the $\beta_N = \frac{q}{2m_N}$ is the nuclear magneton, g_N the nuclear g factor and $\gamma = g_N\beta_N$ is the gyromagnetic ratio (property of the nucleus). When a spin is placed in an external magnetic field it will feel a torque $\vec{T} = \vec{\mu} \times \vec{B_0}$. It also has an associated energy defined as (here we adopt a convention that the $\vec{B_0}$ is applied along z-axis $\vec{B_0} = B_0\hat{z}$):

$$E = -\vec{\mu} \cdot \vec{B_0} = -\gamma B_0 S_z$$

Equation 1:4

In quantum mechanics, the operator which represents the observable quantity energy is called the Hamiltonian operator ($\hat{H}$). For a spin positioned in a magnetic field of strength B_0 (applied along the z-axis) the Hamiltonian which represents the interaction between the field and the spin is:

$$\hat{H}_{one\ spin} = -\gamma B_0 \hat{I}_z$$

Equation 1:5

where S_z is replaced by a corresponding quantum mechanical operator $\hat{I}_z$ representing the z-component of the nuclear spin angular momentum. In quantum mechanics, the angular momentum is an intrinsic property of the nucleus (it is not a result of the literal spinning of the nucleus). It is usually called nuclear spin angular momentum and it is limited to discrete values (it is quantized).

The eigenfunctions and eigenvalues of the angular momentum operator $\hat{I}_z$ are linked to the quantized states and corresponding energies of the angular momentum. The amplitude of the angular momentum is quantized in a number of states equal to the number of eigenvalues of $\hat{I}_z$. This depends on the nucleus in question and it is described by the spin quantum number I. I can be integer $(0, 1, 2 \dots)$ or half-integer $(\frac{1}{2}, \frac{3}{2} \dots)$. The operator $\hat{I}_z$ has $(2I + 1)$ eigenfunctions with the corresponding eigenvalues. Each of these values is characterized by an additional quantum number m which can have values between $-I$ and $+I$ in integer steps. The spin quantum number I of protons, electrons and neutrons is half-integer and equals $\frac{1}{2}$. For nuclei, I can be calculated using the mass and the charge numbers with the following rules:

1. Nuclei with an odd mass number have a half integer I (e.g., ^{1}H, ^{13}C, ^{15}N, ^{23}Na, ^{31}P)
2. Nuclei with an even mass and charge number have a zero I (e.g., ^{12}C, ^{16}O, ^{32}S)
3. Nuclei with an even mass and odd charge number have an integer I (e.g., ^{2}H, ^{14}N)

Table 1:1: Characteristics of commonly used nuclei.

ISOTOPE	NET SPIN (I)	GYROMAGNETIC RATIO $\gamma/2\pi\ [MHz/T]$	NATURAL ABUNDANCE [%]
^{1}H	1/2	42.58	99.98
^{2}H	1	6.54	0.015
^{31}P	1/2	17.25	100
^{23}NA	3/2	11.27	100
^{15}N	1/2	4.31	0.37
^{13}C	1/2	10.71	1.108
^{19}F	1/2	40.08	100

If we take a half-spin nucleus as an example, the $\hat{I}_z$ has only two eigenfunctions characterized by $m = \pm\frac{1}{2}$. These eigenfuctions $(\psi_{+\frac{1}{2}}, \psi_{-\frac{1}{2}})$ comply to the eigenvalue equations:

$$\hat{I}_z \psi_{+\frac{1}{2}} = +\frac{1}{2}\hbar\psi_{+\frac{1}{2}}, \quad \hat{I}_z \psi_{-\frac{1}{2}} = -\frac{1}{2}\hbar\psi_{-\frac{1}{2}} \implies \hat{I}_z \psi_m = m\hbar\psi_m$$

Equation 1:6

Thus, the eigenfunctions $\psi_{+\frac{1}{2}}, \psi_{-\frac{1}{2}}$ have eigenvalues of $+\frac{1}{2}\hbar, -\frac{1}{2}\hbar$ respectively (i.e. $m\hbar$ with the quantum number m).

Since the Hamiltonian of the single spin is just a multiplication of $\hat{I}_z$ by a factor of $-\gamma B_0$, the eigenfunctions of $\hat{I}_z$ ($\psi_{+\frac{1}{2}}, \psi_{-\frac{1}{2}}$) are also the eigenfunctions of the $\hat{H}_{one\ spin}$. To calculate the corresponding eigenvalues, we need to work out the effect of $\hat{H}_{one\ spin}$ on $\psi_{+\frac{1}{2}}$. Using the Equation 1:6 we can obtain:

$$\hat{H}_{one\ spin}\psi_{+\frac{1}{2}} = -\gamma B_0 \left[\hat{I}_z\psi_{+\frac{1}{2}}\right] = -\gamma B_0 \left[\frac{1}{2}\hbar\psi_{+\frac{1}{2}}\right] = -\frac{1}{2}\hbar\gamma B_0\psi_{+\frac{1}{2}}$$

Equation 1:7

Thus, the eigenvalue of the $\hat{H}_{one\ spin}$ corresponding to $\psi_{+\frac{1}{2}}$ is $-\frac{1}{2}\hbar\gamma B_0$. Using the same approach, we find that the eigenvalue corresponding to $\psi_{-\frac{1}{2}}$ is $+\frac{1}{2}\hbar\gamma B_0$. These are the two energy levels of a single half-integer spin in the magnetic field and can also be written as:

$$E_m = -m\hbar\gamma B_0 \quad m = +\frac{1}{2}\ or\ -\frac{1}{2}$$

Equation 1:8

The energy state with $m = +\frac{1}{2}$ is labeled α and described as 'spin up' and the energy state with $m = -\frac{1}{2}$ is labeled β and described as 'spin down'. According to quantum mechanics the allowed transitions are the ones when m changes by $+1$ or -1. The energy of the transition from α to β is derived in Figure 1:1, knowing that the energy of the photon is given by $h\nu$ we can calculate that the photon corresponding to this energy gap has a frequency of $\frac{\gamma B_0}{2\pi}$ $[Hz]$.
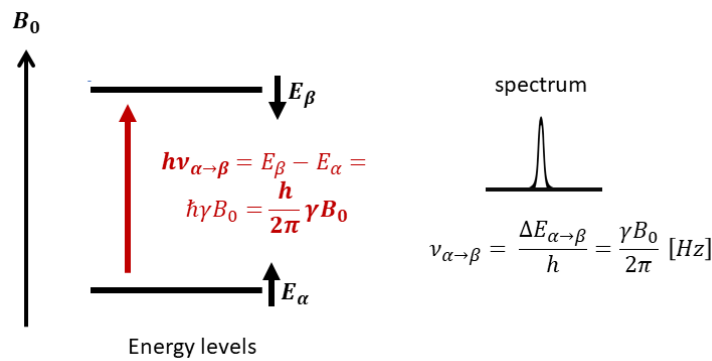
Figure 1:1: Energy levels of a single spin half nucleus. The allowed transition results in a single line at the Larmor frequency.

We can now define the **Larmor frequency** as:

$$\nu_0 = -\frac{\gamma B_0}{2\pi}\ [Hz]\ , or\ \omega_0 = -\gamma B_0\ \left[\frac{rad}{s}\right]$$

Equation 1:9

The Hamiltonians and eigenvalues written I different units are shown in Table 1:2

Table 1:2: The Hamiltonians and eigenvalues written in various units

m	wavefunction	IN ENERGY UNITS $\hat{H} = -\gamma B_0 \hat{I}_z$	IN FREQUENCY UNITS [RAD/S] $\hat{H} = -\omega_0 \hat{I}_z$	IN FREQUENCY UNITS [HZ] $\hat{H} = -\nu_0 \hat{I}_z$
$+\dfrac{1}{2}$	$\psi_{+\frac{1}{2}}$ or ψ_α	$-\dfrac{1}{2}\hbar\gamma B_0$	$-\dfrac{1}{2}\omega_0$	$-\dfrac{1}{2}\nu_0$
$-\dfrac{1}{2}$	$\psi_{-\frac{1}{2}}$ or ψ_β	$\dfrac{1}{2}\hbar\gamma B_0$	$\dfrac{1}{2}\omega_0$	$\dfrac{1}{2}\nu_0$

1.2   Macroscopic magnetization

In the previous section, only single spins were considered, but the typical macroscopic sample measured in an NMR experiment contains a large number of spins. When a sample is positioned in an external magnetic field $(\overrightarrow{B_0})$ the considered nuclei can assume two energy states (as described in the Equation 1:8): the lower energy state (spin up $-\alpha$) and the higher energy state (spin down $-\beta$). Thus, they are divided in two populations whose energies are described by the quantum number m. However, as described by quantum mechanics, the spins in a condensed matter are never in a state α or β, but in a superposition of these states. That is why we can only express the probability of finding the spins in the α or β states upon measurement. As the temperature would go down to the absolute zero $(0\ K)$ the system would try to minimize its energy by alining the spins with the external magnetic field (lower energy state $-$ spin up). Since the NMR experiments are performed at room or body temperature the thermal energy opposes the energy minimization and the probability of populating both lower and upper energy states is described according to the Maxwell-Boltzmann statistics. The population distribution is given by:

$$\left(\frac{n_\alpha}{n_\beta}\right) = e^{\frac{\Delta E}{kT}} = e^{\frac{h\nu}{kT}} = e^{-\gamma\left(\frac{h}{2\pi}\right)\frac{B_0}{kT}}$$

Equation 1:10

If we use the approximation that $h\nu \ll kT$ and with $n = n_\alpha + n_\beta$ (total number of spins in the sample) we can approximate $n_\alpha - n_\beta \approx \dfrac{nh\nu}{2kT} = \dfrac{\gamma\left(\frac{h}{2\pi}\right)B_0}{2kT}$ which gives the difference between spin populations in state α or β, with k the Boltzmann constant and T the absolute temperature. The population difference increases with the strength of the applied magnetic field. The difference in

populations is very small, if we take the magnetic field of 9.4T ($\nu = 400 MHz$ for the ^{1}H nucleus) the difference between α and β states is only 0.0031%. The NMR signal is proportional to this difference, explaining the low sensitivity of the NMR detection.

The macroscopic magnetization is a sum of all individual magnetic moments (μ). Because of the random distribution of the magnetic moments, the transverse component (in the xy plane) of the $\overrightarrow{M_0}$ is zero at equilibrium. Thus, the macroscopic magnetization will be parallel to $\overrightarrow{B_0}$ ($\overrightarrow{M_0} = M_0\hat{z}$).

$$\overrightarrow{M_0} = \sum_{n=1}^{N} \mu_n \hat{z} = \gamma \left(\frac{h}{2\pi}\right)\frac{1}{2}(n_\alpha - n_\beta)\hat{z}$$

Equation 1:11

Giving the amplitude of the magnetization vector to be:

$$M_0 = \left(\frac{\gamma h}{2\pi}\right)^2 \left(\frac{nB_0}{4kT}\right)$$

Equation 1:12

NMR signal is proportional to this magnetization. In addition to the dependence on the magnetic field strength, the Equation 1:12 shows a quadratic dependence of the signal intensity to the gyromagnetic ratio (γ). The Table 1:1 shows that the hydrogen nucleus has the highest γ explaining why ^{1}H is the most commonly chosen nucleus in an NMR experiment.

1.3   Excitation

To illustrate the interaction of the spins with the external magnetic field we will use a classical representation of the macroscopic magnetization vector ($\overrightarrow{M_0}$). Macroscopic magnetization at equilibrium is a static vector aligned with the external magnetic field and does not produce any signal. The signal can only be produced by perturbing the magnetization vector by rotation towards the transverse plane. Since the magnetization is the vector sum of individual magnetic moments, only the field rotating in the same sense as the magnetic moments interacts significantly with them. Thus, the magnetization can be tilted by applying an additional magnetic field at the Larmor frequency (ω_0-on resonance):

$$\overrightarrow{B_1(t)} = B_1(\cos(\omega_0 t)\hat{x} - \sin(\omega_0 t)\hat{y}) = B_1(t)e^{-i\omega_0 t}$$

Equation 1:13

During the application of the $\overrightarrow{B_1}$ field the magnetization will precess around $\overrightarrow{B_0}$ and $\overrightarrow{B_1}$. The frequency of $\overrightarrow{B_1}$ is in the radiofrequency range and it is applied as a radiofrequency (RF) pulse. The RF pulse is an oscillating $\overrightarrow{B_1(t)}$ field perpendicular to the $\overrightarrow{B_0}$ and it is characterized by its frequency

(determined by the resonance condition – Larmor frequency) and its envelope function $B_1(t)$. This function specifies the shape and duration of an RF pulse, for example the envelope of the widely used rectangular pulse is defined as:

$$B_1(t) = B_1 \Pi \left(\frac{t - \tau_p/2}{\tau_p} \right) = \begin{cases} B_1 & 0 \leq t \leq \tau_p \\ 0 & otherwise \end{cases}$$

Equation 1:14

where τ_p is the pulse duration. Since the $\overrightarrow{B_1}$ is perpendicular to $\overrightarrow{M_0}$, the magnetization will feel a torque tilting it towards the transverse plain. The resulting position of the magnetization depends on the time during which we apply the $\overrightarrow{B_1}$ (pulse duration and amplitude). The magnetization in the transverse plane rotates around $\overrightarrow{B_0}$ with the Larmor frequency inducing a signal (electromotive force – Faraday law) in the coil next to or surrounding the sample.
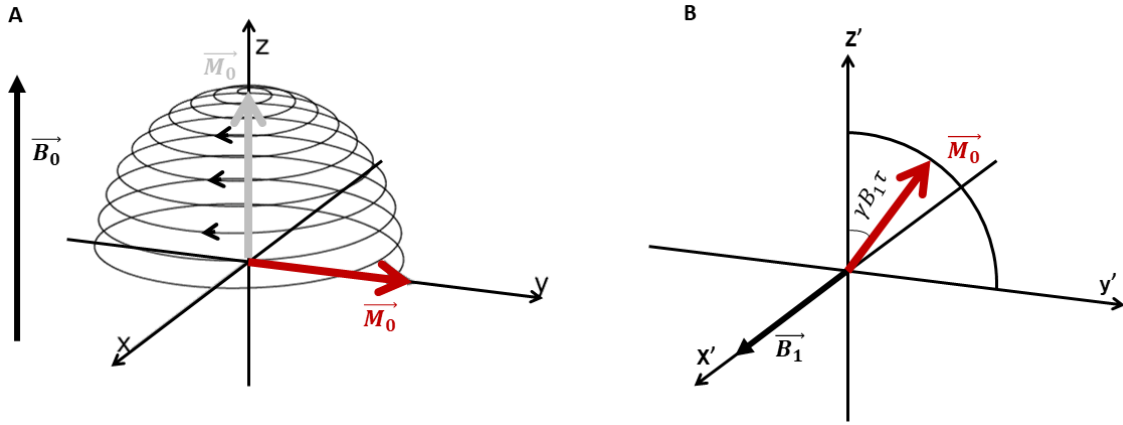
Figure 1:2: The motion of the magnetization as observed in **(A)** the laboratory frame **(B)** rotating frame (at the Larmor frequency). The flip angle of γB_1 τ is expressed as in case of a square pulse.

The equation of motion of the magnetization in the laboratory frame (x, y, z) during an RF pulse (excitation period) in a general form is given by the Bloch equation:

$$\frac{d\vec{M}}{dt} = \vec{M} \times \gamma \vec{B}$$

Equation 1:15

describing the precession of the magnetization around the total magnetic field $\vec{B}$ with the angular velocity $\vec{\omega} = -\gamma \vec{B}$. For simplicity we introduce the rotating reference frame (x', y', z'). This reference frame is rotating, as the magnetization, around $\overrightarrow{B_0}$. When introducing the rotating frame, we also need to introduce relationships associated with this transformation:

$$B_{1,rot}(t) = B_1(t) e^{i\omega_0 t}, \qquad \frac{d\vec{M}}{dt} = \frac{\partial \overrightarrow{M_{rot}}}{\partial t} + \overrightarrow{\omega_0} \times \overrightarrow{M_{rot}}$$

<div align="center">Equation 1:16</div>

Now, we can express the equation of motion for the free precession in the rotating frame by combining the Equations 1:15 and 1:16:

$$\frac{\partial \overrightarrow{M_{rot}}}{\partial t} = \overrightarrow{M_{rot}} \times \gamma \overrightarrow{B_{rot}} - \overrightarrow{\omega_0} \times \overrightarrow{M_{rot}} = \gamma \overrightarrow{M_{rot}} \times \left(\overrightarrow{B_{rot}} + \frac{\overrightarrow{\omega_0}}{\gamma} \right)$$

<div align="center">Equation 1:17</div>

We can rewrite Equation 1:17 as:

$$\frac{\partial \overrightarrow{M_{rot}}}{\partial t} = \gamma \overrightarrow{M_{rot}} \times \overrightarrow{B_{eff}}, \qquad \text{where} \qquad \overrightarrow{B_{eff}} = \overrightarrow{B_{rot}} + \frac{\overrightarrow{\omega_0}}{\gamma}$$

<div align="center">Equation 1:17</div>

$\overrightarrow{B_{eff}}$ is the effective magnetic field which the magnetization "feels" in the rotating frame. If the frequency of the laboratory frame is ω_0 we can introduce $\overrightarrow{B_{rot}} = B_0 \hat{z}$ and $\overrightarrow{\omega_0} = -\gamma \overrightarrow{B_0} \hat{z}$ which gives:

$$\overrightarrow{B_{eff}} = \overrightarrow{B_{rot}} + \frac{-\gamma \overrightarrow{B_0} \hat{z}}{\gamma} = B_0 \hat{z} - B_0 \hat{z} = 0$$

<div align="center">Equation 1:18</div>

Thus, the apparent field vanishes, and the magnetization appears to be stationary in this frame of reference. If we look now at the effect of the RF pulse on the magnetization during excitation, in the rotating frame we have (when the B_1 is perfectly on resonance):

$$\overrightarrow{B_{1,rot}} = B_1(t) \hat{x'}$$

<div align="center">Equation 1:19</div>

Which gives an effective field in the rotating frame as:

$$\overrightarrow{B_{eff}} = B_0 \hat{z'} + B_1(t) \hat{x'} + \frac{\overrightarrow{\omega_{rf}}}{\gamma} = \left(B_0 - \frac{\omega_{rf}}{\gamma} \right) \hat{z'} + B_1(t) \hat{x'}$$

<div align="center">Equation 1:20</div>

For the **on-resonance** condition (the RF rotating frame = Larmor rotating frame), we get:

$$\omega_{rf} = \omega_0 = \gamma B_0 \quad \rightarrow \quad \overrightarrow{B_{eff}} = B_1(t) \hat{x'}$$

<div align="center">Equation 1:21</div>

By substituting this into the Bloch equation (1:17) we obtain the equation of motion for the magnetization in the rotating frame:

$$\frac{\partial \overrightarrow{M_{rot}}}{\partial t} = \gamma \overrightarrow{M_{rot}} \times B_1(t) \hat{x'}$$

<div align="center">Equation 1:22</div>

In the scalar form we have:

$$\begin{cases} \dfrac{dM_{x'}}{dt} = 0 \\[2mm] \dfrac{dM_{y'}}{dt} = \gamma B_1(t)M_{z'} \\[2mm] \dfrac{dM_{z'}}{dt} = -\gamma B_1(t)M_{y'} \end{cases} , \text{ for } M_{x'}(0) = M_{y'}(0) = 0 \text{ and } M_{z'}(0) = M_0 \rightarrow \begin{cases} M_{x'}(t) = 0 \\[2mm] M_{y'}(t) = M_0 \sin\left(\displaystyle\int_0^t \gamma B_1(t)dt\right) \\[2mm] M_{z'}(t) = M_0 \cos\left(\displaystyle\int_0^t \gamma B_1(t)dt\right) \end{cases}$$

Equation 1:23

We can now conclude that the magnetization vector precesses around the x' axis with the angular velocity:

$$\overrightarrow{\omega_1} = -\gamma\overrightarrow{B_1}$$

Equation 1:24

The precession of the magnetization around the $\overrightarrow{B_1}$ field is called the forced precession. As a result, the magnetization develops a measurable transverse component. The flip angle θ is the angle between the magnetization and the z' axis (more generally, for a pulse applied on a magnetization which is not necessarily at equilibrium, it would be the angle between the initial and final magnetization after the pulse application). At the end of an RF pulse, θ can be calculated as:

$$\theta = \int_0^{\tau_p} \omega_1(t)dt = \int_0^{\tau_p} \gamma B_1(t)dt$$

Equation 1:25

For a rectangular pulse (Equation 1:14):

$$\theta = \omega_1\tau_p = \gamma B_1\tau_p$$

Equation 1:26

The flip angle depends both on the amplitude and the duration of an RF pulse. The shape of the pulse will determine the trajectory of the magnetization during the excitation period, but if the area of the envelope is the same ($B_1(t)$) the magnetization will end up at the same spatial position (for a perfect on resonance condition).

When the excitation field is **off resonance** (the RF rotating frame $\neq$ Larmor rotating frame), the effective magnetic field $\overrightarrow{B_{eff}}$ will be tilted from the transverse plain (in the RF rotating frame, Figure 1:3), using the Equation 1:20 we get:

$$\overrightarrow{B_{eff}} = \left(B_0 - \frac{\omega_{rf}}{\gamma}\right)\widehat{z'} + B_1(t)\widehat{x'} = \frac{\Delta\omega_0}{\gamma}\widehat{z'} + B_1(t)\widehat{x'}$$

Equation 1:27

where $\Delta\omega_0 = \omega_0 - \omega_{rf}$ is a measure of the degree of off-resonance. The magnetization will now precess about the $\overrightarrow{B_{eff}}$ leading to a more complex rotation in the case of the off-resonance excitation.
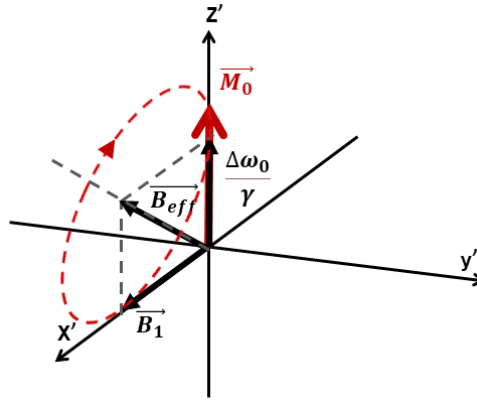
Figure 1:3: Off resonance excitation showing the effective field in the rotating frame and the precession of $\overrightarrow{M_0}$ about $\overrightarrow{B_{eff}}$.

1.4 Relaxation

The Equation 1:15 is a general description of time dependent behavior of the magnetization in the presence of an applied magnetic field during the excitation period only. If we consider also the relaxation process, the Bloch equation takes the following general form:

$$\frac{d\vec{M}}{dt} = \vec{M} \times \gamma\vec{B} - \frac{M_x\hat{x} + M_y\hat{y}}{T_2} - \frac{(M_z - M_0)\hat{z}}{T_1}$$

Equation 1:28

where the M_0 is the initial (equilibrium) value of magnetization ($M_{z,0}$). The magnetization was then perturbed from its equilibrium state by an RF pulse. After the end of this external force and provided that sufficient time has passed it will return to its original state. The recovery of longitudinal magnetization (M_z) is called the longitudinal relaxation (or spin-lattice relaxation) and it is in principle the process in which energy from the spins (accumulated from the RF pulse) is transferred to the surrounding 'lattice'. The destruction of the transversal magnetization ($M_{x,y}$) is called transverse relaxation (or spin-spin relaxation) and it is an entropy process, since the spins exchange energy among themselves causing a decrease in phase coherence (increase of entropy) until they are homogeneously distributed around $\overrightarrow{B_0}$ resulting in a zero transverse component. In the rotating frame Equation 1:28 can be expressed as:

$$\frac{\partial\overrightarrow{M_{rot}}}{\partial t} = \overrightarrow{M_{rot}} \times \gamma\overrightarrow{B_{eff}} - \frac{M_{x\prime}\widehat{x'} + M_{y\prime}\widehat{y'}}{T_2} - \frac{(M_{z\prime} - M_{z,0})\widehat{z'}}{T_1}$$

Equation 1:29

Since $\overrightarrow{B_{eff}} = B_1(t)\widehat{x'}$ and the $B_1(t) = 0$ after the end of the excitation pulse, the longitudinal and transverse relaxations in the rotating frame can be described as (on-resonance conditions):

$$\begin{cases} \dfrac{dM_{z\prime}}{dt} = -\dfrac{M_{z\prime} - M_{z,0}}{T_1} \\ \dfrac{dM_{x\prime y\prime}}{dt} = -\dfrac{M_{x\prime y\prime}}{T_2} \end{cases}$$

Equation 1:30

By solving these equations, we obtain the time evolution of the longitudinal and transverse magnetization:

$$\begin{cases} M_{x\prime y\prime}(t) = M_{x\prime y\prime}(0_+)e^{-\frac{t}{T_2}} \\ M_{z\prime}(t) = M_{z,0}\left(1 - e^{-\frac{t}{T_1}}\right) + M_{z\prime}(0_+)e^{-\frac{t}{T_1}} \end{cases}$$

Equation 1:31

Where the $M_{x\prime y\prime}(0_+)$ and $M_{z\prime}(0_+)$ are the magnetizations immediately after the RF pulse and the $M_{z,0}$ is the longitudinal magnetization before the RF pulse at thermal equilibrium. From the Equation 1:31 we can observe that both the decay of the transverse magnetization and the recovery of longitudinal magnetization follow an exponential function (Figure 1:4). Based on the Equation 1:31 and considering the relaxation after a 90° pulse which implies $M_{x\prime y\prime}(0_+) = M_{z,0}$ and $M_{z\prime}(0_+) = 0$ we can conclude that the T_1 and T_2 are not defined as the times when relaxation is complete but:

$$\begin{cases} M_{z\prime}(T_1) = 63\% M_{z,0} \\ M_{x\prime y\prime}(T_2) = 37\% M_{x\prime y\prime}(0_+) \end{cases}$$

Equation 1:32

The $M_{z\prime}$ will recover 63% of its thermal equilibrium value after the time T_1 and the $M_{x\prime y\prime}$ will lose 63% of its value after the RF pulse in the time T_2. These relaxation times depend on the tissue composition, structure, and surroundings of the spins and for a given system, T_1 is always longer than T_2.

Two different mechanisms cause the loss of the phase coherence of the transverse magnetization (T_2), the first one is described in the beginning of this paragraph and depicts the so called "pure" T_2 decay. The second comes from spatial variations of the magnetic field within the sample (body). These variations come from an imperfect magnet design (non-uniform magnetic field over the sample – macroscopic) and different magnetic susceptibilities of different tissues (local variations – microscopic). The loss of phase coherence caused by this second mechanism is characterized by the T_2^+ relaxation time. The "real" relaxation which dictates the decay of transverse magnetization is a combination of T_2 and T_2^+ and its marked as T_2^*:

$$\frac{1}{T_2^*} = \frac{1}{T_2^+} + \frac{1}{T_2}$$

Equation 1:33
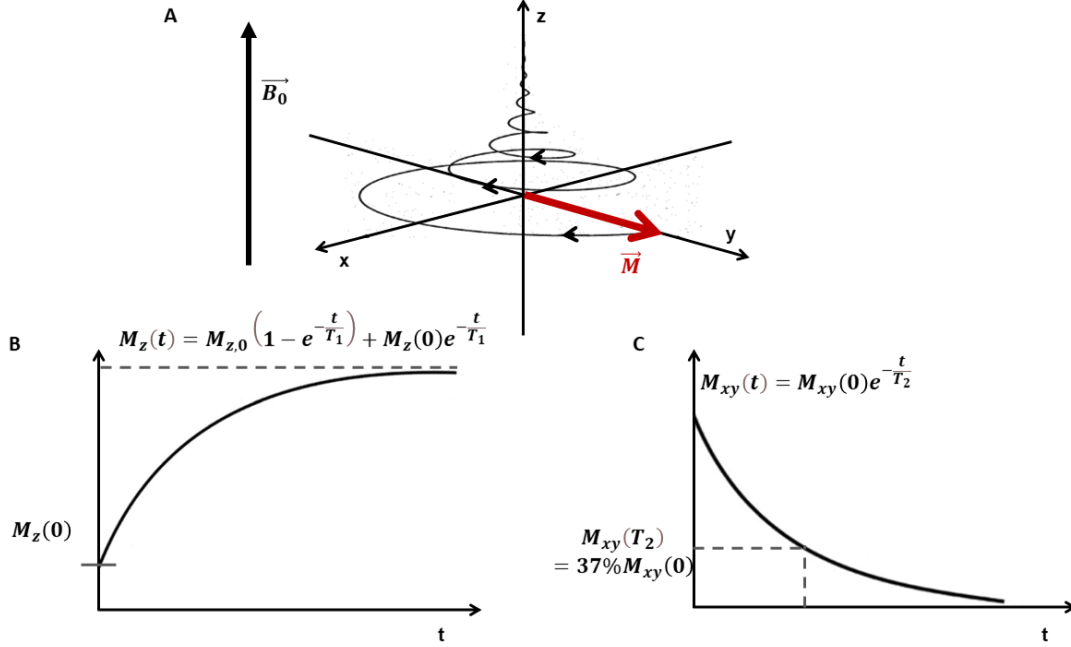
Figure 1:4: T_1 and T_2 relaxations. (A) The trajectory of the tip of magnetization after the excitation period (90° pulse) as observed in the laboratory frame; **(B)** Example of a longitudinal relaxation curve after the excitation pulse; **(C)** Transverse relaxation of the magnetization.

1.4.1   Free induction decay

After the RF pulse, magnetization is flipped to the transverse plane and is precessing around $\overrightarrow{B_0}$ with the Larmor frequency inducing the electromotive force (emf) in the receiving coil. As described in the paragraph 1.4 the transverse magnetization decays because of the T_2 relaxation and consequently reduces the emf. The macroscopic and microscopic $\overrightarrow{B_0}$ inhomogeneities will lead to a distribution of Larmor frequencies causing a more rapid decay (T_2^*). Thus, the acquired signal can be expressed as:

$$M_{xy}(t) = M_{xy}(0)e^{\frac{t}{T_2}} \int e^{+i\gamma\Delta B_0(r)t}dt = M_{xy}(0)e^{\frac{-t}{T_2^*}}$$

Equation 1:34

where the $\Delta B_0 = B_0(\vec{r}) - B_0$ indicates the field inhomogeneity and $B_0(\vec{r})$ being the magnetic field strength at a position $\vec{r}$. The $M_{xy}(t)$ is the complex transverse magnetization $M_{xy} = M_x + iM_y$ whose x and y components are (note that these equations also consider a possible offset in frequency – generalized for any offset ω):

$$M_x(t) = M_0 \cos[(\omega_0 - \omega)t + \varphi]e^{\frac{-t}{T_2^*}}$$

$$M_y(t) = M_0 \sin[(\omega_0 - \omega)t + \varphi]e^{\frac{-t}{T_2^*}}$$

Equation 1:35

where φ is a phase at $t = 0$. The detected time dependent decay of the emf (signal) is called the free induction decay (FID) and it is described by Equation 1:34 ($M_{xy}(t) = S(t)$). The detected FID is the signal in the time domain, and it is converted to the frequency domain signal (spectrum – giving the resonant frequencies present in the FID) using a Fourier transform (FT) according to:

$$F(\omega) = \int_{-\infty}^{+\infty} f(t)e^{-i\omega t}dt \quad \text{or} \quad F(v) = \int_{-\infty}^{+\infty} f(t)e^{-i2\pi vt}dt$$

Equation 1:36

This operation is reversible, meaning that time-domain signals can be calculated from the frequency-domain signal using the inverse FT:

$$f(t) = \frac{1}{2\pi}\int_{-\infty}^{+\infty} F(\omega)e^{+i\omega t}d\omega \quad \text{or} \quad f(t) = \frac{1}{2\pi}\int_{-\infty}^{+\infty} F(v)e^{+i2\pi vt}dv$$

Equation 1:37

Performing the FT on the time domain signal $S(t)$ (Equation 1:34) gives the real and imaginary frequency-domain signals:

$$S(t) \propto M_{xy}(0)e^{\frac{-t}{T_2^*}}e^{i(\omega_0-\omega)t+\varphi} \quad \xrightarrow{\textbf{FT}} \quad S(\omega) \propto M_{xy}(0)\int_0^\infty e^{\frac{-t}{T_2^*}}e^{i\omega_0 t+\varphi}e^{-i\omega t}dt = R(\omega) + iI(\omega)$$

$$R(\omega) = A(\omega)\cos\varphi - iD(\omega)\sin\varphi$$

$$I(\omega) = A(\omega)\sin\varphi + iD(\omega)\cos\varphi$$

Equation 1:38

Where:

$$A(\omega) = \frac{M_0 T_2^*}{1 + (\omega_0 - \omega)^2 T_2^{*2}}$$

$$D(\omega) = \frac{M_0(\omega_0 - \omega)T_2^{*2}}{1 + (\omega_0 - \omega)^2 T_2^{*2}}$$

Equation 1:39

are the absorption and dispersion components of the Lorentzian lineshape. The width of the absorption component at full width half maximum is $\frac{1}{\pi T_2^*}$, while the dispersion component is broader and has the intensity (integral) equal to zero. That is why when we observe the NMR spectrum we choose the absorption mode. When the phase is non-zero ($\varphi \neq 0$) the real part of the spectrum is a combination of absorption and dispersion signals. The desired absorption mode spectrum is then

obtained by phasing the observed/original spectrum. This can be achieved by adding a constant phase correction (φ_0 – zero order phase) or a linear, frequency dependent phase correction (φ_1 – first order phase). The resulting phase correction is performed as:

$$\varphi_c = \varphi_0 + (\omega - \omega_0)\varphi_1$$

Equation 1:40

The signal can also be given in the absolute mode (magnitude); this way of presenting the signal is chosen when the phase adjustment can't be properly carried out. The signal is then defined as:

$$M(\omega) = \sqrt{R(\omega)^2 + I(\omega)^2}$$

Equation 1:41

The addition of the dispersive components additionally broadens the spectrum in the absolute mode when compared to the absorption mode.
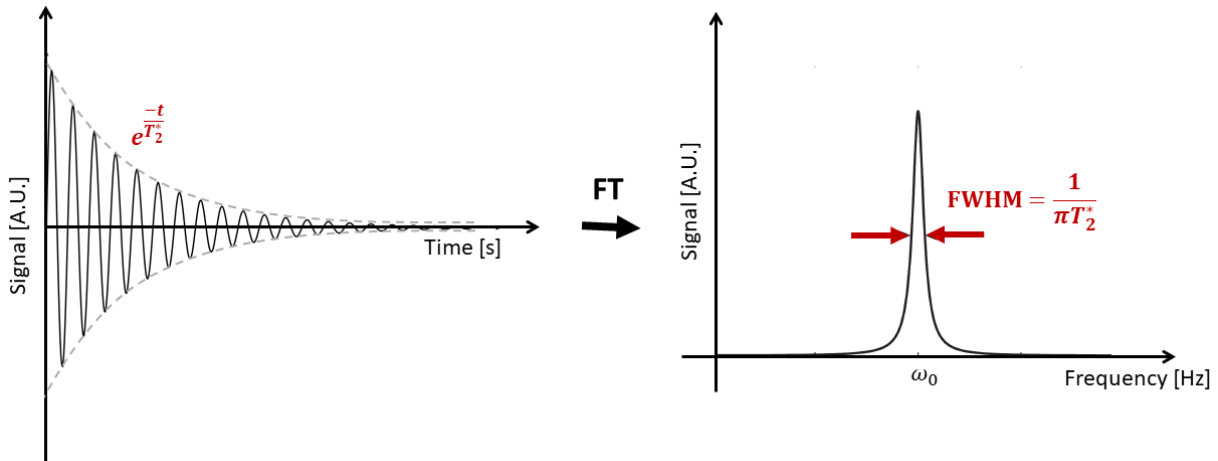
Figure 1:5: Time and frequency domain signal. The time-domain signal (FID) oscillating at the Larmor frequency is shown on the left. Its decay is governed by the T_2^* relaxation. Application of the Fourier transform on the FID gives us the frequency-domain signal. The absorption component of the Lorentzian peak centered at the Larmor frequency is shown on the left.

1.4.2 The Spin Echo and Inversion Recovery

The spin echo sequence is one of the fundamental pulse sequences and it was introduced by Hahn in 1950. This sequence has, in addition to the excitation 90° pulse, which flips the M_z into the transverse plane (M_{xy}), a 180° refocusing pulse (Figure 1:6). The loss of phase coherence of the transverse magnetization (M_{xy}) is explained in the section 1.3.1 and is governed by a "pure" T_2 decay caused by the spin-spin interactions and T_2^+ decay caused by spatial variations of the magnetic field. These spatial variations i.e. B_0 inhomogeneities and local magnetic susceptibilities are static effects and thus the static dephasing they cause is reversible. The application of an 180° pulse rotates the spins in the transverse plane. Leaving the same time after the application of the 180° pulse as the

time elapsed during dephasing ($TE/2$) will cause the spins to rephase (Figure 1:6). After the 180°

pulse, the magnetization is refocused and the spin echo (the signal maximum at the echo time -TE)

is generated[4,6].
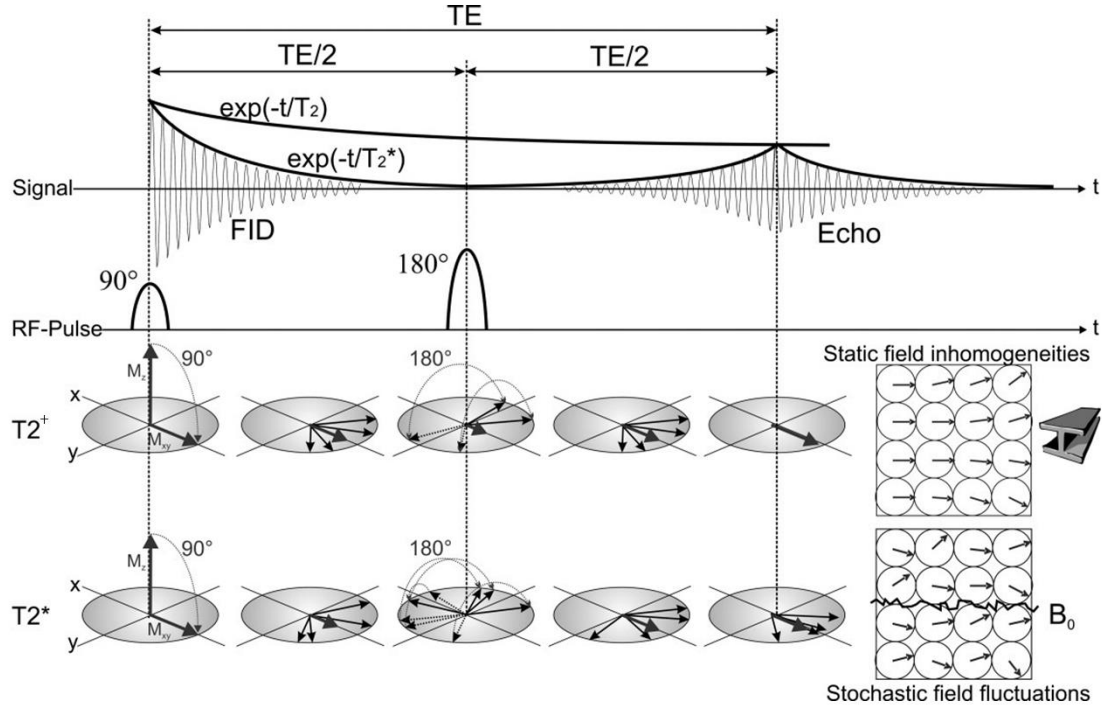
Figure 1:6: The spin echo sequence consists of the 90° excitation pulse and the 180° refocusing pulse. If only the spatial variations of the magnetic field (static field inhomogeneities) are considered (T_2^+ decay) the spins are fully rephased at TE. If in addition the magnetic field fluctuations caused by random spin-spin interactions are considered the signal decay is described by T_2^* according to the equation 1:33 and the signal amplitude at TE is reduced. The figure is taken from[6].

To sum up, the spin echo sequence cancels out the effect of T_2^+. Thus, the value of T_2 can be measured using the spin echo sequence if a series of experiments with n varying TEs is performed. Then the measured signal is proportional to $M_{xy}(0)e^{\frac{-TE_n}{T_2}}$. A graph of $\ln S(TE_n)$ (measured signal on the logarithmic scale) versus TE_n gives a straight line with the slope of $\frac{1}{T_2}$.

In addition to the T_1 relaxation time, the T_1 relaxation time which governs the recovery of longitudinal magnetization (M_z) can also be measured. For this we will introduce the inversion recovery (IR) method with an additional 180° pulse (the inversion pulse) placed before the excitation 90° pulse (Figure 1:7). The time between these two pulses can be varied and it is called the inversion time (TI). The 180° inversion pulse flips (inverts) the longitudinal magnetization ($M_z \rightarrow -M_z$). During the inversion time the magnetization can relax back to its thermal equilibrium value with a T_1

time constant. Since the excitation pulse is applied immediately after the inversion time, the duration of TI determines how much of the magnetization is available for excitation and thus the amplitude of the resulting signal. A series of experiments with different TIs results in the discrete sampling of the inversion recovery curve ($M_{z,0}\left(1 - 2e^{-\frac{TI}{T_1}}\right)$). As for the T_2 measurement, the graph of $\ln S(TI_n)$ versus TI_n gives a straight line with the slope of $\frac{1}{T_1}$. The example of a spin echo based inversion recovery sequence is shown in the Figure 1:7 Relaxation times depend on the tissue type and the molecule size, so by an adequate choice of TI the signal from an unwanted tissue type or molecule can be eliminated[4,6].
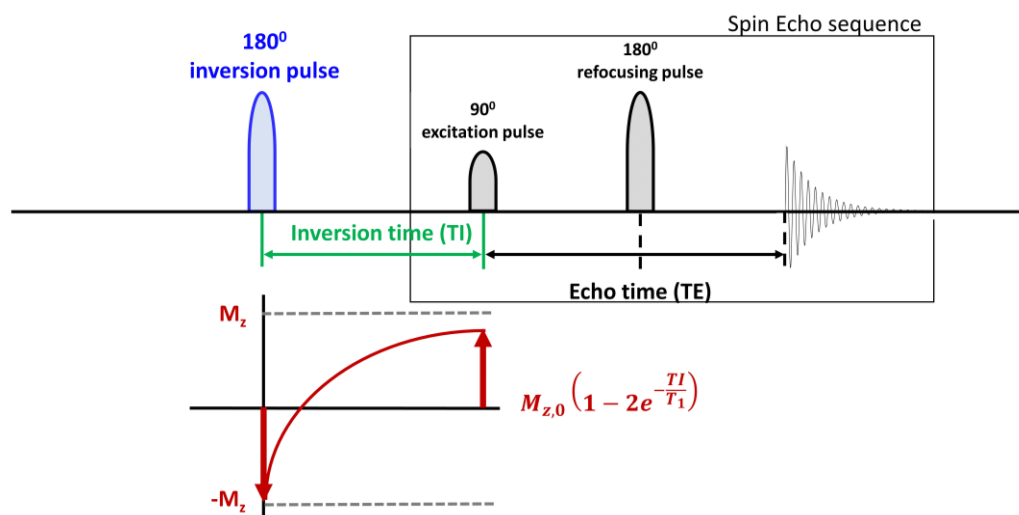
Figure 1:7: A scheme of an inversion recovery spin echo sequence. The inversion pulse inverts the longitudinal magnetization, then it relaxes back to its thermal equilibrium with a T_1 relaxation time constant. The choice of the inversion time (TI) determines how much of the magnetization has recovered and will be further excited by the excitation pulse. A series of experiments with different inversion times will result in a discrete sampling of the T_1 recovery curve.

1.4.3   Chemical shift

As explained in the previous chapters, the resonance frequency of a nucleus depends on its gyromagnetic ratio γ and the external magnetic field B_0. This would mean that the same nucleus in different molecules would resonate at the same frequency since γ is a property of the nucleus. However, the resonance frequency is also highly dependent on its chemical environment (surrounding electrons). The movement of electrons in orbitals is modified when put in an external magnetic field ($\vec{B}_0$) and it results in a small additional magnetic field of opposite polarity to $\vec{B}_0$ and thus reduce it (electrons have both angular momentum and spin). The phenomenon resulting from this shielding

of nuclei from the external magnetic field is called chemical shift. The effective magnetic field that the nucleus feels is given by:

$$B_{eff} = B_0(1 - \sigma)$$

Equation 1:42

Where σ is called a shielding constant and it is dependent on the chemical environment surrounding the nucleus. Now, the Equation 1:9 can be rewritten using the expression 1:42:

$$\nu = -\left(\frac{\gamma}{2\pi}\right)B_0(1 - \sigma)$$

Equation 1:43

Expressing the chemical shift in Hz would make it dependent from the applied B_0 field strength. Instead, the chemical shifts are typically expressed in $[ppm]$ and defined as:

$$\delta = \frac{\nu - \nu_{ref}}{\nu_{ref}} \times 10^6$$

Equation 1:44

Where the ν is the frequency of the nucleus under investigation and ν_{ref} is the frequency of the reference compound. This compound should be chemically inert, have a strong singlet resonance and its chemical shift should be independent of external variables (temperature etc.). For ^{1}H-NMR the tetramethyl silane (TMS) is generally used as a reference and is assigned to $\delta = 0\ ppm$. Because the in vivo samples do not contain TMS, it cannot be used as an internal reference for this application. Therefore, for in vivo brain ^{1}H MRS the methyl resonance of N-acetyl aspartate (NAA) at $\delta = 2.01\ ppm$ is used (in fact, they can be referenced to TMS indirectly through water resonance at 4.6 ppm and then the shift of NAA is derived from it), while for ^{31}P-MRS of the brain and muscle the phosphocreatine (PCr) resonance at $\delta = 0\ ppm$ is used.

1.4.4   Scalar coupling

Apart from the local electron density effect on the Larmor frequency, the surrounding nuclei also affect the Larmor frequency. This affect is called the scalar coupling or J-coupling and it is responsible for the "fine structure" observable in the NMR spectra. J-coupling refers to the splitting of NMR transitions by nuclei connected with chemical bonds in the same molecule. In other words, how the nuclear spin state of one nucleus affects the spin state of another nucleus (chemically bonded) because of the electron spins in the chemical bond (via the polarization of chemical bonds). When a stable chemical bond is created, the molecular orbitals are filled according to the Hund's rules:

1. Electrons in the same molecular and atomic orbitals are more stable when their spins are antiparallel

2. Electrons in the different orbitals are more stable if their spins are antiparallel

3. Electron and nuclear spin angular momenta are more stable if antiparallel

When a bond is created, first the antiparallel electron spin configuration is imposed which influences the nuclear spin orientations.

If we take a two-spin system as an example with two nuclei resonating at different chemical shifts. The resonant frequencies of the two nuclei will be $\nu_{0,1}$ and $\nu_{0,2}$. Following the Hund's rules, if the spin systems 1 and 2 are chemically bonded, the antiparallel orientation between the electron and nuclear spin is not always possible and will cause a shift (increase) in the energy level. However, if the spin states are more favorably combined the energy level decreases (Figure 1:8).

Going back to quantum mechanical description, the Hamiltonian for one spin (Chapter 1.1 – equation 1:5) can be extended to two spins as (in frequency units):

$$\widehat{H}_{two\ spins,no\ coupling} = -\nu_{0,1}\hat{I}_{1z} - \nu_{0,2}\hat{I}_{2z}$$

Equation 1:45

where $\hat{I}_{1z}$ is the operator for the z-component of angular momentum of the first spin and $\hat{I}_{2z}$ of the second spin. The Larmor frequency of the first spin is given by $\nu_{0,1}$ and of the second spin $\nu_{0,2}$. For now, they are considered as uncoupled spins. The corresponding eigenfunctions are just products of the eigenfunctions of $\hat{I}_z$ for each spin:

$$\begin{cases} \hat{I}_{1z}\psi_{\alpha,1} = +\dfrac{1}{2}\psi_{\alpha,1} & \hat{I}_{1z}\psi_{\beta,1} = -\dfrac{1}{2}\psi_{\beta,1} \\ \hat{I}_{2z}\psi_{\alpha,2} = +\dfrac{1}{2}\psi_{\alpha,2} & \hat{I}_{2z}\psi_{\beta,2} = -\dfrac{1}{2}\psi_{\beta,2} \end{cases}$$

Equation 1:46

To show that $\psi_{\alpha,1}\psi_{\beta,2}$ is, in fact, the eigenfunction of $\widehat{H}_{two\ spins,no\ coupling}$ we calculate:

$$\widehat{H}_{two\ spins,no\ coupling}\psi_{\alpha,1}\psi_{\beta,2} = -\big(\nu_{0,1}\hat{I}_{1z} + \nu_{0,2}\hat{I}_{2z}\big)\psi_{\alpha,1}\psi_{\beta,2}$$

$$= -\nu_{0,1}\hat{I}_{1z}\psi_{\alpha,1}\psi_{\beta,2} - \nu_{0,2}\hat{I}_{2z}\psi_{\alpha,1}\psi_{\beta,2} = -\nu_{0,1}\big[\hat{I}_{1z}\psi_{\alpha,1}\big]\psi_{\beta,2} - \nu_{0,2}\psi_{\alpha,1}\big[\hat{I}_{2z}\psi_{\beta,2}\big]$$

Equation 1:47

Using the equation 1:46 we can find:

$$\widehat{H}_{two\ spins,no\ coupling}\psi_{\alpha,1}\psi_{\beta,2} = -\nu_{0,1}\big[\hat{I}_{1z}\psi_{\alpha,1}\big]\psi_{\beta,2} - \nu_{0,2}\psi_{\alpha,1}\big[\hat{I}_{2z}\psi_{\beta,2}\big]$$

$$= -\frac{1}{2}\nu_{0,1}\psi_{\alpha,1}\psi_{\beta,2} + \frac{1}{2}\nu_{0,2}\psi_{\alpha,1}\psi_{\beta,2} = \left[-\frac{1}{2}\nu_{0,1} + \frac{1}{2}\nu_{0,2}\right]\psi_{\alpha,1}\psi_{\beta,2}$$

<div align="center">Equation 1:48</div>

We can now conclude that $\psi_{\alpha,1}\psi_{\beta,2}$ is an eigenfunction of the Hamiltonian and that $-\frac{1}{2}\nu_{0,1} + \frac{1}{2}\nu_{0,2}$ is its eigenvalue (the energy). Repeating the same procedure, we can find that there are three more eigenfunctions with the corresponding eigenvalues shown in the Table 1:3.

<div align="center">**Table 1:3: Eigenfunctions and eigenvalues of the two spins with no coupling** (in Hz)</div>

m_1	m_2	SPINSTATES	EIGENFUNCTION	EIGENVALUE (ENERGY)
$+\dfrac{1}{2}$	$+\dfrac{1}{2}$	$\alpha\alpha$	$\psi_{\alpha,1}\psi_{\alpha,2}$	$-\dfrac{1}{2}\nu_{0,1} - \dfrac{1}{2}\nu_{0,2}$
$+\dfrac{1}{2}$	$-\dfrac{1}{2}$	$\alpha\beta$	$\psi_{\alpha,1}\psi_{\beta,2}$	$-\dfrac{1}{2}\nu_{0,1} + \dfrac{1}{2}\nu_{0,2}$
$-\dfrac{1}{2}$	$+\dfrac{1}{2}$	$\beta\alpha$	$\psi_{\beta,1}\psi_{\alpha,2}$	$+\dfrac{1}{2}\nu_{0,1} - \dfrac{1}{2}\nu_{0,2}$
$-\dfrac{1}{2}$	$-\dfrac{1}{2}$	$\beta\beta$	$\psi_{\beta,1}\psi_{\beta,2}$	$+\dfrac{1}{2}\nu_{0,1} + \dfrac{1}{2}\nu_{0,2}$

From the Table 1:3 we can define the general expression for the energy levels (eigenvalues):

$$E_{m_1,m_2} = -m_1\nu_{0,1} - m_2\nu_{0,2}$$

<div align="center">Equation 1:49</div>

If we now introduce the scalar coupling, we can rewrite the Hamiltonian by adding a third term:

$$\hat{H}_{two\ spins} = -\nu_{0,1}\hat{I}_{1z} - \nu_{0,2}\hat{I}_{2z} + J_{12}\hat{I}_{1z}\hat{I}_{2z}$$

<div align="center">Equation 1:50</div>

Where J_{12} is the scalar coupling between the spins 1 and 2 (in Hz). Here we consider only the weak-coupled system ($|\nu_{0,1} - \nu_{0,2}| \gg J_{12}$). The wavefunctions listed in the Table 1:3 are still the eigenfunctions of the Hamiltonian but have different eigenvalues. We can show this by solving the eigenvalue equation only for the coupling term $J_{12}\hat{I}_{1z}\hat{I}_{2z}$, which gives:

$$J_{12}\hat{I}_{1z}\hat{I}_{2z}\psi_{\alpha,1}\psi_{\beta,2} = J_{12}[\hat{I}_{1z}\psi_{\alpha,1}][\hat{I}_{2z}\psi_{\beta,2}] = J_{12}\left[\frac{1}{2}\psi_{\alpha,1}\right]\left[-\frac{1}{2}\psi_{\beta,2}\right] = -\frac{1}{4}J_{12}\psi_{\alpha,1}\psi_{\beta,2}$$

<div align="center">Equation 1:51</div>

We have now proved that the $\psi_{\alpha,1}\psi_{\beta,2}$ is an eigenfunction of the coupling term of the Hamiltonian with an eigenvalue of $-\frac{1}{4}J_{12}$. Since we already showed that the same wavefunction is an eigenfunction of the $-\nu_{0,1}\hat{I}_{1z} - \nu_{0,2}\hat{I}_{2z}$ (equation 1:48) it can be concluded that it is also the eigenfunction of the sum of these terms ($-\nu_{0,1}\hat{I}_{1z} - \nu_{0,2}\hat{I}_{2z} + J_{12}\hat{I}_{1z}\hat{I}_{2z}$). The resulting eigenvalue is, as follows, the sum of the eigenvalues of the two individual terms ($-\frac{1}{2}\nu_{0,1} + \frac{1}{2}\nu_{0,2} - \frac{1}{4}J_{12}$). Applying the same procedure on to the remaining product functions we can obtain the remaining energy levels (Table 1:4).

From the Table 1:4 we can define the general expression for the energy levels (eigenvalues):

$$E_{m_1,m_2} = -m_1 \nu_{0,1} - m_2 \nu_{0,2} + m_1 m_2 J_{12}$$

Equation 1:50

Table 1:4: Eigenfunctions and eigenvalues of the two coupled spins (in Hz)

m_1	m_2	SPINSTATES	EIGENFUNCTION	EIGENVALUE (ENERGY)
$+\dfrac{1}{2}$	$+\dfrac{1}{2}$	$\alpha\alpha$	$\psi_{\alpha,1}\psi_{\alpha,2}$	$-\dfrac{1}{2}\nu_{0,1} - \dfrac{1}{2}\nu_{0,2} + \dfrac{1}{4}J_{12}$
$+\dfrac{1}{2}$	$-\dfrac{1}{2}$	$\alpha\beta$	$\psi_{\alpha,1}\psi_{\beta,2}$	$-\dfrac{1}{2}\nu_{0,1} + \dfrac{1}{2}\nu_{0,2} - \dfrac{1}{4}J_{12}$
$-\dfrac{1}{2}$	$+\dfrac{1}{2}$	$\beta\alpha$	$\psi_{\beta,1}\psi_{\alpha,2}$	$+\dfrac{1}{2}\nu_{0,1} - \dfrac{1}{2}\nu_{0,2} - \dfrac{1}{4}J_{12}$
$-\dfrac{1}{2}$	$-\dfrac{1}{2}$	$\beta\beta$	$\psi_{\beta,1}\psi_{\beta,2}$	$+\dfrac{1}{2}\nu_{0,1} + \dfrac{1}{2}\nu_{0,2} + \dfrac{1}{4}J_{12}$

The selection rules for the allowed transitions in the two-spin system postulate that the m of one of the spins can change by ∓ 1. In other words, the quantum number of the first spin m_1 can change by ∓ 1 and the quantum number of the second spin m_2 can change by ∓ 1. By applying these rules, we get that only four transitions are allowed (Figure 1:8). For example, for the transition $\alpha\alpha \to \alpha\beta$ we get:

$$\nu_{\alpha\alpha \to \alpha\beta} = E_{\alpha\beta} - E_{\alpha\alpha} = -\frac{1}{2}\nu_{0,1} + \frac{1}{2}\nu_{0,2} - \frac{1}{4}J_{12} - \left(-\frac{1}{2}\nu_{0,1} - \frac{1}{2}\nu_{0,2} + \frac{1}{4}J_{12}\right) = +\nu_{0,2} - \frac{1}{2}J_{12}$$

Equation 1:51

Table 1:5: Resulting frequencies of the allowed transitions for two coupled spins.

SPIN STATES	FREQUENCY
$\alpha\alpha \to \alpha\beta$	$\nu_{0,2} - \dfrac{1}{2}J_{12}$
$\beta\alpha \to \beta\beta$	$\nu_{0,2} + \dfrac{1}{2}J_{12}$
$\alpha\alpha \to \beta\alpha$	$\nu_{0,1} - \dfrac{1}{2}J_{12}$
$\alpha\beta \to \beta\beta$	$\nu_{0,1} + \dfrac{1}{2}J_{12}$

As, emphasized this calculation and the Figure 1:8 are valid when the frequency difference between the two scalar coupled spins is much bigger than the coupling ($\left|\nu_{0,1} - \nu_{0,2}\right| \gg J_{12}$) which is typically valid for heteronuclear scalar coupling. However, for many homonuclear interactions the frequency difference is of the same order of magnitude as the coupling constant, resulting in a strongly coupled

system. This leads to mixing of the $\alpha\beta$ and $\beta\alpha$ states (for a two-spin system) and the resulting spectrum becomes more complicated. If there is more than one coupling partner, the resonance split into (n+1) lines when coupled to "n" equivalent nuclei. The Pascal's triangle (series of numbers with patterns that are predicted from the previous row) can predict this number of splittings and the ratio of amplitudes. Unlike chemical shift, J-coupling is not dependent on the external magnetic field B_0. The J-coupling constant provides crucial information on the molecular structure and composition.
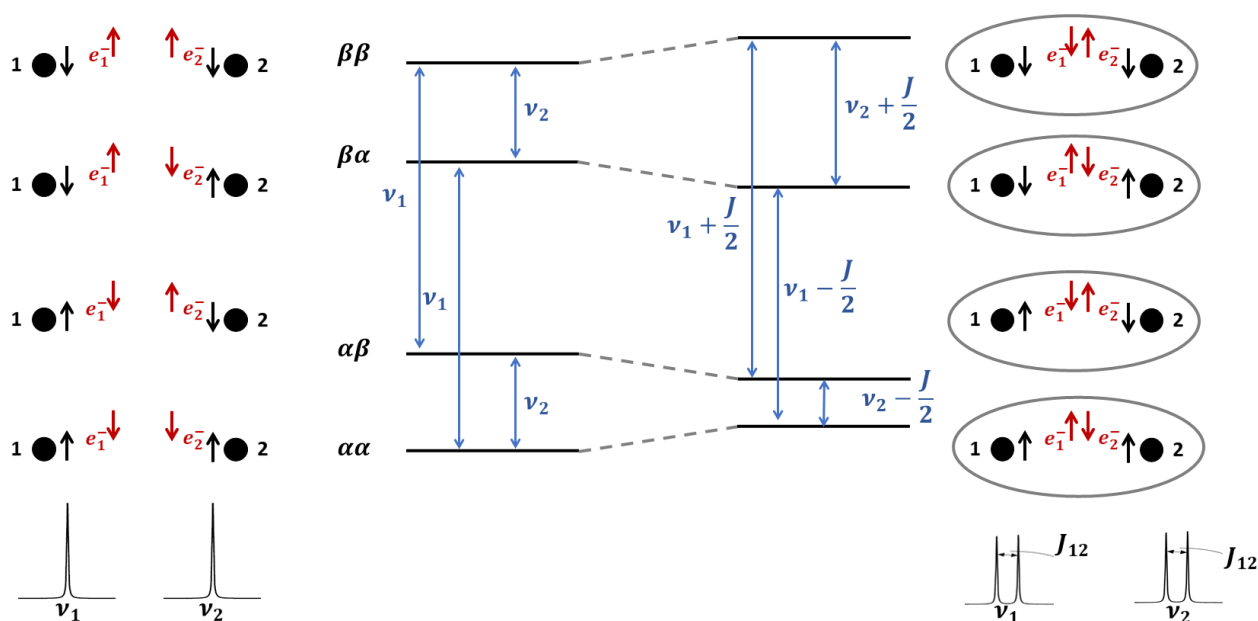
Figure 1:8: J-coupling. (left) Two nuclei (two atoms – nuclear spin in black and electron spin in red) that resonate at different chemical shifts and are not chemically bonded (no scalar coupling). The arrangement between nuclear and electron spin in each atom is antiparallel. The energy level diagram of these spins describes two energy transitions, resulting in only two resonances. **(right)** When the atoms are chemically bonded according to Hund's rules the electron spins prefer the antiparallel orientation among them, and the nuclear and electron spins also prefer the antiparallel orientation. The forced parallel orientation to the nuclear spins will cause the states $\alpha\alpha$ and $\beta\beta$ to have an increase in energy, while $\alpha\beta$ and $\beta\alpha$ will have a decrease because of their favorable spin orientations. The allowed transitions are described in Table 1:5, and result in a splitting of the resonance 1 and 2 by the coupling constant J_{12}. (Heteronuclear interaction)

1.5   MRI principles

The discovery of magnetic resonance imaging (MRI) came from the realization that if there is a varying magnetic field across the sample, the resonant frequencies at each position are different (e.g. frequency becomes linearly dependent on the spatial position). The spatially varying magnetic field (i.e. magnetic field with amplitude varying linearly with position) is called the magnetic field gradient and its creation requires specially shaped coils installed in the magnet bore. There are usually three

sets of gradient coils installed in the magnet depending on the direction in which the magnetic field strength changes (X, Y and Z gradients). If we describe them mathematically, the magnetic field gradient amplitude varies linearly (as a function of the position r) over the region to be imaged:

$$G(r) = \frac{dB(r)}{dr} = constant$$

Equation 1:51

Where B is the strength of the magnetic field and r represents the x, y and z directions or their vectorial combination. The gradient direction always refers to the direction in which the magnetic field strength varies as result of the applied gradient. The MRI systems are usually positioned horizontally, therefore the resulting B_0 magnetic field they produce is also oriented horizontally. Since by definition B_0 is always in the $\hat{z}$ direction, this axis lies along the horizontal (see Figure 1 :9A) and the $\hat{y}$ and $\hat{x}$ are defined accordingly. The gradient coils are designed such that the magnetic field they produce adds to the B_0 on one side, subtracts from it on the other side and has no contribution in the isocenter ($z = 0, y = 0, x = 0$) of the magnet. Thus, in the isocenter the resulting magnetic field is equal to B_0 (Figure 1:9A). The resulting magnetic field over the sample is then dependent on the position as:

$$B(r) = B_0 + rG_r, \qquad e.g. in\ \hat{z}\ direction\ \rightarrow\ B_z = B_0 + zG_z$$

Equation 1:52

Where the G is expressed in Tesla per meter $\left[\frac{T}{m}\right]$ or Gauss per centimeter $\left[\frac{G}{cm}\right]$, with $1T = 10000G$. The position dependent frequency can then be expressed as:

$$\omega_z = -\gamma B_z = -\gamma(B_0 + zG_z) \xrightarrow{rotating\ frame} \omega_z = -\gamma zG_z$$

Equation 1:53

The expression for the spatial dependence of resonant frequencies in the presence of gradients in x and y direction can be obtained in the same way as in the equation 1:53.

The MRI image formation process consists of three parts: slice selection, phase encoding and frequency encoding.
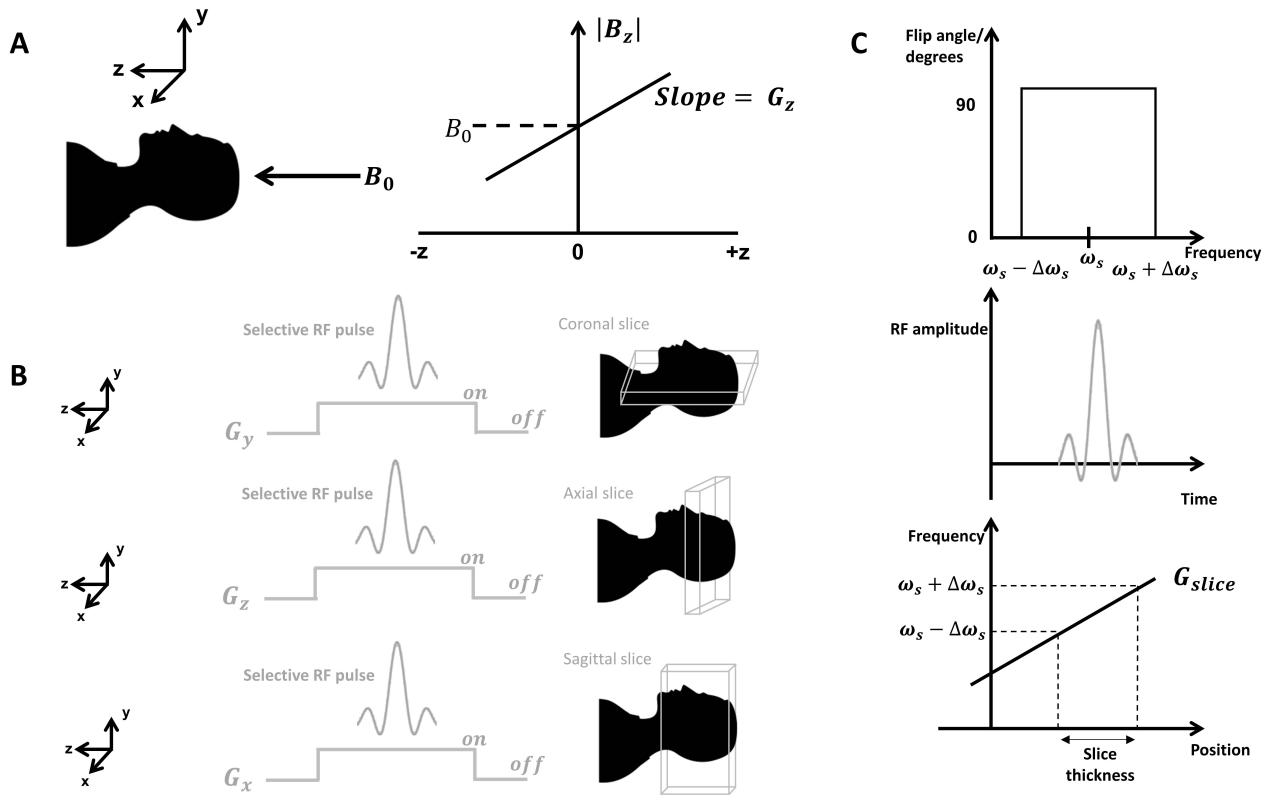
Figure 1:9: Gradients and slice selection. (A) The coordinate system defined (on the left) and the linear magnetic field gradient applied in the $\hat{z}$ direction. A linear magnetic field gradient applied in the z direction creates a linear spatial dependence of the effective magnetic field. **(B)** Slice selection. By using a selective RF pulse in combination with a magnetic field gradient in x, y, z direction a coronal, axial or sagittal slice can be chosen. **(C)** Example of a sinc pulse which flips (excites) the magnetization by 90° only in the selected frequency range between $\omega_s - \Delta\omega_s$ and $\omega_s + \Delta\omega_s$.

1.5.1 Slice selection

The problem of imaging a three-dimensional object is simplified, reducing it to a two dimensional one by selecting a slice with defined thickness and orientation. The slice is selected by simultaneous application of an RF pulse and the magnetic field gradient. If the gradient is applied in the $\hat{z}$ direction, each position in this direction is characterized by a specific magnetic field and thus a specific resonant frequency as described in the equations 1:52 and 1:53. The choice of gradient direction determines the orientation of the slice which can be coronal, axial and sagittal (see Figure 1:9B). When an RF pulse is intended to excite only a selective frequency range it is applied concurrently with the gradient. Thus, only a selected range of frequencies and consequently spatial positions is excited. This kind of RF pulses are called slice selective or frequency selective RF pulses. If, for example, the slice selective RF pulse is applied at a frequency ω_s and has a bandwidth of $\pm\Delta\omega_s$ only the frequencies in the range between $\omega_s - \Delta\omega_s$ and $\omega_s + \Delta\omega_s$ are excited. The thickness (T) of the selected slice is dependent on the pulse frequency bandwidth ($2\Delta\omega_s = 2\pi BW$) and the gradient strength (Figure 1 :9C):

$$T = \frac{2\Delta\omega_s}{\gamma G_{slice}}$$

Equation 1:54

The slice thickness can be changed by changing the gradient strength (G_{slice}, where increasing it leads to a thinner slice and decreasing to a thicker one) or by increasing the bandwith of the RF pulse (e.g. shortening its duration). Because of the FT properties, a longer RF pulse results in a thinner slice (narrower frequency spectrum). Changing the center/transmitter frequency of an RF pulse (ω_s) results in moving the slice to different positions across the sample. The gradient strength affects both the slice thickness and its position, thus for a given RF pulse length the required gradient strength is usually determined first ($G_{slice} = \frac{RF\ bandwidth}{slice\ thickness}$) followed by the transmitter frequency selection which determines the slice position. Multiple slices with an offset between each other can also be acquired.

During an RF pulse the nuclei within the slice continue to precess around B_0 and accumulate different phases depending on their position within the slice. If we take the example of a gradient applied in the $\hat{z}$ direction (G_z) the phase accumulation can be expressed as (valid for most of the symmetric pulse shapes):

$$\phi_{sl}(z) = \gamma G_z z \frac{\tau}{2}$$

Equation 1:55

where τ is the pulse duration and z the position within the slice. To overcome this loss of coherence we apply a rephasing gradient of the opposite polarity (G_z^{ref}, τ^{ref}, in case of a 90° pulse). If we assume that the gradient waveforms are rectangular, the refocusing occurs for:

$$G_z^{ref} \tau^{ref} = \frac{\tau}{2} G_z$$

Equation 1:56

1.5.2   Frequency Encoding

After selecting a slice, two dimensions need to be encoded in order to produce an image. One dimension is encoded by imposing a spatially dependent phase on the signal and the other one by creating a spatially dependent frequency during acquisition. The phase is encoded by a gradient turned on before the data acquisition (while the magnetization is in the transverse plain) and the frequency by a gradient turned on during the data acquisition. The frequency encoding magnetic field gradient causes the water hydrogens nuclear spins at different positions to obtain different

Larmor frequencies linearly dependent on their spatial position. Since this gradient is applied during the acquisition of the signal, different Larmor frequencies are directly detected. The FT of the detected signal will give an MR spectrum representing a 1D projection of the spin density distribution along the direction of the applied gradient. The detected frequency range is determined by the spectral width according to the Nyquist sampling theorem:

$$frequency\ range = spectral\ width\ (SW) = \frac{1}{\Delta t}\ ,\ \ \Delta t - dwell\ time$$

<center>Equation 1:57</center>

Nyquist sampling theorem: Any sinusoidal signal of frequency f can be accurately described when it is sampled at least twice per cycle. The minimum sampling rate is called the Nyquist frequency (f_N). The spectral width is equal to $2f_N$ since the frequencies between $-f_N$ and $+f_N$ are accurately sampeled. The time between the sampled data points is also kown as dwell time ($\Delta t = \frac{1}{SW}$).

For MRI applications the position range (field of view – FOV) is obtained by division of the frequency range (SW) by the gradient strength. The easiest way to acquire the 1D projection of a spin density distribution would be a pulse acquire method where the frequency encoding gradient is applied during acquisition. Because the gradient cannot be turned on instantaneously, the few first data points are acquired during the gradient rise time (time varying gradient) leading to artifacts when the FT is performed. Eliminating the first few points of the FID would greatly reduce the signal to noise ratio (SNR). A more convenient way to attain the spatial information is to acquire an echo instead of an FID. The echo formation belonging to the gradient-echo techniques will be explained in this section. Together with the spin echo techniques (section 1.4.2) represent the basics of the MRI methods.

The **gradient echo** sequence consists of an excitation RF pulse, a gradient applied before the signal acquisition and another gradient of opposite polarity and twice the area applied during the signal acquisition. The first gradient prepares the magnetization for the encoding of spatial information. At a position $\vec{r}$ it generates a phase shift:

$$\phi_1(\vec{r},t) = \gamma\vec{r}\int_0^t \overrightarrow{G_1}(t')dt'\ ,\ \ for\ \overrightarrow{G_1}(t) = \overrightarrow{G_1} \rightarrow \phi_1(\vec{r},t) = \gamma\vec{r}\overrightarrow{G_1}\,t$$

<center>Equation 1:58</center>

The transverse magnetization at each position $\vec{r}$ is now encoded with a specific phase shift $\phi_1(\vec{r})$. The second gradient has twice the area and an opposite polarity to the first one, therefore the total applied gradient in the middle of the second gradient is zero (Figure 1:10) and the acquired phase

shift is also zero. During the first gradient the transverse magnetization acquired a linear position dependent phase shift, thus to fulfill the $\phi(\vec{r}) = 0$ condition in the middle, the spins at different positions need to rotate at different frequencies. The frequencies are related to the initial acquired phase shift according to:

$$\omega(\vec{r}) = \frac{d\phi(\vec{r},t)}{dt} \quad where \quad \phi(\vec{r},t)$$

$$= \phi_1(\vec{r},T_1) + \gamma\vec{r}\int_0^t \overrightarrow{G_2}(t')dt' \xrightarrow{\overrightarrow{G_2}(t)=\overrightarrow{G_2}} \phi(\vec{r},t) = \phi_1(\vec{r},T_1) + \gamma\vec{r}\overrightarrow{G_2}\,t$$

<div align="center">Equation 1:59</div>

Where the T_1 is the lenght of the first gradient and the G_2 the amplitude of the second gradient (opposite polarity to the G_1) resulting in a decrease of $\phi(\vec{r},t)$ in time. The echo forms when the total net gradient is zero:

$$\phi(\vec{r}) = 0 \quad when \quad \phi_1(\vec{r},T_1) = -\phi_2\left(\vec{r},\frac{T_2}{2}\right) \rightarrow G_1T_1 = -G_2\frac{T_2}{2}$$

<div align="center">Equation 1:60</div>

Where $\frac{T_2}{2}$ is equal to half of the acquisition time. The signal is acquired during the 'readout' gradient (second gradient) so that the spatially dependent frequencies from equation 1:59 are stored and will result in the spatial distribution of spins after the FT. The echo is acquired during a period of constant gradient amplitude and will give an undistorted spatial profile after the FT. This procedure is called frequency encoding and it is the most commonly used method to obtain spatial 1D information.
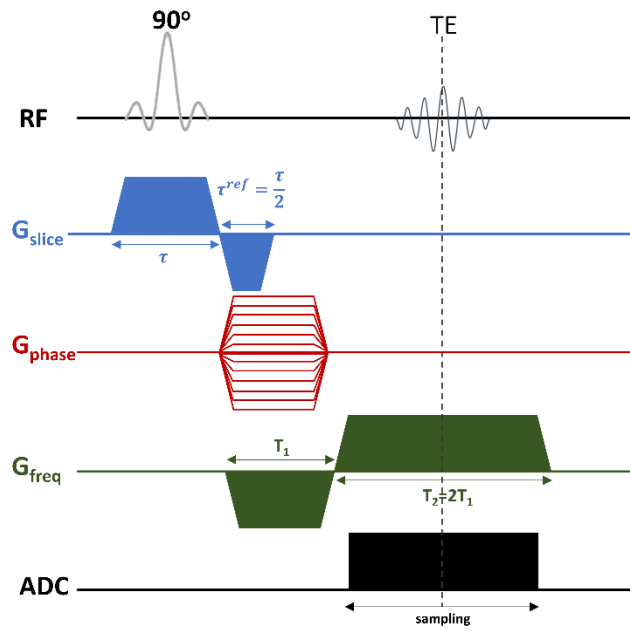
Figure 1:10: Schematic diagram of a 2D gradient echo sequence

1.5.3 Phase encoding

In the Figure 1:10 the frequency encoding gradient is shown as G_{freq} and the phase encoding gradient as G_{phase}. To get the information about the second spatial dimension a series of experiments needs to be performed with linearly incrementing the phase encoding gradient strength. During each of these experiments the signal is acquired in presence of the frequency encoding gradient so the echo is stored in a 2D matrix also called the spatial frequency or k-space. The phase encoding gradient is always positioned before the acquisition (Figure 1:10 in red) so it only influences the phase of the signal. The phase changes linearly with the amplitude of G_{phase} and results in an indirect frequency ($\omega = \frac{d\phi}{dt}$) that is independent of the frequencies acquired during the frequency encoding. The frequency encoding is used to resolve the signal distribution along the first dimension while during the phase encoding, the signal acquires a phase that is linearly dependent on its position along the second dimension (phase encoding gradient direction). The FT of the phase modulated signal with respect to the phase encoding gradient amplitude generates the second dimension of a 2D image of the object.

1.5.4 K-space formalism

A very useful model for understanding how the acquired data matrix is transformed to the final image is the k-space formalism which provides a simple FT relationship between the two. If we

describe the echo formation using an ensemble of spins, the transverse magnetization and its precession can be described as:

$$M_{xy} = M_x + iM_y, \qquad M_{xy}(\vec{r}, t) = M_{xy}(\vec{r}, 0)e^{+i\Delta\omega(\vec{r})t}$$

Equation 1:61

Where

$$\Delta\omega(\vec{r}) = (\omega_0 - \omega) + \gamma\vec{r}\vec{G}$$

Equation 1:62

ω_0 is the Larmor frequency and ω the carrier frequency. Equation 1:61 can then be rewritten as:

$$M_{xy}(\vec{r}, t) = M_{xy}(\vec{r}, 0)e^{+i\Delta\omega t}e^{i\gamma\vec{r}\vec{Gt}}$$

Equation 1:63

If we generalize this expression by describing the observed signal in the presence of time-dependent magnetic field gradient $G(t)$:

$$M_{x,y}(\vec{G}, t) = \int M_0(\vec{r})e^{+i\gamma\vec{r}\int\vec{G}(t')dt'}dr$$

Equation 1:64

where $M_0(\vec{r})$ is the spin density at position $\vec{r}$ after the 90^0 pulse and the second part of the term is the phase, dependent on the position. This equation should be multiplied with a relaxation or a diffusion describing term depending on the characteristics of the sequence used. By defining the frequency variable-position dependence (spatial frequency variable) as:

$$k(t) = \gamma \int \vec{G}(t')dt'$$

Equation 1:65

The equation 1:64 can be written as:

$$M_{x,y}(k(t)) = \int M_0(\vec{r})e^{+ik(t)\vec{r}}dr$$

Equation 1:66

The spatial frequency variable $k(t)$ can be explained as a phase acquired by a spin at a unit distance. The Equation 1:66 is the inverse Fourier transform relation between the detected MR signal, $M_{x,y}(k(t))$ and the spin density at a position $M_0(\vec{r})$ (the spatial distribution of the spin density - image). Thus, the image can be obtained with a Fourier transform of the signal acquired, i.e. the k-space.

If we consider the frequency and phase encoding gradients as constants and define x as a frequency encoding and y as a phase encoding direction then we can define:

$$k_x = \gamma G_x t, \qquad k_y = \gamma G_y \tau_{ph}$$

<div align="center">Equation 1:67</div>

where τ_{ph} is duration of the phase encoding gradient. Then the signal can be expressed as:

$$S(t) \propto M_{x,y}(k_x, k_y) = \int M_0(x,y)e^{+ik_x x}e^{+ik_y y}dxdy$$

<div align="center">Equation 1:68</div>

Thus, the k-space can be represented as a two-dimensional space where the horizontal axis (x axis) corresponds to k_{freq} (in the frequency encoding direction) and the vertical axis (y axis) corresponds to k_{phase} (in the phase encoding direction). After excitation, since no gradient was applied $k_{freq} = k_{phase} = 0$. Then the maximum negative phase encoding gradient is applied at the same time as the dephasing (negative) frequency encoding gradient (Figure 1:11A) pushing the k-space coordinates to the bottom left corner ($-k_{phase,max}, -k_{freq,max}$). In this way we are positioned well in the k-space for the start of the acquisition (Figure 1 :11B). When the acquisition starts a positive frequency encoding gradient is applied increasing linearly the k_{freq} over time and thus filling the selected k-space line in the frequency encoding direction (horizontally-Figure 1:11B). At the top of the echo $k_{freq} = 0$ the maximum signal will be observed. In the following experiments the phase encoding gradient amplitude and thus the k_{phase} is increased in discrete steps to fill in the k-space in the y direction (the phase encoding direction). For the middle experiment when $k_{phase} = 0$ the maximum signal will be observed for $k_{freq} = 0$ (on the top of the echo). The low k_{phase} and k_{freq} values in the center of the k-space are called the low spatial frequencies and the high values towards the edges are called high spatial frequencies. The low spatial frequencies which have the highest intensities give the shape of the image and the high spatial frequencies (lower intensity) give the details (Figure 1:11C).

As it was explained in the section 1.4.2 the relationship between the gradient strength, duration, SW and FOV can be derived using the Nyquist theorem. The signal coming from the gradient echo is just an FID signal sampled at discrete time intervals Δt (dwell time). According to the theorem the signal is only described accurately if it is sampled at least twice per cycle (period). This gives the maximum phase difference between two samplings to be 2π. The signals are only accurately detected if they fall in the frequency range that is determined by the spectral bandwidth ($SW = \frac{1}{\Delta t}$, see equation 1:57). The FOV in the freq. encoding direction can then be expressed as:

$$FOV(cm) = \frac{SW\ [kHz]}{gradient\ strenght\ [kHz/cm]} = \frac{1}{grad.strenght[kHz/cm] \cdot \Delta t\ [ms]}$$

<div align="center">Equation 1:69</div>

The FOV can also be expressed in terms of distance between the sampling points in both phase encoding and freq. encoding directions using equation 1:67:

$$FOV_x = \frac{2\pi}{\Delta k_x} = \frac{2\pi}{\gamma G_x \, \Delta t}, \quad FOV_y = \frac{2\pi}{\Delta k_y} = \frac{2\pi}{\gamma G_y \tau_{ph}}$$

Equation 1:70
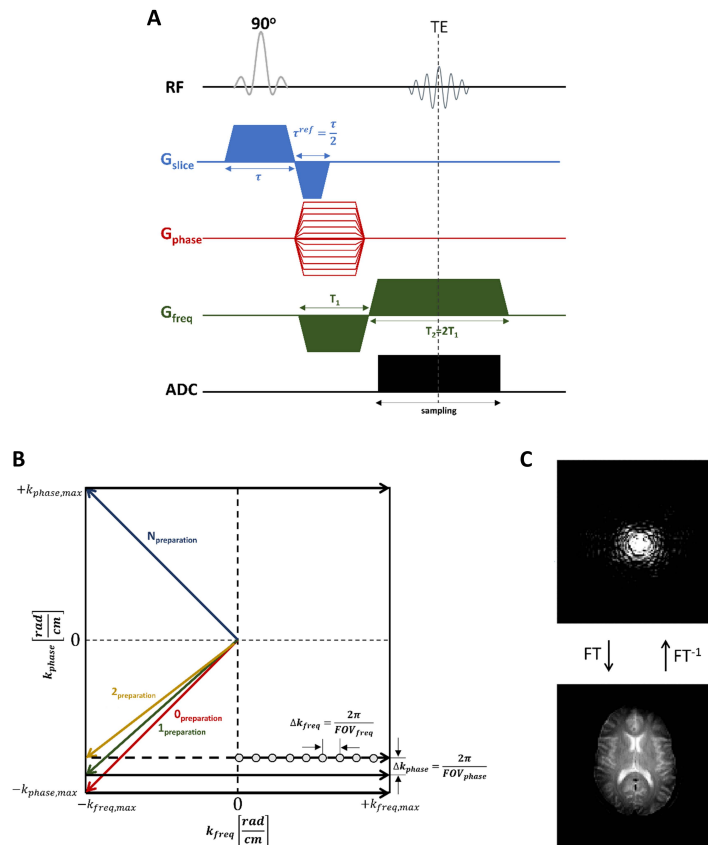
Figure 1:11: k-space sampling (A) Schematic diagram of a 2D gradient echo sequence **(B)** The structure of k-space with respect to the frequency and phase encoding gradients. **(C)** after the k-space is filled the Fourier transformation gives the final MRI image. Adapted from[2].

1.6 Single volume magnetic resonance spectroscopy

In the previous chapter basic principles of MRI were explained, where the frequency and phase encoding are used to determine the location of the measured signal. In localized magnetic resonance spectroscopy (MRS) the MR signal is measured from a predetermined volume of interest (VOI) positioned in human or animal organ or region in the brain. The position of the desired VOI (usually a cuboid) is defined with a combination of frequency-selective RF pulses and magnetic field gradients. In this sub-chapter we will focus on the basic principles of single volume MRS[7].

1.6.1   Single volume localization

1.6.1.1   *Localization using three slice selective pulses*

Magnetic field gradients are used to select the MR signal from a predefined volume. As explained in the MRI chapter (1.4) when a frequency selective RF pulse is applied in the presence of a magnetic field gradient only a selective range of frequencies and consequently spatial positions is excited. This kind of RF pulses are called slice selective or selective RF pulses (see sub-chapter 1.4.1 Slice
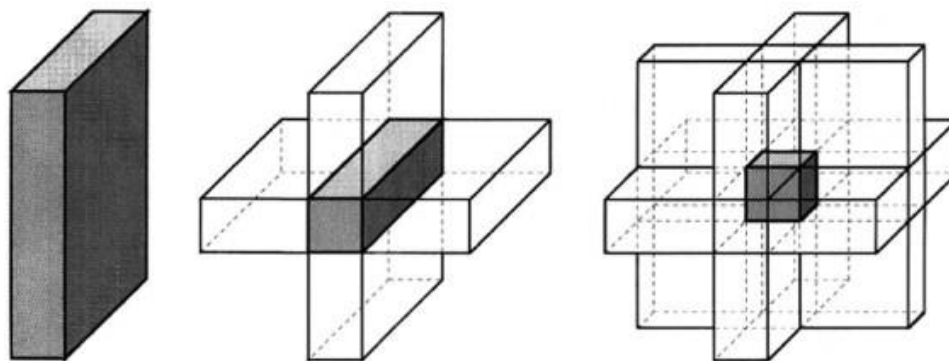
Figure 1:12: Volume selection using three slices (RF pulses in combination with slice selective gradients). Figure taken from[7].

selection). If consecutively a second RF pulse is executed during a magnetic field gradient in an orthogonal direction in space a 2D column is selected, and by addition of a third RF pulse during a gradient in the remaining (third) orthogonal direction a 3D volume (voxel) is selected[7].

1.6.1.2   *Localization based on slice selective inversion*

Image-Selected In vivo Spectroscopy-ISIS

This method was first suggested by Ordidge et al.[8] and it is based on the slice-selective inversion of spins before the signal acquisition. Two scans are needed to obtain a signal from one slice. In the first acquired FID all the spins have the same phase, while in the second acquisition a slice selective 180° pulse (targeting the desired slice) is added before excitation. When the FIDs from the two acquisitions are subtracted the resulting signal comes only from the desired slice (1D ISIS, Figure 1:13 left). A linear combination of three pairs of such scans with slice selections in three orthogonal directions leads to the localization of a 3D volume (3D ISIS, Figure 1:13 right). The signal from the target volume is preserved while the unwanted signals from the outside are canceled out.

This technique can be used for proton (^{1}H) localization but also for other nuclei (e.g. ^{31}P MRS). Since there is no echo time this pulse sequence doesn't suffer from signal loss due to T_2 relaxation or J-evolution. However, inverting of the magnetization in the region of interest can cause signal loss

due to T_1 relaxation and imperfect slice profiles for metabolites with short relaxation times. A minimum of 8 consecutive scans need to be acquired for a volume localization which makes this sequence vulnerable to motion of the sample for the in vivo applications[7].
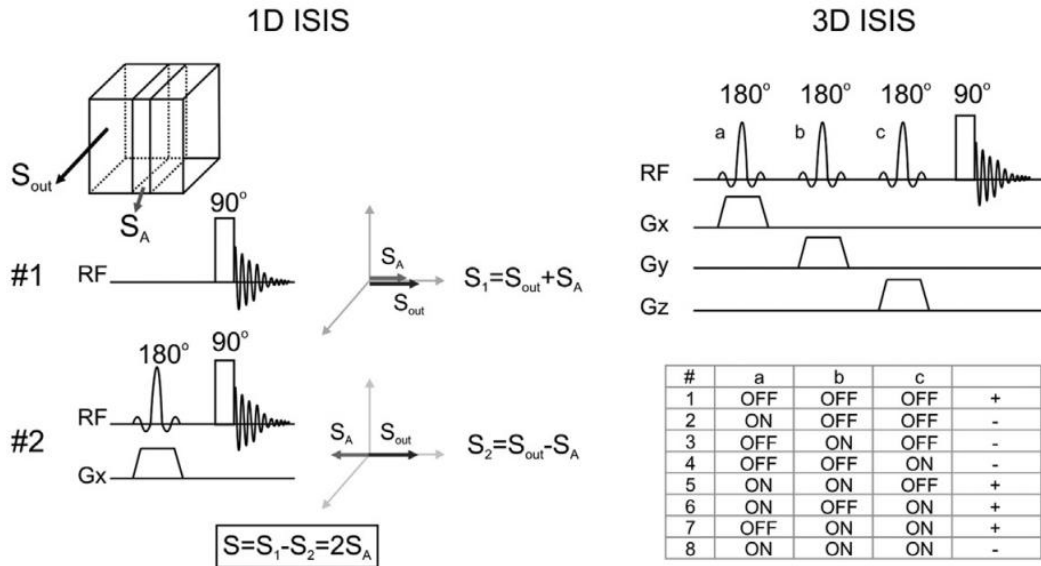
Figure 1:13: ISIS. (left) a schematic drawing of the 1D ISIS scheme where the S_A denotes signal from the desired slice and S_{out} signal from the outside volume, G_x is a specific slice selective gradient and #1 and #2 acquisitions without and with the slice selective inversion respectively. **(right)** a schematic drawing of the 3D ISIS localization with the corresponding 8 consecutive acquisitions needed for the volume localization. Figure adapted from[7].

Outer volume suppression (OVS) localization

The basic principle of OVS is to apply a combination of slice selective RF pulses (e.g. 90° RF pulses) and magnetic field gradients targeting the spins outside the VOI with a purpose of destroying their magnetization. The selected spins around the VOI are flipped into the transverse plane, subsequently a spoiler gradient is used to dephase them, and thus their magnetization is destroyed without perturbing the magnetization inside the VOI. OVS can be used for large VOIs because the suppression slices can be sufficiently thick, making this method suited for magnetic resonance spectroscopic imaging (MRSI) also.

To localize a 1D targeted slice, two suppression slices need to be positioned around it, therefore, to localize a 3D volume, 3 pairs of suppression slices must be used (three pairs of OVS pulses) (Figure 1:12). The pairs of slice selective RF pulses have frequencies centered on the corresponding suppression slices (not on the VOI). After OVS a spectrum can be acquired immediately with a non-

selective excitation RF pulse (Figure 1:14). This method achieves localization in one scan and is therefore resistant to subject motion. However, the adjustment of OVS can be challenging especially for smaller VOIs where strong signals from outer volume need to be suppressed. The OVS alone is often not enough to obtain a clean ^{1}H-spectrum and therefore it is usually used in combination with other localization techniques[7].
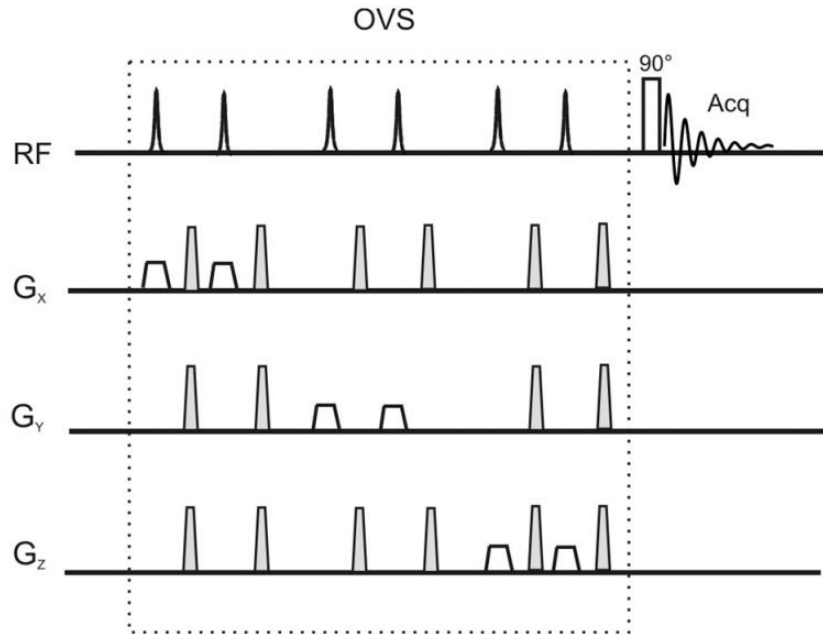
Figure 1:14: OVS. A schematic drawing of the 3D OVS localization module (in the square). The three pairs of slice-selective 90° RF pulses are shown with their corresponding localization gradients in three orthogonal directions (white trapezoid). After every slice-selective RF pulse a spoiler gradient is applied (grey trapezoid) to dephase the magnetization. Immediately after the OVS module a non-selective 90° excitation pulse is applied. Figure adapted from[7].

Localization based on echo formation

The basic principles of a spin echo sequence are explained in the section 1.3.3. In MRS the echo formation is used to refocus only the spins that experience all the 3 RF pulses. The most commonly used echo-based localization sequences are: STEAM (Stimulated Echo Acquisition Mode), PRESS (Point Resolved Spectroscopy Sequence), SPECIAL (SPin ECho, full Intensity Acquired Localized spectroscopy) and LASER (Localization by Adiabatic Selective Refocusing). Only SPECIAL and PRESS localizations will be described here in detail since these two sequences were used in this thesis[7,9].

SPECIAL (Spin Echo, full intensity acquired localized spectroscopy)

This is a hybrid sequence combining the 1D ISIS technique with a slice-selective spin-echo. The 1D-ISIS localization is achieved by application of a slice-selective full-passage adiabatic pulse in alternate

scans, followed by a spoiling gradient. The spin echo is achieved by using 90° and 180° asymmetric slice-selective pulses with gradients in the orthogonal directions to the 1D ISIS (Figure 1:15). The signal is then added in the odd scans and subtracted in even scans corresponding to the add-subtract scheme of 1D ISIS. The asymmetric excitation pulse (90°) provides a broad BW and has a uniform excitation profile. In addition, the peak RF amplitude is in the last quarter of the pulse length, therefore only a small portion of the pulse length (20-30%) contributes to the final TE (Figure 1:15B up). Similarly, the asymmetric refocusing pulse (180°) also produces a satisfactory slice profile with only 20-30% of its duration contributing to the TE (Figure 1:15B down). Very short echo times can be achieved with this method while still preserving the full signal intensity from the desired VOI. The application of an adiabatic pulse in ISIS reduces the B_1 dependence of the acquired signal, making this sequence optimized for a transmit/receive surface coil since 1D ISIS is applied along the axis with the strongest RF field gradient. The slice profile of an asymmetric pulse has positive sidebands in the excitation direction, and thus the signal outside excitation band is only partially canceled out. Therefore, an additional OVS module is applied before the sequence to minimize any potential contribution from outside of VOI. The OVS module is combined with VAPOR water suppression module (see section 1.5.2). An additional frequency selective saturation pulse between the 1D ISIS and spin echo module is also added to further improve the efficiency of water suppression (Figure 1:15)[7,10].
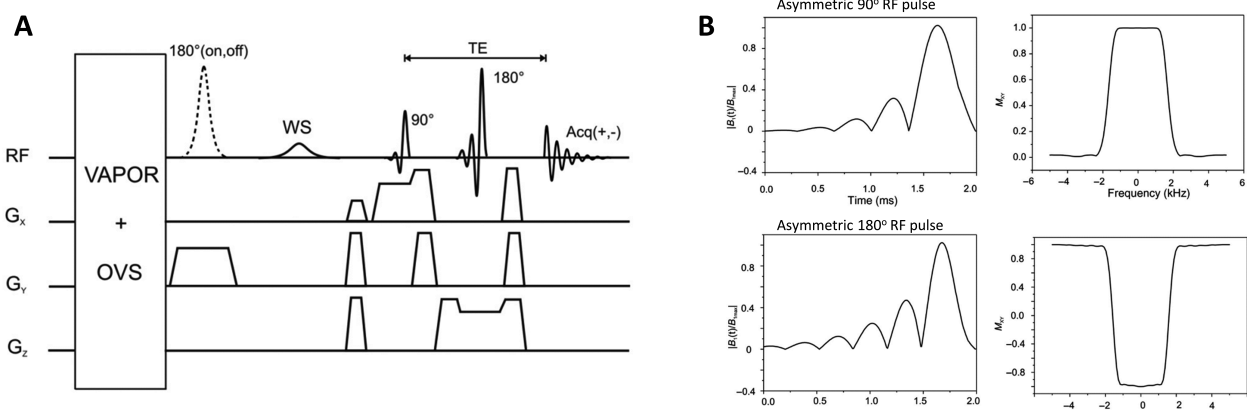
Figure 1:15: SPECIAL sequence. (A) schematic drawing of the SPECIAL sequence. The 180° adiabatic on and off pulse is applied in the Y direction (1D ISIS) while the other two asymmetric slice selective pulses from the spin echo are along the X and Z directions. The OVS and VAPOR water suppression modules are applied before the 1D ISIS with another WS pulse applied before the spin echo module. **(B)** An example of the asymmetric band selective 90° RF pulse ($2\ ms$) in the time and frequency domain (up), example of asymmetric slice selective 180° RF pulse ($2\ ms$) in the time and frequency domain (down). Figure adapted from[7].

PRESS (Point Resolved Spectroscopy Sequence)

The PRESS sequence consists of a slice selective 90º and 180º pulses to form a spin echo with an additional slice selective 180º pulse to create a double spin echo and achieve a 3D localization (Figure 1:16). In combination with the slice selective gradients, strong spoiler gradients around the 180º pulses are necessary to suppress any unwanted coherences. Since the 3D localization is achieved in one scan, this sequence is insensitive to motion and system instabilities. However, even by shortening RF pulse and gradient lengths the shortest achievable TE with this sequence is much longer compared to the other echo-based localization sequences (e.g. minimum achievable TE is between 6-8ms on preclinical UHF scanners). Both water suppression (VAPOR) and OVS are applied before the PRESS sequence[7,11].
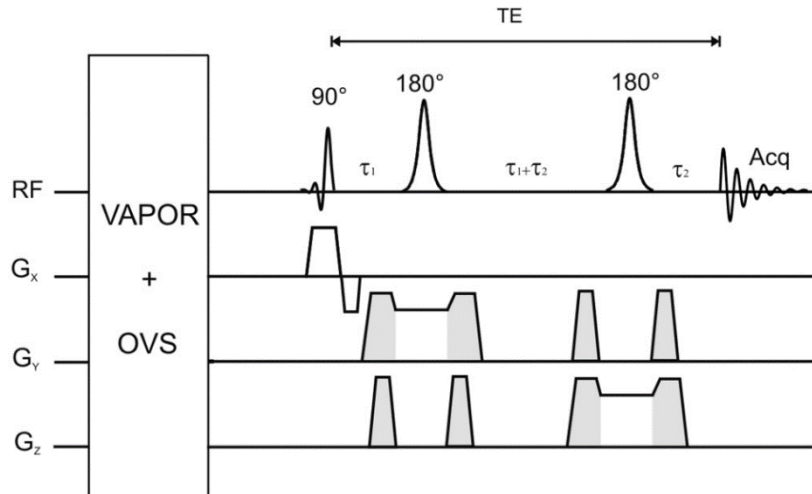
Figure 1:16: PRESS sequence. A slice selective 90º pulse is applied with a gradient in the X direction followed by two slice selective 180º pulses along Z and Y. To achieve a double spin echo, the delays between the pulses and the acquisition should be kept as indicated in the scheme. Strong spoiling gradients are applied around each 180º pulse (light gray). Both water suppression (VAPOR) and OVS are applied before the first 90º excitation pulse. Figure adapted from[7].

1.6.2   Water suppression in ¹H MRS

The goal of the advanced in vivo ¹H MRS methods in the brain is to retrieve the characteristic neurometabolic profiles providing information on a high number of metabolites. Most tissues consist of 70-85% of water; thus, a very strong water signal is present in every ¹H MR spectrum. The signal intensity of protons from the water signal (resonating in vivo at $\sim 4.68 ppm$) is three to four order of magnitudes higher than the signal of the metabolites of interest. In addition, broad shoulders of the water signal and spurious satellites from mechanical vibrations of the gradient coils often overlap with metabolite peaks causing distortions. Therefore, water suppression (WS) is crucial and

almost always included in ^{1}H MRS sequences to improve the detection and ensure a reliable quantification of metabolites.

There are several different WS techniques developed for in vivo ^{1}H MRS brain spectra. Since the metabolite resonances are mostly in the range $< 4.2 \, ppm$ or $> 5.2 ppm$ narrow-band frequency selective RF pulses need to be used to target the water resonance without affecting the metabolites. Chemical Shift Selective (CHESS) RF pulses followed by gradients that dephase (destroy) the transverse magnetization of water are commonly used. The first WS modules consisted of three identical CHESS pulses separated by the same time delay and improved by varying flip angles. However, there are several factors influencing the efficiency of the WS like spatial B_0 and B_1 inhomogeneity, differences of T_1 relaxation times of water in different compartments and frequency and phase fluctuations due to motion.

To overcome these issues, later, a scheme with four consecutive pulses with numerically optimized flip angles decreased the sensitivity to B_1 and T_1 variations, leading to the Water suppression Enhanced through T_1 effects (WET) scheme. For advanced MRS studies Variable Power and Optimized relaxation delays (VAPOR) WS method is recommended[12]. This method is specifically optimized to improve the in vivo WS by reducing the effects of B_1 inhomogeneity's and T_1 variations. The VAPOR technique was used in this thesis and will be further explained[12].

VAPOR (Variable Power and Optimized Relaxation delays) water suppression

The original version of VAPOR WS scheme was designed for application in the rodent brain at 9.4T where surface coils (transmit/receive) are often used[13]. The scheme was optimized to be as insensitive as possible to the inhomogeneous B_1 transmit field produced by the surface coil, and additionally the timing between the pulses was selected so that the OVS blocks can be interleaved with the WS pulse train (reducing the repetition time - TR). The pulse train was constructed and optimized considering relative flip angles of the pulses, inter-pulse delays and a range of water T_1-s from different parts of the brain. The original VAPOR scheme consists of seven CHESS pulses with following flip angles and delays:

Relative flip angles: $\alpha - \alpha - 1.78\alpha - \alpha - 1.78\alpha - \alpha - 1.78\alpha$ (α is the nominal flip angle)

Inter-pulse delays (in ms): $150 - 80 - 160 - 80 - 100 - 30 - 26$

The decreased sensitivity to transmit B_1 is secured by the large differences in flip angles (factor of 1.78) and optimized delays ensuring that the M_z that correspond to the coherence pathway experiencing the different intensities of B_1 cross zero at the same time. This WS technique is very robust and once optimized for the chosen magnetic field can be automatically used significantly reducing the time needed to optimize a pulse sequence for a chosen VOI[12].

1.6.3   Chemical shift displacement error

Spatial localization in single volume MRS is typically achieved by application of three orthogonal slice selective pulses. In other words, frequency selective RF pulses are applied simultaneously with the corresponding magnetic field gradients. When a magnetic field gradient is applied the resonant frequency becomes dependent on the position ($\omega(x) = \gamma B_0 + xG$) and when combined with the frequency selective pulse the resulting selected slice thickness is $\frac{2\pi\, BW}{\gamma G}$ (see section 1.5.1). This volume is selected correctly only for the spins which resonate at the carrier frequency of the applied pulse. However, protons from different metabolites resonate at slightly different frequencies because of their chemical structures (chemical shift). Therefore, a difference in Larmor frequency ($\Delta\omega$) between two different compounds will result in a spatial displacement (Δx) of the localized volume for one compound relative to the other:

$$\Delta x = \frac{\Delta\omega}{\gamma G_x}$$

Equation 1:71

This effect is called chemical shift displacement (CSD) error and it can be reduced by using an RF pulse with larger bandwidth (BW) coupled with an increased gradient strength. CSD error becomes stronger with increased magnetic field strength due to larger spectral dispersions. Therefore, achieving sufficiently large BWs for the used RF pulses can be problematic at higher magnetic fields since the maximum RF bandwidth is limited by the maximum peak power. Chemical shift displacement error can then be calculated as $L \cdot \frac{\Delta\omega}{BW_{max}}$, where L is the size of VOI in the direction of the gradient.

1.6.4   In vivo Brain ^{1}H MR Spectrum at Ultra High Field (UHF)

MRS is a unique tool that has the possibility to assess in vivo and non-invasively the metabolism of different tissues in living organisms. MRS can be performed on any nuclei that has non-zero magnetic moment, but the most widely used is proton MRS (^{1}H MRS) because of its high sensitivity and

natural abundance (see chapter 1.1) leading to the detection of brain metabolites at concentration down to about 0.5 mM in vivo. For a reliable detection of desired metabolites, high quality spectra need to be obtained. Several factors influence the quality of the acquired MR spectrum: magnetic field strength (sensitivity, signal to noise ratio of the acquired spectrum increases with the B_0 strength), B_1 homogeneity (RF coil performance), B_0 homogeneity (shimming), water suppression and localization sequences (see sections 1.5.1 and 1.5.2). The availability of UHF (>7 T) combined with the possibility of acquiring spectra at very short echo time (< 6 ms) have increased the number of in vivo detectable brain metabolites to approximatively 20 metabolites. They are markers of myelination/cell proliferation (phosphocholine (PCho), glycerophosphocoline (GPC), phosphorylethanolamine (PE), NAA, N-acetylaspartylglutamate (NAAG)), energy metabolism (glucose Glc), lactate (Lac), creatine (Cr), PCr, alanine (Ala)), osmoregulation (taurine (Tau), myo-inositol (Ins), creatine (Cr)), neurotransmitter metabolism (glutamate (Glu), glutamine (Gln), aspartate (Asp), γ-aminobutyrate (GABA), glycine (Gly) and antioxidants (ascorbate (Asc), glutathione (GSH)) (Figure 1:17). After acquisition several data processing steps are required (frequency and phase correction, spectral quality control and fitting, concentration referencing) to obtain, as a result, reliable metabolite concentrations[14]. Some of the main characteristics of the ^{1}H MR brain spectrum will be described in this sub chapter.
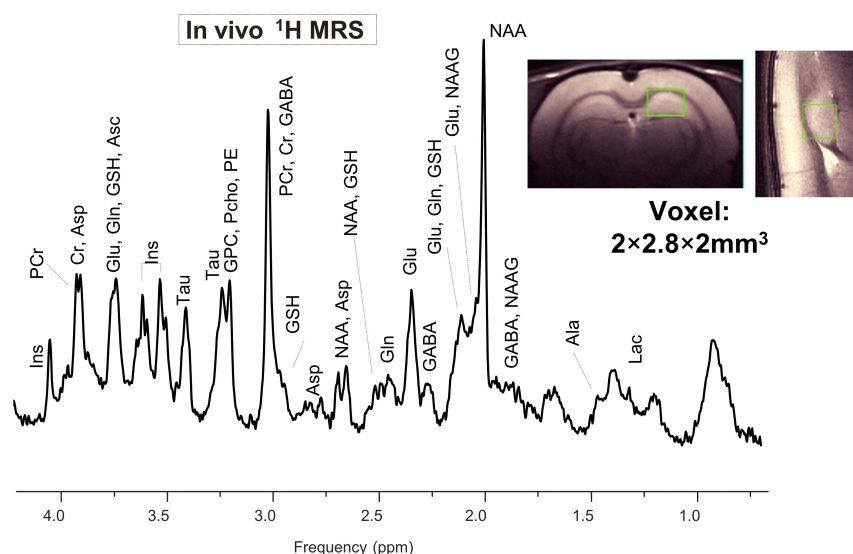
Figure 1:17: **Representative in vivo ^{1}H MR Spectrum** acquired in the rat brain at 9.4T (hippocampus) using the SPECIAL (section 1.6.1.2) sequence (TE=2.8 ms).

1.6.4.1 Spectral quality and noise

In the section 1.3.2 it was explained that signal detected in an MR experiment in the time domain is called the FID, and it is converted to the frequency domain signal (spectrum − giving the resonant frequencies present in the FID) using a Fourier transform. In the MR spectrum every resonance line is characterized by five model parameters: amplitude (peak area in the frequency domain), resonant frequency, phase, T_2^* relaxation time and line shape (Lorentzian, Gaussian or Voigt)[15].

Every FID can be described as a sum of the original/wanted signal and the noise coming from random fluctuations caused by thermal variations in the investigated object or the detection hardware. There can be also other, non-noise contributions to the signal in form of artifacts coming from e.g. spurious echoes, leaking of the RF signal etc. The noise in real and imaginary MR spectrum has uniform spectral power (white noise) and follows a Gaussian intensity distribution. The main characteristic of the noise is its amplitude (σ), defined as a standard deviation of the data in a signal free area either in the time or frequency domain. One of the main criteria for the assessment of the MRS data quality is SNR, calculated as:

$$SNR = \frac{signal}{\sigma_{noise}}$$

Equation 1:72

As explained, both signal and noise can be measured in the frequency and time domain yielding different values for the SNR. In the frequency domain one of the recommended methods is to measure the signal part as the height of the largest metabolite peak in the spectrum. This way the variance coming from incorrect phasing, fit model or baseline definition is eliminated.

In addition to SNR, spectral resolution is another very important factor in assessing the MRS data quality especially for metabolite quantification since it represents the ability to separate spectral features. The spectral resolution is represented in terms of linewidth which is defined as the full width at half maximum (FWHM) of a singlet resonance in the frequency domain measured in Hz or ppm. The optimal/minimum linewidth in an in vivo experiment is determined by the T_2 relaxation time as $1/{\pi T_2}$. The linewidth and line shape are mainly affected by the B_0 inhomogeneities, that is the quality of B_0 shimming in the selected VOI (influenced by the size of the VOI). The final spectral resolution can also be influenced by the eddy currents or frequency variations between averaged signals if not accounted for properly in the preprocessing. The T_2 includes dynamic dephasing effects, so its measured value depends on the rephasing properties of the used pulse sequence.

Therefore, it is sometimes also called apparent T_2 (or T_2^{app}). If the FWHM is measured using a metabolite peak its value is dependent on the fitting algorithm (if not measured directly in the spectrum on a well isolated peak). Therefore, FWHM value obtained from an unsuppressed water signal is most commonly used as a robust indicator of spectral resolution. It should be noted that this value will be different from the one obtained using singlets of i.e. NAA or Cr due to the shorter T_2 of water[15].

1.6.4.2 Baseline

In an in vivo ^{1}H MR spectrum the baseline is defined as smoothly varying signal components underlying the metabolite resonant peaks coming from the VOI. Various factors can contribute to the baseline profile: sub-optimal localization performance (i.e. unwanted resonances such as lipid signals coming from outside of the VOI – outer volume signal bleed), insufficient water suppression, hardware imperfections (i.e. corruption of the first data points in the FID) and eddy currents[15–17]. Additionally, inaccurate timing of the data sampling with respect to the echo formation can cause a strong first order phase distortion (rolling baseline)[15]. Note that mobile macromolecules should not be considered as baseline.

1.6.4.3 Mobile Macromolecules (MM) and Mobile Lipids (ML)

In ^{1}H MR spectra the broad signals underlying the narrower signals of low molecular weight metabolites are defined as mobile macromolecules (MM, Figure 1:18)[18,19]. These signals are observable in the spectra of the human and animal brain at short TEs and remain detectable at intermediate TEs. They display shorter T_1 and T_2 relaxation times[20] and lower apparent diffusion coefficient (ADC)[21] compared to metabolites. In the normal/healthy brain MM result mostly from protons of amino acids within cytosolic proteins e.g. in the area upfield of tissue water (~0.5-4.5ppm); they correspond to aliphatic (methyl, methylene and methine) protons. The MM are composite signals, composed of multiple overlapping and closely spaced multiplets. The distributions of these overlapping multiplets, since they come from amino acids within different proteins, result in the apparent broad linewidths of the MM peaks. It is recommended that the MM signals are described by their resonant frequency. The resolution of the MM signals improves with B_0 [19,22,23]. The patterns of brain MM spectra are very similar between different species. However, some regional differences have been reported in the human brain between gray and white matter[24], although they seem to be consistent over regions in the rodent brain[25].

With onset of disease (e.g. tumors, multiple sclerosis, stroke etc.)[26–29] signals from mobile lipids (ML) appear in addition, overlapping with peaks of mobile proteins/peptides (MM). ML signals come mainly from neutral triglyceride and cholesterol esters which form cytoplasmic lipid droplets with an additional contribution from mobile components of membrane phospholipids (e.g. choline methyl at 3.2 ppm). ML are not subcutaneous lipid signals coming from imperfect localization and they are not present in the healthy brain.

When the target of a study is to obtain metabolite concentrations (narrow signals), the MM are often referred to as a background signal. However, the MM signal is well characterized and the best treated when added as additional signal component (or components) in the fitting algorithm.

The MM can be measured directly in vivo by application of the inversion recovery method (section 1.4.2) which exploits the shorter T_1 relaxation times of the MM compared to metabolites. With the optimal choice of IT, the IR sequences aim for a maximum suppression of the metabolite signals while preserving the MM. Both single and double IR methods have been successfully applied to acquire MM spectra in vivo. While double IR methods give improved metabolite suppression over a wider range of T_1 they result in reduced MM and introduce an increased T_1 weighting. In addition to IR, diffusion-weighting can also be used to measure MM in vivo exploiting the fact that the MM have a 10 to 20 times slower diffusion than metabolites[21,30]. Regardless on the acquisition method the in vivo acquired MM spectrum is never completely free of the metabolite residuals, therefore they need to be removed with the appropriate postprocessing[18,19]. Proper handling and postprocessing of the MM spectrum and its influence on the on the quantification of ^{1}H MR spectra is more closely discussed in the Chapter 2 of this thesis[18].
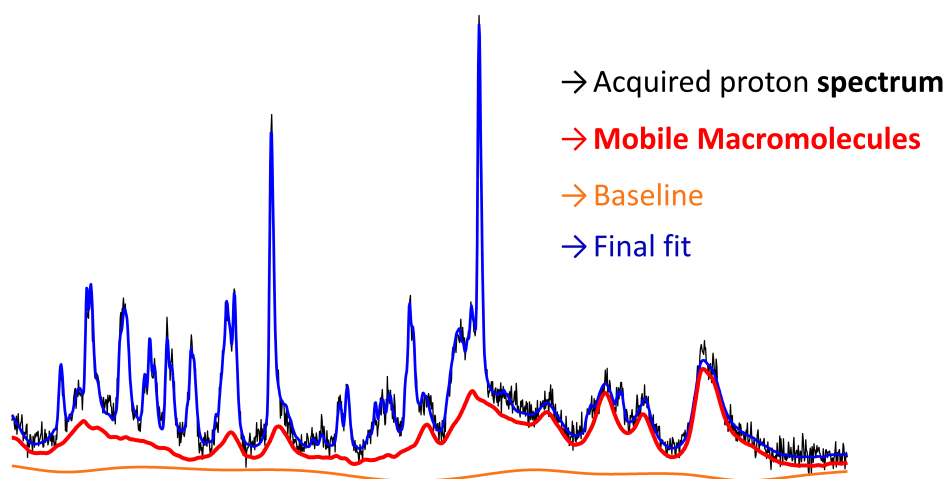
Figure 1:18: ^{1}H MR Spectrum, MM, baseline and the final fit. Representative in vivo ^{1}H MR Spectrum acquired in the rat brain at 9.4T (TE =2.8 ms, TR = 4s, hippocampus VOI=2x2.8x2 mm^3, in black), with the corresponding MM fit (in red), baseline (in yellow) and final model fit (sum of metabolites contributions, MM and baseline – in blue) as an output of the LCModel algorithm.

1.6.4.4   Metabolite quantification

The simplest method to estimate signal intensities from an acquired spectrum is the peak integration. However, this method can be applied only when the peaks are well isolated (separated) and not affected by the baseline offsets[14,31], which is not the case for an ^{1}H MR spectrum. Therefore, model fitting algorithms are widely used in ^{1}H MRS[14]. They are designed to find the optimal model parameters to minimize the cost function (χ^2) representing the deviation of the model signal and the measured signal. Model fitting algorithms need to have prior information used as constraints on the model parameters to facilitate the fitting, direct the fitting towards a desirable and interpretable outcome with reducing the chance of a meaningless result and increasing the fitting precision. Linear combination model fitting (LCModel - linear combination of model spectra of metabolites), the method used in this thesis, analyzes the in vivo ^{1}H MR spectrum, in the frequency domain, as a linear combination of known compound responses of known contributing metabolites[15,32]. To be more specific, the goal of LCModel is to decompose the in vivo ^{1}H MR spectrum into a linear combination of model spectra from the "basis set" (prior information), where the basis set is a database of individual metabolite spectra (compound responses) that contribute to the ^{1}H MR spectrum. This database can be generated by measuring in vitro ^{1}H MR spectra of all the individual metabolites in a solution under the same experimental conditions (Larmor freq. and pulse sequence parameters), or alternatively the compound responses can be simulated using the density matrix formalism and known chemical shift and J-coupling constants. A properly prepared/postprocessed MM spectrum

needs also to be added to the basis set (Figure 1:19). As a result, the LCModel analysis provides areas under the peaks (concentrations if water is used as an internal reference) and the corresponding Cramer-Rao lower bounds (CRLB - estimates of the fitting errors)[9,15,33].
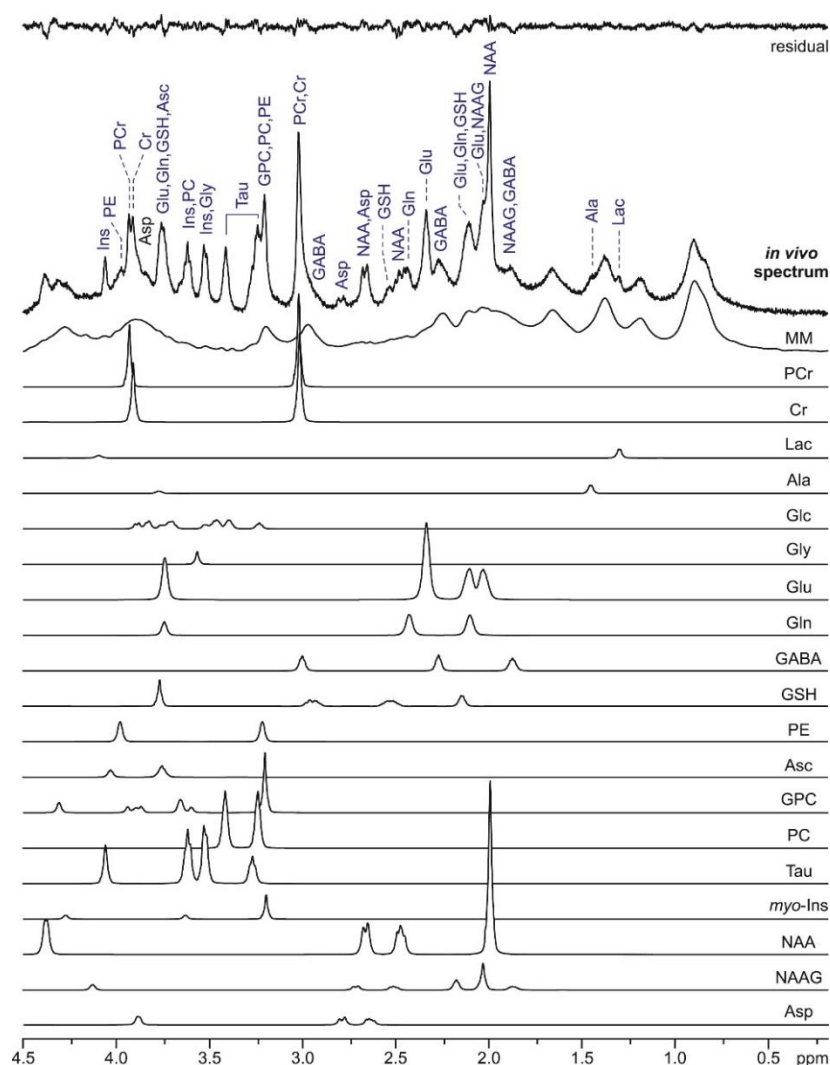
Figure 1:19: The LCModel analysis of an in vivo acquired ¹H MR spectrum from a rat brain at 14.1T using the SPECIAL (TE=2.8ms, TR=4000ms, VOI=70μl, frontal cortex, corpus callosum and striatum) sequence. The in vivo experimentally acquired spectrum is shown with the corresponding spectra of individual metabolites and the spectrum of MM included in the basis set as well as the resulting fit residual. Figure is taken from[9].

The CRLB represent the minimum obtainable variance in estimation of a model parameter (minimal possible theoretical uncertainties), given the measurement data. High CRLB values can result from low spectral SNR or strongly overlapping resonances. The error estimation using the CRLB values is only valid if the model used to describe the data fully applies to the data (FQN≈1, see below) and if the noise is Gaussian. In addition, the CRLB error estimation increases with the number of model parameters. If the spectra contain artifacts or resonances that are not accounted for in the model

the CRLB estimation is not valid. Relative CRLB (ratio between the CRLB and the estimation of the parameter) are often used for data filtering. However, metabolites having low concentrations can be falsely classified as poor-quality data when using the relative CRLB filtering, therefore care must be taken when applying this criterion[15,33].

To estimate the quality of the model fitting, the fit quality number (FQN) can be calculated. It is defined as a relation of χ^2 (minimum of the cost function) to what is expected in the case that fit residuals (signal model subtracted from the experimental signal) come only from the measurement noise. That is, the FQN is a ratio of the variance in the fit residual divided by the variance of pure spectral noise. If the FQN > 1 the model doesn't fully match the experimental signal (part of the signal is unaccounted for). When FQN = 1 the model agrees with the experimental signal with the precision allowed by the noise, and finally FQN < 1 indicates overfitting (i.e. too much flexibility of the model) [15,33].

1.6.5   Phosphorus (^{31}P) MR spectroscopy

^{31}P MR spectroscopy is a very useful method for investigation of energy metabolism in tissue, but also phospholipid metabolism and the redox state of the cell[31]. Brain metabolites that can be measured by ^{31}P MRS are: PCr, nucleotide tri-phosphates (represented mainly by adenosine triphosphate - ATP) and inorganic phosphate involved in cell energy metabolism, phosphomonoesters (PME) as PCho and PE, phosphodiesters (PDE) as GPC and glycerophosphoethanolamine (GPE) involved in phospholipid metabolism, nicotinamide adenine dinucleotide (NAD) and its phosphate (NADP) in its reductant and oxidized forms. The chemical shift positions of the stated metabolite resonances are sensitive to physiological parameters (pH and ionic strength). The resonance of PCr is assigned to $0\ ppm$ (convention) and is used as internal chemical shift reference. When compared to ^{1}H MRS, ^{31}P-MRS has larger chemical shift dispersion (25 ppm compared to 5 ppm) and relatively small number of different metabolites (around 10 compared to 20). This leads to good spectral resolution and clear interpretation and quantification of the spectra. A ^{31}P MR spectrum is additionally characterized by homonuclear (ATP) and heteronuclear (PME, PE, PCho and PDE, GPC and GPE) scalar couplings which are also sensitive to physiological conditions.
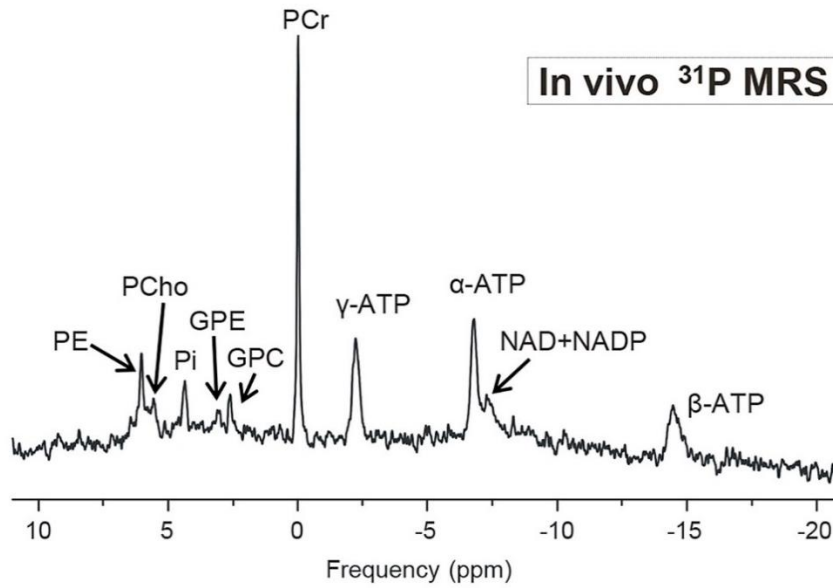
Figure 1:20: In vivo ^{31}P MR example spectrum acquired in the rodent brain at 9.4T (VOI=5 x 9 x 9 mm^3, TR = 8 s, 384 averages, adiabatic half passage pulse for excitation, OVS (x, z) and 1D-ISIS(y) for localization).

Phosphorus has a 100% natural abundance and relatively high resonant frequency (40% of that of the proton), but because the intrinsic sensitivity is proportional to γ^3 (gyromagnetic ratio) it is significantly lower than for the proton (7% compared to the proton). Because of the stated reasons, ^{31}P MRS suffers from low SNR which brings difficulties when analyzing low concentrated metabolites. Thus, high magnetic fields in combination with advanced measurement methodology are needed[2,34].

In ^{31}P MR spectroscopy the usage of slice selective RF pulses for localization is not appropriate for several reasons. Firstly, this localization method requires echo-based acquisition which brings an additional signal loss due to T_2 relaxation. The fact that ^{31}P nuclei in metabolites have substantially shorter T_2 relaxation times than the ^{1}H, combined with already inherently low signal due to low intrinsic sensitivity of ^{31}P, makes signal loss resulting from an echo-based sequence non-affordable. Secondly, large chemical shift dispersion of the ^{31}P metabolite resonances would result in a large chemical shift displacement error if magnetic field gradients were to be used. Therefore, non-selective 90° pulses followed by an immediate FID acquisition are often used in ^{31}P MRS (no chemical shift artifacts)[31,35].

In this thesis all the ^{31}P-MRS spectra were acquired using a non-selective adiabatic half passage RF pulse for excitation[35]. The OVS localization module was applied in the x and z direction combined

with 1D ISIS localization in the y direction. To further decrease the apparent metabolite linewidths and SNR, a WALTZ-16 scheme was used for ^{1}H-decoupling and NOE (nuclear Overhauser effect) enhancement as described and optimized in reference[34]. Processing and quantification were performed in jMRUI (java based magnetic resonance user interface) software, using AMARES for spectral fitting as previously described[34,36].

1.7   MRSI basic principles acquisition and reconstruction

The single volume spectroscopy technique (sub chapter 1.6) involves the detection of the signal from a single well-defined volume. This volume is predetermined and localized in a certain region of interest. Magnetic resonance spectroscopic imaging allows the detection of MR spectra from a multidimensional array of locations providing the characterization of a full object under investigation in 2D or 3D (e.g. characterization of the regional differences in the entire brain at a given time point).

The principles of MRSI are very similar to the phase encoding in MRI (sub chapter 1.5). Addition of the phase encoding gradients can extend any spectroscopy pulse sequence to an MRSI sequence. Here, we will use the basic spin-echo sequence as an example (section 1.4.2). The result of a normal spin-echo acquisition is a 1D MR-spectrum with no spatial information if no magnetic field gradients are used. Adding the phase-encoding gradient adds the spatial encoding to the acquired signal. This phase-encoding gradient (G_{phase}) can be applied in any of the x, y and z orthogonal directions and its amplitude is incremented in every subsequent acquisition as for the phase encoding in MRI. During the gradient application, the precession frequency of spins becomes linearly dependent on the position (r):

$$\omega(r) = \gamma r G, \qquad or\ in\ \hat{y}\ direction \qquad \omega(y) = \gamma y G_y$$

Equation 1:73

For a constant gradient amplitude of duration t, the transverse magnetization would acquire a spatially dependent phase:

$$\phi(r) = \int_0^t \omega(r)dt = \gamma r G t, \quad or\ in\ \hat{y}\ direction\ \ \phi(y) = \gamma y G_y t$$

Equation 1:74

Since the gradient is applied during only one of the $TE/2$ periods (Figure 1:21), the phase acquired during the gradient duration will not be refocused and thus it will encode the FID with spatial

information. The application of an FT with respect to the applied phase-encoding gradient ampli-tude will retrieve the spatial information, that is the spatial distribution of the sample. This descrip-tion corresponds to 1D MR spectroscopic imaging since only one spatial axis is resolved (Figure 1:21 left side).

Now we will introduce the k-space formalism as in the Section 1.5.4. In the time domain, we can express the total acquired signal as a sum of signals from elementary volume elements ($s(y, t)dy$) at each point y in the sample:

$$S(t) = \int_{-\infty}^{+\infty} s(y, t)dy$$

Equation 1:75

By FT of the $S(t)$ we can obtain the total spectrum of the sample as the sum of spectra from ele-mentary volume elements ($f(y, \omega)dy$):

$$F(\omega) = \int_{-\infty}^{+\infty} S(t)e^{-i\omega t}dt = \int_{-\infty}^{+\infty} f(y, \omega)e^{-i\omega t}dy$$

Equation 1:76

By applying the phase-encoding gradient on each elementary volume, we can obtain the spatial distribution according to:

$$f'(y, \omega) = f(y, \omega)e^{-i\gamma y G_y t}$$

Equation 1:77

Then the full spectrum can be expressed as:

$$F(G_y, \omega) = \int_{-\infty}^{+\infty} f(y, \omega)e^{-i\gamma y G_y t}dy$$

Equation 1:78

Now, by introducing the k-space formalism, $k_y = \gamma G_y t$ we can rewrite the Equation 1:78 as:

$$F(k_y, \omega) = \int_{-\infty}^{+\infty} f(y, \omega)e^{-ik_y y}dk_y$$

Equation 1:79

Where $F(k_y, \omega)$ is the phase modulated spectra from the entire sample and according to the Equa-tion 1:79 it represents the inverse FT of the spectra from individual volume elements. Therefore, by applying the FT to $F(k_y, \omega)$ the individual spectra ($f(y, \omega)$) can be obtained:

$$f(y, \omega) = \int_{-\infty}^{+\infty} F(k_y, \omega)e^{-ik_y y}dy$$

Equation 1:80

This general 1D case can be extended to two or three Cartesian directions by applying additional orthogonal gradients (phase encoding gradients).

The signal is not continuously sampled in the k-space; it is acquired at discrete position and thus the spectra are recovered by a discrete FT. The digitalization rate in the spatial frequency is determined by the increments in gradient area (i.e. increase in amplitude) and it is determined by the Nyquist sampling criterion (section 1.5.2). Thus, to avoid aliasing the maximum phase shift between two gradient increments over the whole FOV needs to be 2π :

$$2\pi = \gamma \, FOV \, \Delta G \, t \quad \rightarrow \quad FOV = \frac{2\pi}{\gamma \Delta G t} = \frac{2\pi}{\Delta k}$$

Equation 1:81

The nominal voxel size (ΔV) is then calculated from the FOV and the number of phase-encoding gradient increments (N):

$$\Delta V = \frac{FOV}{N}$$

Equation 1:82

In addition to N and FOV the minimal nominal voxel size is also dependent on the allowed measurement time and sensitivity (see section 1.7.2).
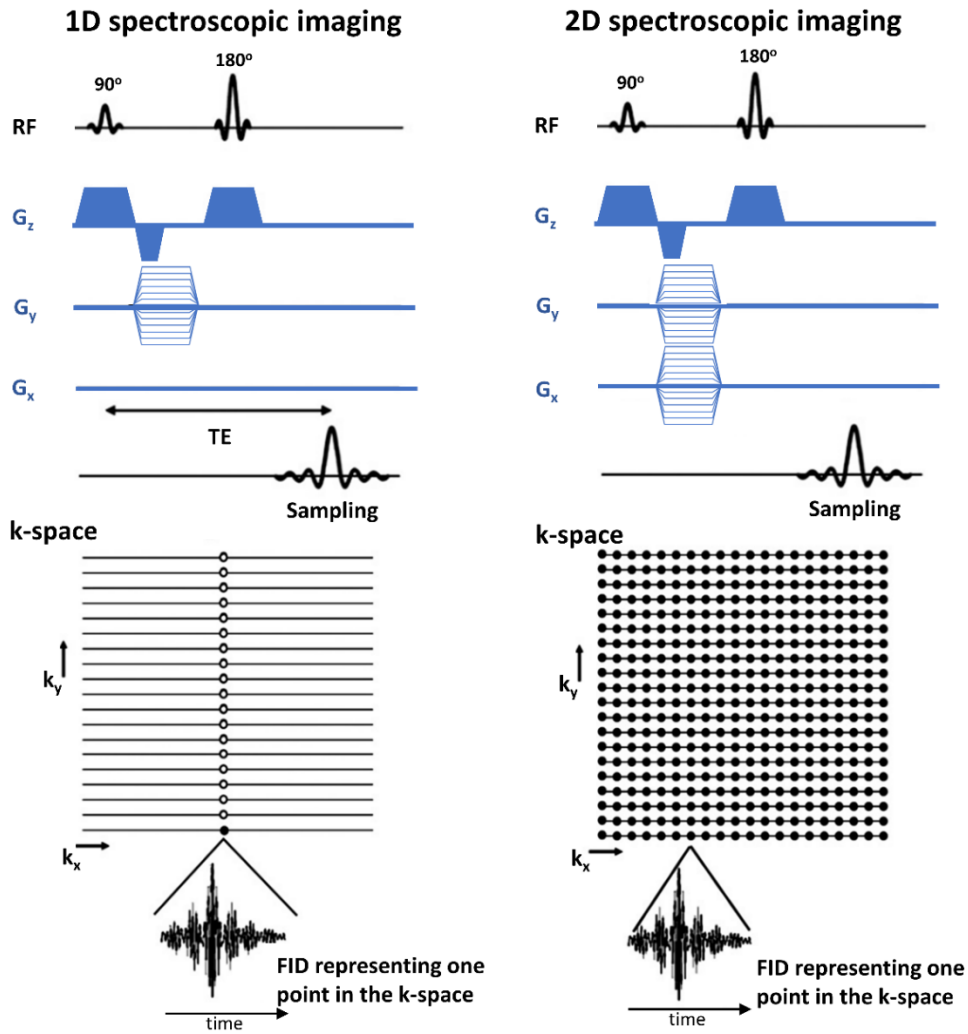
Figure 1:21: Spectroscopic imaging spin echo pulse sequence and the k-space filling. (left) Scheme of a 1D spectroscopic imaging spin echo pulse sequence describing the 1D k-space filling. The FID corresponding to one point of the k-space is shown. By incrementing the phase-encoding gradient in the y direction, the k-space is sampled (note the absence of G_x phas- encoding gradient); **(right)** Scheme of a 2D spectroscopic imaging spin echo pulse sequence describing the 2D k-space filling. Note that the additional gradients for spoiling (elimination of spurious coherences) are not shown. Figure adapted from[37].

1.7.1 Spatial resolution and point spread function (PSF)

The equation 1:82 describes the nominal voxel size of an MRSI experiment to be the entire FOV divided by the number of phase encoding increments, but the origin of the signal does not fully correspond to the rectangular nominal voxel in the grid. From the characteristics of the FT it results that, after data reconstruction, the signal is contaminated with the signals from other nominal voxels. When the signal is measured in the time domain ($s(k)$) over an infinitely long period of time, after the FT it will produce a single resonance (Dirac delta function). In reality, the signal is sampled over a finite time and the sampling is described with the sampling function $F_{sample}(k)$. The FT is then performed over a product of $F_{sample}(k) \cdot s(k)$ leading to a convolution of $s(r)$ and $F_{sample}(r)$

in the spatial domain. The FT of the $F_{sample}(k)$ (sampling points or the sampling grid) is referred to as the point spread function (PSF) (e.g. for a constant grid of N samples the PSF is a sinc function). The PSF always influences the FT data, but it is not a dominant factor for the MRS except when the acquisition time is very short leading to truncation artifacts. However, the effects of the PSF in the MRSI are more obvious because of the limited number of phase encoded increments (limited number of k-space samples). The PSF is positioned with its maximum in the center of the corresponding voxel and it stands as a weighting factor determining how much of the signal comes from the desired voxel and how the signals from other voxels contribute to this particular voxel (voxel bleeding). Figure 1:22 shows the example of a PSF from a k-space region sampled by 32 points. The nominal resolution is no longer defined as a $\frac{FOV}{N}$, but as the FWHM of the PSF which results in $1.21\frac{FOV}{N}$, meaning that the actual voxel is 21% larger than the nominal one. The PSF is not uniform across the voxel resulting in only 87.3% of the signal from the intended spatial location and 12.7% from the adjacent voxel (bleeding).
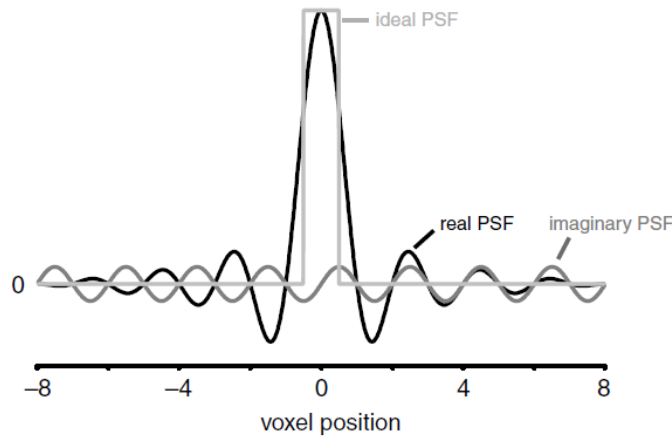
Figure 1:22: Point spread function. Example of a PSF of a nominal voxel from a 1D MRSI experiment with 32 phase encoding steps. The PSF is a sinc function extending outside the nominal voxel dimension (ideal PSF - FOV/N). Figure adapted from[2].

The effects of PSF are particularly enhanced in the edges of the brain. Because the lipid signals from subcutaneous regions can be very important, their contribution to the MRSI signal of metabolites because of the voxel bleeding is significant. Thus, in standard MRSI different techniques/modules to suppress lipid signals are used (i.e. volume pre-localization, outer volume suppression or saturation bands).

The PSF can be artificially improved by applying an apodization function in the spatial frequency domain (k-space). The apodization function needs to be symmetrical with respect to the origin and

theoretically should maximally reduce the rippling effect (side lobes) and minimally increase the FWHM. E.g. Hamming filtering function:

$$W(k) = 0.54 + 0.46 \cos\left(\frac{\pi k}{k_{max}}\right) \, for - k_{max} \le k \le k_{max}$$

Equation 1:82

This filtering function increases the FWHM by 85% compared to the nominal volume but reduces the maximum amplitude of the side lobes by 80%. Thus, the application of post-acquisition functions is not always optimal.

1.7.2   Temporal resolution

Since the conventional MRSI sequences measure one k-space point per repetition time (TR), the total measurement time for, i.e. 2D phase encoded MRSI can be expressed as $T_{measurement} = NA \times N_x \times N_y \times TR$; where NA is the number of averages and $N_{x,y}$ number of phase encoding increments. Consequentially, this leads to long measurement times already for moderately high-resolution datasets (i.e. for a 32×32 matrix with $TR = 2s$ the acquistion time is $32min$). Thus, for most in vivo applications it is essential to increase the temporal resolution. There is a number of techniques which can achieve an increased temporal resolution: (1) conventional methods which require only basic pre- or post-processing (i.e circular and spherical k-space sampling, k-space apodization during acquisition etc.), (2) methods based on fast MRI where the reduction of acquisition time is achieved by reduced or modified k-space sampling (i.e. echo-planar spectroscopic imaging (EPSI), spiral MRSI etc.) and (3) methods based on prior knowledge where object information like spatial position, orientation and etc. is used to increase the efficiency of k-space sampling. A detailed review of the accelerated MRSI techniques can be found in a recent article of Bogner at al[38].

References

1. Keeler, J. *Understanding NMR spectroscopy*. (2005). doi:10.5860/choice.43-5896.
2. de Graaf, R. A. *In vivo NMR spectroscopy.* (2019). doi:10.1007/978-1-4613-1473-8_59.
3. Liang, Z. P. & Lauterbur, P. C. *Basic principles of magnetic resonance imaging*. (2000). doi:10.1142/9789814293686_0020.
4. Webb, A. *Introduction to Biomedical Imaging*. (2003).
5. Logan, T. M. Lecture 2. Chemical Shift and Scalar Couplings. **0**, 1–23 (2005).
6. Jung, B. A. & Weigel, M. Spin echo magnetic resonance imaging. *J. Magn. Reson. Imaging* **37**, 805–817 (2013).
7. Lei, H., Xin, L., Gruetter, R. & Mlynárik, V. Localized Single-Voxel Magnetic Resonance Spectroscopy, Water Suppression, and Novel Approaches for Ultrashort Echo-Time Measurements. *Magn. Reson. Spectrosc. Tools Neurosci. Res. Emerg. Clin. Appl.* 15–30 (2013) doi:10.1016/B978-0-12-401688-0.00002-1.
8. Ordidge, R. J., Connelly, A. & Lohman, J. A. B. Image-selected in Vivo spectroscopy (ISIS). A new technique for spatially selective nmr spectroscopy. *J. Magn. Reson.* **66**, 283–294 (1986).
9. Xin, L. & Tkáč, I. A practical guide to in vivo proton magnetic resonance spectroscopy at high magnetic fields. *Anal. Biochem.* **529**, 30–39 (2017).
10. Mlynárik, V., Gambarota, G., Frenkel, H. & Gruetter, R. Localized short-echo-time proton MR spectroscopy with full signal-intensity acquisition. *Magn. Reson. Med.* **56**, 965–970 (2006).
11. Bottomley, P. A. Selective volume method for performing localized NMR spectroscopy. *U.S. Pat. 4480228* (1984).
12. Tkáč, I. *et al.* Water and lipid suppression techniques for advanced 1H MRS and MRSI of the human brain: Experts' consensus recommendations. *NMR Biomed.* **34**, 1–25 (2021).
13. Tkáč, I., Starčuk, Z., Choi, I. Y. & Gruetter, R. In vivo 1H NMR spectroscopy of rat brain at 1 ms echo time. *Magn. Reson. Med.* **41**, 649–656 (1999).
14. Near, J. *et al.* Preprocessing, analysis and quantification in single-voxel magnetic resonance spectroscopy: experts' consensus recommendations. *NMR Biomed.* 1–23 (2020) doi:10.1002/nbm.4257.
15. Kreis, R. *et al. Terminology and concepts for the characterization of in vivo MR spectroscopy methods and MR spectra: Background and experts' consensus recommendations. NMR in Biomedicine* (2020). doi:10.1002/nbm.4347.
16. Cudalbu, C. *et al.* Contribution of macromolecules to brain 1H MR spectra: Experts' consensus recommendations. *NMR Biomed.* **34**, 1–24 (2021).
17. Provencher, S. Manual. (2019).
18. Simicic, D. *et al.* In vivo macromolecule signals in rat brain 1H-MR spectra at 9.4T: Parametrization, spline baseline estimation, and T2 relaxation times. *Magn. Reson. Med.* **86**, 2384–2401 (2021).
19. Cudalbu, C. *et al.* Contribution of macromolecules to brain 1H MR spectra: Experts' consensus recommendations. *NMR Biomed.* (2020) doi:10.1002/(ISSN)1099-1492.
20. Cudalbu, C., Mlynárik, V., Xin, L. & Gruetter, R. Comparison of T1 relaxation times of the neurochemical profile in rat brain at 9.4 tesla and 14.1 tesla. *Magn. Reson. Med.* **62**, 862–867 (2009).
21. Kunz, N. *et al.* Diffusion-weighted spectroscopy: A novel approach to determine macromolecule resonances in short-echo time 1H-MRS. *Magn. Reson. Med.* **64**, 939–946 (2010).
22. Otazo, R., Mueller, B., Ugurbil, K., Wald, L. & Posse, S. Signal-to-noise ratio and spectral linewidth improvements between 1.5 and 7 tesla in proton echo-planar spectroscopic imaging. *Magn. Reson. Med.* **56**, 1200–1210 (2006).
23. Cudalbu, C., Mlynárik, V. & Gruetter, R. Handling macromolecule signals in the quantification of the neurochemical profile. *J. Alzheimer's Dis.* **31**, (2012).
24. Považan, M. *et al.* Mapping of brain macromolecules and their use for spectral processing of 1H-MRSI data with an ultra-short acquisition delay at 7T. *Neuroimage* **121**, 126–135 (2015).
25. Craveiro, M., Clément-Schatlo, V., Marino, D., Gruetter, R. & Cudalbu, C. In vivo brain macromolecule signals in healthy and glioblastoma mouse models: 1H magnetic resonance spectroscopy, post-processing and metabolite quantification at 14.1 T. *J. Neurochem.* **129**, 806–815 (2014).
26. García-Gómez, J. M. *et al.* Multiproject–multicenter evaluation of automatic brain tumor classification by magnetic resonance spectroscopy. *Magn. Reson. Mater. Physics, Biol. Med.* **22**, 5–18 (2009).
27. Durmo, F. *et al.* Multivoxel 1H-MR Spectroscopy Biometrics for Preoprerative Differentiation Between Brain Tumors. *Tomogr. (Ann Arbor, Mich.)* **4**, 172–181 (2018).
28. Mader, I. *et al.* Proton magnetic resonance spectroscopy with metabolite nulling reveals regional differences of macromolecules in normal human brain. *J. Magn. Reson. Imaging* **16**, 538–46 (2002).
29. Graham, G. D., Hwang, J.-H., Rothman, D. L. & Prichard, J. W. Spectroscopic Assessment of Alterations in Macromolecule and Small-Molecule Metabolites in Human Brain After Stroke. *Stroke* **32**, 2797–2802 (2001).
30. Döring, A, Adalid, V., Boesch, C. & Kreis, R. On the exploitation of slow macromolecular diffusion for baseline estimation in MR spectroscopy using 2D simultaneous fitting. in *Joint 26th Meeting of ISMRM and 35th Meeting of the ESMRMB, Paris (F)* 1315 (2018).
31. Lanz, B., Rackayova, V., Braissant, O. & Cudalbu, C. MRS studies of neuroenergetics and glutamate/glutamine exchange in rats: Extensions to hyperammonemic models. *Anal. Biochem.* (2017) doi:10.1016/j.ab.2016.11.021.
32. Provencher, S. W. Automatic quantitation of localized in vivo 1H spectra with LCModel. *NMR Biomed.* **14**, 260–264 (2001).
33. Pedrosa de Barros, N. & Slotboom, J. Quality management in in vivo proton MRS. *Anal. Biochem.* **529**, 98–116 (2017).
34. Rackayová, V. *Brain metabolism during Chronic Hepatic Encephalopathy studied by in vivo 1H and 31P MRS*. *Epfl-Thesis-8612*

(2018).

35.   Račkayová, V. *et al.* Late post-natal neurometabolic development in healthy male rats using 1H and 31P magnetic resonance spectroscopy. *J. Neurochem.* **157**, 508–519 (2021).

36.   Račkayová, V. *et al.* Late post-natal neurometabolic development in healthy male rats using 1H and 31P MRS. *J. Neurochem.* **submitted**, (2020).

37.   Skoch, A., Jiru, F. & Bunke, J. Spectroscopic imaging: Basic principles. *Eur. J. Radiol.* **67**, 230–239 (2008).

38.   Bogner, W., Otazo, R. & Henning, A. Accelerated MR spectroscopic imaging—a review of current and emerging techniques. *NMR Biomed.* **34**, (2021).

Chapter 2 Mobile Macromolecules in ^{1}H MR spectrum

In vivo localized ^{1}H MR spectra at short TEs contain the contribution of mobile macromolecules (MM, broader resonances characterized by short T_1 and T_2 relaxation times. These resonances overlay with the narrower metabolic peaks and can present a problem during quantification especially for the low concentrated metabolites. Therefore, a reliable detection, post-processing and fitting of MMs is crucial for quantification of short-TE ^{1}H MR brain spectra. Furthermore, MM contribution can change in disease, indicating the necessity for their accurate and appropriate estimation. Recent methodological advancements combined with ultra-high magnetic fields ensured an increased spectral resolution facilitating the separation of MM spectrum in individual components/peaks. As a result, parametrization of MM spectra into components and their consecutive inclusion in the metabolite basis set for quantification was introduced. Moreover, a relatively free spline baseline is often used during the fitting process to address unpredicted spectral components. Both MM parametrization and baseline estimation require a wider implementation at UHF.

In this chapter we used a single IR sequence combined with advanced AMARES prior knowledge to eliminate metabolite residuals, fit and parametrize 10 MM components directly from in vivo ^{1}H MR spectra acquired from the rat brain at 9.4 T using different TEs. Monte Carlo simulations were used in addition to in vivo MR spectra to assess the concomitant influence of parametrized MM and DKNTMN parameter in LCModel.

We observed that a very stiff baseline in combination with a full MM spectrum led to deviations in metabolite concentrations. This effect was less pronounced for parametrized MM spectra. Adding prior knowledge on parametrized MM spectrum improved MM and metabolite quantification. Finally, the implemented method for MM fitting allowed to estimate T_2^{app} for seven individual MM peaks. In this chapter an improved methodological approach allowing reliable post-processing, fitting and quantification of MM spectra is proposed. The described method also provided an efficient tool for parametrization of individual MM. We showed that a degree of flexibility in the spline baseline is required for a most reasonable quantification of real/experimental data.

*This chapter is structured in three sub chapters. The first sub chapter (2.1) is titled "**Handling of the mobile macromolecules in ^{1}H MR spectrum – post processing, parametrization and inclusion in the LCModel basis set**". In this sub chapter the following sections are covered: the acquisition on MM using a single inversion recovery sequence with an optimized inversion time, post-processing (elimination of metabolite residuals), fitting and parametrization of 10 mobile macromolecule's (MM) components directly from in vivo spectra at 9.4T in the rat brain at different TEs using an advanced AMARES prior knowledge. In addition, it provides details on the created basis sets for metabolite quantifications which include the resulting single MM spectrum and the parameterized MM peaks. The second sub chapter (2.2) is titled "**Estimation of T₂ relaxation times".** It describes how the apparent T₂ relaxation times (J evolution not considered) for seven individual MM components were estimated in the rat brain at 9.4T. Furthermore, in the third sub chapter (2.3) titled "**Influence of the MM model and spline baseline stiffness on metabolite quantification"** it is described how the created basis sets with single and parametrized MM were used for quantification and compared concomitantly with varying the LCModel DKNTMN parameter (baseline stiffness), to assess the resulting changes in metabolite and MM concentrations using in vivo acquired ^{1}H MR spectra (rat brain at 9.4T) and Monte Carlo simulations.*

2.1 Handling of the mobile macromolecules in ^{1}H MR spectrum – post processing, parametrization and inclusion in the LCModel basis set

When short echo-time (TE) pulse sequences are used, the resulting ^{1}H MR spectra contain the contribution of mobile macromolecules. These are broader resonances characterized by shorter relaxation times (T_1 and T_2), underlying the narrower peaks of metabolites[1–3] (Figure 2:1A). In healthy brain, MM signals result primarily from protons of amino acids that make up the cytosolic proteins[4–8] in regions undergoing rapid motions on the time scale of NMR, which is highlighted by the term "mobile" used also in an interchangeable manner with the term "macromolecules". The same amino acids have different spectral patterns in different proteins depending on their chemical environment. Thus, the broad MM signals in vivo most likely come from overlapping and closely spaced multiplets (due to scalar coupling) of amino acids within various proteins. In this chapter the MM peaks will be described by their resonant frequencies in ppm according to the recommended nomenclature[3] (Figure 2:1B).
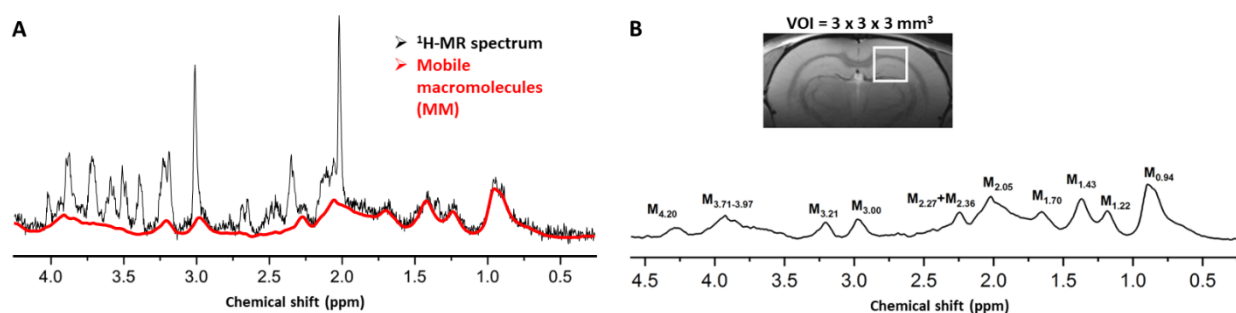
Figure 2:1: Short TE spectrum and macromolecules (9.4T) (A) Example of the short echo time (TE=2.8ms, TR=4sec, NA=160, VOI centered on the hippocampus of the rat brain) spectrum acquired with the SPECIAL sequence at 9.4T with the underlying MM signal (marked in red) **(B)** The MM signal acquired in the rat brain at 9.4T (TE=2.8ms) with marked MM components named according to the recommended nomenclature[3].

The MM spectra can be measured *in vivo* using sequences which are exploiting their shorter T_1 relaxation times compared to metabolites[1,9,10]. Single and double inversion recovery (IR) techniques are recommended for the acquisition of an *in vivo* MM spectrum, both providing improved metabolite suppression[3]. However, both techniques lead to the presence of some residual metabolite resonances in the acquired MM spectrum. In parallel, the availability of ultra-high magnetic fields (UHF ≥ 7T) leads to better resolved MM, thus more sophisticated approaches need to be used for post-processing[11,12](e.g. elimination of residual metabolites) or for further parametrization of the acquired MM spectrum into individual components[13].

For reliable quantification of short TE ^{1}H MR brain spectra, which contain MM contributions, accurate MM fitting is crucial. Generally, an in vivo acquired and post-processed single MM spectrum is included in the basis set for spectral fitting[2,3,14]. Since there is evidence that MM contribution can change in disease [12,15–20], inclusion of full MM signal as a single spectrum from a healthy subject in the basis set can lead to errors in quantification. Moreover, given the potential regional and/or disease[12,15–21] dependent variability[21] of MM, acquisition and incorporation of subject-specific MM into the ^{1}H MR spectral fitting may be preferable and the most direct way to estimate their contribution. However, this approach has been of limited use due to increased scan time needed to acquire a separate spectrum. In this context, recent methodological advancements combined with high magnetic fields ensure an increased spectral resolution facilitating the separation of MM in individual components/peaks[1,13]. As such, information about their individual content is appreciated and is becoming valuable in clinical studies[1,13]. As a result, the parametrization of MM into components and their consecutive inclusion in the metabolite basis sets is a method that is beginning to be used more and more at different B_0. Usually, separately fitted MMs are summed or grouped prior to inclusion in the metabolite basis set to reduce the number of independent components and thus the risk of over-parametrization by the quantification algorithm[1,21–25]. Frequently, no prior knowledge on the individual MM peaks in the form of soft constraints either on the peak amplitudes or ratios has been used in the past. Recently 7T clinical studies showed that the parametrization of MM signals with appropriate prior knowledge (PK) (i.e. chosen signal intensity ratios of individual MM peaks.) is feasible and may facilitate the detection of individual MM components[13]. Considering that an *in vivo* acquired spectrum is preferable compared to a purely mathematical estimation of MM[26], typically pre-acquired representative metabolite-nulled spectra are used for MM parametrization[3]. Using the parametrized MM components in the basis set brings an improved MM model for metabolite quantification compared to a purely mathematical estimation, simultaneously providing information about individual MM content[13]. Although parametrization is an accepted method for estimation of individual MM peaks, its implementation is not sufficiently straightforward since increasing the number of fitted parameters without constraints may lead to overfitting[3]. Therefore, this method needs a more general implementation.

In this section, a single inversion recovery (IR) sequence with an optimized inversion time was used combined with advanced AMARES prior knowledge to eliminate the metabolite residuals, fit and parametrize 10 MM components directly from in vivo spectra at 9.4T in the rat brain at different

TEs. The residual free single MM spectrum (TE=2.8 ms) and the parametrized MM peaks (TE=2.8 ms) were then included in the basis sets for metabolite quantification which will be further used and discussed in the section 2.3.

2.1.1   Methods – Acquisition of MM spectra

Wistar male adult rats (n=6 Charles River Laboratories, L'Arbresle, France) were used and were anesthetized with 1.5-2.5% isoflurane for the ^{1}H MRS experiments. The body temperature of the animals was kept at 37.5 ± 1.0 °C, by circulating warm water. All experiments were approved by The Committee on Animal Experimentation for the Canton de Vaud, Switzerland.

In vivo ^{1}H MRS measurements were performed on a horizontal actively shielded 9.4 Tesla system (Magnex Scientific, Oxford, UK) interfaced to a Varian Direct Drive console (Palo Alto, CA, USA). A home built ^{1}H-quadrature surface coil was used as a transceiver. To measure the in vivo MM spectra, the SPECIAL[27] sequence was extended with a 2 ms nonselective hyperbolic secant inversion pulse[28], applied at TI of 750 ms before starting the localization part of the SPECIAL sequence (the first RF pulse i.e. the slice selective adiabatic inversion pulse – Figure 2:2)[29]. The MM spectra were acquired with a short TR (TR = 2.5 s, to decrease the contribution of residual metabolites), and TE = 2.8 ms if not stated otherwise. This TI was chosen to minimize the metabolites signals using 1) a series of IR spectra acquired with several TIs (i.e. 420, 600, 700, 725, 750, 800, 1000 ms) and 2) an IR spectrum (TI = 750 ms) acquired with a longer TE (TE = 40 ms) to double check the presence of residual metabolites while decreasing the MM contribution. All the *in vivo* MM spectra were acquired in a voxel of 3 x 3 x 3 mm^3 centered on the rat hippocampus (Figure 2:2), first and second-order shims were adjusted using FAST(EST)MAP[30] leading to water linewidths of 11-12 Hz. This VOI was selected in order to increase the SNR while it is well accepted that MM do not substantially change between brain regions rodents[3,31,32]. To estimate the T_2 relaxation times of individual MM peaks, the MM spectra were acquired from n = 6 rats at 13 TEs (TE = 2.8, 4, 6, 8, 10, 12, 16, 20, 40, 60, 100, 120 and 150 ms, TI = 750 ms) (this work is further described in section 2.2 and is briefly mentioned in this sub chapter because of the need of eliminating the residual metabolites and parametrization of the acquired MM at each TE in individual components).
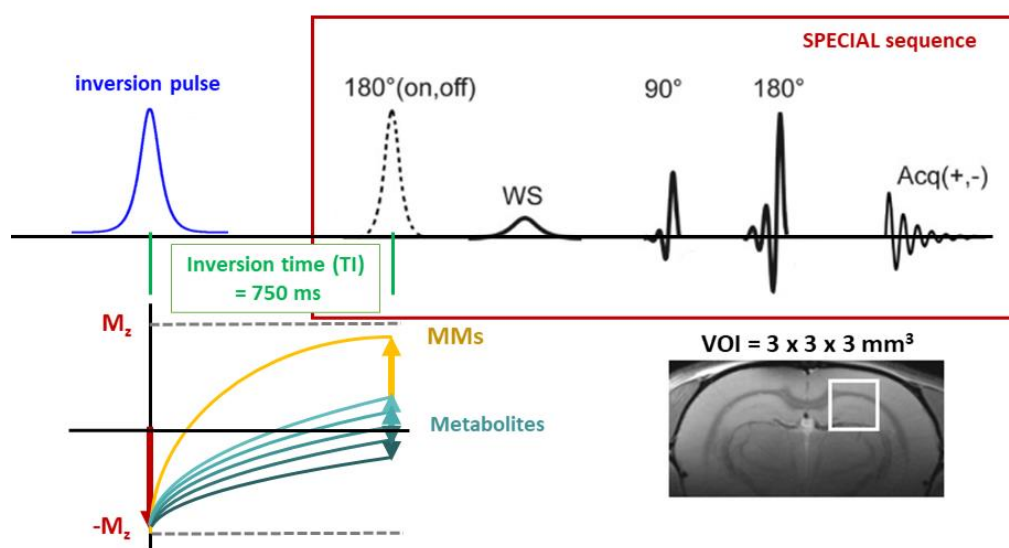
Figure 2:2: SPECIAL sequence extended with an inversion pulse. The scheme of the SPECIAL sequence extended with a 2 ms nonselective hyperbolic secant inversion pulse applied at a TI = 750 ms (TE=2.8ms). The effect of different T1 relaxation times of metabolites[9] is depicted in the IR scheme of the magnetization showing that even though the TI was optimized for metabolite nulling there are still metabolite residuals present in the resulting spectrm which need to me removed by post-processing (see Chapter 2.1.2). The insert image (bottom right corner) shows the VOI = 3 x 3 x 3 mm^3 centered on the rat hippocampus (all the MM spectra were acquired from VOI positioned in this location).

2.1.2 Data processing

2.1.2.1 *Post-processing: elimination of metabolite residuals from MM spectra at different TEs*

Even though the TI was optimized in the acquisition sequence for metabolite nulling, some metabolite residuals were still present in the resulting spectrum and needed to me removed by post-processing. The acquired MM spectra were phased individually in jMRUI (http://www.mrui.uab.es/mrui/), and 2 Hz of Lorentzian line broadening was applied (for visualization only). Metabolite residuals present in the acquired MM spectra at all TEs were identified by implementing the following steps: 1) a series of IR spectra using a full range of TIs (i.e. 420, 600, 700, 725, 750, 800, 1000ms); and 2) IR spectrum with a longer echo time (TE=40ms) to confirm the presence of residual metabolite signals (Figure 2:3A)[3].
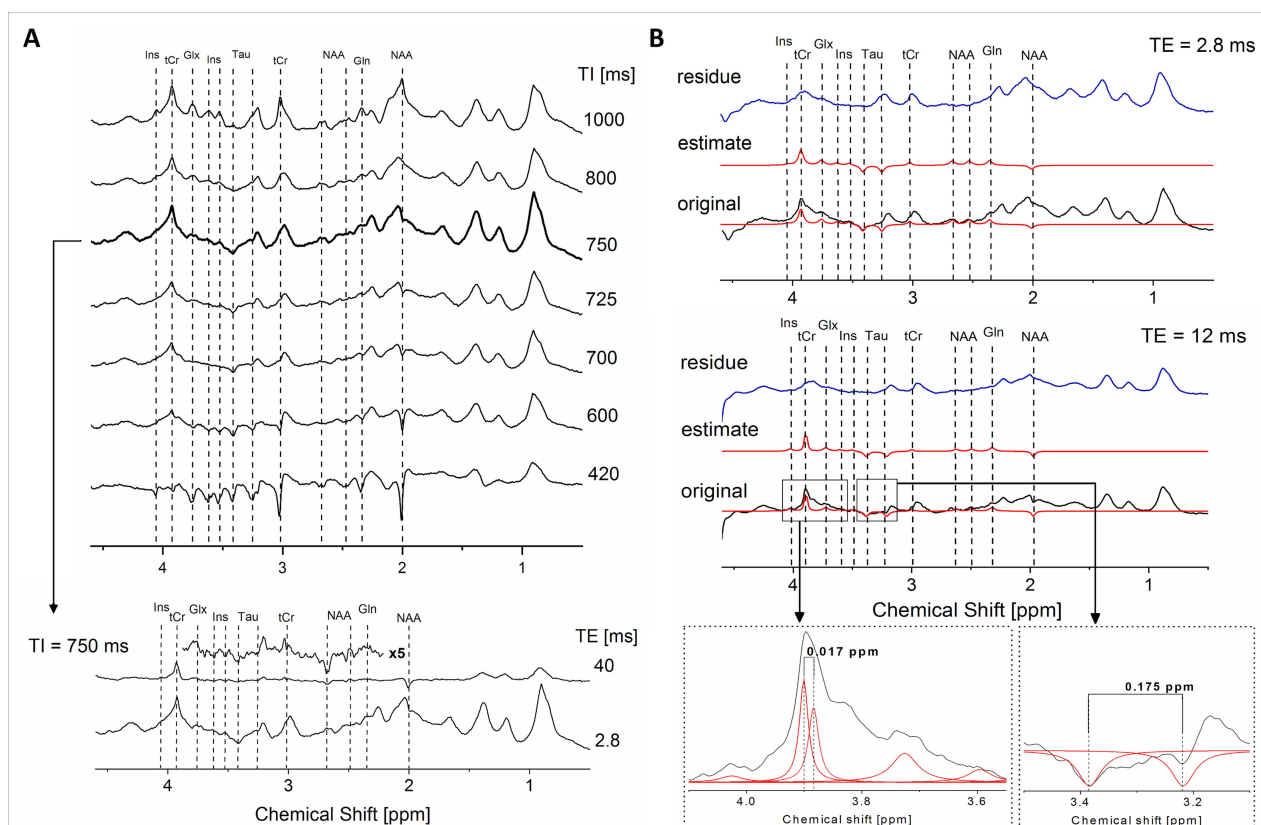
Figure 2:3: Removal of metabolite residuals. **(A)** (**up**) In vivo rat brain series of IR spectra with TI ranging from 420 to 1000 ms revealing the evolution of metabolite intensities over a series of different TIs to identify the optimal TI and the metabolite residuals (acquisition parameters TE/TR=2.8/2500 ms); (**down**) Spectra acquired with the selected TI=750 ms and TE=2.8 ms as well as with TE=40 ms (5x magnified) to confirm the presence of residual metabolite signals; **(B)** (**up**) Original MM spectrum acquired at TI=750 ms and TE=2.8 ms (shown in black), estimated fits of the residual metabolites using AMARES (shown in red) and the residue obtained after subtraction of the estimated metabolites signals from the original spectrum (shown in blue); (**down**) original MM spectrum acquired at TI=750 ms and TE=12 ms (shown in black), estimated fits (shown in red) and obtained residue (shown in blue) with two inserts: 1) an expansion on the fit of tCr at TE=12ms with two peaks with 0.017ppm shift (on the left); 2) an expansion on the fit of two Tau peaks with same amplitude, lw and a chemical shift of 0.175 (on the right).

Using the AMARES algorithm[33] (advanced method for accurate, robust and efficient spectral fitting) we implemented a user-built set of prior knowledge with the constraints on the peak frequency, phase, linewidth and amplitude was used to fit the residual metabolites of Ins, tCr, the sum of glutamine and glutamate (Glu+Gln – Glx), Tau, NAA (sometimes using more peaks per metabolite, as described in Table 2:1) and thus their contribution was removed from the MM spectra (Figure 2:3B). To construct such prior knowledge, all residual metabolite peaks were analyzed individually at a given TI and TE and fitted using singlets. J-coupled metabolites (e.g. Glx, Tau) were fitted with larger linewidths to account for the J-splitting appearance (Table 2:1). This is the best possible approximation used in literature at high B_0 and short TE[12,13,34], with the main difference that in this study more metabolite residuals were reliably identified[13,23,35] (i.e. NAA-2.49 ppm, Tau-3.42 ppm, Glx-3.75 ppm,

Ins-4.05 ppm; see Table 1). The linewidth used for fitting metabolite peaks (singlets and multiples) was in the range of 8 to 25 Hz depending on their multiplicity.

Table 2:1:Information for AMARES prior knowledge. Information on the individual residual metabolite peaks used to build the AMARES prior knowledge. This table was created based on previously published data[36,37]. Note: s – singlet, dd – doublet of doublets, t – triplet, m – multiplet. Soft constraint on the chemical shift of 0.01ppm was added if necessary.

Metabolites	Chemical shift (ppm) - fixed	Multiplicity	Phase-fixed	Number of peaks	Linewidth – soft constraints	Notes
tCr			0	1	15-20	Starting from the TE=12ms it is fitted with two peaks with a shift between them of 0.017ppm (because of different T_2 of Cr and PCr)
Cr & PCr	3.91	s	0 & 0	2	7-10	
tCr	3.027	s	0	1	12-15	T_1 is longer than for the peak at 3.91ppm, thus this peak is smaller
Glx	3.75	dd & t	0	1	22-25	
Ins	3.61 & 3.52	dd & t	0 & 0	1	20 & 20	Similar peaks, both disappear at TE=20ms
Ins	4.05	t	0	1	20	
Tau	3.42 & 3.246	t & t	180 & 180	1	20 & 20	Both peaks must have the same amplitude and lw with a shift between them $\approx$ 0.175ppm
NAA	2.67 & 2.49	dd & dd	0 & 0	1	18-22 & 18-22	Both peaks have similar amplitude and lw, they disappear at TE=20ms
NAA	2.01	s	180	1	10-18	Very well visible even at longer TE
Glu	2.34	m	0	1	20-21	

All the identified metabolites were removed from the MM spectra until TE≤40ms. From TE=60ms most of MM peaks which overlap with metabolite resonances could not be adequately distinguished and thus only $M_{0.94}$, $M_{1.22}$ and $M_{1.43,}$ which do not overlap with any of the identified residuals, were fitted. In addition to three previously mentioned MM components, $M_{3.21}$ was still detectable and thus fitted also at TE=60ms. The subsequent iterations were followed to build up the prior knowledge: 1) every metabolite was individually removed from the MM spectrum using a flexible, metabolite specific prior knowledge; 2) in the second step, the results obtained for individual peaks were combined to form a single rigorous prior knowledge (still leaving some freedom on the amplitude (no more than 10%) for the peeks to adjust to different spectra); 3) the metabolite free MMs (i.e. the residual after AMARES post-processing) was saved separately.

2.1.2.2 Fitting of the individual MM components

MMs were divided into ten components (Figure 2:4) and quantified using AMARES. Each MM component was quantified using several Lorentzian lines and prior knowledge to obtain the best possible match with the original spectra, without accounting for J-evolution of these MM peaks.
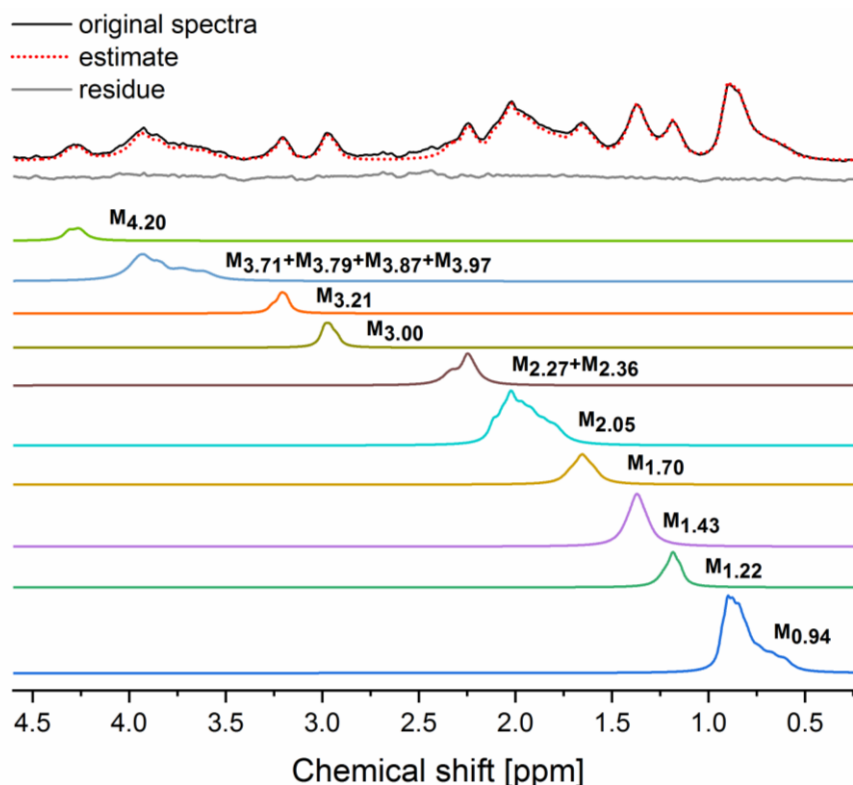
Figure 2:4: 10 MM components. MM spectrum parametrized into 10 individual components (TE = 2.8 ms). The original spectrum was fitted using AMARES and the fits of individual components were saved separately (in color).

Table 2:2 shows the constraints in frequency, number of peaks and linewidth which were given to AMARES as prior knowledge for fitting, while the amplitude was left to be estimated freely by the algorithm. After each fit, the spectra were manually inspected. In some cases (longer TEs) soft constraints on the amplitudes of the peaks were additionally imposed to avoid over or underestimation (e.g. negative or positive residuals, respectively). To assess the goodness of fit (possible over or under fitting) a 'fit quality number' (FQN) was calculated (as a ratio of the variance in the fit residual divided by pure spectral noise) using a Matlab code written in-house[14,39].

Table 2:2: Prior knowledge given to AMARES for the MM fitting: constraints in frequency, number of peaks, linewidth and line shape. Note that if one MM was fitted with multiple peaks, they all had the same constraints on frequency and linewidth. The prior knowledge and example spectra are available online as AMARES files, see the publication[38].

AMARES - prior knowledge for MM fitting					
	Frequency-soft constraints (ppm)	Phase	Number of peaks	Linewidth-soft constraints	Shape
$M_{0.94}$	0.61-1.05	0	8	0-15	lorentzian
$M_{1.22}$	1.10-1.26	0	3	0-25	lorentzian
$M_{1.43}$	1.27-1.50	0	3	0-25	lorentzian
$M_{1.70}$	1.53-1.76	0	3	0-35	lorentzian
$M_{2.05}$	1.77-2.17	0	7	0-30	lorentzian
$M_{2.27-2.36}$	2.17-2.36	0	3	0-25	lorentzian
$M_{3.00}$	2.86-3.05	0	3	0-30	lorentzian
$M_{3.21}$	3.10-3.30	0	3	0-30	lorentzian
$M_{3.71-3.97}$	3.70-4.10	0	5	0-40	lorentzian
$M_{4.20}$	4.20-4.40	0	2	0-30	lorentzian

2.1.2.3 Basis sets – Single MM and parametrized MM components from experimentally measured MM spectra

LCModel, the method used herein, analyzes the in vivo spectrum as a linear combination of known compound responses (obtained from in vitro measurements or simulations using identical acquisition parameters as for the in vivo acquisition) of known contributing metabolites. Complete spectra are used to provide maximum prior information and increase the fitting precision[39,40]. In this study, the metabolites were simulated using NMRScope-B from jMRUI[41], using published values of J-coupling constants and chemical shifts[36,42] and the SPECIAL sequence with the same parameters as the ones used for the in vivo ^{1}H MRS metabolite acquisitions (section 2.3.1.1 -TE=2.8ms, same RF pulse shapes, number of points, acquisition time, etc.). The simulated individual metabolite spectra were put together with an appropriate MM spectrum to make an adequate basis set for quantification. **Two basis sets** were built in this study which will be further used in the section 2.3. In the **first basis set** the experimentally acquired and post processed single MM spectrum (as described in the sections 2.1.1 and 2.1.2.1) was combined with the simulated metabolites to construct the final basis set. For the **second basis set** the ten individual MM components from the MM spectrum acquired at TE=2.8ms and TI=750ms were fitted and saved separately (using AMARES as described in section 2.1.2.2) to create separate/individual MM peaks (Figure 2:4). These individual MM peaks were then

combined with the simulated metabolites to create the final basis set. Additional constraints on the resulting individual MM amplitudes were applied in the control file in the form of soft constraints. The control file specifies the necessary control parameters for the LCModel quantifications corresponding to the conditions of the acquisition and the basis set used (among other commands to run LCModel quantifications)[43].To implement the soft constraints, each MM component was first quantified from three measured spectra at TE=2.8ms (n=3 rats). Signal intensity ratios of $M_{xx}/M_{0.94}$ were then calculated for every spectrum and averaged over the three acquisitions to obtain a mean value and SD for each ratio (Table 2:3). These values were included in the LCModel control files using the parameter CHRATO as described in[13]. It is important to emphasize, once more, that these two basis sets match the in vivo ^{1}H MRS metabolite acquisitions described in the section 2.3.1.1: the metabolites were simulated, and the MM were acquired using the corresponding sequence while the VOI was centered in the hippocampus. In this manner we have set the best conditions for a reliable metabolite quantification.

Table 2:3: MM soft constraints. Signal intensity ratios presented as mean values (n=3 MM spectra from 3 different rats) and their SDs obtained using AMARES.

Signal intensity ratios		
Ratios:	**Mean**	**SD**
$M_{1.22}/M_{0.94}$	0.28	0.01
$M_{1.43}/M_{0.94}$	0.59	0.08
$M_{1.70}/M_{0.94}$	0.45	0.12
$M_{2.05}/M_{0.94}$	1.14	0.20
$M_{2.27-2.26}/M_{0.94}$	0.35	0.07
$M_{3.00}/M_{0.94}$	0.24	0.08
$M_{3.21}/M_{0.94}$	0.30	0.17
$M_{3.71-3.97}/M_{0.94}$	0.68	0.09
$M_{4.20}/M_{0.94}$	0.21	0.11
Derived from n=3 spectra		

2.1.3   Results – post processing, parametrization and fitting into 10 individual components.

The high quality of the *in vivo* acquired MM is shown in Figure 2:3 with SNR of 19.1 $\pm$0.5 (for TE=2.8 ms - calculated in jMRUI as a ratio between the highest peak ($M_{0.94}$) and standard deviation of spectral noise). The proposed post-processing method using AMARES and advanced prior knowledge based on different TI and TE=40 ms was efficient and robust in removing all the residual metabolites

providing clean MM spectra for MM fitting, metabolite and MM quantification (Figure 2:3). Thus, the proposed post-processing was extended at longer TEs also. Our approach allowed the reliable identification of 12 metabolite residuals from Ins, tCr, Glx, Tau, NAA (Table 2:1).

MM were fitted and parametrized as described in section 2.1.2.2 (Figure 2:4, Table2:2). The fitting procedure provided reliable values for MM ratios (mean ± SD, Table 2:3) as prior knowledge to be used in LCModel for the parametrized MM basis set. The final residual spectrum (Figure 2:4 in grey) was flat and clean of any major MM residual contribution, thus provided an excellent approximation of the in vivo measured MM spectrum demonstrating a very good performance of parametrization. Goodness of fit was confirmed by calculating the FQN. The mean value of FQN, of all the fitted spectra, was 1.2 ± 0.2 indicating that the model (fit) agrees with the data within the precision allowed by the noise.

2.1.4 Discussion and conclusion - post processing, parametrization and fitting into 10 individual components.

In this study, ten individual MM peaks were successfully fitted, after removing the metabolite residuals, and parameterized directly from in vivo short TE spectra at 9.4T in the rat brain. AMARES is a well-known and efficient algorithm used to remove residual metabolites from MM spectra[12,13,24]. AMARES was used with advanced prior knowledge for removal of metabolite residuals from MM spectra at TE=2.8ms and extended to MM spectra acquired at different TEs (up to 40 ms). Furthermore, additional metabolite residuals were identified and reliably removed from MM spectra compared with previous preclinical[12,35] (Ins-4.05 ppm) and clinical (tCr-3.0 ppm, Ins-3.6 ppm, Tau-3.25 ppm)[11,13,23,44] studies. The implemented set of prior knowledge allows the removal of residual metabolites in an automatic and user-friendly way and it can be implemented in different labs, brain regions and also adapted for different B_0. The prior knowledge and example spectra are available online as AMARES files, see the publication[38].

Parametrization of MM into individual signal components is difficult since the signal is a result of many chemical entities whose number and nature are predominantly unknown. To date the MM spectrum has been parametrized into an arbitrary number of Lorentzian, Gaussian or Voigt lines to interpret distinguishable signal entities which were then grouped or combined together to avoid over parametrization[3,13,21–25,45–47]. These grouped or combined MM were then included into the basis set for quantification. At high B_0, nine to 24 distinct MM peaks can be distinguished based on the

nomenclature used[3,11,13], with some peaks needing further investigations. When parametrized, these peaks have been previously fitted using mainly singlets[13,44,48], while some studies used several peaks to fit the individual MM without specific prior knowledge. Even though MM can be modeled using singlets, it is well known that they have complex spectral patterns. In the present study we fitted and parametrized the *in vivo* acquired MM into ten components using AMARES, formerly recommended tool[13] for MM parametrization. In parallel, we aimed at fitting the maximum number of individual MM components, which in our case was ten with two of them containing several MM peaks ($M_{3.71-3.97}$, $M_{2.27}$). The MM peaks at 2.56 and 2.70 ppm, previously reported in a human study at 9.4T[11,48], were not fitted in the present study. These two peaks had a relatively small contribution in our rat brain spectra and based on the IR curve they were well modeled by the residual NAA resonances, in agreement with a study performed at 3T[44]. However, a small MM contribution cannot be excluded. Each of the ten MM components was parametrized by fitting with several Lorentzian functions to take into account various unknown constituents that might be contained in one broad resonance. This approach reduced the overlap between MM resonances, which might arise when broad functions are used. This parametrization was the result of an iterative process, which lead to a very efficient fitting procedure giving artifact free fitting residuals. Moreover, we used three MM acquisitions *in vivo* that were individually parametrized. The resulted signal intensity ratios of $M_{xx}/M_{0.94}$ were averaged to obtain mean values and standard deviations which were then used as prior knowledge and soft constrains in the LCModel control files. The prior knowledge and soft constraints used herein were in agreement with a previous study in the human brain at 7T[49], while another study in the rat brain at 7T[35] has reported higher overall MM amplitudes/ratios. These results can be extended to pathological conditions by measuring the MM in 1-2 patients and then parametrizing the *in vivo* MM as performed in the present study, or by using the soft constrains provided. The soft constrains can then be adapted based on the visual appearance of the spectra (e.g. fits, residuals and baseline). For instance, if it is known or visible in the ¹H MR spectrum that a specific MM moiety is changing, then more freedom can be provided for this MM moiety through soft constraints on the prior knowledge or a separately simulated MM or lipid component can be added to the basis set[20]

2.2 Estimation of T_2 relaxation times

For accurate assessment, distinction and understanding of MM behavior, the knowledge of their individual T_1 and T_2 relaxation times is necessary[25,51]. The apparent T_2 ((J evolution not considered, T_2^{app}) relaxation times have been previously measured by acquiring MM spectra over a range of TEs. The signal amplitudes of the individual MM components were then plotted as a function of TEs and fitted assuming a mono-exponential decay (see sub chapter 1.4 Equation 1.31) where the two unknown parameters of the fit are the T_2^{app} and the signal amplitude at the TE=0.

There are few studies assessing the T_2 values of MMs[25,52,53], with only two recent studies reporting T_2s of individual MM peaks in the full ppm range at 9.4 T and 3 T in human brain[44,47,48]. Otherwise, T_2 values have only been reported for the entire MM spectrum[53], grouped MM signals[25] or for the peaks up to 1.7 ppm. Estimating T_2 for individual MM signals is not straightforward due to the overlapping metabolites and requires advanced approaches.

In this section the T_2^{app} for seven individual MM components was estimated in the rat brain at 9.4T.

2.2.1 Measurement and fitting of the MM T_2^{app}

For the measurement of MM T_2^{app} relaxation times (n=6 rats), the TE was varied from 2.8 to 150ms (TE=2.8, 4, 6, 8, 10, 12, 16, 20, 40, 60, 100, 120 and 150ms, TI=750ms, 1024 averages per TE). For minimizing the anesthesia effects due to very long acquisition time (1024 averages per TE) the TE-s were iterated among. As a result, two acquisitions for each TE (e.g. 2 rats) were performed with an additional acquisition used for MM parametrization at TE=2.8ms (e.g. 3 rats).

The spectra were acquired and post-processed as described in sections 2.1.1. and 2.1.2 to eliminate metabolite residuals and finally fitted in individual components as described in section 2.1.2.2. Figure 2:5 shows some examples of metabolite clean MM spectra at various TEs.
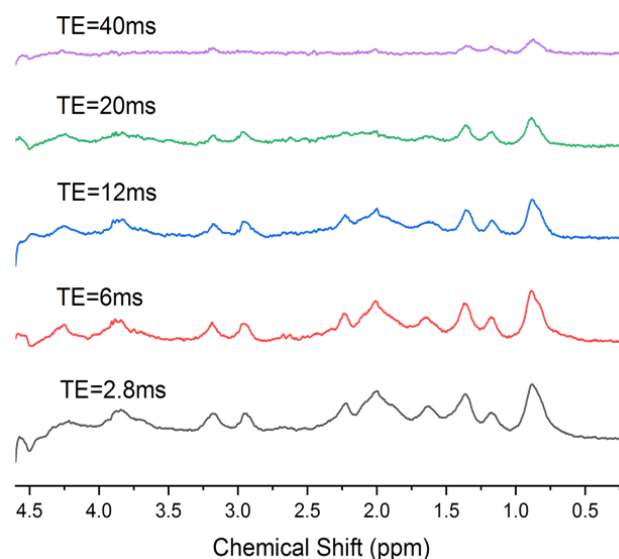
Figure 2:5: MM spectra at different TEs. MM spectra after the elimination of metabolite residuals at different TEs (TE = 40, 20, 12, 6, 2 ms); example from one rat (only few spectra are shown in this figure as an example).

To allow pooling data from all 6 animals in a joint T_2 fitting, inter-animal scaling of peak amplitudes was done. $M_{0.94}$ was used as a reference since it is reliably quantified and does not overlap with metabolite resonances. A scaling factor was calculated for each animal using the ratios between the $M_{0.94}$ components at TE = 2.8 ms. The quantified and normalized amplitudes from all rats were fitted to a single exponential decay across the TE series for each MM component to estimate the T_2 relaxation times.

2.2.2   Results - T_2^{app}

All the 10 MM components were fitted (at different TEs) to estimate the T_2^{app} relaxation times. For seven components reliable exponential decay fits were obtained (standard deviation of the fit was lower than 20%), leading to reliable T_2^{app} estimations (Figure 2:6). As can be seen the MM at 0.94, 1.22, 1.43 and 3.00 ppm all presented similar T_2 relaxation times in-between 22-24 ms, while the ones at 1.70, 2.05, 3.21 ppm were in-between 12-15 ms (Table 2:4).
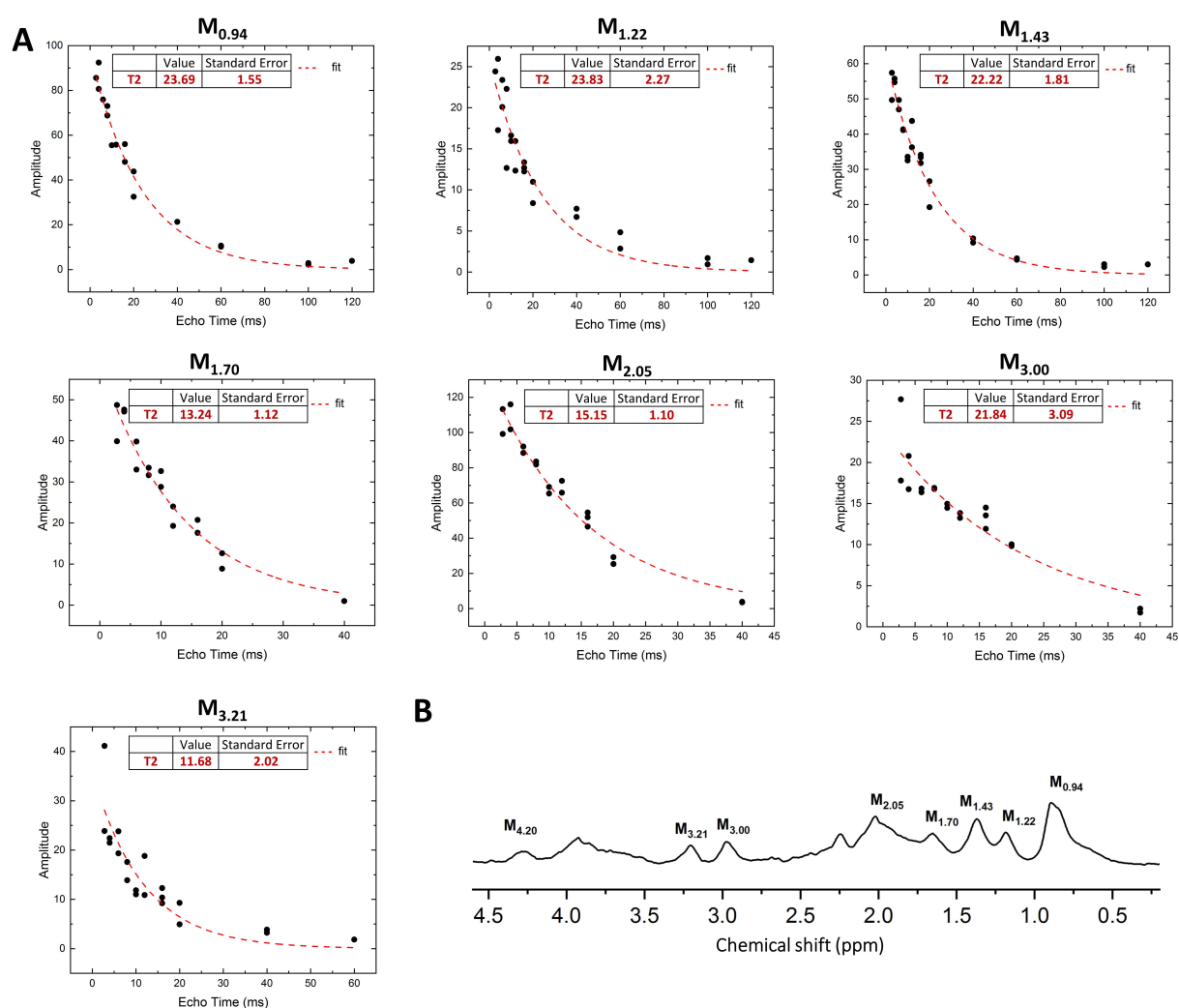
Figure 2:6: T$_2^{app}$ relaxation fits. **(A)** Exponential fits providing T$_2^{app}$ relaxation estimates, **(B)** The MM spectra with marked components for which the relaxation times were estimated

Table 2:4: T$_2^{app}$ estimates obtained from the exponential fits of MM decay over TEs and its SDs for 7 out of 10 MM

	T$_2^{app}$ [ms]	SD of the fit
M$_{0.94}$	24	2
M$_{1.22}$	24	3
M$_{1.43}$	22	2
M$_{1.70}$	13	1
M$_{2.05}$	15	1
M$_{2.27-2.36}$	–	–
M$_{3.00}$	22	3
M$_{3.21}$	12	2
M$_{3.71-3.97}$	–	–
M$_{4.20}$	–	–

2.2.3 Discussion and conclusion T_2^{app}

We reported the T_2^{app} of seven individual MM peaks at 9.4T in the rat brain. High quality spectra and fits were obtained at all TEs. It is well known, that the choice of TEs is important for achieving reliable estimates for T_2^{app} relaxation times, but the optimal choice remains an open question and is sometimes dictated by the achievable SNR. Nine to thirteen TEs were used in the present study for the calculation of T_2^{app} relaxation times of MM, the longest being 150ms for $M_{0.94}$, $M_{1.22}$ and $M_{1.43}$. The chosen approach appeared to be adequate for modeling the T_2^{app} relaxation of MM peaks as evidenced by the appropriate modelling of observed signal decay and low standard deviation. Despite the smaller number of acquisitions per TE, more than nine TEs for each fit were used resulting in a good confidence curve fit for seven T_2^{app} values. Although previous studies assessing the T_2 relaxation times of the MM in the rat brain mainly reported results for grouped or full MM rather than individual components, the present results are in good agreement with these published values[25,52,53]. Our results predominantly fall in range of T_2^{app} relaxation times recently reported for human brain at 9.4T for fourteen individual MM peaks[48] and at 3T for ten individual MM peaks assessed in different brain regions[44].

2.3 Influence of the MM model and spline baseline stiffness on metabolite quantification

To reliably quantify metabolite concentrations from ^{1}H MR spectra containing the contribution of MM, the MM spectrum needs to be subtracted before the spectral fitting or included into the basis set for the spectral fitting. Normally, the second option is used more often where the in vivo acquired MM spectrum is first appropriately processed (elimination of metabolite residuals) and then included it in the basis set. Hence, incorporating the MM signal in the basis set (single MM spectrum) improves the fitting stability. Alternatively, the MM signal can be parametrized into individual components to quantify the MM individually. This approach results in higher analysis flexibility, but the increased number of fitted parameters can lead to overfitting[3]. The LCModel basis sets used for quantifications in this section are described in the section 2.1.2.3.

In addition to the MM, a relatively free spline baseline is used during the fitting process to address unpredictable spectral components[40,43] (smoothly varying components and spurious signals arising through imperfections during data acquisition). Recently, the effect of the stiffness of the fitted spline baseline on the resulting metabolite concentrations when using LCModel gained a lot of

interest[54]. Finding the optimal degree of baseline flexibility is mandatory for reliable metabolite concentration estimates, yet few studies have investigated this topic in detail[53–57]. Stiffness of the spline baseline in LCModel is controlled by the parameter *DKNTMN* (minimum allowed spacing between spline knots)[43,54]. The default value is set to 0.15 ppm (low stiffness), and all the values equal to or higher than 1 ppm give a high baseline stiffness[54]. A study performed at 9.4T in humans has reported several changes in metabolite concentrations when quantifying with different *DKNTMN* values, but no conclusion on best value was drawn[54,58] due to lack of ground truth. To draw such a conclusion, an extensive Monte-Carlo simulation-study is necessary.

In this section the two created basis sets (section 2.1.2.3.) including an appropriately processed single (section 2.1.2.1.) and parametrized (section 2.1.2.3) MM spectrum were used for metabolite quantification and compared concomitantly with varying the DKNTMN parameter for both approaches, to assess the resulting changes in metabolite and MM concentrations using in vivo acquired ^{1}H MR spectra (rat brain at 9.4T) and Monte Carlo simulations.

2.3.1   Methods

2.3.1.1   *Acquisition of metabolite spectra*

Wistar male adult rats (n=6 Charles River Laboratories, L'Arbresle, France) were used and were anesthetized with 1.5-2.5% isoflurane for the ^{1}H MRS experiments. The body temperature of the animals was kept at 37.5 ± 1.0 °C, by circulating warm water. All experiments were approved by The Committee on Animal Experimentation for the Canton de Vaud, Switzerland.

In vivo ^{1}H MRS measurements were performed on a horizontal actively shielded 9.4 Tesla system (Magnex Scientific, Oxford, UK) interfaced to a Varian Direct Drive console (Palo Alto, CA, USA). A home built [1]H-quadrature surface coil was used as a transceiver. Spectra were acquired using the SPECIAL sequence (TE=2.8ms) in a voxel located in the rat hippocampus ($2x2.8x2mm^3$, n=7, 160averages), First and second order shims were adjusted using FASTMAP[30] (fast automatic shimming technique by mapping along the projections, water linewidths 9 - 11 Hz in the 2.0 x 2.8 x 2.0 mm^3 VOI for metabolite spectra). OVS was interleaved with water signal suppression RF pulses from the VAPOR[59] scheme.

2.3.1.2   Monte-Carlo simulations (MC)

To assess the reliability of the estimated concentrations, artificial rat brain ^{1}H MR spectra were simulated (Matlab, MathWorks, Natick, MA, USA) to mimic optimal experimental conditions (metabolites with MM only = "**Optimal MC**"). Real experimental conditions were mimicked by combining both metabolites and MM with a baseline (metabolites with MM including baseline = "**Real MC**"), which imitates minor outer volume contamination and insufficient water suppression effects (Figure 2:7).

To create these artificial rat brain spectra, 20 metabolites (Ala, Asc, Asp, Cr, PCr, GABA, Gln, Glu, GSH, Ins, Lac, NAA, scyllo-inositol - Scyllo, Tau, Glc, NAAG, PE, GPC, PCho, β-Hydroxybutyrate-bHB) were simulated using NMRScope-B from jMRUI[41], published values of J-coupling constants and chemical shifts[36,42] and the SPECIAL sequence with the same parameters as the ones used for the *in vivo* acquisitions (TE=2.8ms, same RF pulse shapes, number of points, acquisition time, etc.). The *in vivo* measured MM spectrum, after removal of residual metabolites, was also added (section 2.1.1 and 2.1.2.1). Then using an in-house written Matlab script the individual metabolites were weighted with a coefficient equal to their *in vivo* concentration (Ala : Asc : Asp : Cr : PCr : GABA : Gln : Glu : GSH : Ins : Lac : NAA : Scyllo : Tau : Glc : NAAG : PE : GPC : PCho : bHB = 0.8 : 1.5 : 2:4 : 4.5 : 1.6 : 3 : 10 : 1.5 : 6.5 : 0.8 : 9 : 0.1 : 6.5 : 1.7 : 0.3 : 1.3 : 0.8 : 0.6 : 0.2) and summed up, to obtain spectra mimicking the *in vivo* appearance of a rat brain spectrum. A random normally distributed noise was added. One hundred high signal-to-noise spectra (SNR=182 in LCModel) were generated for each experimental condition to estimate any systematic deviation from the real values without any bias induced by the quantification algorithm.

Allowing for a baseline estimation during the fitting of experimentally acquired MRS data is necessary to account for the possible minor outer volume contamination or baseline deformation resulting from insufficient water suppression, eddy currents and any spurious signals from imperfections during data acquisition. In addition, low concentrated metabolites which are not included in the basis set can sometimes contribute to the baseline, even though the baseline definition refers in general to imperfections during data acquisition. As such, for the real experimental conditions, a baseline mimicking minor outer volume contamination and insufficient water suppression was added to the second MC study. The baseline contained three broad signals at 1.4, 3.2 and 4.7 ppm and was simulated in jMRUI using the "Simulation" tool (Figure 2:7).
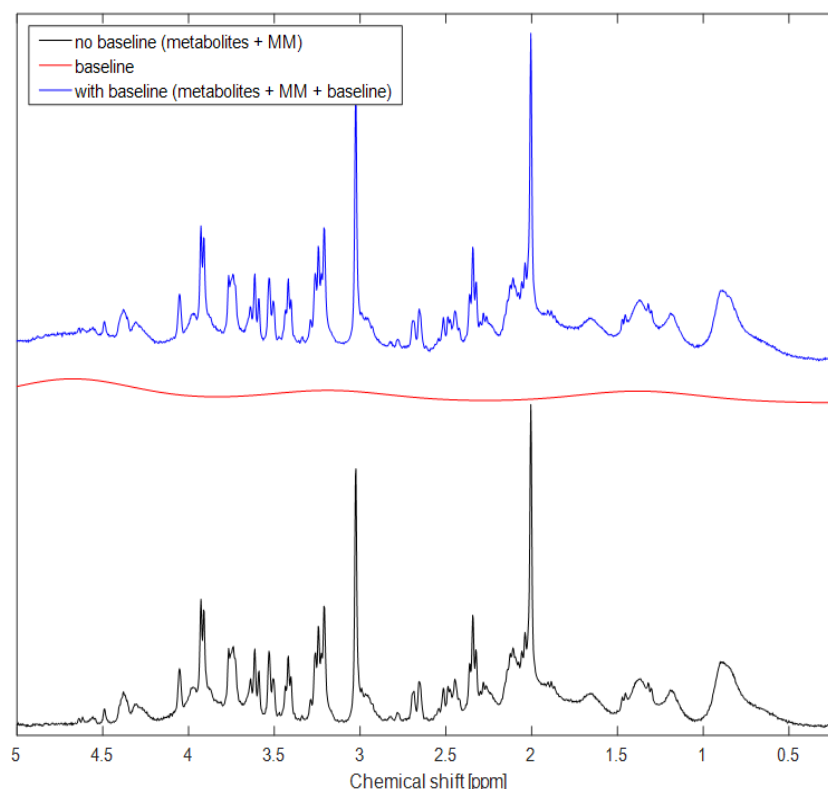
Figure 2:7: Optimal and Real MC spectrum. (down) Simulated spectra mimicking optimal experimental conditions – metabolites with MM only (shown in black); **(middle)** baseline mimicking minor outer volume contamination and insufficient water suppression (shown in red) contains three resonances at 1.4, 3.2 and 4.7 ppm (simulated in jMRUI) ; **(up)** spectra simulated to mimic real experimental conditions - metabolites with MM and baseline (shown in blue).

2.3.1.3 Quantification of brain metabolites using single vs parametrized MM spectra with varying DKNTMN values

The MC spectra and each *in vivo* rat brain spectrum (TE=2.8 ms, n=7) were quantified with LCModel using single MM (standard) and parametrized MM included in the metabolite basis set with varying *DKNTMN* values (0.1 ppm, 0.25 ppm, 0.4 ppm, 0.5 ppm, 1 ppm, 5 ppm) for every basis set. The fitting and parametrization of MM components and their subsequent inclusion in the LCModel basis set used for quantification herein, as well as the soft constraints added to the LCModel control file are explained in the section 2.1.2.3. In the further text, the following terminology will be used:

- ***Single MM -*** single MM spectrum in the quantification basis set.
- *Parametrized MM* - parametrized MM spectrum in the quantification basis set.
- ***Parametrized MM + PK*** - parametrized MM spectrum in the quantification basis set with soft constraints on individual MM (Table 2:3, section 2.1.2.3) included in the LCModel control file (prior knowledge-PK).

- **Optimal MC** - MC simulated data without baseline (metabolites + MM only) to mimic optimal experimental conditions.

- **Real MC** - MC simulated data with baseline (metabolites with MM and a baseline) to mimic real experimental conditions.

Since nine different quantifications sets were analyzed they will be referred to as follows:

1. **In vivo + single MM**
2. **In vivo + parametrized MM**
3. **In vivo + parametrized MM + PK**
4. **Optimal MC + single MM**
5. **Optimal MC + parametrized MM**
6. **Optimal MC + parametrized MM + PK**
7. **Real MC + single MM**
8. **Real MC + parametrized MM**
9. **Real MC + parametrized MM + PK**

2.3.1.4 Statistics

Data are presented as mean ± SD. Percentage changes (values shown in both figures and text) were always calculated comparing results for DKNTMN value of 0.25 vs 5.

Metabolites concentrations were compared for all the *DKNTMN* values within groups (single and parametrized-MM) using 1-way ANOVA with respect to each metabolite in the neurochemical profile followed by Bonferroni's multi-comparisons post-test (*DKNTMN* value). Significance level in 1-way ANOVA was attributed as follows: $*p < 0.05$, $**p < 0.01$, $***p < 0.001$, $****p < 0.0001$. The comparison between groups (single and parametrized MM) was performed using 2-way ANOVA with respect to each metabolite in the neurochemical profile followed by Bonferroni's multi-comparisons post-test (with MM type and *DKNTMN* as factors) ($^\#p < 0.05$, $^{\#\#}p < 0.01$, $^{\#\#\#}p < 0.001$, $^{\#\#\#\#}p < 0.0001$). All tests were two-tailed.

2.3.2 Results

2.3.2.1 Quality of in vivo ^{1}H MR spectra

The overall quality of *in vivo* acquired metabolite spectra together with an example of LCModel quantification is shown in Figure 2:8B. The SNR (calculated by LCModel upon quantification) was

25±2 when quantified using single MM spectra and DKNTMN=0.25. It should be noted that LCModel calculates the SNR value as the ratio of the maximum signal intensity corrected for the baseline and the double of the root mean square (RMS) of fitting residuals, not the spectral noise. Since the LCModel calculated SNR depends not just on residuals SD but also on the baseline estimate, we evaluated how baseline properties affect the LCModel SNR. The SNR showed a tendency of decrease with increasing DKNTMN, which was expected since LCModel takes into account standard deviation of the residual when calculating this value[43] (from 26±3 to 23±2 when using single MM and from 24±3 to 21±2 when using parametrized MM). A slight trend of decrease in SNR was also observed when changing the quantification approach from single to parametrized MM (i.e. for DKNTMN=0.25 the SNR using single MM was 25±2 while for parametrized MM it was 23±2). For Real MC data, an important drop in SNR was noticed when increasing DKNTMN to 5 (i.e. from 180 to 70 when using single MM and from 164 to 125 when using parametrized MM). The overall *in vivo* linewidth calculated as full width half maximum by LCModel at default settings (single MM, DKNTMN=0.25) upon quantification was 5±1 Hz and stayed consistent throughout different quantification approaches. This value demonstrates a high consistency in the B_0 shimming and achieved spectral quality. However, it is important to emphasize that these FWHM values provided by the standard LCModel output underestimate the real linewidth values of metabolite signals (i.e., using a deconvolution of the methyl tCr peak 3.02 ppm).

A *Real MC* + single MM
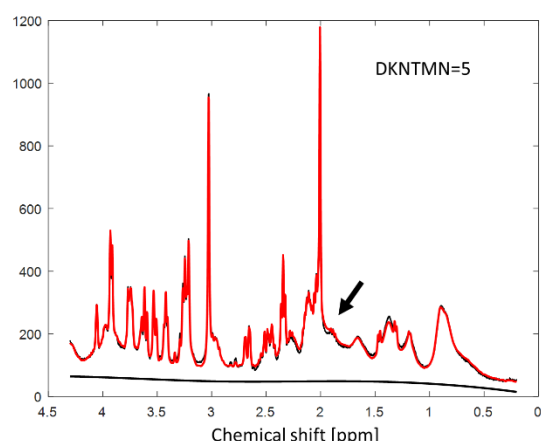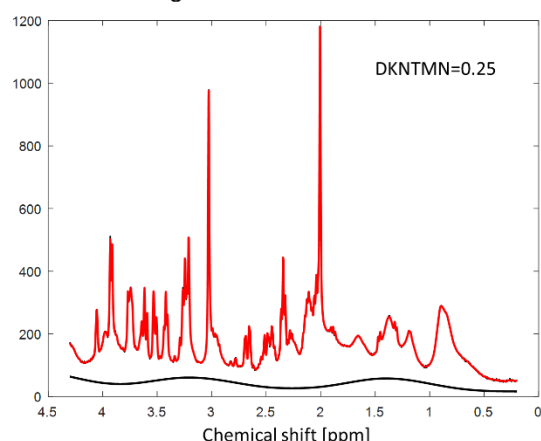
B *In vivo* + single MM
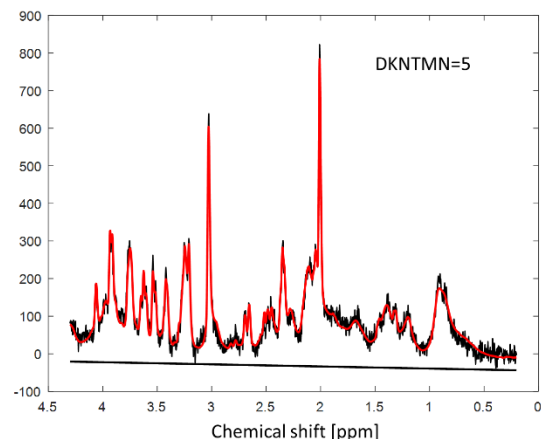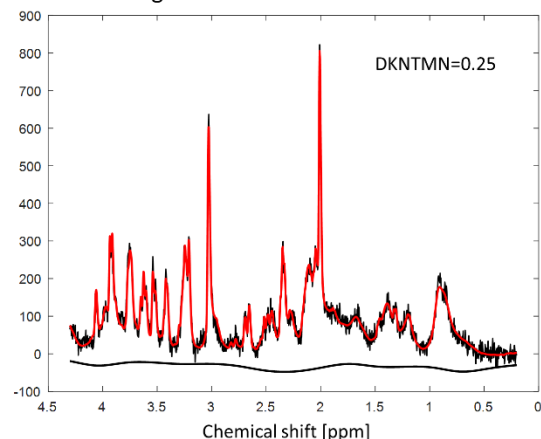
Figure 2:8: LCModel fitting of MC simulated and In vivo spectra. (A) Monte Carlo simulation of real experimental conditions (with baseline) showing a mismatch between the raw data and the LCModel fit (arrow) when quantifying with *DKNTMN=5 ppm*; (B) In vivo acquired spectra from the same rat using DKNTMN = 0.25 ppm (left) and DKNTMN = 5 ppm (right).

2.3.2.2   *Quantification of brain metabolites*

In vivo and Real MC data quantified using single MM: impact of the DKNTMN parameter

When using **single MM** for *in vivo* data quantifications, **increasing the stiffness in the spline baseline** lead to a significant decrease of Gln (-16%, *), Glu (-7%, **) and GABA (-30%, ***) concentrations. Other metabolites like tCho (GPC+PCho - total Choline, +23%) and some overlapping and low concentrated metabolites like Asp (-18%), Asc (+37%), Ala (+18%), Lac (+15%) and GSH (-7%) showed strong but non-significant changes (note that percentage changes were always calculated comparing results for DKNTMN value of 0.25 to 5, for all results presented) (Figure 2:9, black plots).
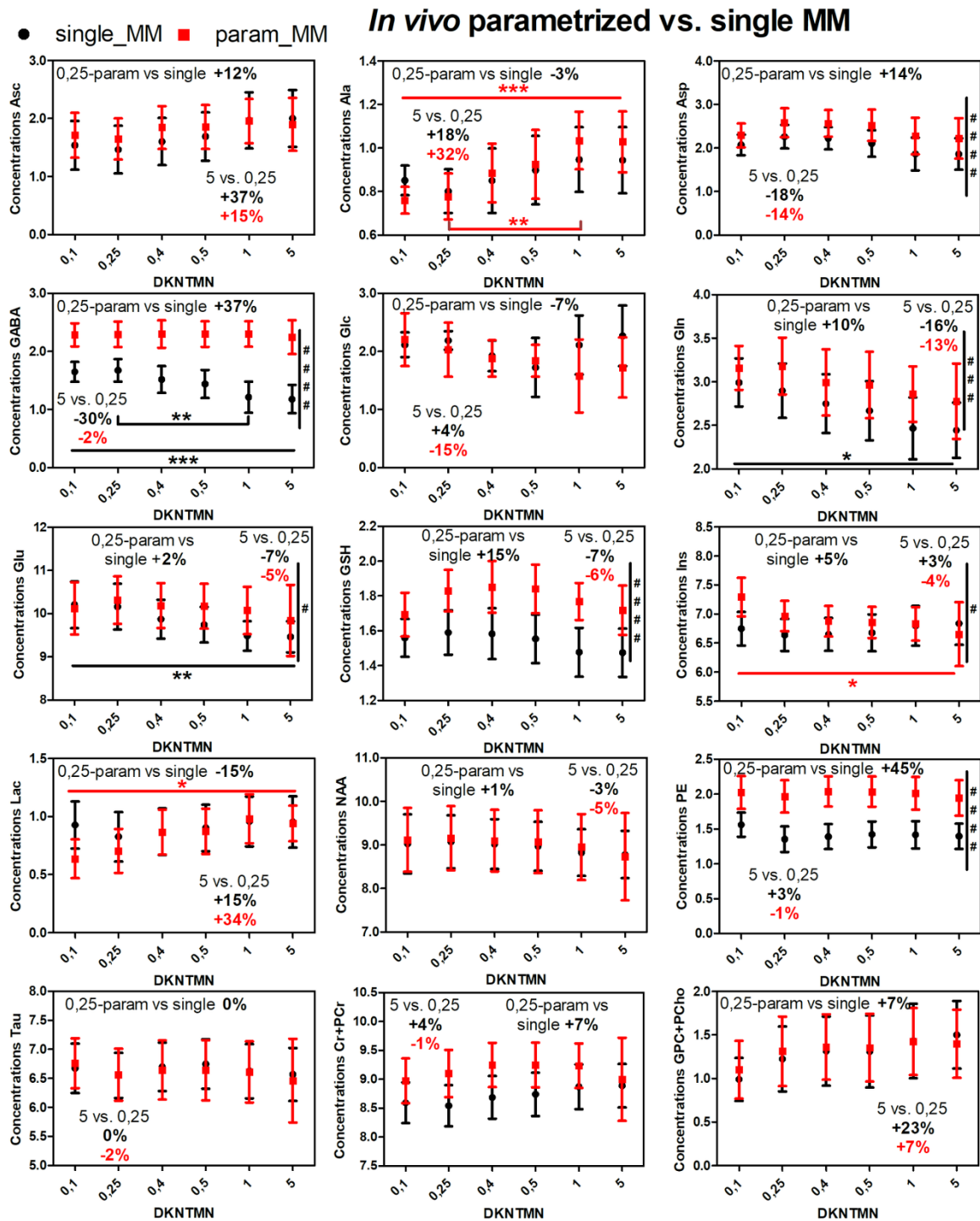
Figure 2:9: In vivo parametrized vs. single MM. In vivo metabolite changes using two different quantification approaches in LCModel: single MM spectra (black) and parametrized MM spectra (red) over different *DKNTMN* values (One-way ANOVA, Bonferroni correction *p<0.05, **p<0.01, ***p<0.001, ****p<0.0001). The percentage change between metabolite concentrations when quantified with *DKNTMN = 0.25 ppm* and *DKNTM = 5 ppm* are shown in the insert (always in red for the parameterized MM with PK and black for the single MM). The comparison between groups single vs parametrized MM was calculated using 2-way ANOVA (#p<0.05, ##p<0.01, ###p<0.001, ####p<0.0001) and is shown on the right in each plot if significant.

To validate the changes observed *in vivo* for varying DKNTMN and single MM, two different MC studies were used. As expected, the optimal MC study with single MM showed a negligible impact of *DKNTMN* on metabolite concentrations (Figure 2:10, black plots). The real MC study with single MM revealed changes in metabolite concentrations when *DKNTMN* was increased (i.e. when a stiffer baseline was used; Figure 2:11, black plots). These changes were present as a decrease for Asp (-52%), GABA (-42%), Glc (-41%), Gln (-20%), Glu (-10%), GSH (-9%), while additional metabolites like Ala, Lac, PE, Tau, tCr (Cr+PCr - total creatine) and tCho displayed an increase of 45%, 59%, 16%, 15%, 6% and 10%, respectively.

The Real MC combined with the single MM spectrum and DKNTM of 5 ppm showed stronger deviations from the ground truth for most metabolites, suggesting that a too flat baseline should not be used (Table 2:5, Figure 2:11). These changes in metabolite concentrations when a high *DKNTMN* value was used, were also supported by the difference in the LCModel resulting baseline shape when compared to the real baseline used in the simulation (Figure 2:12 and Figure 2:13). In parallel, there was also a decrease of SNR and a mismatch between the raw data and the LCModel fit when increasing *DKNTMN* (Figure 2:8A), which was visible for the MC study supporting our quantitative results. Of note, due to the high number of MC realizations and the consistent changes in metabolite concentrations, all changes in both MC studies were statistically significant. In this context, we choose to report only changes which were higher than 5% and thus could lead to biologically relevant changes.

In vivo and Real MC data quantified using parametrized MM+PK: impact of the DKNTMN parameter

When using **parametrized MM** with **PK**, the overall *in vivo* metabolite changes over ***DKNTMN* values** became less important than for the single MM, except for Ala (+32%, p=0.0003(***)), Ins (-4%, p=0.0364(*)) and Lac (+34%, p=0.0118 (*)), (Figure 2:9, red plots). In this case also, few overlapping and low concentrated metabolites showed appreciable but non-significant changes (e.g. Asc (+15%), Asp (-14%), Gln (-13%), tCho (+7%). The smaller impact of DKNTMN when using a parametrized MM signal can be explained by the additional flexibility brought by the parametrized MM. These findings were also supported by the results obtained using the real MC (Figure 2:11, red plots, Table 2:5) where the metabolite changes due to *DKNTMN* were less pronounced than for single MM but followed the same trend like in vivo (ranging from -7% to +16%).
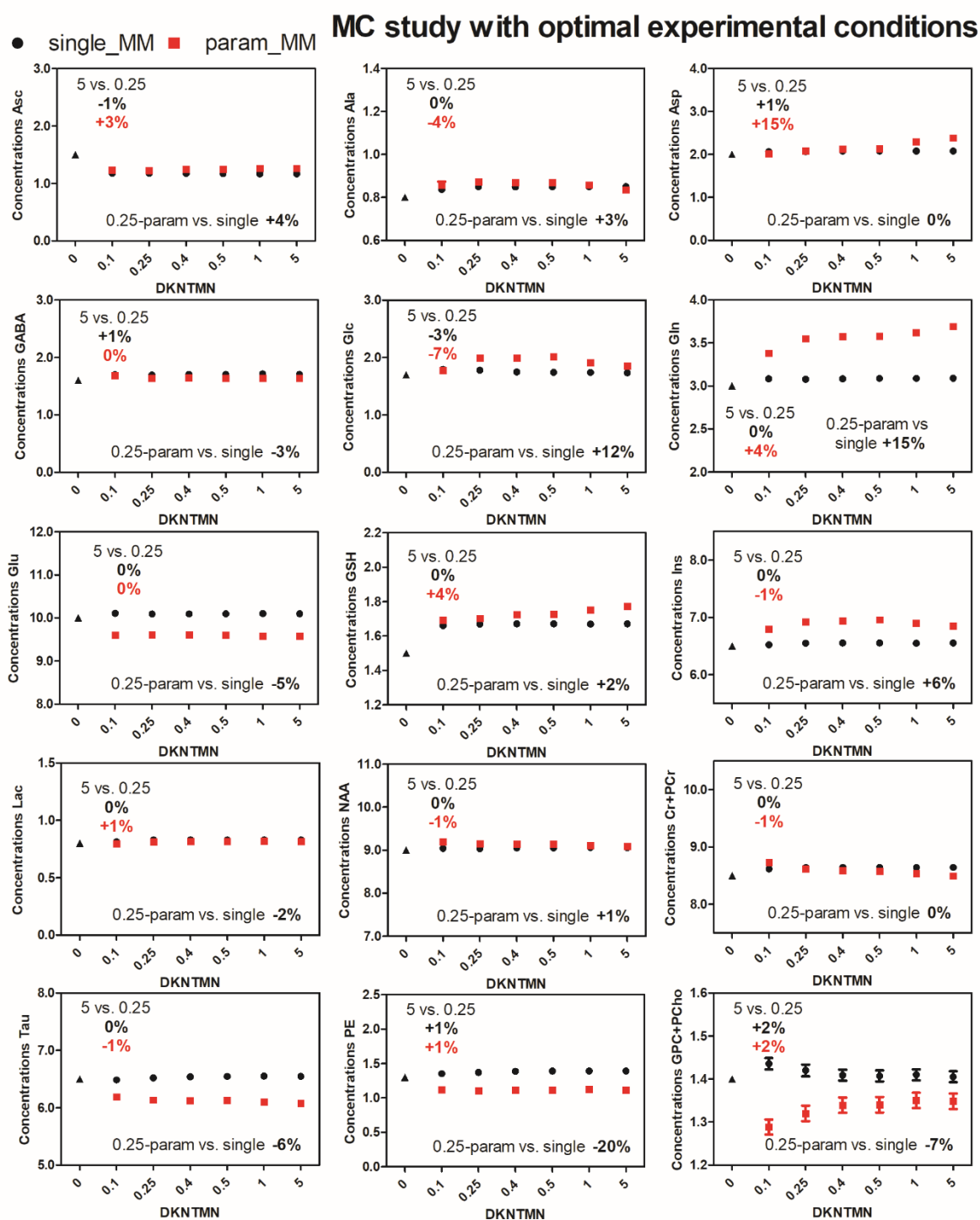
Figure 2:10: MC study with optimal experimental conditions. Metabolite concentrations obtained when quantifying Monte Carlo spectra mimicking optimal experimental conditions (without baseline) with different DKNTMN values. Quantifications were done using the two approaches single MM (black) and parametrized MM with PK (red) in LCModel. True concentration of each metabolite is represented with a triangle symbol at DKNTMN = 0.
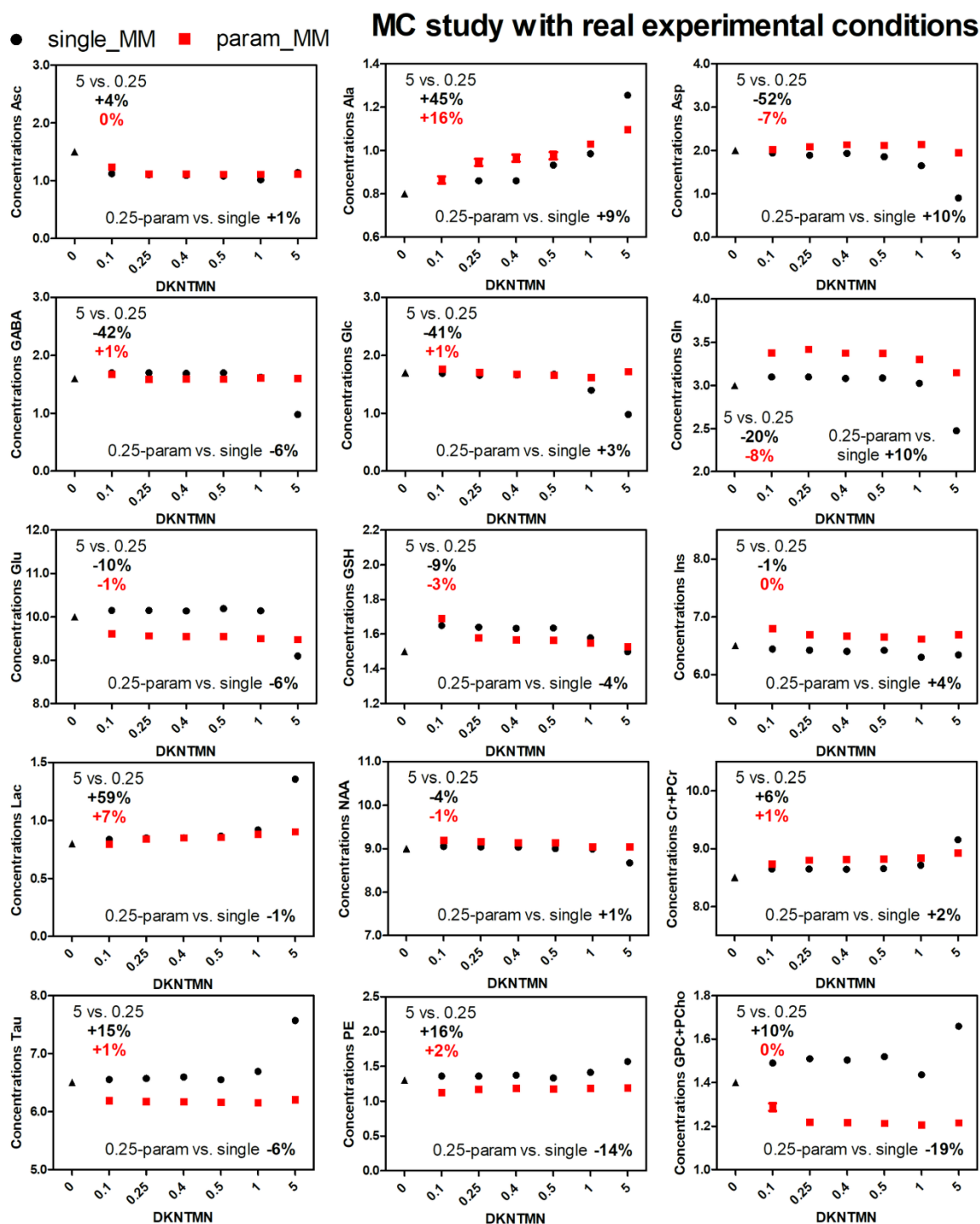
Figure 2:11: MC study with real experimental conditions. Metabolite concentrations obtained when quantifying Monte Carlo spectra mimicking real experimental conditions (with baseline) with different DKNTMN values. The quantifications were done using the two approaches single MM (black) and parametrized MM with PK (red) in LCModel. The true concentration of each metabolite is represented with a triangle symbol at DKNTMN = 0.

Table 2:5: Quantification results of the Real MC spectra. The exact values of metabolite concentrations obtained when quantifying Monte Carlo spectra mimicking real experimental conditions (with baseline) with DKNTMN = 0.25, 1 and 5 ppm. The corresponding percentage change compared to DKNTMN = 0.25 ppm is also reported.

Real MC	full MM			param MM		
	DKNTMN = 0.25	DKNTMN = 1	DKNTMN = 5	DKNTMN = 0.25	DKNTMN = 1	DKNTMN = 5
Asc	1.10	1.02	1.14	1.11	1.11	1.11
%		-7%	4%		0%	0%
Ala	0.86	0.98	1.25	0.94	1.03	1.10
%		14%	45%		9%	16%
Asp	1.89	1.65	0.90	2.09	2.15	1.95
%		-13%	-52%		3%	-7%
GABA	1.70	1.63	0.98	1.59	1.61	1.60
%		-5%	-42%		1%	1%
Glc	1.66	1.40	0.98	1.71	1.62	1.72
%		-16%	-41%		-5%	1%
Gln	3.10	3.03	2.48	3.42	3.31	3.15
%		-2%	-20%		-3%	-8%
Glu	10.15	10.14	9.10	9.56	9.50	9.48
%		0%	-10%		-1%	-1%
GSH	1.64	1.58	1.50	1.58	1.55	1.53
%		-4%	-9%		-2%	-3%
Ins	6.42	6.30	6.34	6.69	6.62	6.69
%		-2%	-1%		-1%	0%
Lac	0.85	0.92	1.36	0.84	0.88	0.91
%		8%	59%		5%	7%
NAA	9.04	8.99	8.67	9.16	9.04	9.04
%		-1%	-4%		-1%	-1%
Cr + PCr	8.65	8.71	9.15	8.80	8.84	8.93
%		1%	6%		0%	1%
Tau	6.57	6.69	7.57	6.18	6.16	6.21
%		2%	15%		0%	1%
PE	1.36	1.41	1.57	1.17	1.19	1.19
%		4%	16%		1%	2%
GPC + Pcho	1.51	1.44	1.66	1.22	1.21	1.22
%		-5%	10%		-1%	0%
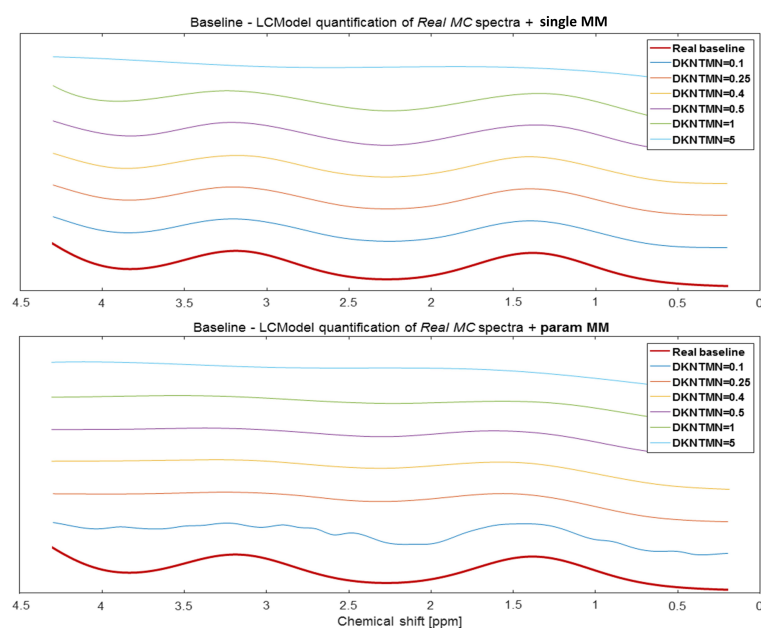
Figure 2:12: LCModel baseline from Real MC quantifications. Baseline extracted from the LCModel quantification of one real MC simulated spectra quantified using different DKNTMN values and single (top panel) or parametrized (bottom panel) MM in the basis set. The original baseline used in MC simulation to create the real MC spectra is shown in bold red.
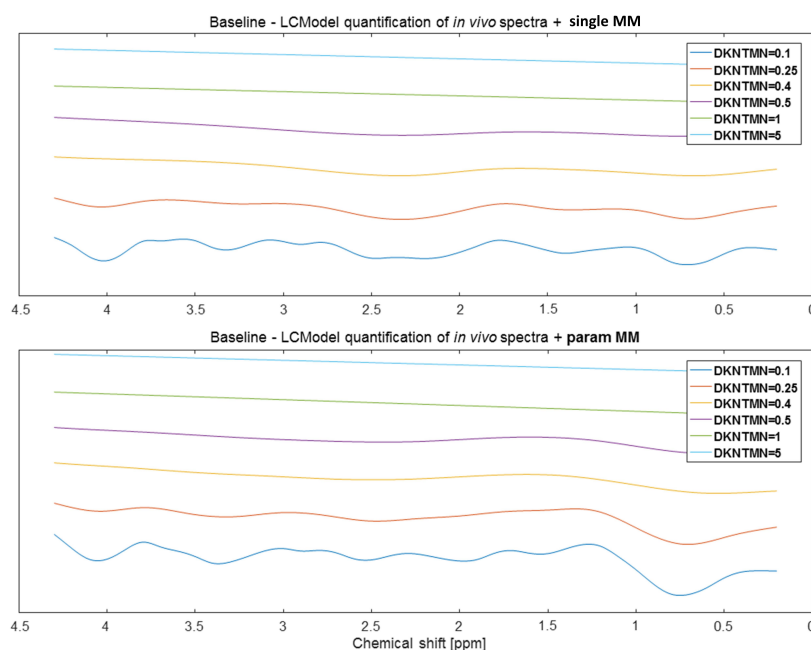
Figure 2:13: LCModel baseline from in vivo quantifications. Baseline extracted from the LCModel quantification of one in vivo acquired spectra quantified using different DKNTMN values and single (top panel) or parametrized (bottom panel) MM in the basis set.

Impact of the MM model (parametrized vs single MM) on the metabolite quantification

When comparing **the parametrized MM+PK vs the single MM model**, the *in vivo* spectra revealed an overall increase in metabolite concentrations when parametrized MM+PK were used, which were significant for Asp (+14%,####), GABA (+37%,####), Gln (+10%,###), Glu (+2%,#), GSH (+15%,####),

Ins (+5%,$^#$), PE (+45%,$^{####}$) and tCr (+7%,$^{####}$) (Figure 2:9, of note the changes in Glu and Ins are low in % change, there is an insert in every figure for DKNTMN 0.25 showing a comparison between parametrized vs single). When using the MC studies, these changes were better assigned due to the known ground truth and were overall in agreement with the *in vivo* changes with some minor exceptions for low and/or overlapping metabolites (i.e. GABA, GSH, Glu, PE, tCr, Tau, tCho). In both MC studies (Optimal MC and Real MC) for some metabolites there was an overall change in metabolite concentrations when using the parametrized MM+PK which was independent of DKNTMN, when compared to single MM, i.e. Gln (+10 to +15%), Glu (-5 to -6%), Ins (+4 to +6%), Tau (-6%), PE (-14 to -20%), tCho (-7 to -19%) (the exact deviation from the true value only at DKNTMN = 0.25 ppm is shown in the table Table 2:6).

Table 2:6: Metabolites showing concentration deviations after quantification. The exact values of metabolite concentrations obtained when quantifying Monte Carlo spectra mimicking real experimental conditions (with baseline) with DKNTMN = 0.25 ppm compared with their true value. The metabolites, which have a bigger deviation from the true value when using parametrized MM, are shown in red.

Real MC	True value	full MM - DKNTMN = 0.25	param MM - DKNTMN = 0.25
Asc	1.5	1.10	1.11
%		-27%	-26%
Ala	0.8	0.86	0.94
%		8%	18%
Asp	2	1.89	2.09
%		-5%	4%
GABA	1.6	1.70	1.59
%		7%	-1%
Glc	1.7	1.66	1.71
%		-2%	1%
Gln	3	3.10	3.42
%		3%	14%
Glu	10	10.15	9.56
%		1%	-4%
GSH	1.5	1.64	1.58
%		9%	5%
Ins	6.5	6.42	6.69
%		-1%	3%
Lac	0.8	0.85	0.84
%		6%	5%
NAA	9	9.04	9.16
%		0%	2%
Cr + PCr	8.5	8.65	8.80
%		2%	4%
Tau	6.5	6.57	6.18
%		1%	-5%
PE	1.3	1.36	1.17
%		4%	-10%
GPC + Pcho	1.4	1.51	1.22
%		8%	-13%

Impact of PK on MM and metabolite quantification

We have also evaluated the impact of adding prior knowledge on parametrized MM and thus performed quantifications **without prior knowledge** on the MM components. For the *in vivo* spectra, the lack of prior knowledge led to an overall increase in the MM content ranging from 19% to ~250% (Figure 2:14), while an overall decrease in metabolite concentrations ranging from -7% to -28% (with significant changes for Ala, Asp, GABA, Glu, GSH, PE, Tau, tCr, tCho) was also measured (Figure 2:15). For the real MC study, no changes were observed when comparing prior knowledge with no prior knowledge for parametrized MM which can be justified by the fact that the MC study contained the same MM like those included in the basis set (Figure 2:16).

To assess further the impact of PK on metabolite concentrations, the in vivo results obtained with parametrized MM, parametrized MM+PK and single MM were compared at DKNTMN = 0.25 and 5 ppm (Figure 2:17). For most metabolites, PK led to a better agreement with concentrations obtained when using the single MM spectrum, except for GABA, GSH and PE where the resulting concentrations for parametrized MM+PK were significantly higher (37%, 15% and 45%, at DKNTMN = 0.25 ppm respectively).
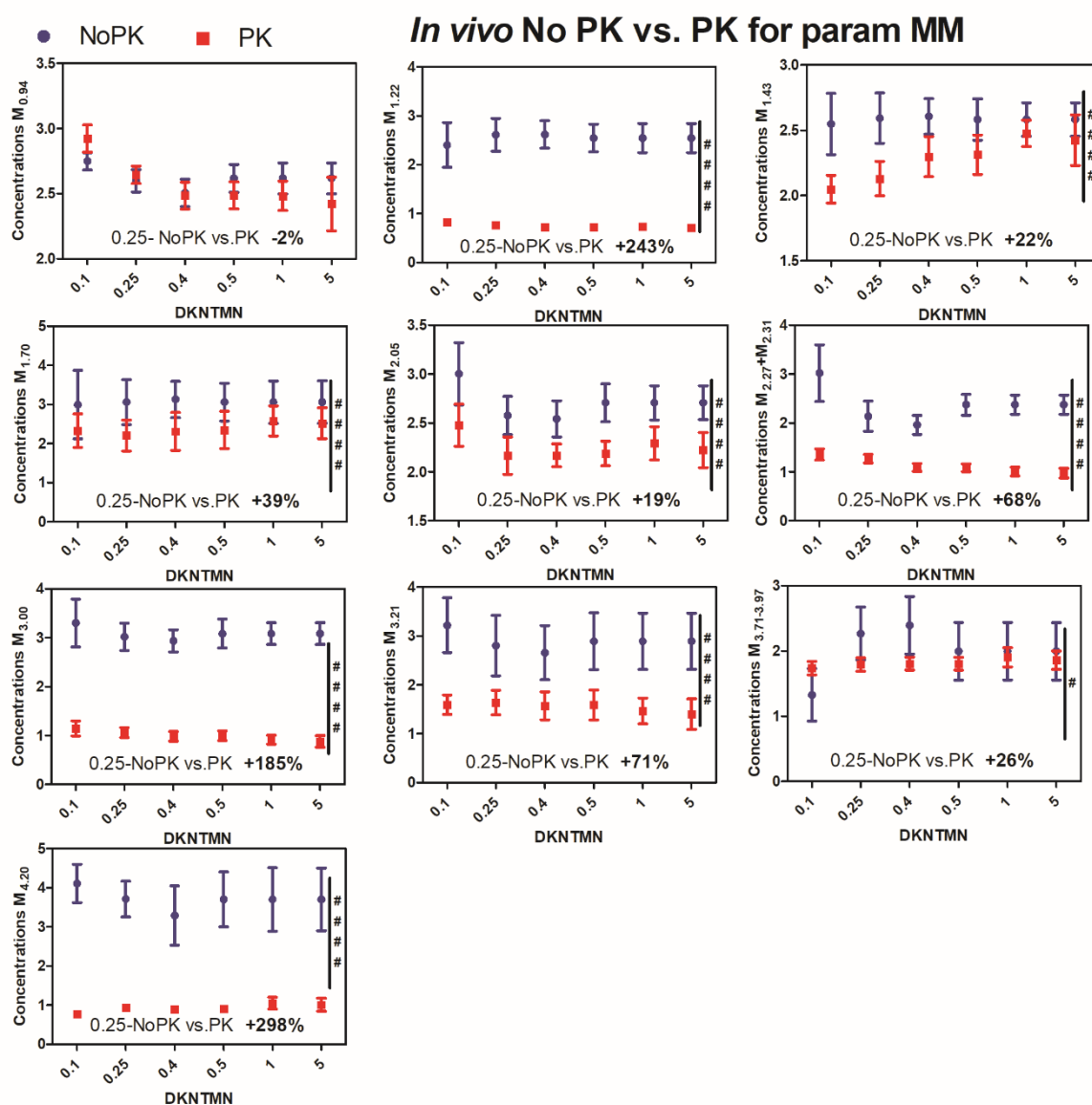
Figure 2:14: In vivo results for no prior knowledge vs. prior knowledge for parametrized MM (for MM components). In vivo macromolecule changes obtained by the quantification in LCModel using parametrized MM with constraints (with prior knowledge – PK) in form of signal intensity ratios and their standard deviations (included in the control file) – shown in red, and without constraints (no prior knowledge –NoPK) – shown in purple. The comparison between groups NoPK vs PK was calculated using 2-way ANOVA (#$p<0.05$, ##$p<0.01$, ###$p<0.001$, ####$p<0.0001$) and is shown on the right in each plot if significant.
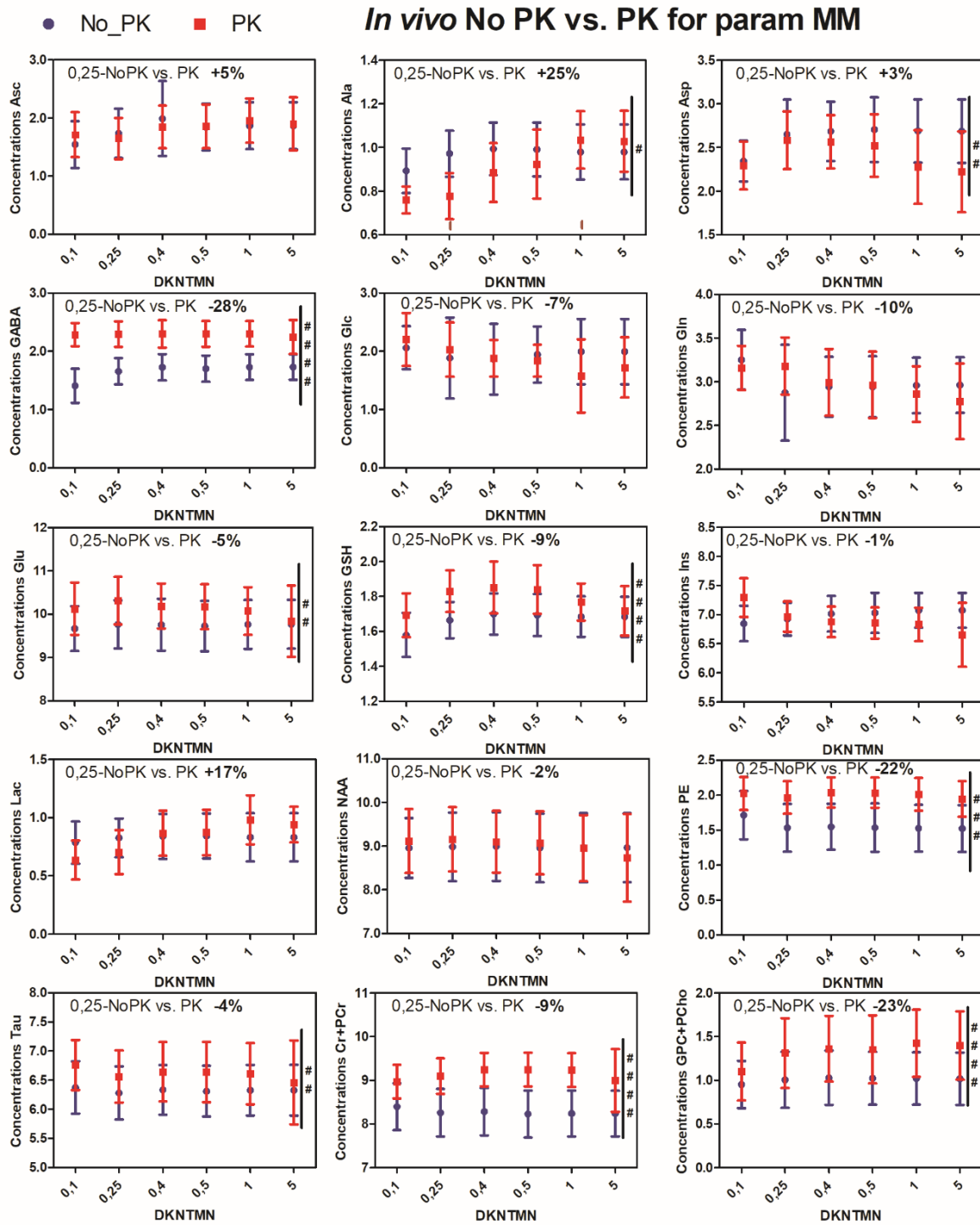
Figure 2:15: In vivo results for no prior knowledge vs. prior knowledge for parametrized MM (for metabolites). In vivo metabolite changes obtained by the quantification in LCModel using parametrized MM with constraints (with prior knowledge – PK) in form of signal intensity ratios and their standard deviations (included in the control file) – shown in red, and without constraints (no prior knowledge –NoPK) – shown in purple. The comparison between groups NoPK vs PK was calculated using 2-way ANOVA (#p<0.05, ##p<0.01, ###p<0.001, ####p<0.0001) and is shown on the right in each plot if significant.
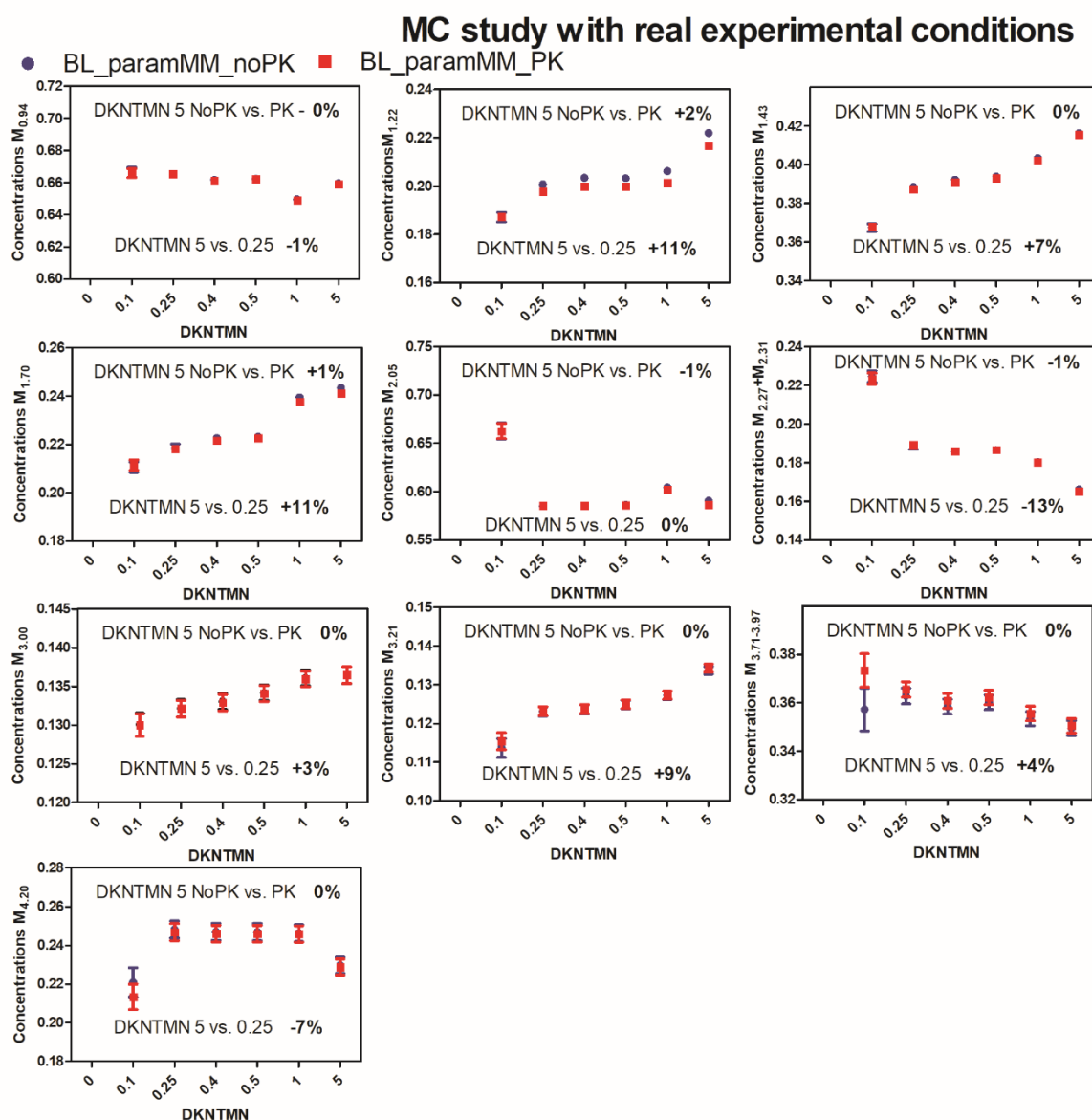
Figure 2:16: MM components as a result of LCModel fitting of Real MC. Macromolecule concentrations obtained when quantifying (in LCModel) Monte Carlo spectra mimicking real experimental conditions using parametrized MM with constraints (with prior knowledge – PK) in form of signal intensity ratios and their standard deviations (included in the control file) – shown in red, and without constraints (no prior knowledge –NoPK) – shown in purple.
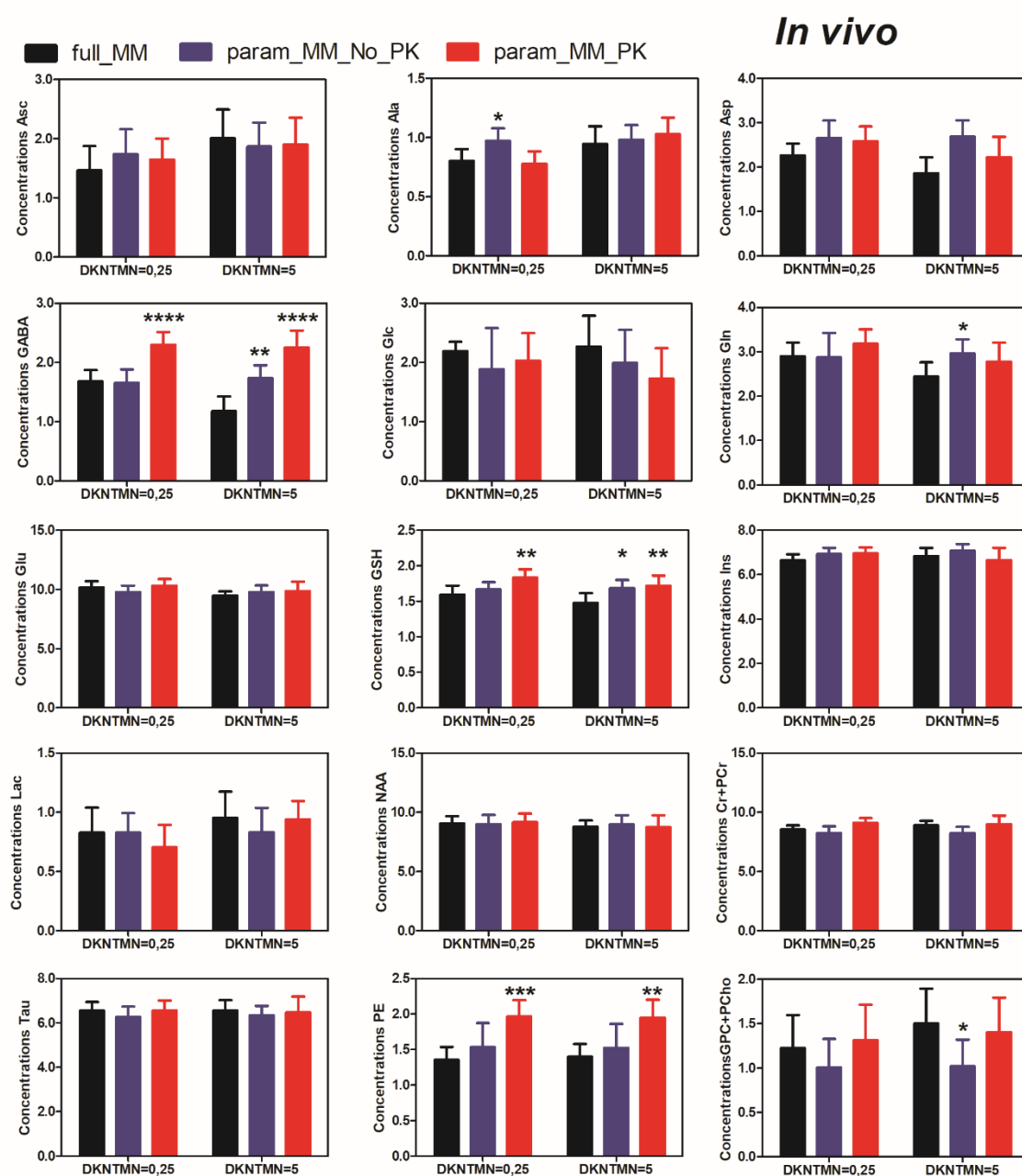
Figure 2:17: Comparison of quantification results obtained for in vivo spectra (single MM vs. param MM PK and no PK). *In vivo* metabolite changes obtained from LCModel quantifications using single MM spectra-shown in black, parametrized MM without constraints (no prior knowledge –NoPK) – shown in purple and with constraints (with prior knowledge – PK) in form of signal intensity ratios and their standard deviations (included in the control file) – shown in red at DKNTMN = 0.25 and 5 ppm. One-way ANOVA, Bonferroni correction *p<0.05, **p<0.01, ***p<0.001, ****p<0.0001.

2.3.3 Discussion and conclusion

In the study presented in this section the parametrized MM peaks (section 2.1.2.3) were included in the metabolite basis set as individual components and their influence on the resulting metabolite concentrations and MM content was evaluated using two types of simulated MC spectra (with and without baseline) and *in vivo* acquired data. In addition, the impact of DKNTMN parameter value on LCModel quantification was evaluated using the same set of MC simulated spectra and *in vivo* data. Thus, for the first time, an extensive assessment was conducted on how the inclusion of either single or parametrized MM spectrum in the LCModel basis set and changes in the spline baseline stiffness affect the metabolite quantification. Our results showed that using a very stiff baseline with single MM spectrum leads to deviations in metabolite concentrations. This effect was less pronounced when parametrized MM spectra were used. Highly significant increase in concentrations of some metabolites (Asp, GABA, Gln, GSH, PE and tCr) were observed when parametrized MM spectrum was used instead of the single MM spectrum. Moreover, adding prior knowledge on parametrized MM improved MM and metabolite quantification.

2.3.3.1 Quantification of brain metabolites: impact of varying DKNTMN

It is well accepted that accurate and reliable quantification of metabolites depends strongly on the MM and **baseline estimation**. However, very few studies have assessed the impact of baseline properties (stiffness vs flexibility) on metabolite quantification. These studies have been performed in humans at $B_0 \geq$ 7T using LCModel where the baseline flexibility can be adjusted by changing the DKNTMN (spline spacing) parameter[54,58]. In one of these studies[54], an overall tendency of increase in metabolite concentrations was observed with increasing baseline stiffness. Metabolites like Ins, Glu, GSH and Asp displayed a general change (an average of 18%, 6%, 17% and 15% respectively) while for NAA and tCho the change (5% and 15%) was brain region specific. Thus, a flexible baseline has been reported as leading to overestimation or underestimation of metabolic concentrations. Another study performed in humans at 7T, analyzed the effect of MM and DKNTMN parameter in different quantification approaches. Condition matched and condition mismatched MM spectra were used in combination with default (0.15) DKNTMN and a very high stiffness (5) DKNTMN[58]. These previous studies have suggested that the default LCModel baseline flexibility may not be optimal in some cases but the conclusion on the "good" value could not be drawn due to lack of ground truth when using only *in vivo* spectra.

In the present study we analyzed a total number of six different DKNTMN values ranging from 0.1 (high flexibility) to 5 (high stiffness). These settings were applied to both *in vivo* and MC simulated data sets (optimal and real conditions) combined with single and parametrized MM basis sets making in total nine different quantification sets. Metabolic concentrations from our ***in vivo* data (single MM)** mainly displayed a decrease in metabolite concentrations with increasing the DKNTMN value (Gln, Glu, GABA, Figure 2:9) while some additional low concentrated and overlapping metabolites showed important but statistically non-significant changes. When analyzing the quantifications of **real MC spectra (single MM)** most of metabolite concentrations (Ala, Asp, GABA, Glc, Gln, Glu, Lac, PE, Tau, tCr, tCho) displayed a change which deviated from their real values when increasing the stiffness, suggesting that a moderate DKNTMN value might be preferable, i.e. below 1 ppm (Figure 2:11). Moreover, we observed a deviation from the real baseline shape (Figure 2:12), decrease of SNR and mismatch between the raw data and the LCModel fit when increasing *DKNTMN* (Figure 2:8), all supporting our quantitative results. A recent study presenting a newly developed algorithm for baseline smoothness has reported that the main sources of baseline fitting errors are bias from an inflexible baseline (underfitting) and an increased variance from an overly flexible baseline (overfitting) [60]. It has been suggested that for realistic spectra a reasonable compromise in baseline flexibility needs to be found [60]. This recommendation is in good agreement with our results, which suggested that moderate DKNTMN value might be a better solution then the high one. Additionally, in a previous study performed in rat brain at 9.4T DKNTMN of 0.25 (moderate value) was used together with a single MM spectrum[53]. Of note, metabolite concentrations were more stable over DKNTMN values when using **parametrized MM** for all data sets. This can be explained by the additional flexibility of the individual MM. However, when using parametrized MM in combination with a low DKNTMN value the baseline displayed stronger features and distortions with a drop at 0.9 ppm, which was not the case for single MM. The 0.9 ppm drop is explainable since the MM component at this position was used as a reference for the other components. This drop and other residual features became smaller already at a DKNTMN value of 0.25, being comparable to those with single MM. The value of 0.4 already led to a similar baseline for both parametrized and single MM basis sets (Figure 2:18).

A *In vivo* + parametrized MM   **B** *In vivo* + full MM
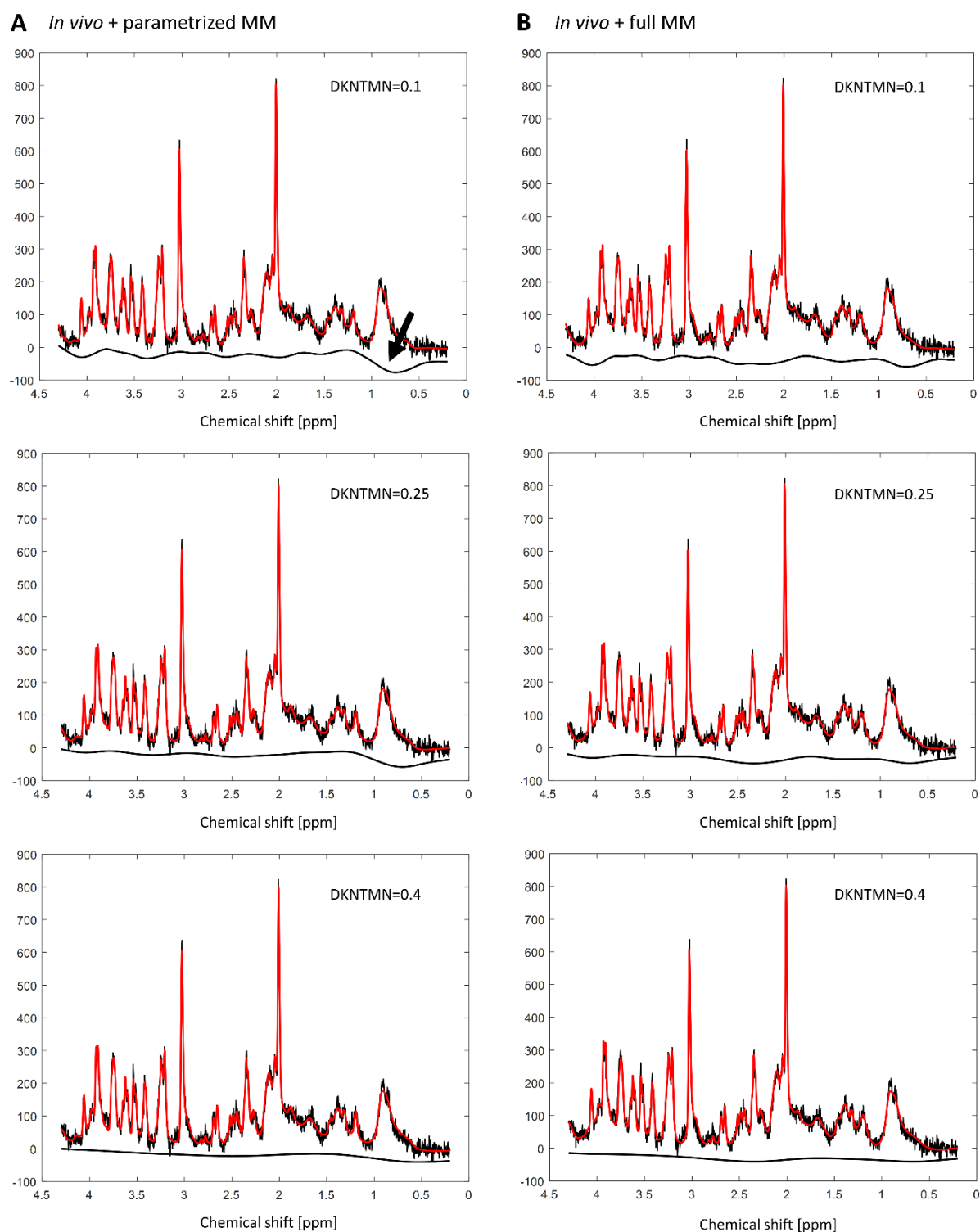
Figure 2:18: Influence of the MM model on the baseline. (A) LCModel quantification of in vivo acquired spectra with parametrized MM + PK showing a baseline drop at around 0.9ppm (arrow) when varying the DKNTMN; (B) LCModel quantification of in vivo acquired spectra with single MM.

2.3.3.2   Quantification of brain metabolites: single MM vs parametrized MM

The standard approach for handling MM during metabolite quantification consists inclusion of a full MM spectrum in the basis set or subtraction of the full MM from the *in vivo* acquired spectrum before quantification. Since individual MM components might change due to disease (e.g. brain tumors, multiple sclerosis and stroke[3,21]), this approach can lead to substantial errors in quantification when assessing metabolites or MM changes in pathologies. The usage of a parametrized MM has been proven helpful for quantification of spectra in pathologically altered cases in humans at 1.5T[21]. However, there are very few studies evaluating the impact of parametrized MM on quantification including incorporation of individual MM in the metabolite basis set together with assessment of the best soft constraints while still keeping enough flexibility to estimate their changes[13,49].

In this context, in the present study we fitted and parametrized 10 MM components, which were subsequently included with and without PK (i.e. soft constrains) in the LCModel basis set used for quantification (section 2.1) and finally the results were compared. The comparison between **single and parametrized MM approach (*in vivo*)** revealed a significant increase in concentration of several metabolites (Asp, GABA, Gln, Glu, GSH, Ins, PE, tCr). These findings were overall confirmed by our MC studies and were consistent with previous studies[13]. Importantly our study evaluated the changes in MM content in addition to metabolite concentrations. We observed an important impact on MM content when no prior knowledge was used, emphasizing the need of prior knowledge as previously suggested in humans at 7T[13].
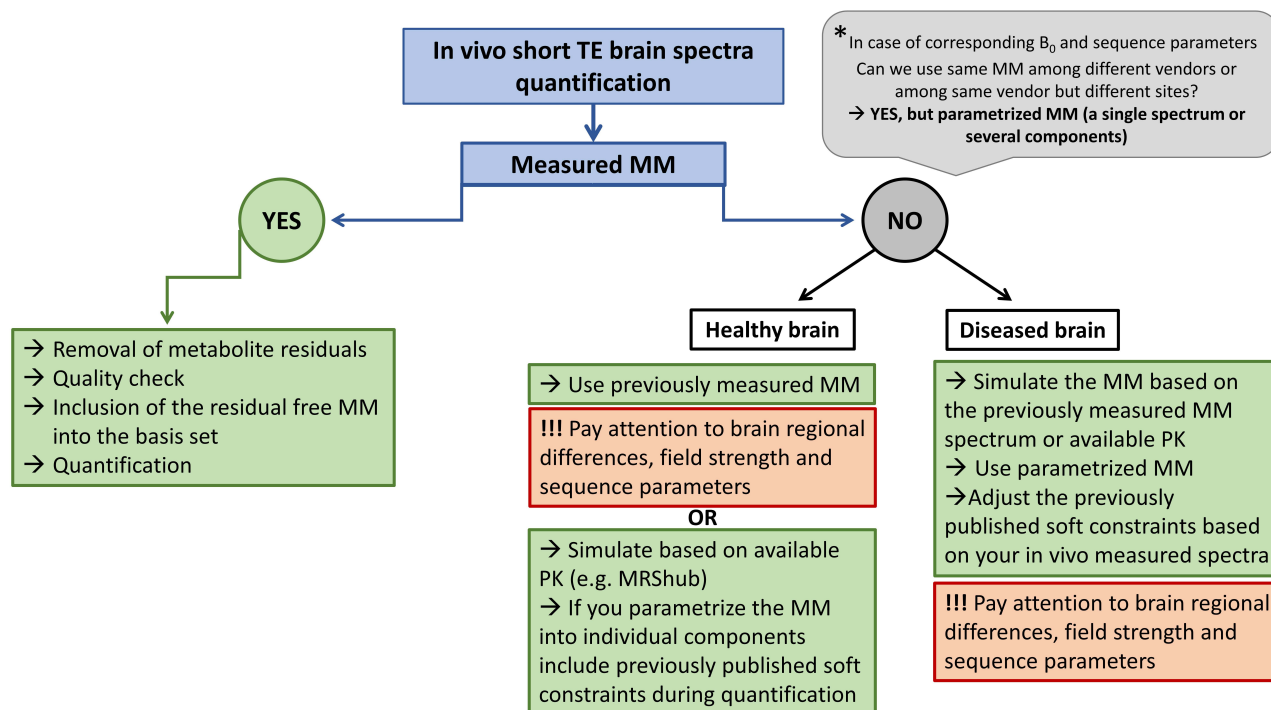
Figure 2:19: Graphical summary for MM handling during short TE brain spectra quantification.

Limitations and perspectives

The first limitation concerns the usage of only high-quality data (in vivo and MC studies without and with a small baseline contribution) to evaluate how the inclusion of a single or parametrized MM spectrum together with changes in spline baseline stiffness affect the metabolite quantification. We made this decision since only high-quality data should be used for metabolite quantification. Moreover, our aim was to assess the "real impact" of MM in the spectral fitting and quantification process, thus we did not use lower quality data (e.g., low SNR, B_0 shimming effects on linewidths, outer volume contamination). In this context, note that the baseline influence on metabolite concentrations can be slightly different when low-quality data are used (e.g., baseline can become almost flat when processing noisy data or can become critical for spectra with low spectral resolution due to bad quality shimming). An additional limitation of the study concerns the lack of data with outer volume contamination or spectra with important changes in MM content due to different pathological conditions. For spectra with lipid contamination that typically appears at around 1.5 ppm, it would be beneficial to include in the basis set one additional broad peak at 1.5 ppm with full flexibility in phase and moderate flexibility in chemical shift and linewidth. Finally, in this study the purely mathematical estimation of MM was not considered since the smooth approximation of

mathematical fitting for MM does not completely reproduce the in vivo spectral pattern at UHF and as such experimentally measured MM are recommended for all B_0[61–65].

Conclusion

In this chapter we proposed an improved methodological approach allowing reliable post-processing, fitting and quantification of the MM spectra. An extensive assessment was performed on how the inclusion of either a single or parametrized MM spectrum with or without PK in the basis set concomitant with changes in the spline baseline stiffness affect the metabolite quantification. The described method also provided an efficient tool for parametrization of individual MM and estimation of apparent T_2 relaxation times of seven individual MM components in the rat brain at 9.4T. The MM spectra were fully characterized at different TIs and TEs providing a comprehensive set of information necessary in a MM dictionary for MR fingerprinting[50]. Using *in vivo* and MC data we showed that a degree of flexibility in the spline baseline is required for quantification of real/experimental data. In addition, a highly stiff baseline led to important metabolite changes when using the single MM for *in vivo* rat brain spectra at 9.4T, while for parametrized MM this effect was less pronounced, but an overall deviation from the ground truth was measured using MC studies. Therefore, we conclude that a generally valid value for DKNTMN cannot be predicted and it needs to be adapted to the experimental and fitting conditions. Finally, our results showed some metabolite changes when including a parametrized MM in the basis set *vs* a single MM and support the need of prior knowledge when using parametrized MM. Therefore, we conclude that a parametrized characterization of the MM contribution to short-echo spectra is feasible and yields reliable quantification results.

References

1. Hofmann, L., Slotboom, J., Boesch, C. & Kreis, R. Characterization of the macromolecule baseline in localized 1H-MR spectra of human brain. *Magn. Reson. Med.* **46**, 855–863 (2001).

2. Cudalbu, C., Mlynárik, V. & Gruetter, R. Handling macromolecule signals in the quantification of the neurochemical profile. *J. Alzheimer's Dis.* **31**, (2012).

3. Cudalbu, C. *et al.* Contribution of macromolecules to brain 1H MR spectra: Experts' consensus recommendations. *NMR Biomed.* (2020) doi:10.1002/(ISSN)1099-1492.

4. Behar, K. L & Ogino, T. Characterization of macromolecule resonances in the 1H NMR spectrum of rat brain. *Magn. Reson. Med.* **30**, 38–44 (1993).

5. Behar, K. L & Ogino, T. Assignment of resonances in the 1H spectrum of rat brain by two-dimensional shift correlated and J-resolved NMR spectroscopy. *Magn. Reson. Med.* **17**, 285–303 (1991).

6. Behar, K. L., Rothman, D. L., Spencer, D. D. & Petroff, O. A. C. Analysis of macromolecule resonances in 1H NMR spectra of human brain. *Magn. Reson. Med.* **32**, 294–302 (1994).

7. Kauppinen, R. A., Niskanen, T., Hakumäki, J. & Williams, S. R. Quantitative analysis of 1H NMR detected proteins in the rat cerebral cortex in vivo and in vitro. *NMR Biomed.* **6**, 242–7 (1993).

8. Kauppinen, R. A., Kokko, H. & Williams, S. R. Detection of Mobile Proteins by Proton Nuclear Magnetic Resonance Spectroscopy in the Guinea Pig Brain Ex Vivo and Their Partial Purification. *J. Neurochem.* **58**, 967–74 (1992).

9. Cudalbu, C., Mlynárik, V., Xin, L. & Gruetter, R. Comparison of T1 relaxation times of the neurochemical profile in rat brain at 9.4 tesla and 14.1 tesla. *Magn. Reson. Med.* **62**, 862–867 (2009).

10. Murali-Manohar, S., Wright, A. M., Borbath, T. & Henning, A. Longitudinal Relaxation times of Macromolecular Resonances at 9.4 T in Human Brain. *27th Annu. Meet. Exhib. Int. Soc. Magn. Reson. Med. (ISMRM 2019), Montréal, QC, Canada* (2019).

11. Murali-Manohar, S. *et al.* T2 relaxation times of macromolecules and metabolites in the human brain at 9.4 T. *Magn. Reson. Med.* **84**, 542–558 (2020).

12. Craveiro, M., Clément-Schatlo, V., Marino, D., Gruetter, R. & Cudalbu, C. In vivo brain macromolecule signals in healthy and glioblastoma mouse models: 1H magnetic resonance spectroscopy, post-processing and metabolite quantification at 14.1 T. *J. Neurochem.* **129**, 806–815 (2014).

13. Považan, M. *et al.* Simultaneous mapping of metabolites and individual macromolecular components via ultra-short acquisition delay 1 H MRSI in the brain at 7T. *Magn. Reson. Med.* **79**, 1231–1240 (2018).

14. Near, J. *et al.* Preprocessing, analysis and quantification in single-voxel magnetic resonance spectroscopy: experts' consensus recommendations. *NMR Biomed.* 1–23 (2020) doi:10.1002/nbm.4257.

15. Mader, I. Proton MR spectroscopy with metabolite-nulling reveals elevated macromolecules in acute multiple sclerosis. *Brain* **124**, 953–961 (2001).

16. Pedrosa de Barros, N. *et al.* On the relation between MR spectroscopy features and the distance to MRI-visible solid tumor in GBM patients. *Magn. Reson. Med.* **80**, 2339–2355 (2018).

17. Howe, F. A. *et al.* Metabolic profiles of human brain tumors using quantitative in vivo 1H magnetic resonance spectroscopy. *Magn. Reson. Med.* **49**, 223–232 (2003).

18. Opstad, K. S., Griffiths, J. R., Bell, B. A. & Howe, F. A. Apparent T2 relaxation times of lipid and macromolecules: A study of high-grade tumor spectra. *J. Magn. Reson. Imaging* **27**, 178–184 (2008).

19. Opstad, K. S., Wright, A. J., Bell, B. A., Griffiths, J. R. & Howe, F. A. Correlations between in vivo 1H MRS and ex vivo 1H HRMAS metabolite measurements in adult human gliomas. *J. Magn. Reson. Imaging* **31**, 289–297 (2010).

20. Öz, G. *et al.* Assessment of adrenoleukodystrophy lesions by high field MRS in non-sedated pediatric patients. *Neurology* **64**, 434–441 (2005).

21. Seeger, U., Klose, U., Mader, I., Grodd, W. & Nägele, T. Parameterized evaluation of macromolecules and lipids in proton MR spectroscopy of brain diseases. *Magn. Reson. Med.* **49**, 19–28 (2003).

22. Pfeuffer, J., Juchem, C., Merkle, H., Nauerth, A. & Logothetis, N. K. High-field localized 1H NMR spectroscopy in the anesthetized and in the awake monkey. *Magn. Reson. Imaging* **22**, 1361–1372 (2004).

23. Hong, S.-T. *et al.* Enhanced neurochemical profile of the rat brain using in vivo 1 H NMR spectroscopy at 16.4 T . *Magn. Reson. Med.* **65**, 28–34 (2011).

24. Lee, H. H. & Kim, H. Parameterization of spectral baseline directly from short echo time full spectra in 1H-MRS. *Magn. Reson. Med.* **78**, 836–847 (2017).

25. Lopez-Kolkovsky, A. L., Mériaux, S. & Boumezbeur, F. Metabolite and macromolecule T 1 and T 2 relaxation times in the rat brain in vivo at 17.2T. *Magn. Reson. Med.* **75**, 503–514 (2016).

26. Cudalbu, C. *et al.* Contribution of macromolecules to brain 1H MR spectra: Experts' consensus recommendations. *NMR Biomed.* **34**, 1–24 (2021).

27. Mlynárik, V., Gambarota, G., Frenkel, H. & Gruetter, R. Localized short-echo-time proton MR spectroscopy with full signal-intensity acquisition. *Magn. Reson. Med.* **56**, 965–970 (2006).

28. Cudalbu, C., Mlynrik, V., Xin, L. & Gruetter, R. Quantification of in vivo short echo-time proton magnetic resonance spectra at 14.1 T using two different approaches of modelling the macromolecule spectrum. *Meas. Sci. Technol.* **20**, 104034 (7pp) (2009).

29. Mlynárik, V., Cudalbu, C., Xin, L. & Gruetter, R. 1H NMR spectroscopy of rat brain in vivo at 14.1 Tesla: Improvements in quantification of the neurochemical profile. *J. Magn. Reson.* **194**, 163–168 (2008).

30. Gruetter, R. & Tkáč, I. Field mapping without reference scan using asymmetric echo-planar techniques. *Magn. Reson. Med.* **43**, 319–323 (2000).

31. Craveiro, M., Cudalbu, C. & Gruetter, R. Regional alterations of the brain macromolecule resonances investigated in the mouse brain using an improved method for the pre-processing of the macromolecular signal. **20**, 2012 (2012).

32. Xin, L., Mlynarik, V., Lei, H. & Gruetter, R. Influence of regional macromolecule baseline on the quantification of neurochemical profile in rat brain. *Proc. Intl. Soc. Mag. Reson. Med.* 5 (2010).

33. Vanhamme, L., Van Den Boogaart, A. & Van Huffel, S. Improved Method for Accurate and Efficient Quantification of MRS Data with Use of Prior Knowledge. *J. Magn. Reson.* **129**, 35–43 (1997).

34. Lee, H. H. & Kim, H. Parameterization of spectral baseline directly from short echo time full spectra in 1H-MRS. *Magn. Reson. Med.* **78**, 836–847 (2017).

35. Fowler, C. F., Madularu, D., Dehghani, M., Devenyi, G. A. & Near, J. Longitudinal quantification of metabolites and macromolecules reveals age- and sex-related changes in the healthy Fischer 344 rat brain. *Neurobiol. Aging* **101**, 109–122 (2021).

36. Govindaraju, V., Young, K. & Maudsley, A. A. Proton NMR chemical shifts and coupling constants for brain metabolites. *NMR Biomed.* **13**, 129–153 (2000).

37. Xin, L., Gambarota, G., Cudalbu, C., Mlynárik, V. & Gruetter, R. Single spin-echo T 2 relaxation times of cerebral metabolites at 14.1 T in the in vivo rat brain. *Magn. Reson. Mater. Physics, Biol. Med.* **26**, 549–554 (2013).

38. Simicic, D. *et al.* In vivo macromolecule signals in rat brain 1H-MR spectra at 9.4T: Parametrization, spline baseline estimation, and T2 relaxation times. *Magn. Reson. Med.* **86**, 2384–2401 (2021).

39. Kreis, R. *et al. Terminology and concepts for the characterization of in vivo MR spectroscopy methods and MR spectra: Background and experts' consensus recommendations. NMR in Biomedicine* (2020). doi:10.1002/nbm.4347.

40. Provencher, S. W. Automatic quantitation of localized in vivo 1H spectra with LCModel. *NMR Biomed.* **14**, 260–264 (2001).

41. Starčuk, Z. & Starčuková, J. Quantum-mechanical simulations for in vivo MR spectroscopy: Principles and possibilities demonstrated with the program NMRScopeB. *Anal. Biochem.* **529**, 79–97 (2017).

42. Govind, V., Young, K. & Maudsley, A. A. Corrigendum to Proton NMR chemical shifts and coupling constants for brain metabolites. [NMR Biomed. 13, (2000), 129-153]. *NMR Biomed.* **28**, 923–924 (2015).

43. Provencher, S. Manual. (2019).

44. Landheer, K., Gajdošík, M., Treacy, M. & Juchem, C. Concentration and T2 Relaxation Times of Macromolecules at 3 Tesla. *Magn. Reson. Med.* **In Submiss**, 1–11 (2020).

45. Snoussi, K. *et al.* Comparison of brain gray and white matter macromolecule resonances at 3 and 7 Tesla. *Magn. Reson. Med.* **74**, 607–613 (2015).

46. Otazo, R., Mueller, B., Ugurbil, K., Wald, L. & Posse, S. Signal-to-noise ratio and spectral linewidth improvements between 1.5 and 7 tesla in proton echo-planar spectroscopic imaging. *Magn. Reson. Med.* **56**, 1200–1210 (2006).

47. Hoefemann, M., Bolliger, C. S., Chong, D. G. Q., van der Veen, J. W. & Kreis, R. Parameterization of metabolite and macromolecule contributions in interrelated MR spectra of human brain using multidimensional modeling. *NMR Biomed.* 1–18 (2020) doi:10.1002/nbm.4328.

48. Borbath, T., Manohar, S. M., Wright, A. M. & Henning, A. T2 Relaxation Times of Macromolecules in Human Brain Spectra at 9.4 T. *Proc ISMRM* 2244 (2019).

49. Heckova, E. *et al.* Effects of different macromolecular models on reproducibility of FID-MRSI at 7T. *Magn. Reson. Med.* **83**, 12–21 (2020).

50. Hoefemann, M., Bolliger, C., van derVeen, J. W. & Kreis, R. About the need for a comprehensive description of the macromolecular baseline signal for MR fingerprinting and multidimensional fitting of MR spectra. *Ismrm* 1069 (2019).

51. Kunz, N. *et al.* Diffusion-weighted spectroscopy: A novel approach to determine macromolecule resonances in short-echo time 1H-MRS. *Magn. Reson. Med.* **64**, 939–946 (2010).

52. De Graaf, R. A. *et al.* High magnetic field water and metabolite proton T1 and T 2 relaxation in rat brain in vivo. *Magn. Reson. Med.* **56**, 386–394 (2006).

53. Pfeuffer, J., Tkáč, I., Provencher, S. W. & Gruetter, R. Toward an in Vivo Neurochemical Profile: Quantification of 18 Metabolites in Short-Echo-Time 1H NMR Spectra of the Rat Brain. *J. Magn. Reson.* **141**, 104–120 (1999).

54. Giapitzakis, I. A., Borbath, T., Murali-Manohar, S., Avdievich, N. & Henning, A. Investigation of the influence of macromolecules and spline baseline in the fitting model of human brain spectra at 9.4T. *Magn. Reson. Med.* **81**, 746–758 (2019).

55. Deelchand, D. K., Marjańska, M., Hodges, J. S. & Terpstra, M. Sensitivity and specificity of human brain glutathione concentrations measured using short-TE 1H MRS at 7 T. *NMR Biomed.* **29**, 600–606 (2016).

56. Terpstra, M., Ugurbil, K. & Tkac, I. Noninvasive quantification of human brain ascorbate concentration using1H NMR spectroscopy at 7 T. *NMR Biomed.* **23**, 227–232 (2010).

57. Near, J. *et al.* Unedited in vivo detection and quantification of γ-aminobutyric acid in the occipital cortex using short-TE MRS at 3T. *NMR Biomed.* **26**, 1353–1362 (2013).

58. Marjanska, M. & Terpstra, M. Influence of Fitting approaches in LCModel on MRS quantification focusing on age-specific macromolecules and the spline baseline. *NMR Biomed.* (2019).

59. Tkáč, I., Starčuk, Z., Choi, I. Y. & Gruetter, R. In vivo 1H NMR spectroscopy of rat brain at 1 ms echo time. *Magn. Reson. Med.* **41**, 649–656 (1999).

60. Wilson, M. Adaptive Baseline Fitting for 1H MR Spectroscopy Analysis. *bioRxiv* 1–25 (2020) doi:10.1101/2020.02.17.949495.

61. Chong, D. G. Q., Kreis, R., Bolliger, C. S., Boesch, C. & Slotboom, J. Two-dimensional linear-combination model fitting of

magnetic resonance spectra to define the macromolecule baseline using FiTAID, a Fitting Tool for Arrays of Interrelated Datasets. *Magn. Reson. Mater. Physics, Biol. Med.* **24**, 147–164 (2011).

62. Marjanska, M. *et al.* Altered macromolecular pattern and content in the aging human brain. *NMR Biomed* 1–8 (2018) doi:10.1002/nbm.3865.

63. Coenradie, Y., Beer, R. De, Ormondt, D. Van & Lyon, B. Background-signal Parameterization in In Vivo MR Spectroscopy. *Time* 6–8.

64. Cudalbu, C., Beuf, O. & Cavassila, S. In vivo short echo time localized 1H MRS of the rat brain at 7 T: Influence of two strategies of background-accommodation on the metabolite concentration estimation using QUEST. *J. Signal Process. Syst.* **55**, (2009).

65. O'Gorman, R. L., Michels, L., Edden, R. A., Murdoch, J. B. & Martin, E. In vivo detection of GABA and glutamate with MEGA-PRESS: Reproducibility and gender effects. *J. Magn. Reson. Imaging* **33**, 1262–7 (2011).

Chapter 3   Brain regional vulnerability during type C Hepatic Encephalopathy

Type C hepatic encephalopathy (HE) is a complication of chronic liver disease, characterized by cognitive and motor deficits which is difficult to diagnose in its early stages. Worldwide, the incidence of chronic liver disease is increasing in adults, and children with the disease now live to adulthood. Children and adults respond differently to the disease and its related toxic accumulation of molecules (i.e. ammonium, glutamine, cytokines, etc). Despite considerable advances in understanding the pathogenesis of type C HE, the exact metabolic mechanisms and their regional variations are not completely understood.

The advantages of UHF short TE single voxel spectroscopy were used in this chapter to describe brain regional distribution of metabolites in the developing and adult brain using a well-known rat model of type C HE (the bile duct ligated – BDL adult and post-natal day 21 rats). In addition, changes in cell morphology throughout the disease evolution were followed in multiple brain regions using histology measurements while electron paramagnetic resonance was used for a quantitative detection of reactive oxygen species to measure the course of central nervous system and systemic oxidative stress. The beneficial effect of Cr supplementation on the brain neurometabolic profile of pups (BDL at post-natal day 15) was finally investigated using ^{1}H MRS and ^{31}P MRS.

The reported longitudinal metabolic changes in striatum, hippocampus and cerebellum during type C HE led to the conclusion that there is a differential brain regional vulnerability to the disease. The highest metabolic changes were observed in cerebellum suggesting an increased vulnerability of this region. The increase of Gln was the first observable metabolic change in all measured brain regions suggesting that Gln can be considered as the first brain metabolic marker of type C HE which could potentially serve to assess the severity of HE independently of the results of neuropsychological tests. Alterations in the morphology of both astrocytes and neurons indicate that their interdependence influences the overall activity of the neuronal network during disease progression. An elevated oxidative stress was reported, together with the decreased antioxidants measured by ^{1}H MRS emphasizing its important role in HE. The brain regional measurements confirmed the higher susceptibility of developing brain to the disease and the increased vulnerability of cerebellum. Finally, the beneficial effect of Cr supplementation suggests that an appropriate treatment may have significant public health impact.

My contribution to this chapter is in its entirety (including all the data acquisitions, processing, quantification and statistical analysis as well as drafting the text) except for the following two sections where the specific contribution statements are:

- *Section 3.2.2 (Study 2: Brain regional vulnerability – histology measurements): The work presented in this section was done by Dr. Katarzyna Pierzchala, an expert for histology measurements in our laboratory and was included in my thesis to provide an overview of the influence of neurometabolic changes presented in section 3.2.1. The obtained results are presented in this thesis with her consent and will be a part of the joint publication including the ^{1}H MRS and histology measurements. My contribution to this work includes statistical analysis, help with figure preparation and drafting the text of this section.*
- *Section 3.2.3 (Study 3: CNS and systemic oxidative stress in a BDL model of type C HE): Part of the work presented in this chapter was published as an article in Free Radical Biology and Medicine (Pierzchala et al., 2022)[1]. I am the second author of this publication and I made a substantial contribution to the acquisition; analysis of the data and I drafted this section.*

*This chapter is structured into five sub chapters. The first sub chapter ("**Introduction to type C Hepatic Encephalopathy**", 3.1) provides a general introduction and background on Type C HE as a consequence of chronic liver disease, especially highlighting deleterious mechanisms/molecules involved in the disease pathogenesis (ammonium, inflammation and oxidative stress). Moreover, the role of ^{1}H MRS in understanding the disease mechanisms is highlighted. The second sub chapter titled "**Brain regional vulnerability in the adult brain during type C HE (adult BDL rats)**" (3.2) is divided into three studies. The first study (3.2.1) provides an extensive description of longitudinal metabolic changes during type C HE (^{1}H MRS, bile duct ligated rat model) in three brain regions (cerebellum, hippocampus and striatum). The second study (3.2.2) describes astrocytic and neuronal morphological changes (immunohistochemistry) throughout the disease evolution in multiple brain regions, while in the direct measurements of brain and systemic oxidative stress using the electron paramagnetic resonance technique are presented in the third study (3.2.3). Results from all three studies are jointly discussed (3.2.4) in the end of this sub chapter therefore providing a global description of the disease evolution in the central nervous system. The brain regional vulnerability in the developing brain model of type C HE (bile duct ligation performed at postnatal day 21) is presented in the third sub chapter ("**Brain regional vulnerability in the developing brain: an ^{1}H MRS study**", 3.3). Finally, the beneficial effect of Cr supplementation on the neurometabolic profile is described using ^{1}H MRS and ^{31}P-MRS in a developing brain model (bile duct ligation performed at postnatal day 15) in the fourth sub chapter ("**The beneficial effect of oral Cr supplementation in an early childhood rat model of type C HE: a preliminary ^{1}H and ^{31}P MRS study**", 3.4).*

3.1 Introduction to type C Hepatic Encephalopathy (HE)

Chronic liver disease (CLD) and cirrhosis are responsible for 2 million deaths worldwide every year. The estimated, age standardized, incidence of CLD and cirrhosis was 20.7 per 100 000 people in 2015 (in adults)[2,3]. Moreover, its incidence is increasing worldwide every year[2] and the children with the disease now live to adulthood. As the disease progresses the patients develop several complications, and one of the most common decompensating events is hepatic encephalopathy (HE)[2]. On average 40% of patients develop HE within 5 years. In general, HE is defined as a neuropsychiatric disorder associated with liver disease or portosystemic shunting. However, depending on the underlying type of the disease, HE is differently classified. Type C HE is, by definition, secondary to CLD and/or cirrhosis with or without the presence of portosystemic shunting[4]. Neuropsychiatric symptoms associated with type C HE appear subtly, starting with changes in personality and sleep alterations, followed by deficits involving both cognitive and motor performances. In the most severe cases these symptoms progress eventually trough lethargy to stupor and coma[5]. The classification of type C HE by different criteria is described in Table 3:1. **While the consequential neuropsychological deficits of type C HE are well described, the underlying pathophysiological mechanisms, their chronological involvement and brain regional difference remain unclear**[6].

Table 3:1: The classification of type C HE by different criteria. Classification according to West Haven Criteria (WHC) and International Society for Hepatic Encephalophagy and Nitrogen Metabolism (ISHEN); PHES stands for Psychometric Hepatic Encephalopathy Score, CFF stands for Critical Flicker Frequency, EEG stands for electroencephalography. Table adapted from[7].

WHC grade	ISHEN	Clinical features
Unimpaired		No present or previous HE
Minimal	Covert	Alterations of psychometric or neuropsychological tests (i.e. PHES, CFF, EEG) without clinical manifestations
Grade I		• Trivial lack of awareness • Euphoria or anxiety • Shortened attention span • Impairment of addition or subtraction • Altered sleep rhythm
Grade II	Overt	• Lethargy or apathy • Disorientation for time • Obvious personality change • Inappropriate behavior • Dyspraxia • Asterixis
Grade III		• Somnolence to semi-stupor • Responsive to stimuli • Confused • Gross disorientation • Bizarre behavior
Grade IV		Coma

The pathological foundation of type C HE is complex and multifactorial. First, it is generally accepted that the blood derived toxic molecules (i.e. ammonium, bile acids, proinflammatory cytokines, reactive oxygen and nitrogen species (ROS/RNS)) are mainly responsible for the development of neurological deterioration. Liver dysfunction causes toxic accumulation of these blood derived molecules which in turn alter the permeability and integrity of the blood brain barrier (BBB). Therefore, the molecules which normally cross the BBB and also the ones which are normally prevented from crossing it, flood the brain and stimulate a cascade of pathophysiological pathways/mechanisms having consequentially deleterious effects on the brain (i.e. brain glutamine accumulation, neuroinflammation, central ROS/NOS).

In the present chapter I will: 1) briefly describe some of these mechanisms that I also investigated during my PhD; and 2) investigate their brain regional difference and chronology using a multimodal approach in a rat model of type C HE during adult and brain development, the bile duct ligated (BDL) rat[8].

3.1.1 Ammonium in type C HE

Out of all neurotoxic candidates, ammonia has been pinpointed and has been the most studied to explain the observed neurological alterations. This molecule's ability to cross BBB and substantially cause harmful effect on the central nervous system (CNS) function isolated it as a crucial factor in the pathogenesis of HE[4,6,7]. Ammonia is mainly produced in the gut, as a product of protein digestion, amino acid deamination and bacterial urease activity. The concentration of ammonia present in the systemic circulation is then regulated by the liver, where its metabolized by the urea cycle and subsequently eliminated in the kidneys. Therefore, a healthy liver regulates the concentration of systemic ammonia[6]. In addition, ammonia is generated and used in different chemical reactions taking place in various organs including brain, muscle and kidney. Ammonia (NH_3) has different properties depending on the pH and under normal physiological conditions, over 98% off ammonia is present in ammonium form (NH_4^+)[9]. In the further text, both of these forms will be referred to as ammonium. NH_4^+ can enter cells in several ways e.g. aquaporins, ammonium transporters, K^+ pumps etc[10]. The diseased liver is not able to adequately eliminate ammonium and therefore excess ammonium enters the systemic circulation (hyperammonemia) which in turn leads to increase of cerebral ammonium. Brain ammonium level under normal physiological conditions is lower than 0.05 mM while in CLD it can reach 0.3-0.5 mM range[11,12]. The cerebral ammonium detoxification mainly

relies on the conversion of Glu to Gln catalyzed by glutamine synthetize (GS) enzyme[7,11]. Since the brain lacks an effective urea cycle (that can be found only in liver), astrocytes are the only cells containing the necessary metabolic machinery (GS) for ammonium removal. Glutamine, as a product of this process, accumulates in the cells reaching high concentrations[9,11,13–16]. Prof Kreis[15] was one of the pioneers showing changes in brain Gln, Ins and tCho in chronic HE patients by using ^{1}H MRS. In our group we have performed the first longitudinal measures of brain metabolite changes in an animal model of type C HE (the bile duct ligated rat) at UHF and we have shown that longitudinal changes in adult hippocampus are seemingly driven by increases in plasma NH_4^+ and brain Gln in turn leading to decreases in antioxidants and Cr, molecules previously unknown in this role[14]. Our longitudinal studies (in some of these studies I was personally involved) allowed the measurement of the time course of Gln increase and showed that this increase is gradual in CLD, leaving the time for astrocytes to respond progressively. The astrocytes try to regulate the osmotic pressure caused by increased Gln via the osmoregulatory processes leading to a decrease of other endogenous osmolytes (e.g. myo-Inositol, total choline) and therefore to compensate for this increase. This could be the reason why brain edema is not often present in case of type C HE[4] leading to sometimes conflictual results[17]. However, the increased ammonium is still a burden for astrocytes. Few histological studies showed alterations in astrocytes morphology and function[7,14,18–20] while EM studies are controversial[17,21]. In our group we have performed the first longitudinal measurements of morphological changes in astrocytes and neurons, and some of the recent data will be presented in section 3.2.2. and will also be presented in parallel to the metabolic changes. In addition to astrocyte-Gln alterations some additional ammonium-induced changes were observed in the CNS (e.g impairment on glutamate neurotransmitter system, altered cerebral blood flow (CBF), impaired oxygen consumption and brain oxygenation etc.)[7,22]. Even though the importance of ammonium in the pathophysiology of type C HE is clear, there is no converging evidence of a direct correlation of the circulating ammonium levels and the severity of type C HE, suggesting that other mechanisms might also be involved[4,7,23]. The lack of correlation between circulating ammonium values and the severity of HE[24] can also be due to the difficulty of measuring circulating ammonium and its variability in CLD[25].

3.1.2   Inflammation in type C HE

Systemic inflammation (systemic inflammatory response syndrome – SIRS) is a common phenomenon in CLD, mainly due to the injured liver, characterized by systemic release of proinflammatory

cytokines (e.g. interleukins – IL-1β, IL-6, IL-8, IL-12 and necrosis factor alpha (TNF-α)[26]. Studies have shown that majority of patients with severe form of type C HE present evidence of systemic inflammation, moreover it was associated with worse cognitive performance of patients that developed type C HE compared to the ones that didn't[27]. Proinflammatory markers, particularly serum IL-6 and TNF-α correlate well with the degree of neurocognitive disfunction (severity of HE)[23,28].

There are several pathways that result in the systemic (peripheral) inflammation leading to neuroinflammation, of which the most important are humoral (circulating cytokines) and immune (activated immune cells) pathways[29]. Circulating cytokines enter the brain directly either by affecting the permeability of the BBB or by binding their receptors (TNF-α, IL-1β) expressed by endothelial cells in the BBB[30]. This leads to a release of secondary messenger molecules into the brain which can induce microglial activation. The microglia can also produce inflammatory mediators on their own (e.g. IL-6). Similarly, the activated immune cells can bind to endothelial cells in the BBB causing release of secondary molecules in turn leading to microglia activation[31–33]. Numerous studies proved the presence of microglia activation in type C HE (adults and rodents)[7]. In parallel, neuroinflammation can lead to changes in neurotransmission, oxidative stress and other mechanisms suggesting that it plays an important role in the pathogenesis of type C HE[7,23]. In this context, during my PhD I have been involved in a project in our group where we showed the presence of systemic (increase in lympochites and plymorphonuclear neutrophils number) and brain inflammation (increased IL-6) in the rat model of type C HE (BDL)[1].

There is increased evidence of a cooperative interaction between inflammation and hyperammonemia, meaning that these two mechanisms don't drive the severity of type C HE individually but synergistically making the brain more susceptible to each other's effects. Although the precise underlying mechanisms of their synergetic actions are not fully understood, it is suggested that ammonium makes astrocytes more susceptible to the cytotoxic effect of inflammatory cytokines, and that the coactions of these mechanisms induce oxidative/nitrosative stress[7,23].

3.1.3 Oxidative stress in type C HE

The role of oxidative and nitrosative stress (formation of reactive oxygen and reactive nitrogen species) has been more and more recognized in the pathogenesis of HE[1]. Having an unpaired electron in outer shell makes ROS/RNS highly reactive with a potential damaging effect in various cellular compartments. Under normal conditions the cells are in a redox (balanced) state, having an

equilibrium between ROS formation and neutralization. An imbalance between their production and neutralization will lead to oxidative stress and in turn cellular dysfunction[23,34]. However, direct evidence and impact of central and systemic OS on type C HE progression is limited due to the difficulty in measuring them.

In CLD, the diseased liver cannot properly regulate the oxidative stress (OS) causing: reduced antioxidant production, increased systemic release of oxidant enzymes, generation of ROS and impaired neutrophil function (a type of white blood cells)[35], in agreement with our work[1]. Liver has a major role in production of antioxidants and thus, in oxidative stress regulation. During the disease, production of proteins (e.g. albumin) by liver diminishes leading to reduced antioxidant capacity[35]. Consequently, there is an alteration in antioxidant enzymes (glutathione peroxidase, superoxide dismutase and catalase) activity in the brain both in mitochondria and cytosol. Moreover, the diseased liver can cause ROS production by neutrophils (immune cells)[1]. As a response to microbial aggression, neutrophils produce ROS causing an oxidative outbreak which has been observed in cirrhotic patients[36]. Oxidative stress has been suggested as one of the mechanisms of ammonium neurotoxicity particularly affecting astrocytes[37,38]. The exact mechanism of ammonium induced free radical formation is not completely understood. A rise in intracellular Ca^{2+} has been observed as one of the early events in astrocytes following ammonium exposure, causing the activation of Ca^{2+} dependent enzymes such as constitutive nitric oxide synthetase (cNOS), NADPH oxidase (NOX) and phosphorylase A2 (PLA2) which are known to trigger the generations of ROS/RNS (e.g. nitric oxide and superoxide radicals)[38]. Except the above described linear event, complex interactions between OS-derived factors (e.g. Mitochondrial Permeability Transition-mPT, Mitogen-Activated Protein Kinases-MAPKs etc.) can generate additional ROS/RNS resulting in a self-amplifying circle. OS is considered as a principle mean by which ammonium exerts harmful effect on astrocytes[37,38]. Furthermore, it is now well accepted that inflammation and ammonium act in synergy causing formation of ROS, e.g. like the formation of ROS in peripheral immune cells such as neutrophil granulocytes[39], as showed by our group[1].

MRS allows the direct measurement of antioxidants (e.g. Asc and GSH) and NAD+/NADH redox state in vivo, however the main limitation consists in the low concentration of these metabolites. In addition, changes in these antioxidants represent an indirect evidence of the presence of OS in disease. In our group we measured a decrease in Asc in the BDL rats (adults and pups)[13,14] together with

increased ammonium and Gln (section 3.2.1). Electron paramagnetic resonance (EPR) provides a direct, quantitative and highly efficient technique for the direct measurement of ROS (i.e. free radicals) ex vivo directly. Thus, the combined usage of EPR and MRS will allow us to perform a direct assessment of OS in type C HE in different brain regions and investigate their potential brain regional difference, something I performed during my PhD and that will be described in this chapter (section 3.2.3).

3.1.4 MR Spectroscopy in Hepatic encephalopathy

Localized MRS is a powerful technique which allows a non-invasive investigation of brain metabolism in human and rodent brain in vivo and longitudinally. Using single voxel spectroscopy (SVS - Sub chapter 1.6) a characteristic spectrum can be acquired from a well-defined volume positioned in a specific region of interest[17].

^{1}H MRS remains the most widely applied and one of the most sensitive techniques. In addition, it is the only technique capable of measuring a large number of metabolites simultaneously in vivo. Since majority of brain metabolites contain hydrogen nuclei, a number of biologically relevant metabolites can be observed and quantified (section 1.6.4). In the human patients the MRS acquisitions were largely performed at $1.5 - 3\ T$ and $TE \geq 20\ ms$ leading to quantification of Glx, Cr, tCho (total choline), Ins. This technique was one of the first to characterize changes in brain organic osmolytes in type C HE by describing a decrease in myo-Inositol and choline in response to an increased Glx resonance[15,40–42]. At present, the availability of high magnetic fields ($\geq 7T$) enabled researchers to quantify more metabolites (e.g. GABA) and separate closely spaced peaks (e.g. Glu and Gln). A recent study performed in our laboratory provided a precise description of HE profile over several weeks in an animal model of CLD induced HE (at 9.4T)[14]. Taking advantage of the UHF some previously unknown metabolic abnormalities, such as decrease in antioxidants and Cr in response to brain Gln increase, were described. These longitudinal changes in adult hippocampus are seemingly driven by increases in plasma NH_4^+ and brain Gln causing a decrease of the above mentioned molecules (antioxidants and Cr) that were previously unknown to assume this role[14]. These results suggest that in addition to metabolomics, MRS could be a useful tool to study the metabolic pathways involved in HE in vivo and in humans[43,44]. The parameters measurable by MRS are shown to be affected by the neurological status of the patient, but also by therapeutic strategies (e.g. liver transplantation). Although MRS is not currently used as a diagnostic tool in HE, it was proposed as a non-

invasive surrogate marker for evaluation of treatment strategies, especially at high magnetic fields[44].

The regional distribution of metabolites in the brain during type C HE is yet unknown. Its understanding will provide additional mechanistic insights into disease processes. Therefore, an important part of this chapter is focusing on the advantages of UHF short TE single voxel spectroscopy to answer this question in a rat model of type C HE.

To sum up, although the exact molecular mechanisms leading to type C HE are not fully understood, the increase in ammonium delivery to the brain, Gln concentration increase due to ammonium detoxification, and excess in formation of ROS/RNS and inflammation are a common thread in this complex and multifactorial disease. In this chapter we aim to decipher, for the first time, the molecular underpinnings behind the differential brain regional vulnerability and to identify key molecular steps in type C HE in the adult and developing brain. For that, we will use magnetic resonance spectroscopy combined with histology and electron paramagnetic resonance.

3.2 Brain regional vulnerability in the adult brain during type C HE (adult BDL rats)

3.2.1 Study 1: Brain regional vulnerability using ^{1}H MRS

The symptoms of HE include attention deficits, changes in personality, cognitive and motor performance impairments together with memory deficits[5] (see sub chapter 3.1). Since the type C HE patients present various symptoms with different extent of severity, the susceptibility to type C HE and the mechanisms causing the damage may be dependent on the brain region. What are the brain metabolites regional differences in type C HE and how their changes impact the morphology of astrocytes or neurons remains an unanswered question.

Hippocampus is the brain region responsible for spatial cognition, balance control, emotion, addiction, memory and learning. Therefore, abnormalities in this region can cause spatial cognitive anomalies and balance disorders[45,46]. It was shown that patients with cirrhosis who developed Minimal HE have structural and functional connectivity disturbances in the hippocampus which correlate with their cognitive impairment and memory performance[46]. Moreover, in the rat model of fibrosis, a significant decrease in the hippocampal dopamine was shown and connected with the observed behavioral disorder[45]. Changes in morphometry of hippocampal pyramidal neurons were also connected to behavioral deficits (disturbed memory and motor function) in a rat model of chronic liver failure induced mild HE (induced by thioacetamide administration)[47]. Furthermore, neuroinflammation was observed in hippocampus of rats with Minimal HE and connected to spatial learning and memory impairment[48].

Cerebellum has a role in basic motor abilities (movement, coordination, etc.), as well as in several cognitive processes such as spatial navigation, working memory and procedural, motor and spatial learning[49]. In cirrhotic patients, an increase in cerebellar blood flow was shown especially for those who developed Minimal HE together with a reduced gray matter volume in the cerebellum[50]. In parallel, it was reported that neuroinflammation, especially in this brain region, occurs very early in the liver disease (even before reaching cirrhosis)[51]. Studies in animal models have suggested that neuroinflammation, induced by systemic inflammation, might be stronger in cerebellum leading to cognitive and motor alterations[48,51]. Moreover, it was previously shown that the ammonium uptake rate and thus the burden of ammonium is not the same in all the brain regions. The basal ganglia

and cerebellum are predominantly affected by alterations in cerebral ammonium, suggesting that there is a higher ammonium supply in these brain regions[52].

It is known that striatum plays a role in refinement and control of motor movement, but also in reward and executive systems (decision making)[53]. It was found that cirrhotic patients with Minimal HE have disturbed structural connectivity between the thalamus and striatum and it has been suggested that thalamic-striatal system is connected with cognitive deficits observed in the disease. Mitochondrial disfunctions and increase in mitochondrial reactive oxygen species was observed in striatum as well as cerebellum, cortex and hippocampus of rats with bile duct ligation induced HE[54].

Therefore, hippocampus, cerebellum and striatum are already proven to be among the main regions implicated in the pathogenesis of HE, and their alterations were related to neuropsychiatric disturbances in rat models and patients. Few previous studies in human patients with type C HE evaluated brain regional differences in metabolic ratios of Cho, Glx and NAA relative to Cr. Significant regional variations in these metabolite ratios, the lowest Cho/Cr in the occipital cortex and highest Glx/Cr in the basal ganglia, were observed. All this evidence leads to a conclusion that information from different brain regions might be useful for a better understanding of the mechanisms underlying the disease[40]. Moreover, the ability of UHF to pinpoint previously unreported metabolic changes has been already proven by our group in the hippocampus of a BDL rat model of HE[14].

The aim of this study was to describe the evolution of metabolic profiles throughout the disease duration in hippocampus, cerebellum and striatum, and furthermore identify the potential metabolic differences between these key brain regions implicated in the manifestation of type C HE. In addition to ^{1}H MRS, a multimodal approach combining histology with blood biochemistry and EPR will be used to complete the brain regional investigation of type C HE (please see sections 3.2.2 and 3.2.3).

3.2.1.1   *Materials and methods*

BDL rat model of CLD

All experiments were approved by the Committee on Animal Experimentation for the Canton de Vaud, Switzerland (VD3022/VD2439). Wistar male adult rats (n=36, 125-150g, Charles River Laboratories, L'Arbresle, France) were used: 31 rats underwent bile duct ligation surgery (BDL surgery) as

described in[55]. The BDL rat model of type C HE is associated with liver disease, portal hypertension, hyperammonemia and it is accepted by ISHEN[8,56].

Biochemical measurements

Liver parameters (plasma bilirubin, aspartate aminotransferase (AST/GOT) and alanine aminotransferase (ALT/GPT)) and Glc were measured using Reflotron Plus system (F. Hoffmann-La roche Ltd.) and blood NH_4^+ on blood ammonium meter (PocketChem[TM] BA PA-4140).

In vivo ^{1}H MRS

^{1}H MRS spectra were acquired on 9.4 T system (Varian/Magnex Scientific) using the SPECIAL sequence (TE=2.8ms) as previously described[14]. Three different volumes of interest (VOI) were selected in hippocampus ($2x2.8x2mm^3$), cerebellum ($2.5x2.5x2.5mm^3$) and striatum ($2.5x2x2.5mm^3$). LCModel was used for quantification with water as internal reference allowing the quantification of a total of 18 metabolites. The scans were performed before (week 0) and after BDL at weeks 2, 4, 6, and 8, thus each animal was its own control. A total of n=27 rats underwent ^{1}H MRS. N=24 rats were scanned in the hippocampus (week 0 - n=23, week 2 - n=15, week 4 - n=21, week 6 - n=21, week 8 - n=8), n=23 rats were scanned in the cerebellum (week 0 - n=22, week 2 - n=15, week 4 - n=21, week 6 - n=18, week 8 - n=7) and n=15 rats were scanned in the striatum (week 0 - n=15, week 2 - n=14, week 4 - n=13, week 6 - n=10, week 8 - n=4). There is a different number of rats at each week because some of the rats were used for histology and OS measurements (see sections 3.2.2 and 3.2.3) or they needed to be sacrificed earlier than week 8 because they reached the end point allowed by the Committee on Animal Experimentation for Canton of Vaud (e.g. 15% of weight loss) hence the low number of rats at week 8.

Statistical analysis

The results were presented in three different ways: bar plots, scatter plots and 1st axis of STATIS analysis.

In the bar plots the results were always presented as mean $\pm$ SD. The % change was calculated in comparison to week 0. For metabolites in the neurochemical profile and the reported blood values one-way ANOVA (Prism 5.03, Graphpad, La Jolla CA USA) followed by Bonferroni's multiple comparisons post-tests were used and displayed in figures. Additionally, differences between brain regions were assed using two-way ANOVA and presented in figures ($^\$p<0.05$, $^{\$\$}p<0.01$, $^{\$\$\$}p<0.001$, $^{\$\$\$\$}p<0.0001$). To test the correlations between longitudinally acquired data for brain metabolites

and plasma/blood values Pearson correlation analysis was performed. Significance level in all tests was attributed as follows: *p<0.05, **p<0.01, ***p<0.001, ****p<0.0001.

The scatter plots display relative increase of metabolic concentrations over time in the disease. The plotted values were obtained by subtracting the week 0 concentration of a metabolite for every rat and brain region from the corresponding week 2, 4, 6 and 8 measured concentrations, and therefore keeping only the relative (to week 0) change in the disease. This way the starting differences in metabolic concentrations between the brain regions[57,58] were removed, and the figure describes only the metabolite evolution due to the disease while clearly pointing to the brain regional difference for the concerned metabolites. The plots were created in RStudio[59] where additionally a LOWESS (Locally Weighted Scatterplot Smoothing) regression was applied and plotted to better visualize and distinguish data trends between brain regions.

The details on the 1st axis of STATIS analysis are provided in the following section.

Application of the STATIS method on the ^{1}H MRS and blood data

Principal component analysis (PCA)

According to linear algebra any rectangular matrix A of dimension $n \times m$ can be factorized into:

$$A = U\Sigma V^T$$

Equation 3:1

Where U are left singular vectors in m dimensions, V are right singular vectors in n dimensions and Σ is a diagonal matrix of singular values (σ - positive or zero). This factorization is called singular value decomposition (SVD). Since $A^T A$ and AA^T are both symmetric and positive definite matrices they can be factorized using the spectral theorem ($S = Q\Lambda Q^T$, where Q is an orthogonal matrix and Λ are the eigenvalues):

$$A^T A = V\Lambda V^T, \qquad AA^T = U\Lambda U^T$$

Equation 3:2

Therefore, it can be concluded that both U and V are orthogonal matrices while $A^T A$ and AA^T have the same eigenvalues (one matrix has m and the other one n eigenvalues but the different/missing ones are zero). Moreover, we can factorize $A^T A$ and AA^T as:

$$A^T A = V\Sigma^T U^T U \,\Sigma V^T = V(\Sigma^T \Sigma)V^T \;and\; AA^T = U \,\Sigma V^T V\Sigma^T U^T = U(\Sigma^T \Sigma)U^T$$

Equation 3:3

Since $U^T U = I$ and $V^T V = I$, the Equation 3 :3 is valid and we can conclude that U are the eigenvectors of AA^T, V the eigenvectors of $A^T A$ and σ^2 the eigenvalues of both $A^T A$ and AA^T. By convention the singular values in the diagonal Σ are in a descending order ($\sigma_1 \geq \sigma_2 \geq \sigma_3$ ...). The SVD can also be written as:

$$A = \sum_{i=1}^{r} \sigma_i u_i v_i^T$$

Equation 3:4

Where $r \leq min\{m, n\}$ is the rank of A (since after the rank σ are zero).

Now we will introduce principal component analysis as a statistical interpretation of SVD applied on a data matrix. PCA gives us a data driven hierarchical coordinate system (in terms of directions that capture the maximum amount of variance in a given dataset) to represent the statistical variations. Since it's a statistical representation of SVD there are some extra steps that need to be applied.

To introduce the PCA convention we start by introducing a data matrix X with the independent experiments as row vectors (x_1 measurements from a single experiment, e.g. rows are measurements from person 1 while columns are measured variables such as age, height etc.). Therefore, if matrix X is of a dimension $n \times m$ there are for example n samples (people) and m measurements (different variables).

$$X = \begin{bmatrix} \cdots & x_1 & \cdots \\ \cdots & x_2 & \cdots \\ \vdots & \cdots_n & \vdots \end{bmatrix}$$

Equation 3:5

There is a statistical variability of data in this matrix and we are trying to uncover the dominant features of the data with PCA according to the following steps:

1. Compute the mean row and build an average matrix.

$$\bar{x} = \frac{1}{n} \sum_{j=1}^{n} x_j \rightarrow \overline{X} = \begin{bmatrix} 1 \\ 1 \\ \cdot \\ \cdot \\ \cdot \\ 1 \end{bmatrix} * [\quad \bar{x} \quad]$$

Equation 3:6

2. Subtract the average matrix from the original data matrix to obtain the mean centered data matrix (center of the distribution is at the origin).

$$B = X - \overline{X}$$

3. SVD of the mean centered data ($B = U\Sigma V^T$) or eigen decomposition of the covariance matrix:

   a. Compute the covariance matrix: $C = \frac{B^T B}{m-1}$ (dimension $m \times m$)

   b. Perform the eigen decomposition of the covariance matrix: $CV = V\Lambda$, where V are the eigenvectors of C and Λ the eigenvalues ($\lambda = \sigma^2$, see Equation 3:3).

   c. The principal components are now $T = BV$ or (when looking at the SVD) $T = U\Sigma$. The principal components are ordered and the eigenvalues give an indication of the amount of variance that each component captures.

If we want to describe high-dimensional data in terms of first r principal components, we can compute how much of the variance is captured in the r components using the eigenvalues $\frac{\sum_{k=1}^{r} \lambda_k}{\sum_{k=1}^{n} \lambda_k} = \%$ (fraction of variance captured in the first r components).

STATIS multi-table principal component analysis (description)

STATIS method is created as an extension to PCA designed to manage multiple data tables that contain set of variables collected on the same observations. It is usually applied to three-way data. As an example, the data (in the data tables) can be measurements performed on the same observations (individuals or objects) at different time points with the goal to evaluate how the observations change over time.

First the structure of individual data tables is analyzed (e.g. the relation between individual data tables) to derive the optimal set of weights for these data tables in order to create an optimum weighted average called a compromise. The elements of each table are multiplied by the corresponding optimal weight and the compromise is obtained by addition of these 'weighted' tables (the compromise is a linear combination of the tables). The weights should be derived so that the compromise gives the best representation (in a least square sense) of the whole set of tables.

The next step is to preform a PCA of the compromise. The PCA decomposes the variance of the compromise into a set of new orthogonal variables called principal components which are ordered (1st, 2nd … axis) by the amount of variance they explain[60,61].

RStudio-application of STATIS analysis on the data set

The pipeline for application of the STATIS method was validated by Dr. Pierre Bady (biostatistician at CHUV-UNIL), who provided us with the RStudio script applied on his datasets[62,63]. I further adapted and modified the data preparation process and the RStudio script to make it compatible with our dataset.

As described in the previous section ("In vivo ^{1}H MRS) the animals were scanned (in three brain regions) and the blood sampling was performed longitudinally at week 0, 2, 4, 6 and 8. For one brain regions this provides us with several quantified metabolites for each rat at five different time points. Therefore, we have a three-dimensional dataset suitable for the STATIS analysis. The analysis was performed on each brain region individually first using only the brain metabolites and then repeated on a combined dataset consisting of the brain metabolites and blood parameters.

The data was prepared by stacking rats at different time points as rows and metabolites as columns (for each brain region). This resulted in six datasets: brain metabolites – striatum, brain metabolites – hippocampus, brain metabolites – cerebellum, brain metabolites + blood parameters – striatum, brain metabolites + blood parameters – hippocampus, brain metabolites + blood parameters – cerebellum. Every dataset was processed using the following procedure. The matrix/dataset (rats at different time points -rows, metabolites -columns) was centered by subtracting the mean of every column to the corresponding column (e.g. the mean value of Gln measured for all the rats at all time points was subtracted from every Gln measurement). The few missing values due to low spectral quality or missing a scan were imputed using missMDA package (RStudio). The function estim_ncpPCA was used to estimate the optimal number of dimensions for imputing the data using the imputePCA function. The dataset was then reshaped into N (equal to the number of rats) "Ktables" based on the within analysis (function ktab.within from R package ade4). Each table represented one rat with metabolites as rows and weeks (time points) as columns. The STATIS analysis was then performed on the "Ktables" (package ade4 from R studio, function statis).

3.2.1.2 Results

Results – ^{1}H MRS and blood parameters: Characterization and validation of CLD-induced HE in BDL rats by biochemical measurements

All the BDL operated animals showed significant increase in plasma bilirubin from week 2 validating the presence of CLD (Figure 3:1). Increase in blood ammonium was also observed for all BDL rats when compared to week 0 (before BDL), reaching significance at week 6 (Figure 3:1). Values of both measured parameters were in normal ranges before BDL (week 0). The additional measures (GPT, GOT, Glc) are presented in the STATIS analysis in the following section (title: "STATIS analysis of ^{1}H MRS and blood data").
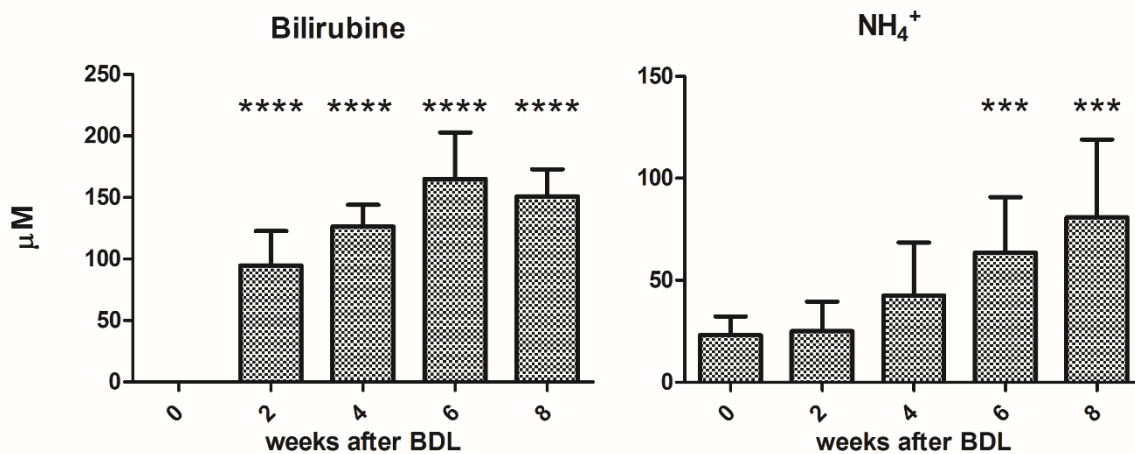
Figure 3:1 Longitudinal changes in total plasma bilirubin and blood NH$_4^+$ induced by bile duct ligation. Bilirubin was non-measurable before BDL. Significance level between week 0 and weeks 2-8: *p<0.05, **p<0.01, ***p<0.001, ****p<0.0001 (1-way ANOVA).

BDL-induced changes in Gln and other osmolytes, neurotransmitters and antioxidants measured by ^{1}H MRS.

The excellent quality of ^{1}H MRS spectra in all brain regions is shown in the Figure 3:2.
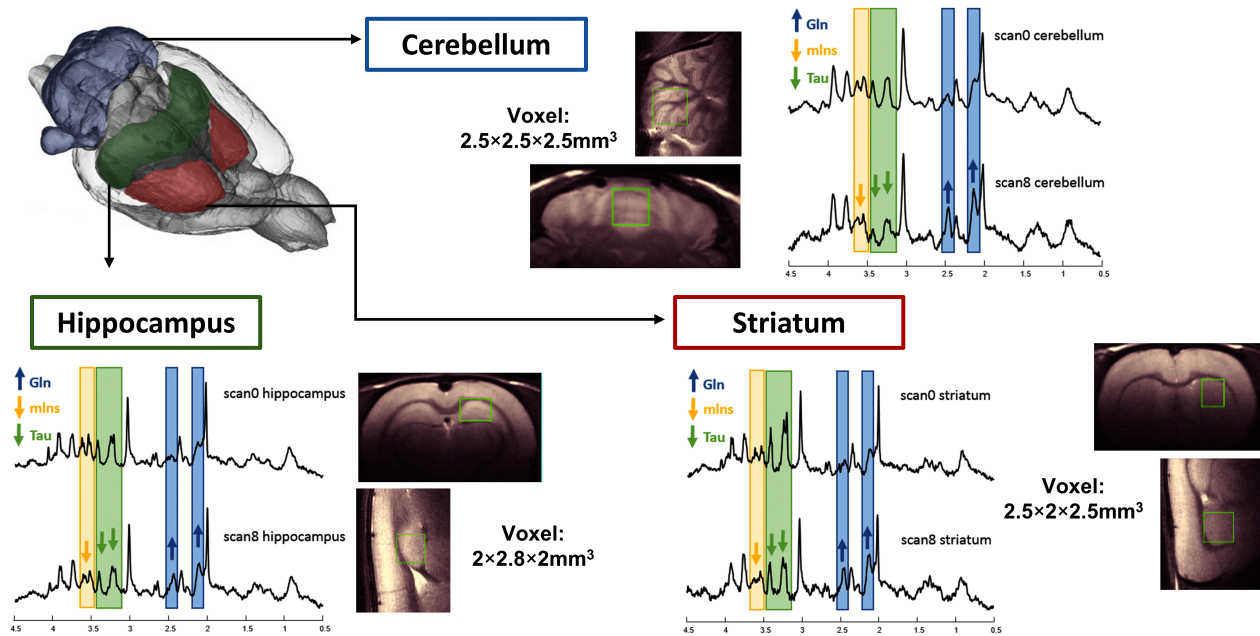
Figure 3:2: Representative *in vivo* ^{1}H MRS spectra acquired from 1 animal at week 0 (before BDL) and at post-operative week 8 in the striatum, hippocampus and cerebellum (the corresponding VOI for each regions are also highlighted in neon green) . Increase in Gln and the decrease of Ins and Tau can be clearly observed directly form the spectra.

The increase of **Gln** was observed already at week 2 post-BDL (compared to week 0) for all the brain regions being the first metabolite to show a consistent overall change early in the disease evolution (i.e. already at week 2 post-BDL). This increase reached significance at week 4 post-BDL (+41% in striatum, +63% in hippocampus, +64% in cerebellum) and continued increasing till week 8 post-BDL (Figure 3:3). The overall increase of Gln was statistically stronger in *cerebellum* reaching +134% at week 8 (Figure 3:3A, Figure 3:4) and was also visible in the acquired ^{1}H MR spectra (Figure 3:2).

The main CNS osmolytes and cell volume regulators Ins, Tau, Cr and tCho displayed a trend of decrease in concentration as a response to Gln increase indicating an osmoregulatory response of the cell (Figure 3:3). **Ins** decreased in all three brain regions reaching significance at week 6 post-BDL (-14%) for *cerebellum* and at week 8 post-BDL (-14%) for *hippocampus* (Figure 3:3, Figure 3:4). Furthermore, **tCho** (GPC + PCho) showed an overall trend of decrease being statistically the most pronounced in *striatum* where it reached a significant -40% at week 6 and continued to decrease till week 8 post-BDL (Figure 3:3, Figure 3:4). **Tau** showed a consistent trend of decrease reaching

significance at week 4 post-BDL for all the brain regions (-9% - striatum, -9% - hippocampus, -19% - cerebellum) and continued decreasing to week 8 (Figure 3:3, Figure 3.4). This global decrease was statistically stronger for cerebellum when compared to hippocampus and striatum. **Cr** also displayed an overall trend of decrease being the most pronounced in ***cerebellum*** where it reached significance at week 4 post-BDL (-9%) (Figure 3:3, Figure 3.4). To evaluate the osmotic stress induced in the cell by the load of Gln, the sum of these main CNS osmolytes was computed (Figure 3:3B). The sum (without Gln) showed a trend of decrease reaching significance at week 6 post-BDL with -11% and -13% for ***striatum and cerebellum,*** respectively and at week 8 post-BDL with -11% for hippocampus (Figure 3:3B). Interestingly, despite the smallest absolute Gln increase, ***striatum*** showed a more pronounced decrease of these osmolytes in absolute concentration (at 8 weeks post-BDL: Gln +2.3 mmol/kg$_{ww}$ *vs* sum of osmolytes -4.2 mmol/kg$_{ww}$) than hippocampus (at 8 weeks post-BDL: Gln +3.2 mmol/kg$_{ww}$ *vs* sum of osmolytes -2.6 mmol/kg$_{ww}$) and cerebellum (at 8 weeks post-BDL: Gln +5.3 mmol/kg$_{ww}$ *vs* sum of osmolytes -4.1 mmol/kg$_{ww}$, Figure 3:3B).
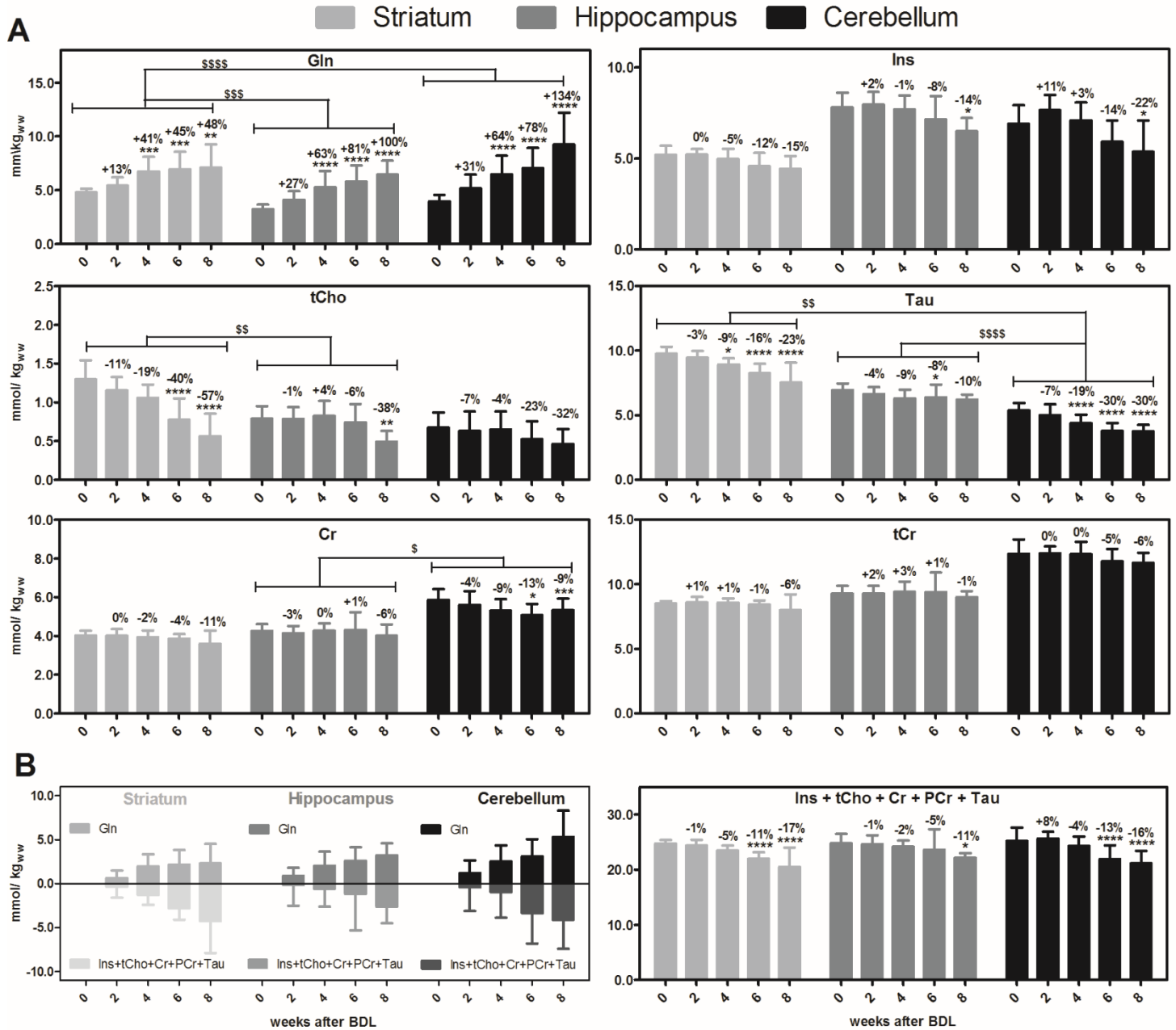
Figure 3:3: Longitudinal ^{1}H MRS evolution of glutamine and CNS osmolytes in three brain regions (A) Longitudinal ^{1}H MRS evolution of glutamine and CNS osmolytes in all three brain regions studied from week 0 to week 8 post BDL. Mean ∓ SD, significance level between week 0 and weeks 2-8: *p<0.05, **p<0.01, ***p<0.001, ****p<0.0001 (1-way ANOVA). **(B)** . Absolute increase of Gln compared with an absolute decrease of main CNS osmolytes-on the left. Longitudinal evolution of sum of the osmolytes (without Gln)-on the right Mean ∓ SD, significance level between week 0 and weeks 2-8: *p<0.05, **p<0.01, ***p<0.001, ****p<0.0001 (1-way ANOVA). Additionally, differences between brain regions were assed using two-way ANOVA ($p<0.05, $$p<0.01, $$$p<0.001, $$$$p<0.0001).

Figure 3:4: Relative changes of glutamine and CNS osmolytes in three brain regions The scatter plots display the relative increase of metabolite concentrations (for Gln, Ins, tCho - GPC.PCho, Tau, Cr and tCr – Cr.PCr) over time during the disease. The plotted values were obtained by subtracting the week 0 concentration of each corresponding metabolite for every rat and brain region from the corresponding week 2, 4, 6 and 8 measured concentrations, and therefore keeping only the relative (to week 0) increase during the disease. This way the starting differences in metabolic concentrations between the brain regions were removed, and the figure describes only the metabolite evolution due to the disease while clearly pointing to the brain regional difference for the concerned metabolites. The plots were created in RStudio where additionally a LOWESS (Locally Weighted Scatterplot Smoothing) regression was applied and plotted to better see and distinguish data trends between brain regions.

The neurotransmitter **Glu** showed a decrease in the later stage of the disease for all three brain regions being the most pronounced in *striatum* where it reached a significant -10% at week 6 post-BDL (Figure 3:5, Figure 3:6). However, **Asp** (data not shown) and ***γ*-aminobutyric acid (GABA)** displayed no significant changes even though for GABA an overall tendency of decrease was observed especially for hippocampus and cerebellum (Figure 3:6). No significant changes in neuronal marker **NAA** were observed throughout the course of the disease. The **Lac** evolution showed no significant changes in the striatum and hippocampus, but a striking increase of 84% was observed in *cerebellum* at the end-point of the disease (week 8 post-BDL, Figure 3:5 and Figure 3:6). The antioxidant **Asc** showed a tendency of decrease in *cerebellum* at week 6 post-BDL (-32%, Figure 3:5, Figure 3:6) without reaching significance. **GSH** displayed no significant changes throughout the disease, although a significantly different GSH behavior was measured in *cerebellum* compared to the other brain regions where a tendency of increase was observed (Figure 3:5, Figure 3:6).
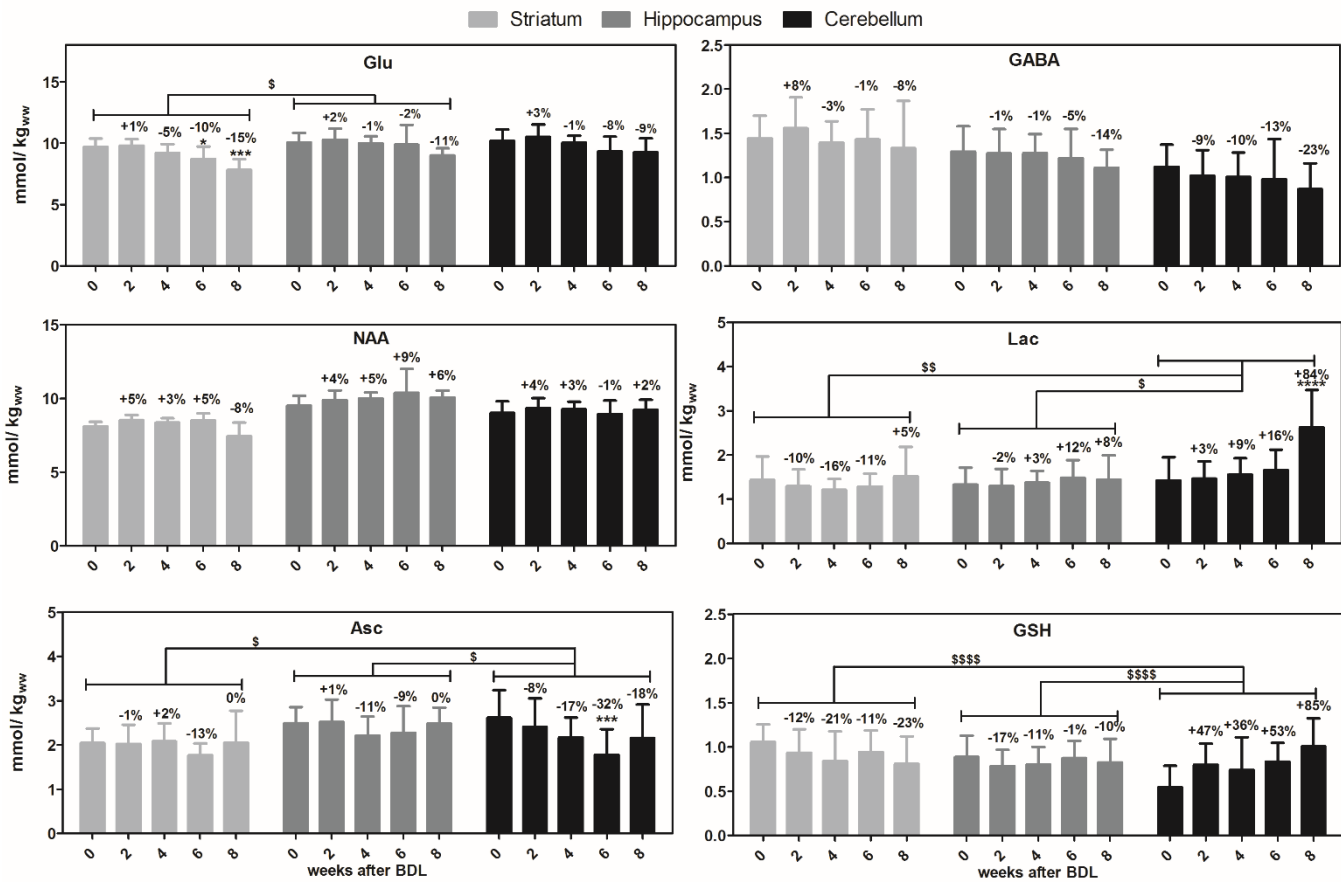
Figure 3:5: Longitudinal ¹H MRS evolution of other main brain metabolites in three brain regions (neurotransmitters, neuronal markers, metabolites involved in energy metabolism and antioxidants) for all brain regions from week 0 to week 8 post-BDL. Mean ∓ SD, significance level between week 0 and weeks 2-8: *$p < 0.05$, **$p < 0.01$, ***$p < 0.001$, ****$p < 0.0001$ (1-way ANOVA). Additionally, differences between brain regions were assed using two-way ANOVA ($^{\$}p < 0.05$, $^{\$\$}p < 0.01$, $^{\$\$\$}p < 0.001$, $^{\$\$\$\$}p < 0.0001$).
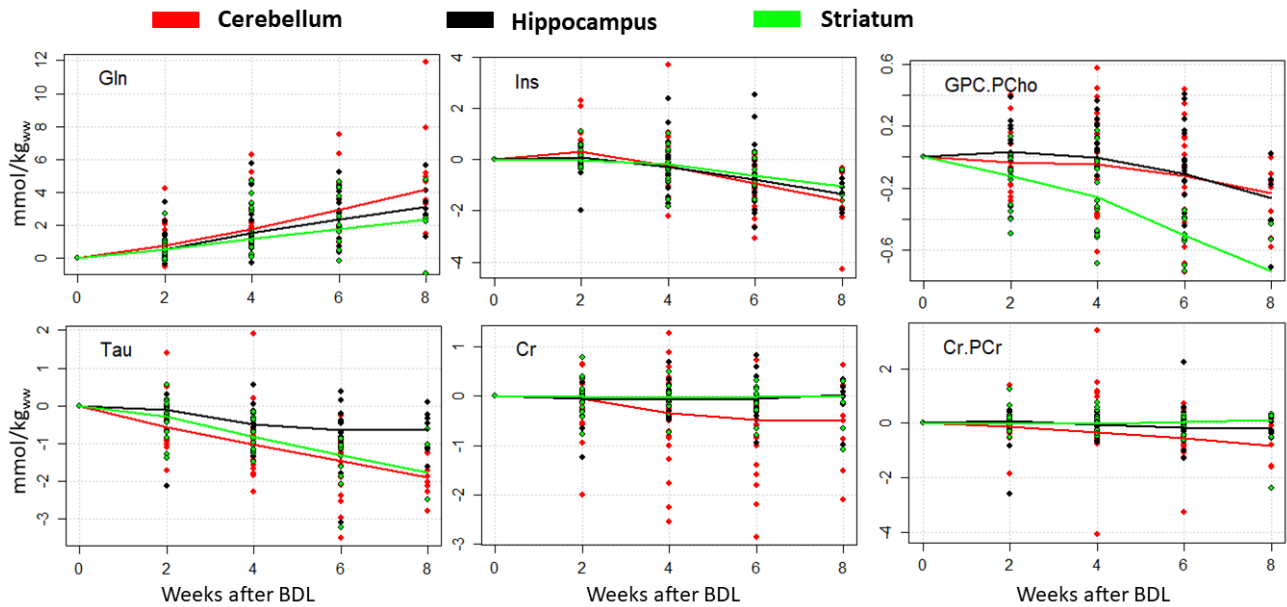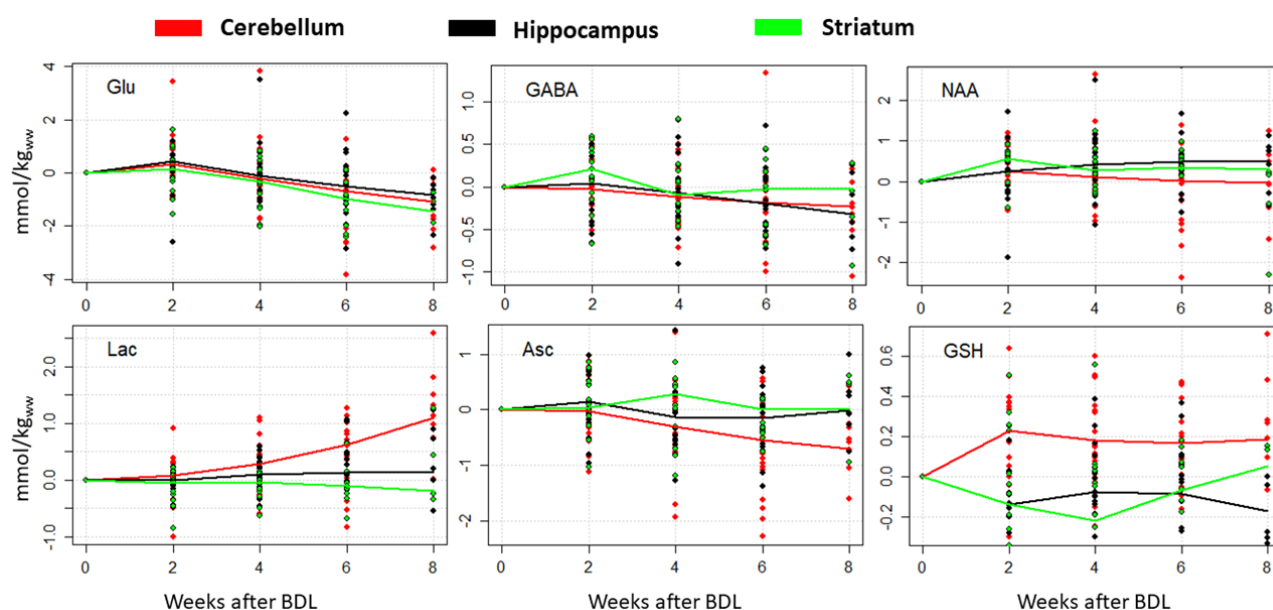
Figure 3:6: Relative changes of other main brain metabolites in three brain regions. The scatter plots display relative increase of metabolic concentrations (for Glu, GABA, NAA, Lac, Asc and GSH) over time in the disease. The plotted values were obtained by subtracting the week 0 concentration of a metabolite for every rat and brain region from the corresponding week 2, 4, 6 and 8 measured concentrations, and therefore keeping only the relative (to week 0) increase in the disease. This way the starting differences in metabolic concentrations between the brain regions were removed, and the figure describes only the metabolite evolution due to the disease. The plots were created in RStudio where additionally a LOWESS (Locally Weighted Scatterplot Smoothing) regression was applied and plotted to better see and distinguish data trends between brain regions.

STATIS analysis of ^{1}H MRS and blood data

The STATIS method was applied on the six datasets, for every brain region on the brain metabolites only, and on the metabolites combined with the blood measurements (Figure 3:7). It is important to emphasize that every dataset was centered prior to the analysis, as described in the section 3.2.1.1. ("Application of the STATIS method on the ^{1}H MRS and blood data"). By centering the data, we removed the contribution to the variance introduced by differences within the same metabolic profile (different starting concentrations of the metabolites). What remains is the contribution of the time evolution of metabolites throughout the disease and the contribution of varying response of the rats to the disease (some rats were more affected by the disease than the others). The within analysis performed in Rstudio tries to consider the mentioned difference between rats, therefore the highest contribution to the variance (of the compromise – see section 3.2.1.1.) comes from the metabolic changes during the disease evolution. The 1st Axis of PCA analysis (performed on the compromise) is the axis of maximum variance of the data, which in our case, as previously explained, mainly represents the time evolution during the disease. The 1st Axis resulting from every analyzed dataset is shown in the Figure 3:7 with the corresponding and the resulting contributions of the

metabolites/blood parameters. We can say that the metabolites highly contributing to the 1st Axis (positive or negative) are the ones driving the variance and they can be grouped based on their contribution. Note that the orientation of the Axis is not correlated with weather the metabolites increase or decrease, but depends on the underlying dataset. However, the metabolites which evolve differently are always on the opposite sides of the Axis.
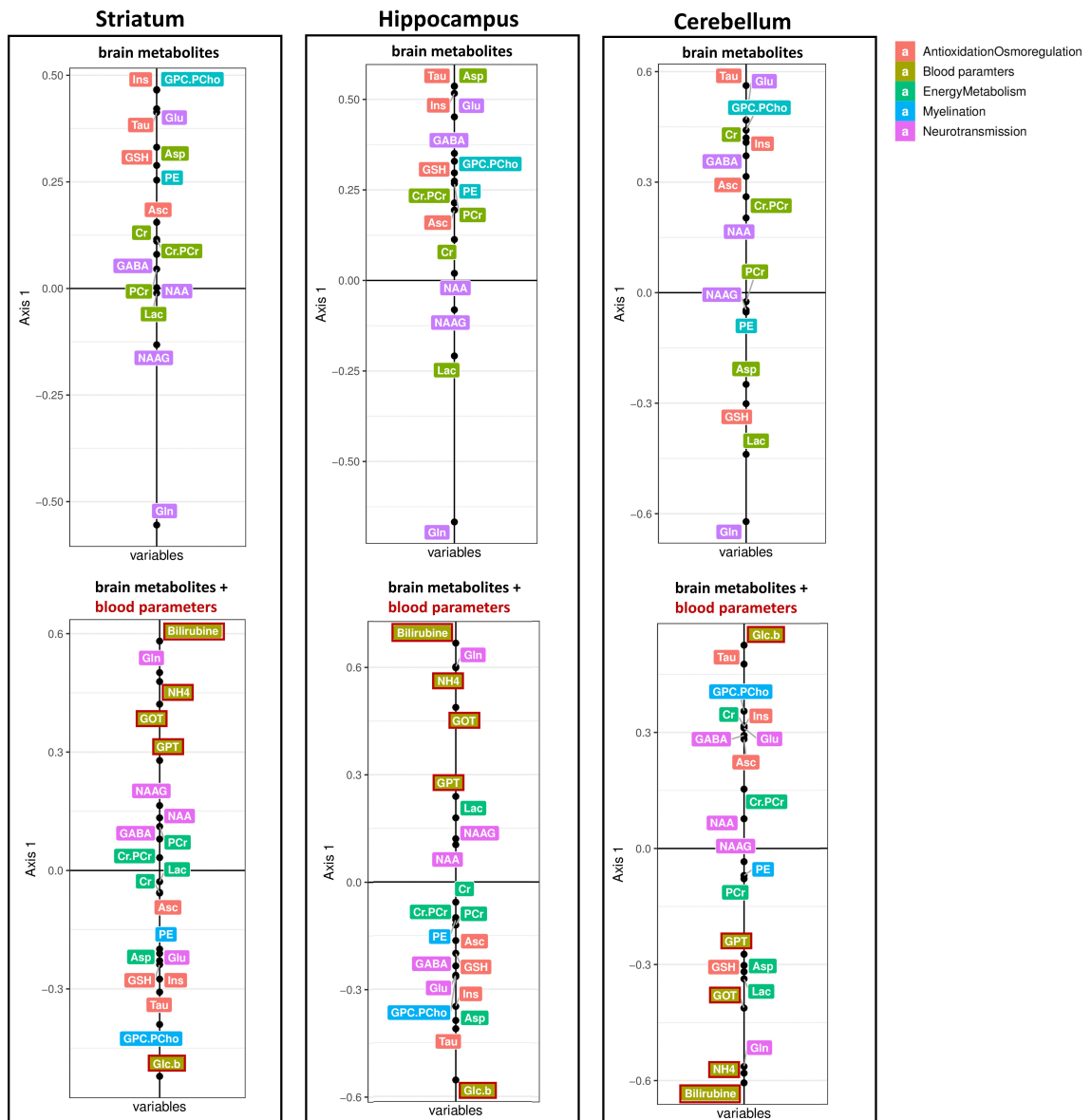
Figure 3:7: The first axis resulting from the STATIS analysis of the datasets described in the section 3.2.1.1. The axis corresponding to the dataset containing only brain metabolites are shown up, and for the datasets containing brain metabolites + blood parameters are shown down. The added blood parameters between the groups of datasets (shown up and down) are circled in red.

From the results presented for the brain metabolites only (Figure 3:7up) it is clear that Gln has a high contribution to the variance (high contribution to the 1st Axis) for all brain regions, corresponding to its previously described strong and consistent increase (Figure 3:3, Figure 3:4). For **striatum**,

on the opposite side of Gln we have Ins, Tau and tCho (GPC.PCho), which are showed in the previous section to be decreasing as an osmotic response to the Gln increase. The strong contribution of tCho to the 1st Axis corresponds to the strongest decrease of this metabolite in striatum as already observed in Figures 3:3 and 3:4. Very strong contributions of Ins, Tau and tCho are also present for **cerebellum** and **hippocampus** (corresponding to Figure 3:2 and Figure 3:3). For **cerebellum**, a contribution of Lac is also observed (on the same side as Gln) corresponding to a strong increase of Lac at week 8 (contributing to the variance) in this brain region. Additionally, a different behavior of GSH as well as a stronger change of Asc are confirmed in cerebellum. Therefore, we can conclude that this method of data analysis is another, interesting and reliable way of describing our dataset.

The results obtained for the brain metabolites + blood parameters are shown on the Figure 3:7down (the added blood parameters are circled in red). It can be observed that bilirubin has the highest contribution to the variance, which describes its constant and very strong increase throughout the disease (Figure 3:1). Bilirubin is one of the first indicators of liver disease, and its increase is a sign of a successful bile duct ligation. Interestingly, NH_4^+ and Gln have a similar contribution to the variance among the two, and similar to bilirubin (in all brain regions, but the closest to each other in the cerebellum). Our results already showed a corresponding behavior between NH_4^+, bilirubin and Gln (Figures 3:1 and 3:3). The STATIS analysis additionally confirmed that Gln is driving the data in a similar way to NH_4^+ and bilirubin.

Pearson correlations between metabolites and NH_4^+

Pearson correlation coefficients were used to pin point dependencies between measured parameters and thus identify the metabolic pathways involved in the progression of the disease (Figure 3:8). Brain Gln and blood NH_4^+ correlated strongly for all the brain regions ($p \leq 0.0001$). Since those two metabolites display the strongest and earliest changes their correlations with other measured parameters were also analyzed (Figure 3:8 and Figure 3:9). Ins and tCho correlated significantly with both Gln and NH_4^+ (in all the brain regions). Brain Gln showed a significant correlation with Tau for hippocampus and cerebellum while NH_4^+ correlated significantly with Tau in all the brain regions. Similarly, Gln correlated significantly with Cr in hippocampus and cerebellum however the correlation with NH_4^+ was not observed for this metabolite. The correlation with Glu was more pronounced for NH_4^+, where it was significant for all the brain regions, than for Gln where the correlation was weaker and showed significance for hippocampus and cerebellum. GABA and NAA correlated

significantly with Gln only in cerebellum and hippocampus, respectively. Lac also showed a correlation in these two brain regions, the correlation being more pronounced with Gln than NH_4^+. For the antioxidants, only GSH showed a significant correlation with Gln uniquely for hippocampus.
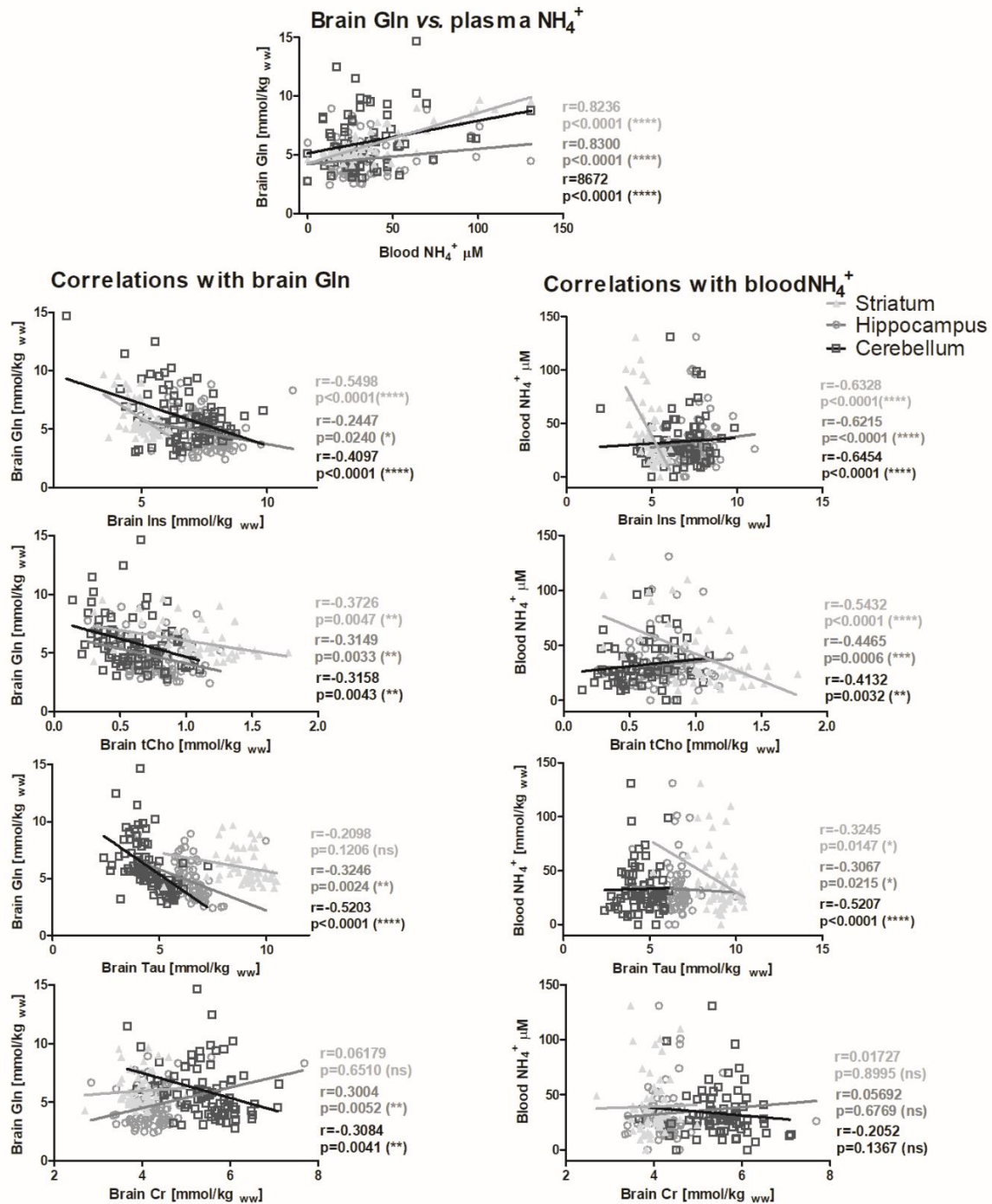
Figure 3:8: Pearson correlations between brain metabolites (Gln, Ins, tCho, Tau and Cr) and blood NH₄⁺ throughout the full course of the study for striatum, hippocampus and cerebellum. The corresponding *p* values are shown along with the Pearson correlation coefficients. Statistical significance: *p<0.05, **p<0.01, ***p<0.001, ****p<0.0001.
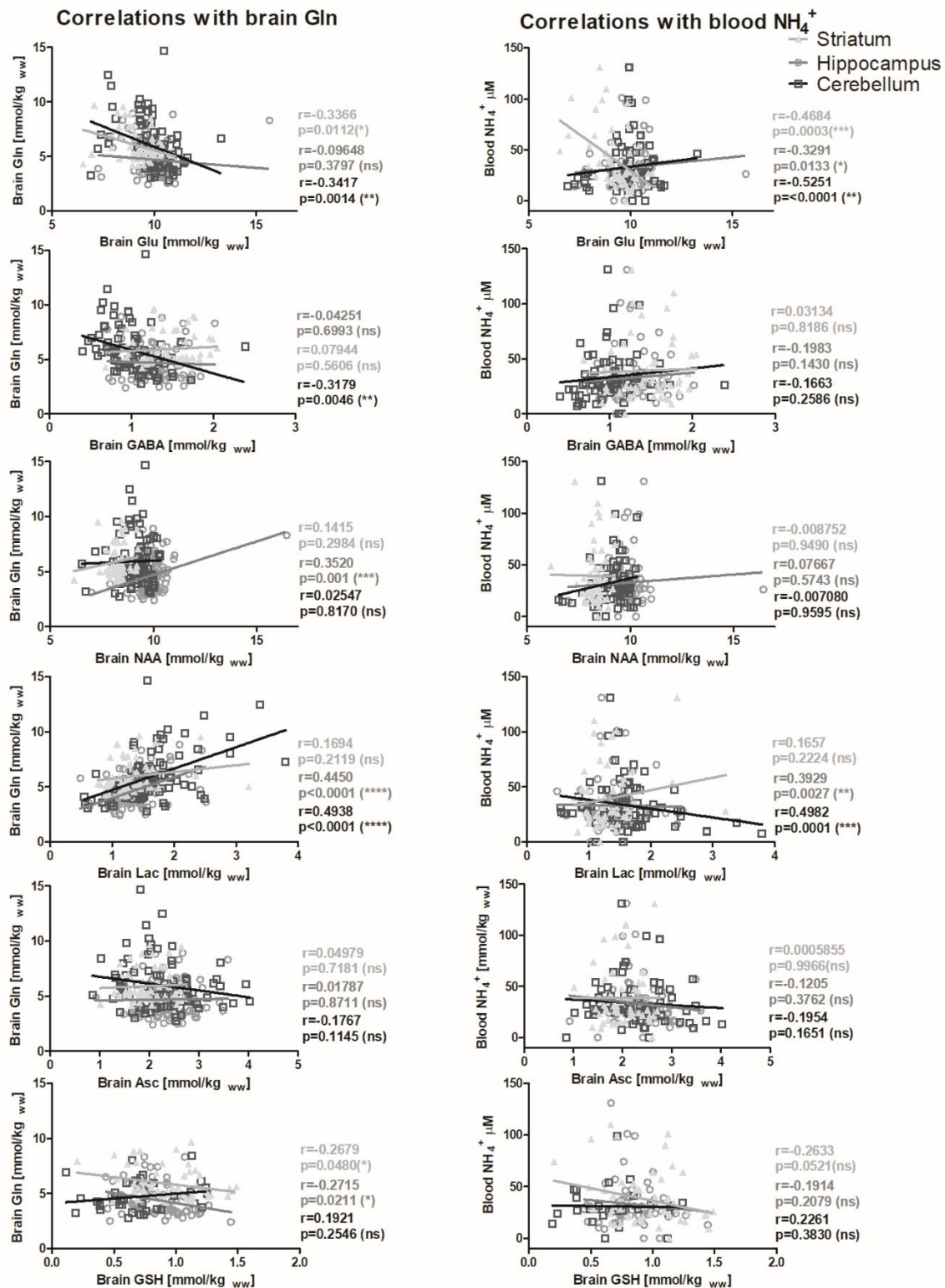
Figure 3:9: Pearson correlations between brain metabolites (for Glu, GABA, NAA, Lac, Asc and GSH) and blood NH₄⁺ throughout the full course of the study for striatum, hippocampus and cerebellum. The corresponding *p* values are shown along with the Pearson correlation coefficients. Statistical significance: *p<0.05, **p<0.01, ***p<0.001, ****p<0.0001.

3.2.2 Study 2: Brain regional vulnerability – histology measurements

The synthesis of Gln in the brain is mostly limited to astrocytes (site of glutamine synthetase activity[64], see section 3.1.1). Brain edema (excessive accumulation of fluid in intracellular or extracellular space) is commonly proposed as a pathological process occurring in HE[17]. It was suggested that astrocytes swelling and/or "Alzheimer type II astrocytosis" due to increase osmotic pressure triggered by Gln accumulation[65,66] (Gln acting as an osmolyte driving water into the cells[67]) is behind the clinical manifestation of HE. While this is true in case of the acute HE (HE as a consequence of acute liver failure) where the osmotic pressure is very strong and rapid, in type C HE ^{1}H MRS studies have shown a gradual release of brain osmolytes as an osmotic response[15,17,68] to compensate for Gln increase (section 3.1.1). Therefore, it was proposed that brain edema is not often present in case of type C HE[4]. This proposition is furthermore confirmed by the contradictory findings on astrocytes swelling or edema in humans and animal models using different MRI or ex-vivo techniques[17]. Even though the evidence of edema in type C HE is not conclusive, the exposure to increased ammonium (and consequently Gln leading to osmotic stress) together with a synergistical action of oxidative stress combined with systemic and central inflammation are still a burden for astrocytes and can induce alterations in their morphology and function[14], as we have previously shown in hippocampus of BDL rats[14]. Moreover, in addition to astrocytes, changes in morphology of neurons have sometimes been reported in type C HE and connected with the observed motor and intellectual impairments[47,69]. However, these data are sparse and sometimes controversial.

In the previous section (3.2.1) we described the evolution of metabolic profile during type C HE in three brain regions, giving a global description of metabolic alterations in the disease (BDL rat model of CLD induced type C HE). The observed changes in metabolic concentrations can cause or be a consequence of alterations in astrocytic and neuronal functions and potentially their morphology. Therefore, to put the previously reported metabolic changes into a wider context, in this sub chapter we aimed to investigate for the first-time changes in cell morphology throughout the disease evolution (using histology measurements) and to relate these changes to the observed metabolic alterations.

3.2.2.1 Materials and methods

BDL rat model of CLD

All experiments were approved by the Committee on Animal Experimentation for the Canton de Vaud, Switzerland (VD3022/VD2439). Wistar male adult rats (125-150g, Charles River Laboratories, L'Arbresle, France) were used and underwent BDL surgery as described in[55] (the same procedure as in section 3.2.1.1).

Histology measurements

Immunohistochemistry (IHC): Mouse monoclonal anti-GFAP (glial fibrillary acidic protein, MAB360 Merck Millipore) (2 hr at RT) at 1/100 dilution with secondary Alexa Fluor® 594-AffiniPure Rat Anti-Mouse IgG (Jackson ImmunoResearch Europe Ltd.) (1 hr at RT) at 1 / 200 dilution antibodies were used to characterize the astrocytes morphology[14]. After the blood sampling and ^{1}H MRS scans (data presented in the previous section 3.2.1) animals were sacrificed for histological measurements at week 4 (n=3 for BDL rats) and 8 (n=3 for BDL rats, n=3 for sham-operated rats) To investigate the morphometrical changes of astrocytes the Sholl analysis was used as previously described[14] (Figure 3:10). A total number of 200 representative protoplasmic astrocytes of each group of BDL rats were randomly traced for all processes revealed by GFAP staining in hippocampus, cerebellum, striatum and thalamus.
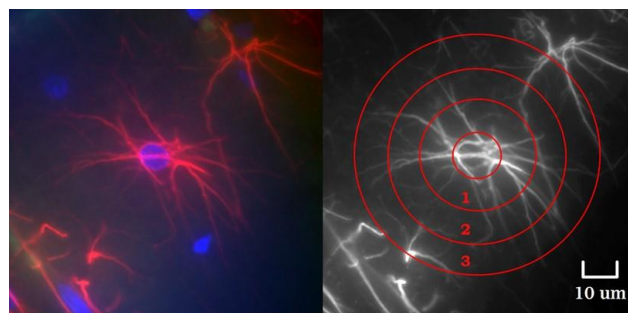
Figure 3:10: Astrocytes Sholl analysis - morphological characterization of the number of intersections of branches with radii at various distances from the cell body. Figure adapted from[14].

Golgi Cox staining based on the principle of metallic impregnation of neurons was applied to reveal the cytoarchitecture of the hippocampus, cerebellum and their detailed neuronal morphology. Extracted brains were immediately immersed in Golgi Cox staining solution and kept in the dark at room temperature for 25 days followed by PBS wash and 48h cryopreservation in 30% sucrose in PBS at 4°C. The n=3 for BDL week 8 and n=2 for sham rat brains were uniformly stained and used

for the analysis (25 slides / hemisphere). These rats were checked for the well-known pattern of CLD (increased bilirubin, NH_4^+ and brain Gln).

One-way ANOVA followed by post-hoc Turkey HSD was used to compare BDL and Sham-operated rats. All tests were 2-tailed. Significance level in all tests was attributed as follows: *p<0.05, **p<0.01, ***p<0.001, ****p<0.0001.

3.2.2.2   Results

A significant increase in GFAP+ cells and nuclei number was observed at 4 weeks post-BDL surgery in the hippocampus (+47.5%), cerebellum (+45.2%) and striatum (+30.7%) (Figure 3:11). In parallel, a decrease of astrocytes number was detected in the thalamus at week 4 reaching significance at week 8 post-BDL (-33.4%) (Figure 3:11Cup). Although a significant reduction of astrocytosis was observed at week 8 when compared to week 4 post-BDL (from +48% at week 4 to + 8% at week 8 in hippocampus, from +45% to +23% in cerebellum and from +31 to +15% in striatum, Figure 3:11Cdown) the number of astrocytes remained increased and they were altered morphologically showing a shortening and a decreased number of processes, significant already at week 4 in all the brain regions and continued to be more pronounced at week 8 post-BDL (Figure 3:12B). Sholl analysis[70] of GFAP-labelled astrocytic intermediate filaments (IMF) showed a significant time dependent decrease of the number of processes and the mean length of the IMF in all brain regions. The number of processes decreased significantly already at week 4 in hippocampus (-6%), cerebellum (-32%) and thalamus (-16%), however in striatum the decrease became significant only at week 8 (-12%) indicating that the changes in this region might be less important. The mean length of IMF showed also an overall trend of decrease reaching significance at week 4 for all the brain regions (striatum -18%, hippocampus -13%, cerebellum -17%, thalamus -3%, Figure 3:12B).

A significant decrease in the processes (IMF) intersections in the hippocampus and cerebellum was observed already at 4 weeks post-BDL (In hippocampus -27%-Ring2, -45%-Ring3 while in cerebellum -8%-Ring1) surgery and displayed an even more significant decrease at week 8 (in all 3 concentric rings, in hippocampus -14%-Ring1, -39%-Ring2, -72%-Ring3, in cerebellum -18%-Ring1, -27%-Ring2, -59%-Ring3, Figure 3:12C). No significant decrease in the number of intersections was observed for striatum and thalamus (data not shown).
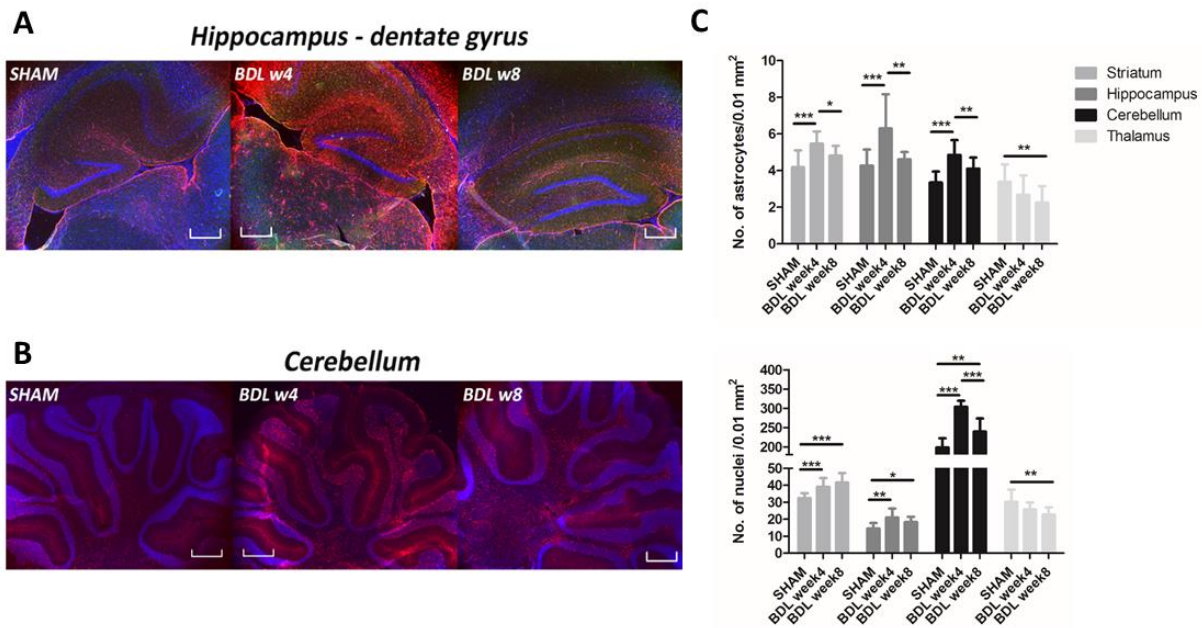
Figure 3:11: Anti-GFAP (red) and DAPI (blue) staining of hippocampus and cerebellum, and astrocyte density. Representative micrographs of double staining for anti-GFAP (red) and DAPI (blue) of **(A)** the hippocampus and **(B)** cerebellum of sham, week 4 post BDL and post 8 after BDL, and **(C)** the astrocytes density quantification at the hippocampus hilus, cerebellum granular layer, striatum and thalamus. Note the significant increase in astrocytes number at week 4 post BDL, scale bar: 500μm One-way Anova with post-hoc Tukey HSD) *p<0.05, **p<0.01, ***p<0.001, ****p<0.0001 presented as mean ± SD.

Figure 3:12: GFAP (red) and DAPI (blue) staining and astrocytic morphology analysis (A) Brain sections from Sham and BDLs rats at 4 and 8 weeks post-BDL were stained with GFAP (red) and DAPI (blue) (hippocampus and cerebellum). **(B)** Astrocytic processes (left panel) were quantified according to the process lengths (right panel) **(C)** and the number of intersections across the indicated rings from the center point of the cell body (Sholl analysis). A total number of 70–100 representative astrocytes (per rat) from BDLs and

Sham rats were randomly traced for all processes revealed by GFAP staining and plotted according to subregions (1-3) (Figure 3:10) (One-way Anova with post-hoc Tukey HSD, *p<0.05, **p<0.01, ***p<0.001, ****p<0.0001 presented as mean ± SD).

Golgi-Cox staining showed a significant increase in CA1 (67%) and DG (54% - data not shown) neuronal soma surface and a significant loss of dendritic spines density in CA1 ~49% (apical and basal) and dentate gyrus (DG) ~43% (apical – data not shown) in hippocampal neurons (Figure 3:13A). In contrary to hippocampal neurons, Purkinje cells showed a significant decrease of the neuronal soma surface (-22%) and dendritic spines density depletion of (-24%, apical Figure 3:13B).
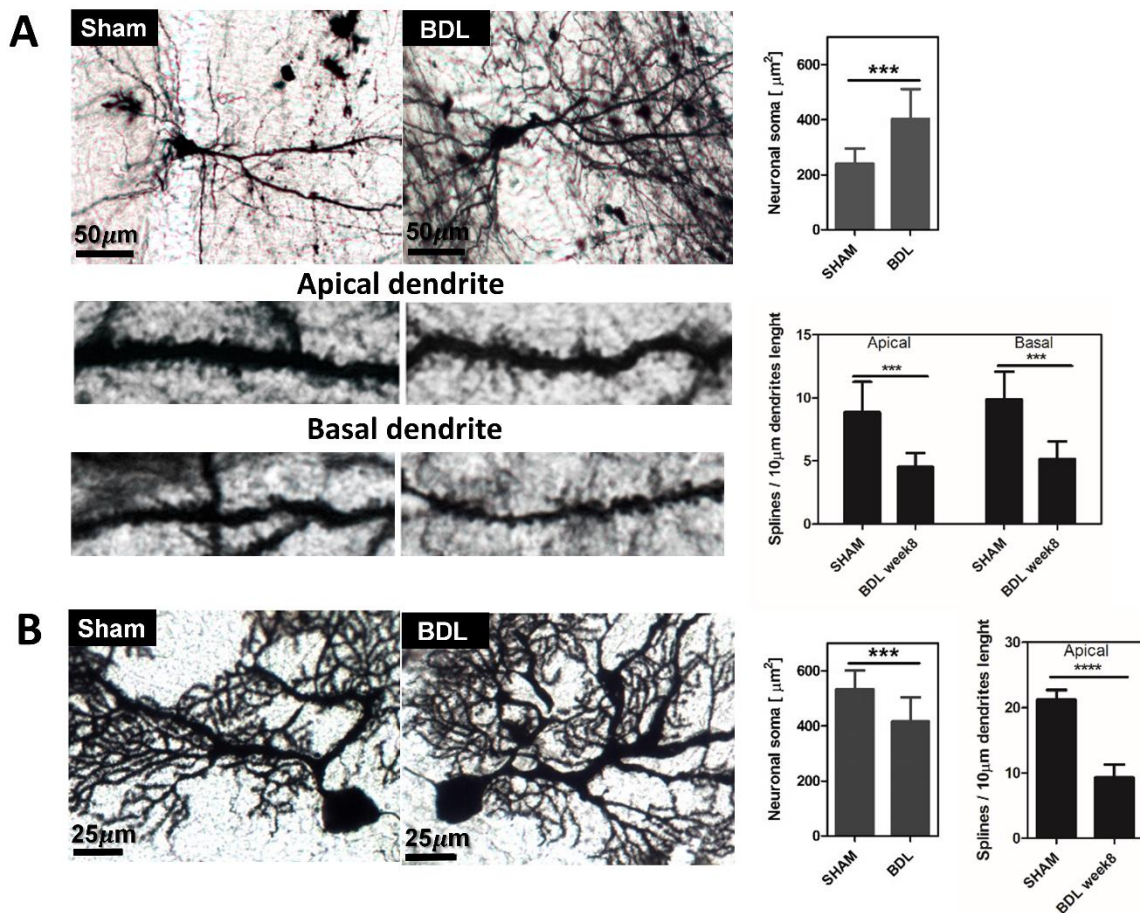
Figure 3:13: Golgi-Cox staining and neuronal morphology analysis for hippocampus and cerebellum. Hippocampus and cerebellum: A representative photomicrograph of histological sections of Golgi-Cox staining and neuronal morphology analysis of **(A)** pyramidal CA1 neurons of SHAM (left panel) and BDL rat (right panel) and **(B)** Cerebellum Purkinje cells SHAM (left panel) and BDL rat (right panel). Data are presented as mean ± SD and statistical significance (One-way Anova with post-hoc Tukey HSD): *p<0.05, **p<0.01, ***p<0.001, ****p<0.0001.

3.2.3 Study 3: CNS and systemic oxidative stress in a BDL model of type C HE

3.2.3.1 Introduction

It is becoming more accepted that OS plays an important role in development and acceleration of type C HE (section 3.1.3). The disease toxic molecules which include ammonium and inflammatory cytokines can induce oxidative/nitrosative stress and trigger a self-amplifying loop of harming events (sections 3.1.1, 3.1.2, 3.1.3). The presence of systemic OS was previously shown in BDL rats[71] and the OS was pointed out as a feature of HE[72]. Moreover, we showed changes in the main brain antioxidants (Asc and GSH – section 3.1.3) suggesting that there is an oxidative imbalance which in turn leads to OS. However, the direct evidence of OS and its impact on CNS during type C HE is still limited.

ROS in the biological systems have very short lifetimes (ranging from nanoseconds to seconds) making their direct in vivo detection very difficult. Therefore, probes/traps are used in biological milieus that react rapidly with ROS (competing with antioxidants) creating a stable radical which can be measured and quantified (see section 3.2.3.2). The stable radicals are measured using EPR a unique analytical technique which allows for a reliable detection of ROS yielding quantitative data. Therefore, in the present section we aimed to measure the time course of CNS and systemic OS using ex vivo (brain tissue) and in vitro (blood) EPR spectroscopy to further elucidate the role of OS in type C HE.

3.2.3.2 Method - Electron Paramagnetic Resonance Spectroscopy for CNS and systemic OS measurements

BDL rat model of CLD

All experiments were approved by the Committee on Animal Experimentation for the Canton de Vaud, Switzerland (VD3022/VD2439). Wistar male adult rats (125-150g, Charles River Laboratories, L'Arbresle, France) were used and underwent BDL surgery as described in[73] (the same procedure as in section 3.2.1.1) or a sham surgery (control animals). Animals were sacrificed for EPR measurements at week 2, week 4, week 6 and week 8 after ^{1}H MRS measurements (data presented in the previous section 3.2.1). The number of rats used for each experiment is highlighted in the next sections.

Electron paramagnetic resonance – basic principles

EPR is an experimental technique used to detect and characterize chemical systems containing one or more unpaired electrons. In contrast to NMR (Chapter 1) which is sensitive to nuclear magnetization, EPR is based upon the behavior of an unpaired electron in the magnetic field. When an electron is placed in an external magnetic field, the field interacts with its magnetic moment and breaks the degeneracy of electron spin energy level (splitting), phenomenon known as Zeeman Effect, causing it to align parallel or antiparallel to the field direction. The electromagnetic irradiation at a frequency which matches the difference between the described energy levels, results in a resonant transition from the lower spin energy level to the upper one (absorption). The spectroscopic detection of this transition (EPR signal) is the fundamental principle of EPR. This technique has its application in various fields including the detection of organic free radicals and transition metal ion compounds in biological systems[74]. EPR is considered to be one of the most powerful tools for qualitative and quantitative analysis of ROS in biological milieus[75,76]. A direct detection of ROS is almost impossible because of their short lifetime. As such the EPR spin-trapping technique allows the detection of these short-lived radicals. The main principle is a reaction of the radical with a non-radical molecule (spin trap) to form a product (spin adduct) which is long lived and can be directly detected[75,76] (Figure 3:14A). The spin adduct usually has a hyperfine splitting which gives a characteristic EPR signal (Figure 3:14B). From the time evolution of this signal one can calculate the rate of radical formation. This method gives the possibility to characterize biological samples from the radical formation point of view[77].

Brain tissue preparation

Two EPR studies were performed. We first measured the OS in cerebellum and hippocampus at 6-weeks post-BDL (BDL: n=3 and SHAM: n=3). Then a pilot longitudinal study was performed only in the hippocampus at week 2 (BDL n=2, SHAM n=2), 4 (BDL n=2, SHAM n=2), 6 (total: BDL n=5, SHAM n=5) and 8 post-BDL (BDL n=2, SHAM n=2) to identify early and longitudinal changes in OS.

Rats were pre-anesthetized with 4% isoflurane for 5 min followed by subcutaneous injection of the analgesic (Temgesic, 0.03 mg/ml in 0.9% NaCl) and perfused with cell culture medium RPMI 1640 (pH 7.4, Sig-ma), supplemented with 10% of Fetal Bovine Serum (FBS, Sigma) and 1% of antibiotics (50.5 units/ml penicillin, 50.5 µg/ml streptomycin and 101 µg/ml neomycin, Sigma) to wash out blood and keep the brain cells alive. To preserve cells viability after extraction, the cerebellum, right

and left hippocampi were weighted and immediately transferred into a 5ml Eppendorf tube with whole RPMI-1640 medium immersed in ice. Afterwards, tissue was sliced into small pieces, transferred into a 2ml syringe with whole RPMI-1640 medium and 10mM CMH (cyclic hydroxylamine 1-hydroxy-3-methoxycarbonyl-2,2,5,5tetramethyl pyrrolidine hydrochloride) cell-permeable spin-trap (Noxygen Science Transfer & Diagnostics GmbH) and incubated at 37°C. After each incubation time (1h of incubation with 6 time points) ~50µL of cell suspensions were transferred into 1.5mm ID and 1.8mm OD quartz capillary tubes (VitroCom, USA, sample height of 25mm) and sealed with Leica Critoseal™ (Leica Microsystems GmbH) for further EPR measurements.

Blood sample preparation

Blood samples were withdrawn from the sublingual vein before BDL or SHAM surgery and post-surgery at weeks 2, 4, 6 and 8 (BDL n=4, SHAM n=2, per time point). 1mL of blood was collected into sterile tube pretreated with EDTA (ED2P Sigma, 1.5 mg/mL) and mixed with cyclic hydroxylamine 1-hydroxy-3-methoxycarbonyl-2,2,5,5tetramethyl pyrrolidine hydrochloride (CMH) spin-trap. The final CMH concentration was 10mM. Prior to EPR measurements, the blood samples were incubated for 1h, during which, at equal intervals (6 time points), six aliquots of ~7µL were collected and transferred into 0.7mm ID and 0.87mm OD quartz capillary tubes (VitroCom, USA, sample height of 25mm) and sealed with Leica Critoseal™ (Leica Microsystems GmbH).

EPR measurements

EPR spectra were collected at room temperature (RT) using an X-band EPR spectrometer, Model ESP300E (Bruker-BioSpin, Karlsruhe, Germany) equipped with a standard rectangular TE$_{102}$ cavity. For each experimental time point of ROS detection with CMH, two-scan field-swept EPR spectra were recorded. The instrumental setting for brain tissue and systemic OS detection were: microwave frequency ~ 9.78 GHz, microwave power 2 mW, sweep width 100 G, modulation frequency 100 kHz, modulation amplitude 0.5G, receiver gain 5x10^3, time constant 40.9 ms, conversion time 81 ms.

The double-integration of EPR traces yielded the total EPR signal intensities of the paramagnetic, i.e. oxidized form, of the CMH spin-trap. Subsequently, the actual intracellular concentrations of the CMH-related signals (Figure 3:14B) were calculated using 1mM TEMPOL sample as a reference. The

ROS generation rates were calculated from EPR kinetic plots (EPR signal levels versus the elapsed time), normalized to the tissue weight and averaged (presented as mean ± SD).
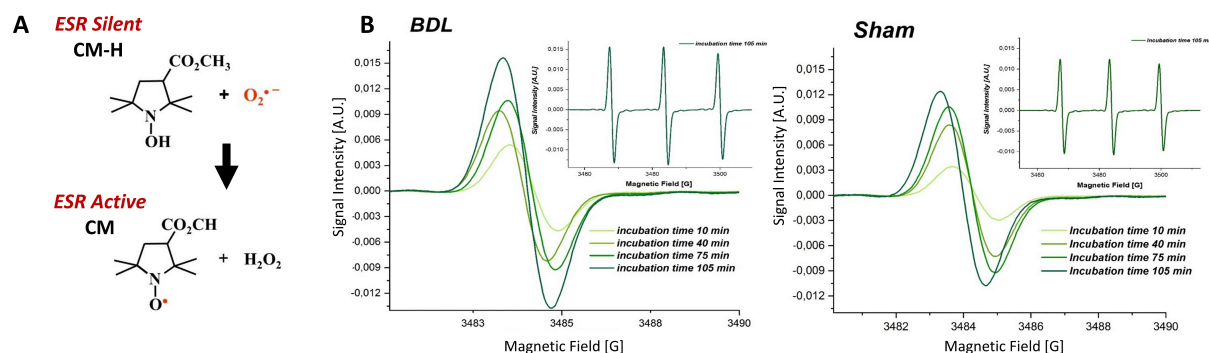
Figure 3:14: Characteristic EPR signal of CMH spin-trap. (**A**) The characteristic reaction of CMH spin-trap with the superoxide radical to form an EPR active spin adduct. (**B-left) Insert**-Characteristic signal (hyperfine splitting) for CMH spin trap in hippocampus of a BDL rat (week 6 - last time point at 105min of incubation). Blow up on one line to observe the signal intensity increase over incubation times. (**B-right) Insert**-Characteristic signal (hyperfine splitting) for CMH spin probe in hippocampus of a Sham (control) rat (week 6 - last time point at 105min of incubation). Blow up on one line to observe the signal intensity increase over incubation times. It can be observed how the signal intensity is stronger for the BDL rat indicating stronger radical formation at the same time points.

3.2.3.3 Results

The release of intracellular $O_2^{\cdot-}$ was evaluated and quantified using the EPR CMH cell-permeable and non-toxic spin-trap (Figure 3:14) on in vitro blood and ex vivo hippocampus and cerebellum samples.

CNS OS

A significant increase in relative OS (compared to sham operated animals at the same time point) was observed in BDL rats at week 6 in both cerebellum and hippocampus (Figure 3:15). This increase was similar among the two brain regions (~42%, for hippocampus 103.6±19.1μM/g/min (L+R m=0.142±0.01g) vs. 73.5±16.3μM/g/min (L+R m=0.175±0.03g) and ~42%, for cerebellum 136.8±22.7μM/g/min (m=0.290±0.02g) vs. 96.2±27.4μM/g/min (m=0.298±0.02g)). There was, however, a significant difference for the baseline redox state of the sham operated animals between hippocampus and cerebellum (~31%, at 6 weeks after surgery, Figure 3:15).

The longitudinal EPR measurement in hippocampus revealed a significant increase of the OS (intracellular $O_2^{\cdot-}$) already at 2 weeks post BDL (+63%) which continued to increase until week 8 (Figure 3:16A). Note that sham operated animals showed a physiological pattern of age-related increase CNS redox state (a trend of increase in intracellular $O_2^{\cdot-}$, Figure 3:16A). Pearson correlation coefficients were used to highlight the dependency of the increased hippocampal OS with previously

measured parameters (NH_4^+, Gln and Asc, Figure 3:16B). The increase of hippocampal OS showed a significant positive correlation with the increase in hippocampal Gln and blood NH_4^+ (section 3.2.1.2). Additionally, the measured increase in OS showed a significant correlation with decrease of the antioxidant Asc (section 3.2.1.2).
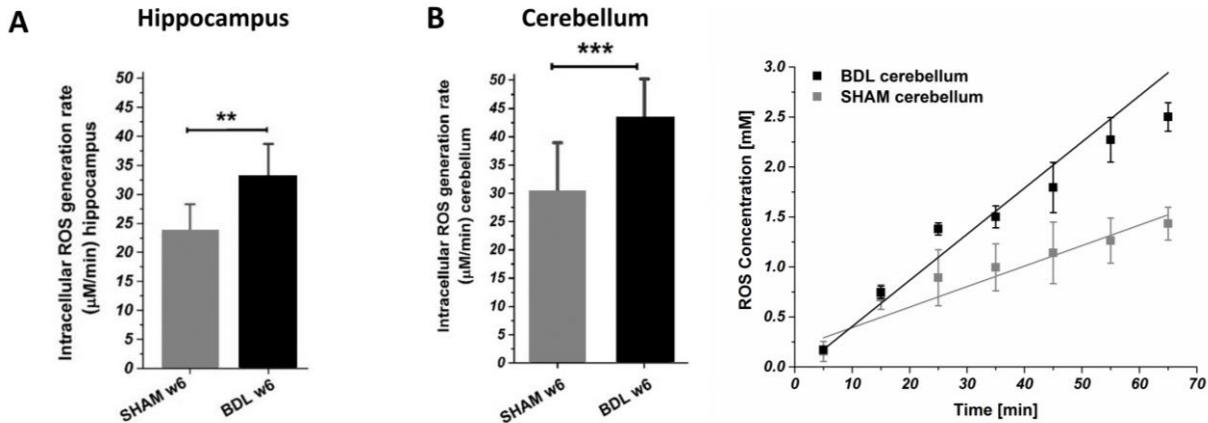
Figure 3:15: CNS OS (A) OS detection in the hippocampus at week 6 for BDL operated vs sham operated animal. **(B)** OS detection in the cerebellum at week 6 for BDL operated vs sham operated animal. The ROS concentration rate kinetic at weeks 6 (left) in the cerebellum of sham vs BDL rats (every point is obtained by integration of the signal shown in Figure 3:14 and referenced to 1mM TEMPOL as explained in 3.2.2.1)
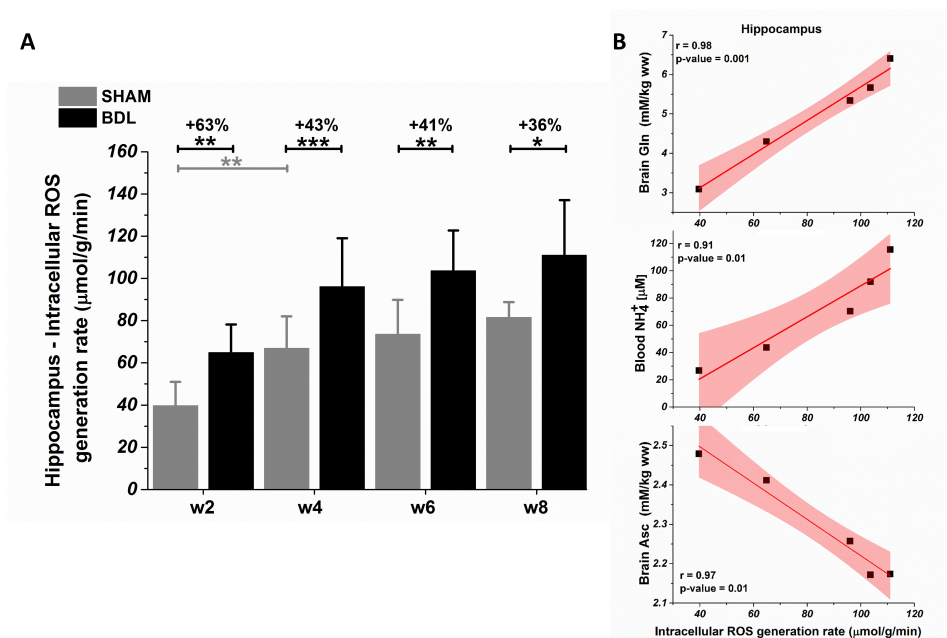
Figure 3:16: Longitudinal OS in the hippocampus (A) Longitudinal OS detection in the hippocampus from week 2 to 8 post-BDL compared to the sham operated animals at every time point (sham operated animals show a physiological pattern of age-related increase CNS redox state). **(B)** Pearson correlations showing a very strong correlation between ROS generation rate in the hippocampus with brain Gln, blood NH_4^+ and brain Asc (the metabolite and blood data used for correlations were presented in section 3.2.1).

Systemic OS

An increase in blood OS was observed both after the BDL and the sham surgery (Figure 3:17). While for the sham operated animals the systemic OS stabilized at week 4 (decreased to the pre-surgery range), for the animals which underwent BDL surgery the systemic OS continued to increase (+26% at week 4, Figure 3:17), reaching significance at week 6 (+48%) and the maximum at week 8 (+60%). Once again, Pearson correlation coefficient was used to highlight the dependency of the blood OS with previously measured blood NH_4^+ (section 3.2.1.2) and showed a significant correlation between the two measured parameters (increase in systemic OS and increase in blood NH_4^+, Figure 3:17).
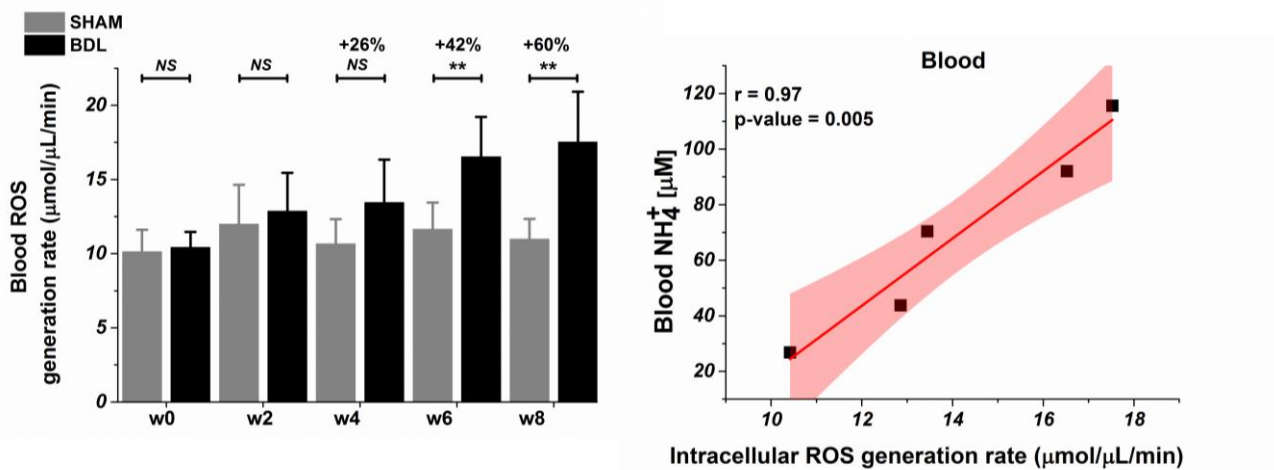
Figure 3:17: Longitudinal systemic OS. (left) Longitudinal systemic OS detection in the blood from week 2 to 8 post-BDL compared to the sham operated animals at every time point. **(right)** Pearson correlations showing a very strong correlation between ROS generation rate in the blood and blood NH_4^+ (the blood data used for correlations were described in section 3.2.1.2).

3.2.4 Discussion

3.2.4.1 Summary of main results and novelty

Brain regional differences in type C HE has been previously suspected but the published data are sparse[17]. This is the first study assessing the neurometabolic and cellular changes in three different brain regions (striatum, hippocampus and cerebellum) providing a global information on metabolic alterations caused by CLD induced-HE in a BDL rat model using a multimodal approach (in vivo ^{1}H MRS and ex vivo IHC combined with EPR). Cerebellum is pointed out as a region with the heaviest burden of Gln leading to a stronger and faster decrease of other osmolytes (Cr, Ins). Moreover, some unique changes were observed in cerebellum like an increase in GSH and Lac. In parallel the antioxidant changes were validated using ex-vivo EPR while the histological measures confirmed the

metabolic changes. Since cerebellum is not easily accessible by ^{1}H MRS in human brain and thus not deeply investigated region, these novel findings provide a new perspective on the disease and its effects on the brain. In addition, the present study assessed three brain regions, each one having a different role, providing a specific but in the same time a global overview of neurometabolic and cellular changes affecting the brain. This allows us to point out Gln, the metabolite which displays the most rapid change in all regions, as a surrogate of the disease.

3.2.4.2   Brain regions: response to NH_4^+ increase and osmotic stress.

Cerebellum

It is commonly accepted that increase of blood NH_4^+ causes a rise in brain Gln (see section 3.1.1). This rise was observed already at 2 weeks after BDL surgery in cerebellum and continued thought the course of the disease. Although Gln increase, as a first observable metabolic change, was present in all the studied brain regions, it reached its maximum in cerebellum (+ 134%, Figures 3:3 and 3:4). A higher cerebral blood flow (CBF) for basal ganglia and cerebellum as compared to cortical areas has been previously shown in cirrhotic patients[52]. Furthermore, it has been observed (in the same study) that for cirrhotic patient's cerebellum has the highest ammonium extraction factor. Therefore, cerebellum seems to be the region predominantly exposed to ammonium (followed by basal ganglia)[52]. The strongest burden of ammonium could be one reason for the highest increase of Gln in this brain region. In parallel, there is evidence that neuroinflammation occurs very early in the disease evolution and is also stronger in the cerebellum[48,51], something we also confirmed in a study performed during my PhD (the highest increase in IL-6 at week 4 post-BDL in cerebellum)[1]. It can be suggested that the high CBF in the cerebellum makes this brain region more exposed to ammonium and inflammatory cytokines among other deleterious molecules of the disease. Alternatively, higher ammonium burden would play in hand to higher inflammation and vice versa since it was proposed that these two mechanisms act synergistically making the brain (e.g. cerebellum) more susceptible to each other's effect[7,23], proposed also by a study performed during my PhD[1].

A heavy load of Gln in astrocytes lead to an osmotic imbalance which resulted in gradual decrease of other brain osmolytes (Ins, tCho, Tau and Cr, Figure 3:3 and 3.4). Tau showed a consistent and significantly stronger decrease in the cerebellum than in the other brain regions (confirmed by the STATIS analysis, Figure 3:7up). This decrease was strongly correlated with the Gln increase,

suggesting that even though Tau is present in both glial cells and neurons[78], its role in astrocytic osmoregulation is most probably dominant in this brain region. Cr also showed a higher decrease, confirmed by its high contribution to the variance in the STATIS analysis of the cerebellum data. It can be proposed that due to the high load of Gln, it is likely that Cr also assumes its osmoregulatory role. Additionally, the high exposure to NH_4^+ can cause an inhibition of Cr synthesis in the CNS which could also be a contributing factor to the decrease of this metabolite[79].

The STATIS analysis performed on the brain metabolites combined with blood parameters showed that Gln is driving the variance of the dataset very similarly to NH_4^+ and bilirubin (Figure 3:7down). This result corresponds to gradual but strong increase in concentrations of these factors observed thought the disease. Since NH_4^+ to Gln conversion is most probably the main source of brain Gln, the above described results confirm that NH_4^+ increase in the blood induces a very rapid cascade of events causing a stress in the CNS (e.g. Gln increase).

Hippocampus

The results obtained in the present study for hippocampus display a common pattern with previously reported results[14]. A strong rise in Gln concentration was observed already early in the disease evolution (week 2 and 4) and continued to rise until week 8 (reaching a 100% increase, Figure 3:2), making hippocampus a second (in terms of magnitude of Gln increase) brain region affected by Gln increase after cerebellum. Brain Gln was strongly correlated with blood NH_4^+ (Figure 3:8). The strong increase in brain Gln towards the end of the disease lead to a significant decrease of brain osmolytes (Ins, Tau, tCho and Cr). Ins showed the strongest absolute decrease (-1.3 mmol/kg$_{ww,}$ Figure 3:3) followed by Tau, tCho and Cr. The strongest change in Ins is supported by the fact that this molecule is predominantly located in the glial cells having the main function of an osmolyte[80]. Moreover, a strong decrease is also observed for tCho (-38% at week 8, Figure 3:2) which is, together with Ins, considered to be glial marker and changes in the diffusivity of this metabolite where connected with microglial reactivity[81]. All the osmolytes showed a significant correlation with brain Gln and blood NH_4^+ (except Cr in the case of NH_4^+, Figure 3:8).

Striatum

A significant Gln increase was also observed in striatum and it correlated with blood NH_4^+ (Figure 3:8). However, the pattern of Gln increase was different in this brain region compared to the other

studied regions. While in cerebellum and hippocampus Gln was consistently increasing over the disease progression (peaking at week 8 post-BDL), the Gln concentration increase started to decelerate at week 4 in striatum (absolute increase of Gln concentration from week 0 to 4 was +1.96 mmol/kg$_{ww}$, while from week 4 to week 8 only +0.35 mmol/kg$_{ww}$). Interestingly the main CNS osmolytes continued to strongly decrease even after week 4 post-BDL (sum of osmolytes decrease from week 0 to 4 was -1.26 mmol/kg$_{ww}$, while from week 4 to week 8 an additional -2.98 mmol/kg$_{ww}$, Figure 3:3B). Even though there was a smaller Gln induced osmotic pressure (than in e.g. cerebellum) Tau showed a strong and significant decrease starting from week 4 post-BDL (Figure 3:3). This behavior can be explained as a delayed osmotic response or suggest that Tau assumes an additional role to the osmoregulatory one (supported also by a significant correlation of Tau with NH_4^+ but not with Gln, Figure 3:8). Tau is localized in both neurons and glial cells, and apart from it being an osmoregulatory molecule it was proposed as a neurotransmitter or neuromodulator and an antioxidant[82]. It was shown previously that Tau plays a role in striatal plasticity, and exerts a neuroprotective role under metabolic stress. In addition, Tau deficiency was shown to cause modifications of neuronal GABA$_A$ receptors and therefore alter GABAergic neurotransmission in striatal cell cultures[83]. Decrease of Tau was shown in the extracellular space of rat striatum during hepatic failure and attributed to Tau redistribution as a cell-protective response[84]. Therefore, a strong change in Tau has important molecular implications in this brain region. In addition to Tau, tCho showed the strongest and significantly different decrease in striatum. Apart from its osmoregulatory role tCho is associated with cellular membranes[85] as it is required for membrane phospholipid synthesis and myelination, therefore its strong decrease could be considered as a sign of neurodegeneration. Choline is also a precursor in acetylcholine synthesis, and striatum is a region which normally contains high levels of acetylcholine mainly coming from striatal cholinergic interneurons. Potential alterations in acetylcholine concentrations due to tCho decrease can have strong pathological consequences on striatal physiology[86].

Astrocytic and neuronal morphological changes in presence of osmotic stress

It is suspected that the osmotic stress due to the Gln increase and the release of main CNS osmolytes as reported in this study in the 3 brain regions will affect astrocytes morphology. While some astrocytic morphological changes have been previously reported[17,20], there are very few studies of the neuronal changes. Some past studies have even reported the presence of brain edema and astrocytes swelling in type C HE but the results till date are controversial[17,87–89] mainly due to limitations

related to studies in cell cultures, fixation and post-mortem changes[90]. To investigate the potential effects of the observed osmotic stress on cellular morphology, we preformed the first concomitant and detailed longitudinal assessment of astrocytic and neuronal morphological changes in type C HE.

In the present study, a significant decrease in the number of astrocytes processes was observed at 4 weeks post BDL surgery (hippocampus, cerebellum and thalamus), while in striatum this change reached significance only at the end point of the disease (week 8 post-BDL).Astrocytes modulate neuronal circuits by controlling the energy homeostasis using their morphological plasticity to re-model processes[91,92]. Therefore, processes shortening, and intersection number decrease in addition to increased levels of NH_4^+ and Gln as measured herein could contribute strongly to CNS function decline.

Astrocytes are responsible for a variety of fundamental functions. They are involved in neurotransmitter metabolism - uptake of Glu and GABA, provision of nutrients from blood vessels, ion homeostasis maintenance, process of neuronal migration, promotion of myelination as well as formation and regulation of the blood-brain barrier, maintenance and pruning of the synapses, formation of the gap junctions, vasomodulation in response to neuronal activity and scar formation[93–95]. In response to brain injury and/or inflammation astrocytes become reactive and show changes in their roles and morphology. Of note, our previous results showed the presence of systemic and central inflammation in BDL rats[1]. The roles of reactive astrocytes comprise scar formation and inhibition of the inflammation spreading to protect neurons[94]. However, when astrocytes remain reactive and unable to repair, they became deleterious to the surrounding neurons and cause dysfunction of the CNS [96]. Researchers argue that HE is a disorder of astrocyte function. GFAP, an intermediate filament expressed in astrocytes is responsible for both cell motility and cytoskeleton stability [97]. It has been shown that GFAP expression decreases with HE progression and the influenced morphology alters the astrocytes function [89,98], in agreement with our previous results in hippocampus of BDL rats[14].

Although, the relative % change of GFAP+ cells number was quite similar for hippocampus and cerebellum, +47.5% vs. +45.2% respectively, the overall response to the disease progression was different in striatum with only +31% increase and in thalamus where a decrease in GFAP+ was

measured. Therefore, brain regional difference to type C HE onset observed for astrocytes shows striatum as a region having a different behavior to type C HE. In parallel, it is known that there is significant difference between brain regions and baseline astrocytes density[93,95], which was also confirmed in this study as shown for sham operated rats. This change of GFAP+ astrocytes is a hallmark of its reactivity and could be related to the stimulation of mature astrocytes and reentering into proliferation cycle which is a common feature in various neuropathological disorders[99,100]. The astrocyte activation is an important element of brain immune response which may significantly compromise the thiol antioxidant capacity[101]. It was demonstrated that oxidative stress plays an important role in astrocytes and that by increase of GSH concentration, as we observed in the cerebellum of BDL rats (+85% at week 8, section 3.2.1.2), they try to overcome the increased formation of ROS[101] (see also section 3.2.3.3). To maintain their antioxidant system neurons relay on the GSH freed by astrocytes. Therefore, chronic astrocytes activation combined with the presence of oxidative stress as shown herein (sections 3.2.2 and 3.2.3) could contribute to the inability of adequate supply of GSH to neurons.

Decrease of spine densities in V layer of cortical (~30%) and hippocampal CA1 (~37%) pyramidal neurons has been previously shown in BDL rats at week 4 post-surgery [102]. Here we report even more pronounced changes of the hippocampal and cerebellar neurons morphology at week 8 post BDL. Our data shows for the first time a significant and brain differential change in soma surface size of hippocampal CA1 (+67%) and DG (+54%) and of the cerebellar Purkinje cells (-22%) neurons. A much stronger decline of the spine's density was also depicted, reaching ~49% for CA1 (basal and apical), ~42% for DG and ~24% Purkinje cell. Numerous studies have shown that neurons change their morphology under a variety of physiological and pathophysiological conditions, like dendritic spine turnover and remodeling, change of shape and size of soma as well as structural changes of dendrites[103]. Astrocyte processes sheath all neuronal soma, dendrites, and synapses. The ensheathment varies in brain regions, which is related with specific astrocytic-neuronal interactions [103]. Spines are a major substrate of brain plasticity and serve as the postsynaptic component for the vast majority of central nervous system excitatory synapses. Their numbers and shape are regulated by both physiological and pathological events, therefore decreasing dendritic spines density can contribute to the memory decline and cause cognitive dysfunction[104,105] in type C HE patients. The

alterations of dendritic morphology due to metabolic-degenerative disorders are often associated with cognitive impairment as in mental retardation[106].

3.2.4.3 Energy metabolism and neurotransmitters

Cr and PCr are metabolites involved in energy metabolism. A tendency of decrease in Cr and tCr was observed in all the brain regions being in agreement with previously reported result in hippocampus[14]. The decrease of Cr was significantly stronger in cerebellum confirmed by its higher contribution to the 1st axis of STATIS analysis in this brain region (Figures 3:3, 3:4 and 3:7). A harmony between Cr and PCr influences the high-energy phosphate metabolism of the brain[107], and alterations in ^{1}H MRS detectable tCr were connected with several neuropsychiatric disorders[108,109]. Since Cr in the brain is synthetized in the glial cells it is transported to neurons via creatine transporters and most of the brain's creatine transporter proteins are produced in the cerebellum[110,111]. It was shown, in the rat brain, that Cr measured by ^{1}H MRS positively correlates with creatine transporter protein density[107]. Therefore, alterations in Cr concentrations in the brain whether caused by osmotic stress or Cr synthesis inhibition can potentially alter neuronal energy metabolism. In addition to Cr and PCr, another metabolite involved in the brain energy metabolism is Lac. The behavior of Lac was significantly different in cerebellum then in the other brain regions. Lac peaked in cerebellum at week 8 (+84%), a unique change which was additionally confirmed by its higher contribution to the 1st axis of STATIS analysis (Figures 3:3 and 3:7). The previously published results of Lac changes are contradictory. An ex-vivo study performed on BDL rats reported a big increase in Lac playing a role in pathogenesis of CLD and edema[87]. Another study reported a decrease of Lac in the extracellular space in the cortex which would point towards its intracellular accumulation [112], however recent data measured in our group by ^{1}H MRS report a decrease in Lac cortical concentration. In the brain, Lac is produced from the Glc metabolism via glycolysis, it is generated and metabolized by lactate dehydrogenase which can be found both in neurons and astrocytes[113]. It was proposed that Lac is produced mainly in astrocytes, then released into extracellular space to be taken up by neurons to satisfy their energy demand as an additional fuel to Glc (astrocyte-neuron lactate shuttle hypothesis)[113] and suggested that this is a possible pathway in HE leading to Lac increase. Our results show high decrease in blood Glc[114] that is significantly driving the data variance (STATIS analysis – Figure 3:7), however brain Glc could not be reliably quantified probably due to its decrease. The fact that blood-borne Glc is at the start of brain Lac production[115] suggests that the high accumulation

of Lac in the end stage of the disease could rather be a result of high neurometabolic stress in cerebellum, however further investigation of Lac metabolism in HE is needed.

A tendency of decrease (although not significant) in the neurotransmitter GABA concentration was observed in hippocampus and cerebellum, further confirmed by their contribution to the 1st axis in the STATIS analysis (Figures 3:4, 3:5 and 3:7). GABA decrease was more pronounced in cerebellum (-23% at week 8) and possible deleterious implications of this metabolite were further promoted by its significant correlation with Gln in this brain region. The function of cerebellum in motor coordination and learning is mainly modulated by extracellular GABA and GABAergic neurotransmission[48]. It was shown that neuroinflammation in HE is connected with increased levels of GABA in extracellular space and enhanced GABAergic neurotransmission and that these changes are related to impaired motor coordination[48]. Another study in patients found evidence of GABAergic inhibition in cerebellum whose degree increased with disease severity[116]. Moreover, the decrease of GABA might relate to changes in Glu and Tau which are the precursor of GABA and GABA$_A$ receptor antagonist respectively[117]. Because of the importance of GABA in cerebellum, alterations in GABA concentrations in this brain region could potentially have degrading neuropsychiatric implications. A decrease in concentration of Glu was observed in all the brain regions, being the most significant in striatum (the correlation of Glu with NH_4^+ was stronger than with Gln in striatum and hippocampus, Figure 3:9). Alterations in glutamatergic neurotransmission due to inflammation were shown for hippocampus in HE[48]. In parallel, a decreased Glu could be a consequence of an increased synthesis of Gln from NH_4^+ in astrocytes. Furthermore, NH_4^+ induced oxidative stress can cause an inhibition of Glu uptake in astrocytes[38], suggesting that multiple factors can be involved in the observed Glu decrease.

3.2.4.4   *Response to oxidative stress*

It is known that OS plays an important role in many neurodegenerative disorders and the possible implications of OS in type C HE were already described in the section 3.1.3. The UHF ^{1}H MRS gives us a unique opportunity to measure in vivo Asc and GSH, the small molecular weight antioxidants who provide a quick response to OS by rapid reactions with ROS. A significant decrease in Asc concentration and a unique increase in GSH were observed in cerebellum (Figure 3:2). This observation goes in hand with the results discussed in previous section to point out cerebellum as the region with a more affected neurometabolic profile. Asc is primarily considered as a neuroprotective

antioxidant but can also act as a pro-oxidant and neuromodulator[118]. Neurons can contain high doses of Asc and therefore exhibit high rates of oxidative metabolism[119]. Ascorbate regulates oxidative turnover and redox reactions involving this molecule drive cellular detoxification. Therefore, the observed decrease in Asc concentration could indicate the existence of oxidative imbalance. GSH has an important role in maintaining redox homeostasis as an essential factor in brain antioxidant defense[120]. GSH concertation is the highest in astrocytes[121,122] and these cells play a major role in its synthesis and transport assuming a role of neuroprotector against OS[121,122]. Increase in GSH concentration could imply a higher need for antioxidant protection. Our results demonstrate potential alterations of brain redox homeostasis in type C HE, being in agreement with previously reported important involvement of oxidative/nitrosative stress in pathology of HE[72]. However, the exact impact of OS in type C HE progression is unknow an requires further investigation as our ^{1}H MRS results are just an indirect observation for the presence of OS.

In this context, we performed a first study investigating directly the longitudinal evolution of CNS and systemic OS in a rat model of type C HE using ex vivo and in vitro EPR detection of ROS.

We observed a significant increase in $O_2^{\cdot-}$ production in hippocampus (longitudinally, Figure 3:16), cerebellum (at week 6, Figure 3:15) and blood (longitudinally, Figure 3.17). Interestingly, the increase in hippocampal OS reached significance already at week 2 post BDL, while the systemic (blood) OS only at week 6 post BDL. This rise in production od $O_2^{\cdot-}$ in BDL rats can cause an increase in H$_2$O$_2$ leading to a harmful effect on long term potentiation[123–125]. In addition, the observed pattern of increase in intracellular $O_2^{\cdot-}$ for sham operated animals confirms the increase of OS with age[126,127].

The present results are in agreement our previously measured Asc decline in the hippocampus[14] of BDL rats by *in-vivo* and longitudinal ^{1}H MRS (see also section 3.2.1.2). We observed a strong negative correlation between the increase of $O_2^{\cdot-}$ and decrease of Asc concentrations in brain of BDL rats suggesting an increased scavenging in response to excessively produced ROS (Figure 3:16). Asc reacts with the ROS (i.e. $O_2^{\cdot-}$, $NO_2^{\cdot}$) by donating a hydrogen atom and therefore forming ascorbyl radical and dehydroascorbic acid[128]. This study also showed that a higher amount of ROS at the basic level (for sham operated animals) was produced in cerebellum than in hippocampus, suggesting that this brain region could be more susceptible to OS (in agreement with the results obtained with ^{1}H MRS, section 3.2.1)[129].

Type C HE is characterized by deficits in cognitive, psychiatric, and motor function (sub chapter 3.1). Therefore, the elevated oxidative stress in cerebellum and hippocampus suggests that ROS may play an important role in brain functions disruption, and thereby providing a further link between disease progression and cognitive decline in type C HE patients.

3.2.5   Summary

Using in vivo longitudinal ^{1}H MRS we followed the evolution of metabolic profiles during type C HE in three different brain regions (striatum, hippocampus and cerebellum) in a BDL rat model providing a global description of the disease evolution in the CNS. While all the previously described changes[14] were confirmed (increase in Gln and NH_4^+, decrease of osmolytes and Asc in all brain regions), some novel brain region specific alterations were highlighted. The highest Gln increase was observed in the cerebellum resulting in a stronger decrease of other osmolytes (e.g. Tau, Ins, Cr). Moreover, energy metabolism disturbances (e.g. Lac increase), neurotransmitter changes (GABA decrease) and antioxidant alterations (GSH and Asc) were more pronounced in this brain region. Therefore, we described an increased vulnerability of cerebellum to the disease probably connected to its higher exposure to NH_4^+. Additionally, some differences in metabolic response were observed for striatum when compared to other brain regions (e.g. smaller and less accelerating increase of Gln and a strong decrease in tCho). Using the STATIS analysis on the metabolite data combined with the blood parameters we confirmed Gln as one of the main driving forces of the disease (driving the data variance) and therefore we can point it out as a surrogate of the disease. The histology results showed that the reported neurometabolic changes in combination with the previously reported inflammation (neuro and systemic)[1] affected the astrocytes reducing their capacity to remodel processes. Moreover, there was an interdependence in astrocytic and neuronal morphological changes influencing the overall activity of the neuronal network during disease progression. BDL rats showed an increased CNS and systemic OS when compared with SHAM animals, suggesting that the increase of OS is more probably a consequence of intra- and extra-cellular ROS than that of reduced antioxidants capacity. The presented results highlighted the important role of OS in type C HE, another aspect which needs further investigation and offers possibilities for potential neuroprotective strategies.

3.3 Brain regional vulnerability in the developing brain: an ^{1}H MRS study

3.3.1 Introduction

Very little is known on the effects of CLD on the developing brain. Clinical evidence suggests that the developing brain is much more susceptible to the deleterious effects of acute NH_4^+ exposure than the adult/fully developed brain[34,130]. It has been shown that significant neurocognitive (e.g. executive functioning, language skills) and motor deficits preside in children after liver transplantation and appear not to be reversible[131–133], suggesting some degree of injury or arrested development together with a potential brain regional difference. The mechanisms leading to these unique effects on the developing brain are poorly understood. Moreover, an immature BBB in early childhood[134,135] presumably contributes to this CNS development-dependent vulnerability. Additionally, in children with CLD, plasma NH_4^+ is usually highly variable and not elevated enough to explain the degree of neurocognitive impairment, suggesting that other circulating compounds may be involved.

There are very few studies performed in vivo in a developing brain during type C HE. In our group, we reported, using an animal model of CLD-induced type C HE that the hippocampus of a developing brain shows stronger metabolic changes compared to the adult one[13]. Additionally, the results presented in this thesis for the adult brain during type C HE show that cerebellum is affected differently than other brain regions (see sub chapters 3.2.1, 3.2.2, 3.2.3), suggesting a differential brain regional vulnerability which was unknown up to date. Nevertheless, how the infant or child's brain responds to the metabolic changes of CLD, what is the brain regional vulnerability to the disease, and how these mechanisms differ from those in adult patients is still not completely understood. To the best of our knowledge, there are no published studies on developing brain during CLD assessing the potential brain regional differences. Therefore, the aim of this study was to investigate longitudinally, using in vivo ^{1}H MRS, the metabolic differences between hippocampus, cerebellum and striatum of a developing brain as key brain regions involved in the disease (section 3.2.1), using an animal model of CLD-induced type C HE during CNS development.

3.3.2 Methods

3.3.2.1 BDL rat model of CLD in the developing brain

All experiments were approved by the Committee on Animal Experimentation for the Canton de Vaud, Switzerland (VD3022/VD2439). BDL surgery (accepted model of type C HE [56]) was performed on 5 male Wistar rats at postnatal day 21 (P21). The maturation of rat brain at this age approximates a 9 month- old human[136]. BDL rats were always compared to sham operated animals at the same age (n=6) in order to: (1) consider the ongoing brain development and (2) take into account the well-known brain regional differences in healthy animals and thus highlight only the brain regional difference due to disease. The study was performed until week 6, not week 8 as for the adult rats, the overall physiological state of P21 operated BDL rats started to deteriorate rapidly after week 6, therefore the study was stopped after this time point.

3.3.2.2 Biochemical measurements

Plasma bilirubin (liver parameter) was quantified on Integra and blood NH_4^+ on blood ammonium meter (PocketChem™ BA PA-4140). AST/GOT, ALT/GPT and Glc were measured using Reflotron Plus system (F. Hoffmann-La roche Ltd.).

3.3.2.3 In vivo ^{1}H MRS

Hippocampus ($2x2.8x2mm^3$), cerebellum ($2.5x2.5x2.5mm^3$) and striatum ($2.5x2x2.5mm^3$) were scanned longitudinally using in vivo ^{1}H MRS on a 9.4 T system (Varian/Magnex Scientific). First scan, as well as blood tests, were performed at week 2 after BDL and every two weeks up to week 6 (week 2, 4, 6). MRS experiments were performed using the SPECIAL sequence (TE=2.8ms) [14]. First and second order shims were adjusted using FASTMAP[137]. Metabolite concentrations were calculated by LCModel using water as reference. Seventeen metabolites were reliable quantified, but only those showing a brain regional difference as a response to the disease are presented.

In the bar plots the results were always presented as mean $\pm$ SD. The % change was calculated in comparison to the corresponding sham operated group (with the adequate error propagation calculation). The BDL group was always compared to the sham operated group using two-way ANOVA and presented in figures (*$p<0.05$, **$p<0.01$, ***$p<0.001$, ****$p<0.0001$).

3.3.3 Results and discussion

All the BDL operated rats showed increase in plasma bilirubin starting from week 2 post-BDL validating the presence of CLD (Figure 3:18A). Increase in blood ammonium was also observed for all BDL rats when compared to the sham operated animals, reaching significance at week 4 post-BDL (Figure 3:18A).

Increase in brain Gln concentration, as a response to NH_4^+ increase, was present in all three brain regions (week 6: +173% in cerebellum, +112% in hippocampus, +68% in striatum) (Figure 3:19B). This increase was significant, compared to the sham animals, already at week 4 in hippocampus and at week 6 post-BDL in cerebellum and striatum, while cerebellum showed the most pronounced increase in percentage at the end point of the disease (week 6) (Figure 3:19B). Increase in blood ammonium correlated significantly with brain Gln for all brain regions, and the correlation was stronger in cerebellum (Figure 3:18B). The strongest Gln increase in the cerebellum of the developing brain matches with the results observed in the adult brain (sub chapter 3.3) confirming that this brain region is more exposed to the precipitating factors of the disease (e.g. ammonium[52]). Moreover, Gln increase was stronger at week 6 post-BDL in the developing brain than even at week 8 post-BDL in the adult brain (+173% vs. +134% in cerebellum, 112% vs. 100% in hippocampus, 68% vs. 48% in striatum, section 3.2.1.2), suggesting an increased vulnerability of the developing brain to the insults of CLD (in agreement with the study published for P21 rats in hippocampus only[13]).
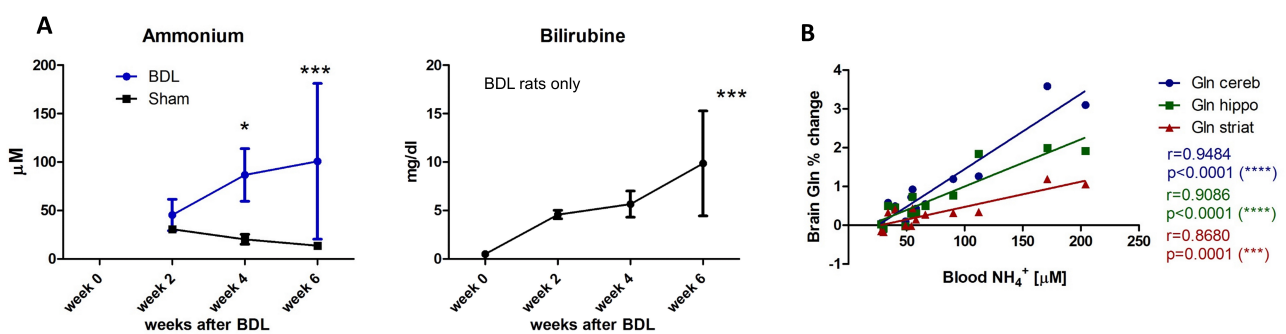
Figure 3:18: Blood parameters and correlation with Gln (P21 operated BDL rats) (A) Blood NH_4^+ in BDL (blue line) and sham (black line) operated rats at each time point (left, Two-way ANOVA) and bilirubin for BDL rats only (black line, right) **(B)** Positive correlation between increase of blood NH_4^+ in BDL rats and brain Gln percentage change of BDL rats compared to the sham rats during evolution of CLD was significant in all brain regions studied. The slope of linear regression was the steepest for cerebellum, followed by hippocampus and striatum indicating different response of these brain regions to the burden of ammonium.
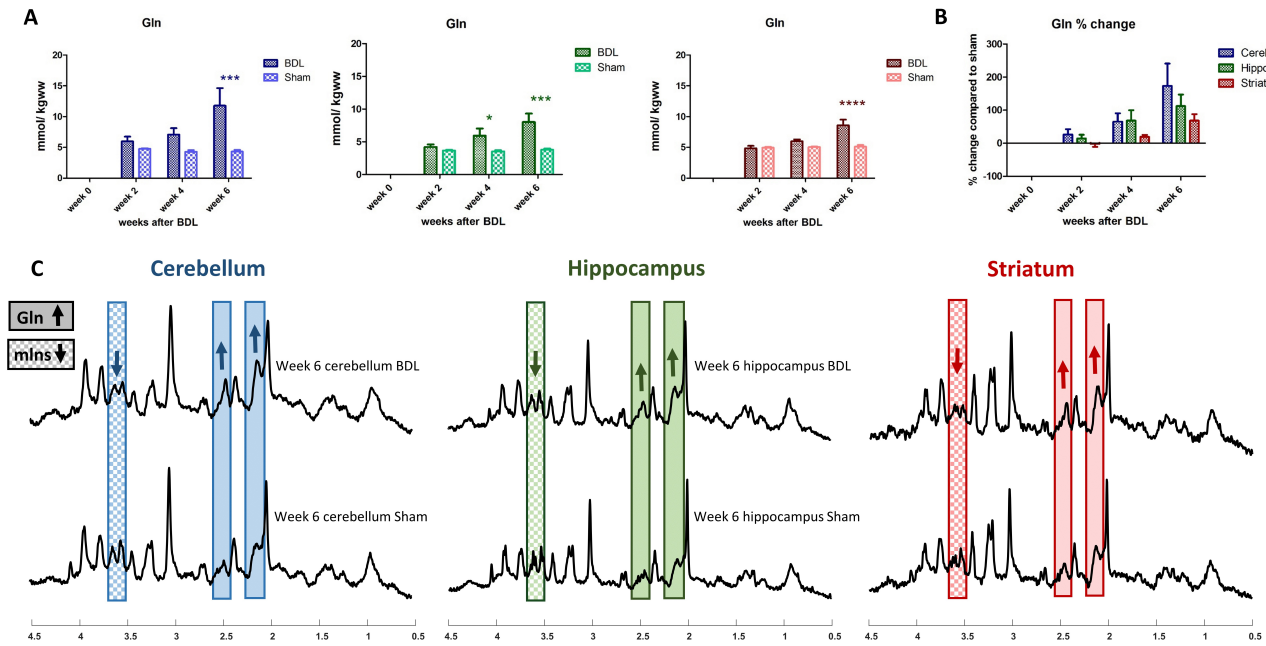
Figure 3:19: Longitudinal regional evolution of Gln and the neurometabolic profile (A) Longitudinal evolution of Gln in hippocampus, cerebellum and striatum of BDL compared to sham rats (Two-way ANOVA). **(B)** Percentage change of Gln concentration in BDL rats compared to sham operated animals at each time point. **(C)** Representative spectra from a BDL and a sham operated rat at week6 in cerebellum, hippocampus and striatum with a visible increase of Gln and decrease of mIns in all brain regions studied; (all results are shown always in blue for cerebellum, green for hippocampus and red for striatum), * significance shown always compared to the sham rats.

The main brain organic osmolytes decreased as a response to Gln increase (osmoregulation): Tau, tCr, tCho and Ins. All of them displayed a stronger decrease in cerebellum at week 6 (Figure 3:20), probably due to stronger Gln increase in this region. Interestingly, striatum of the developing brain didn't have the strongest osmolyte decrease (as observed in the adult brain, see section 3.2.1). In fact, the decrease of osmolytes in striatum doesn't fully compensate the increase of Gln (at 6 weeks post BDL: Gln +3.48 mmol/kg$_{ww}$ *vs* sum of osmolytes (Ins, Tau, tCr and tCho) -2.11 mmol/kg$_{ww}$). This result suggests that the diseased metabolic profile during development is unique and differs from the adult one.

Significant increase of Lac concentration at the end of the disease (week 6) was observed in all brain regions and again, it was stronger in cerebellum (+150% in cerebellum, +88% in hippocampus, +114% in striatum, Figure 3:20) and different from the adult brain where Lac was increased only in cerebellum. This increase correlated significantly with the increase of brain Gln and blood NH$_4^+$ for all three brain regions (data not shown). The strong peak of Lac at week 6 corresponds to the behavior of this metabolite in the cerebellum of the adult brain (peak at week 8, section 3.2.1.2). Lac is a metabolite involved in the brain energy metabolism, however previously published results on

its changes during type C HE are contradictory (see section 3.3.4.3). In the adult brain we suggested that the high increase of Lac in the cerebellum could be assigned to high neurometabolic stress in this brain region especially at the end stage of the disease (week 8, section 3.2.4.3). Thus, we can say that in the developing brain there is a strong metabolic stress in all three brain regions causing the rise in Lac at week 6, once again confirming the increased vulnerability of the CNS during development.

The neurotransmitters Glu and GABA and the antioxidant Asc showed a stronger decrease in cerebellum (Figure 3:21B). The importance of GABA and GABAergic neurotransmission for the cereberal function were already highlighted[48] (section 3.2.4.3) and changes in its concentrations were related to changes in Glu as a GABA antagonist[117]. The main role of cerebellum is in motor coordination and learning[48], therefore stronger alterations of these neurotransmitters (particularly in the cerebellum) may be connected to long term irreversible damage observed in children after liver transplantation. The observed decrease of Asc indicates a presence of OS once again highlighting its importance in type C HE.
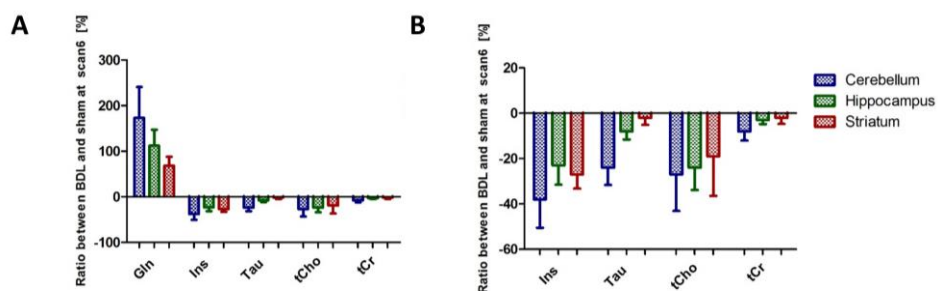
Figure 3:20: Evolution of the main brain osmolytes (P21 operated BDL rats) (A) Evolution of the metabolites in different brain regions in form of percentage change between concentrations (BDL compared to the sham rats) at scan6 (end-point of the disease) **(B)** Zoom on the evolution of the main brain osmolytes as a response to Gln increase in form of percentage change between concentration for BDL compared to sham rats at week 6 post-BDL.
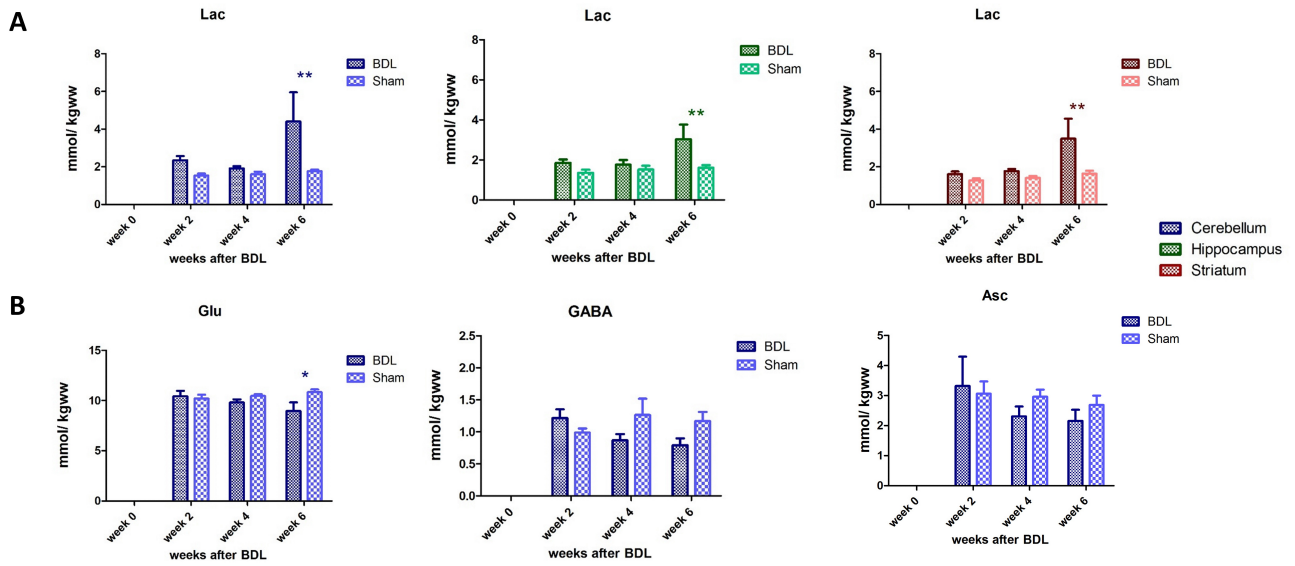
Figure 3:21: Longitudinal evolution of Lac, GABA, Glu, Asc (A) Longitudinal evolution of Lac in cerebellum, hippocampus and striatum compared with the sham (Two-way ANOVA) showing significant increase at week 6 in all brain regions studied (all results are shown always in blue for cerebellum, green for hippocampus and red for striatum). **(B)** Additional more pronounced changes in cerebellum for GABA, Glu and Asc.

3.3.4 Conclusion

This is the first study showing in vivo longitudinal overview of metabolic responses of the hippocampus, cerebellum and striatum to CLD in the developing brain. Overall, all three brain regions showed similar tendency of changes in metabolite concentrations. However, the changes in cerebellum seem to be the most pronounced suggesting increased vulnerability. Moreover, the observed changes (e.g. Gln and Lac increase) seemed to be stronger than the ones described for the adult brain (section 3.2.1). Further delineation of regional changes in the brain in response to CLD may help elucidate the molecular and regional origins of neuromotor and neurocognitive changes associated with CLD.

3.4 The beneficial effect of oral Cr supplementation in an early childhood rat model of type C HE: a preliminary ^{1}H and ^{31}P MRS study

3.4.1 Introduction

The only curative treatment for patients with liver disease and HE is liver transplantation. Until a transplant can be performed, the main challenge is to protect the brain from NH_4^+ and other toxins and to reduce HE symptoms. Current treatments for HE target various mechanisms of NH_4^+

production and absorption or removal from the systemic circulation, but their efficacity is sometimes low. Developing strategies for neuroprotection are essential to protect patients from long-term damage. Creatine is a key candidate for several reasons. First, Cr stabilizes mitochondrial function, which is important given that energy failure-induced mitochondrial dysfunction is associated with neuronal cell death and progression of disease[138]. Second, it was shown *in vitro* in 3D organotypic brain cell cultures that Cr is neuroprotective both in hyperammonemia conditions and in the context of the toxic guanidinoacetate accumulation under GAMT (guanidinoacetate N-methyltransferase) deficiency[79,139–141]. Further, and given its essential functions played in CNS, Cr has been suggested as a potent neuroprotective agent in several neurodegenerative conditions with clinical trials (e.g. Huntington's and Parkinson's diseases[142,143]). Therefore, exploring methods to efficiently sustain Cr concentration in the developing CNS exposed to HA (or other insults) may have potentially considerable clinical implications.

It is known that children are more affected by CLD and its related toxic accumulation of NH_4^+ and Gln than adult patients, with long-lasting cognitive deficits after liver transplantation[34,132,133,144]. BDL rat is a model of CLD induced type C HE validated in the adult and developing brain[13,14] (sections 3.2, 3.3). Our group showed that rats having acquired CLD as pups display more profound neurometabolic disturbances than adults with the same disease (more important Gln increase, stronger osmotic response, stronger decrease of tCr[13], see also sections 3.3 and 3.2). In parallel, a decrease in tCr has been shown in developing rat brain-cells aggregates after NH_4^+ exposure by our collaborator Prof. Olivier Braissant (CHUV/UNIL), due to downregulation of Cr synthesis[79]. Recently we showed differences in brain metabolic changes between post-natal 15 (P15) and post-natal 21 (P21) operated BDL rats, suggesting that age of disease onset and its coincidence with neurodevelopmental processes play an important role and may result in different vulnerability to the disease[145]. Moreover, NH_4^+ induced impaired axonal growth was shown to be rescued by Cr treatment in organotypic 3D brain cell cultures[139] and P21 BDL rats treated with Cr showed less pronounced metabolic changes[146].

Therefore, we hypothesized that high Cr diet might be beneficial in type C HE in P15 BDL rats. Our aim was to test whether oral Cr supplementation dampens the neurometabolic changes observed in type C HE in a longitudinal model of CLD acquired in early childhood and if these changes are similar to those in P21 rats[146] (a study performed in our group). For that we assessed the effect of Cr supplementation on the longitudinal evolution of brain metabolites using ^{1}H and ^{31}P MRS.

3.4.2   Method

3.4.2.1   BDL rat model of CLD in the developing brain

All experiments were approved by the Committee on Animal Experimentation for the Canton de Vaud, Switzerland (VD3022/VD2439). BDL surgery (accepted model of type C HE[56]) was performed on 6 male Wistar rats at postnatal day 15 (P15). BDL rats were compared with sham (n=6) operated animals at the same age to consider the ongoing brain development. Rats were divided into 4 groups: BDL (n=3), BDL with Cr treatment (BDL + Cr, n=3), sham (n=3), sham with Cr treatment (sham + Cr, n=3). The animals from the treated groups received high Cr supplemented diet with a concentration of 40g/kg.

3.4.2.2   Biochemical measurements

Plasma bilirubin (liver parameter) was quantified on Integra and blood NH_4^+ on blood ammonium meter (PocketChem^{TM} BA PA-4140). These blood parameters were measured longitudinally every two weeks (week 2, week 4, week 6 post-BDL). AST/GOT, ALT/GPT and Glc were measured using Reflotron Plus system (F. Hoffmann-La roche Ltd.).

3.4.2.3   In vivo ^{1}H MRS and ^{31}P-MRS

^{1}H MRS and ^{31}P-MRS scans were preformed longitudinally every two weeks (week 2, week 4, week 6). The experiments were done using a 9.4T MRI-system (Varian/Magnex Scientific) together with home-built coil (quadrature ^{1}H-loops with a single ^{31}P-loop). First and second order shims were adjusted using FASTMAP[137]. ^{1}H MRS spectra were acquired in hippocampus (2 x 2.8 x 2 mm^3) using the SPECIAL sequence (TE=2.8ms)[147]. ^{31}P MRS spectra were acquired using a non-selective AHP pulse for excitation, localized by OVS (x,z) and 1D-ISIS (y) (TR = 8 s, 384 averages), WALTZ-16 for NOE and ^{1}H-decoupling as described and optimized in[148] (VOI = 5 x 9 x 9 mm^3). ^{31}P MR spectra were quantified using AMARES (jMRUI)[149] and normalized for each rat using its PCr concentration from ^{1}H MRS (as previously described[148,150], see also section 1.6.5) acquired in VOI = 4 x 7.5 x 6.5mm^3 centered in ^{31}P VOI for reaching narrow enough linewidths (14 Hz or lower measured on the water signal) for a reliable quantification of Cr and PCr separately.

Figure 3:22: Timing of the ^{1}H and ^{31}P MRS measurements. Graphical representation of the longitudinally performed MRS experiments on four groups of animals.

In the bar plots the results were always presented as mean $\pm$ SD. Diseased rats where always compared with the corresponding sham operated group (sham vs. BDL and sham + Cr vs. BDL + Cr). The longitudinal data of the groups was compared using 2-way ANOVA with Bonferroni correction and at a given time point only using the unpaired students t-test (*p<0.05, **-p<0.01, ***-p<0.001, ****-p<0.0001).

3.4.3 Results and discussion

All BDL operated rats showed increase in plasma bilirubin and blood NH_4^+ validating the presence of CLD (data not shown). Some minor improvements in the neurometabolic profile were noticed for BDL rats under Cr treatment when looking at the differences Sham / BDL vs Sham + Cr / BDL + Cr. Cr treatment seemed to restore the decrease in Cr and tCr leading to a higher Cr concentration in the BDL + Cr group (+13% at week 6, Figures 3:23 and 3:24). Of note, all treated rats seemed to show higher Cr concentrations in the brain following treatment, probably due to a more permeable and immature BBB at this age (Figures 3:23 and 3:24). The decrease in Asc concentration is a recently shown hallmark in HE (here not yet significant due to small n, see sections 3.2.1.2 and 3.3.3) and as previously shown[145] appears later in P15 BDL rats (week 6 post-BDL) compared to P21 BDL rats (week 4 post-BDL). Cr treatment restored Asc in BDL rats emphasizing the antioxidant role of Cr[151]. Treatment seems to have a positive effect on other osmolytes as well (Ins, Tau and tCho), which appear to have a less significant decrease in BDL + Cr than in BDL rats even though Gln is as high in treated rats as in non-treated (Figures 3:23 and 3:24).

This study confirmed a previously shown delayed increase in Gln, as a consequence of NH_4^+ detoxification, for P15 BDL rats probably caused an by immature glutamine synthetase[152] enzyme at a very early age thus delaying NH_4^+ detoxification (Figure 3:23). There was no effect on Gln concentration

due to Cr treatment for the P15 BDL rats (Figures 3:23 and 3:24), although a positive impact of Cr treatment was previously seen only at week 8 in the P21 BDL rats[146]. Because of the high impact of NH_4^+ on the immature brain, P15 BDL rats didn't survive so late during the disease progression (they were sacrificed at week 6 post-BDL).
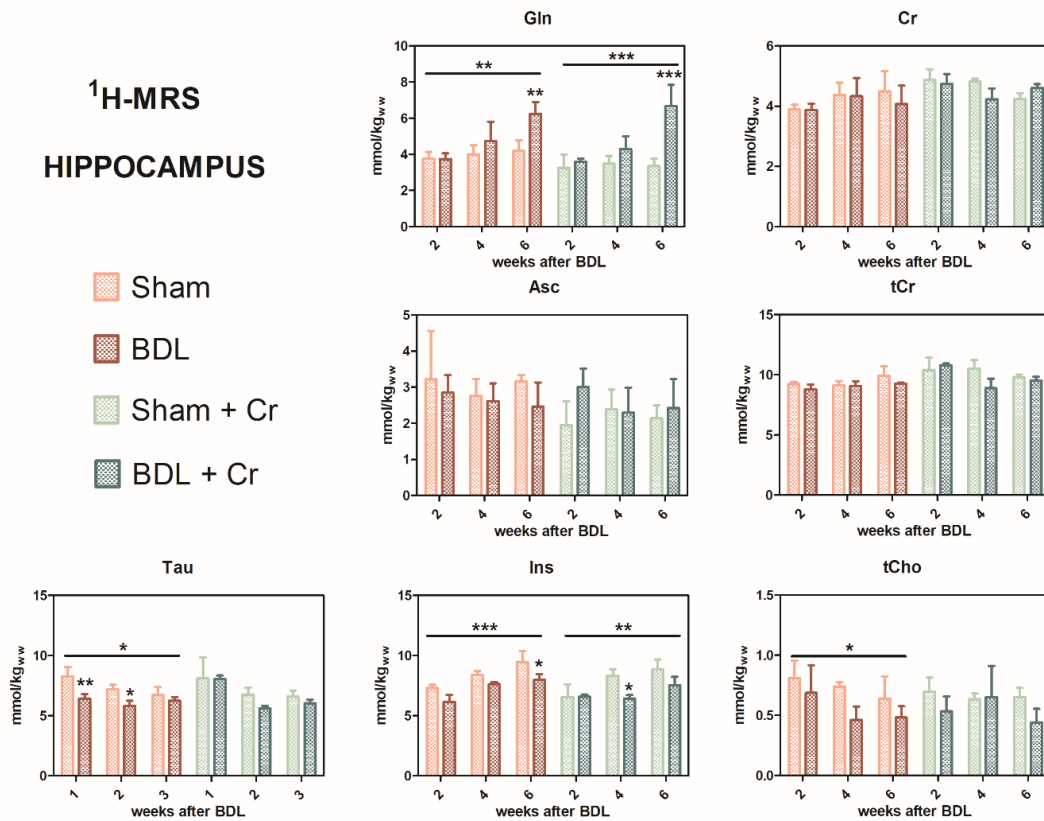
Figure 3:23: Hippocampal metabolic changes in P15 BDL rats. Brain metabolic changes measured longitudinally by ^{1}H MRS in hippocampus at week 2, week 4 and week 8 after BDL. Rats which received Cr treatment (shown in green) show higher Cr concentrations in the brain. Treatment restored Asc in the BDL rats and had a positive effect on the osmolytes (Ins, Tau and tCho). Diseased rats where always compared with sham operated rats (sham vs. BDL and sham + Cr vs. BDL + Cr) using 2-way ANOVA with Bonferroni correction (*p<0.05, **-p<0.01, ***-p<0.001, ****-p<0.0001).
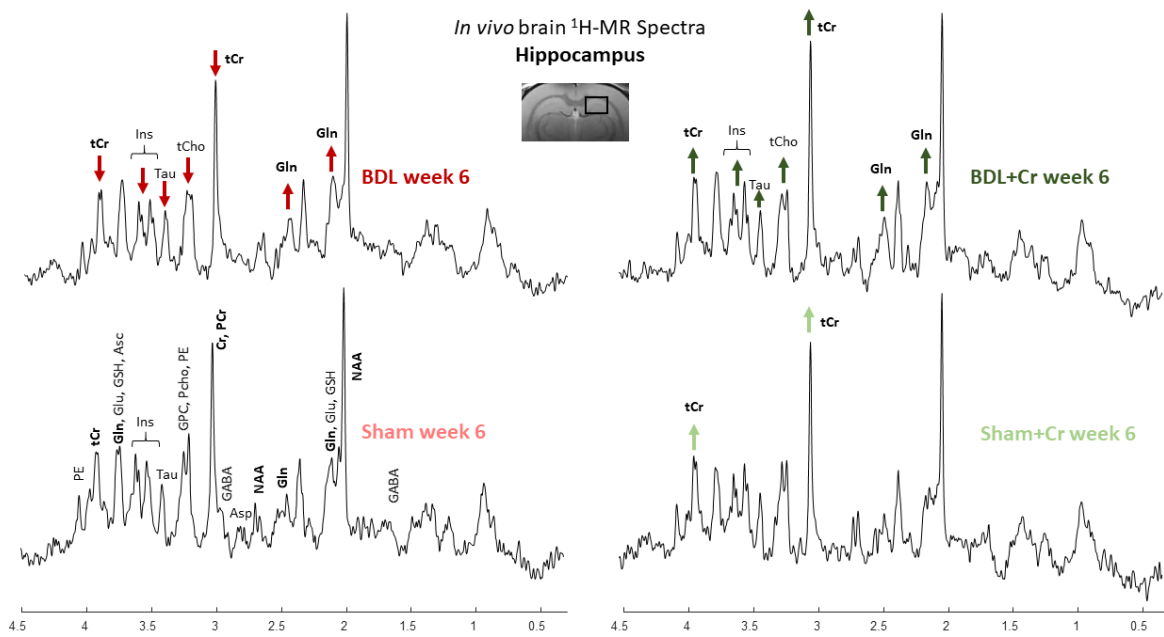
Figure 3:24 In vivo ^{1}H MR spectra from hippocampus (VOI = 2 x 2.8 x 2 mm^3) of P15 BDL rats acquired at week 6 after BDL or sham surgery, each spectrum is from one animal. Spectra clearly show increased tCr in both BDL + Cr and Sham + Cr. The positive effect of Cr treatment on other osmolytes (Ins, Tau and tCho) is also visible on BDL + Cr spectrum.

Treated BDL rats showed a stable PCr concentration at week 4 (ns, BDL + Cr vs Sham + Cr) compared to BDL rats without treatment which displayed a significant decrease (*p<0.05, BDL vs Sham), with this effect diminishing at week 6 post-BDL. Treatment had no effect on γATP, contrary to previously reported P21 results which showed a positive effect of Cr for both PCr and γATP at week 6[146]. However, treated BDL rats have a more stable tNAD pool (similar to sham and sham + Cr) compared to non-treated ones. Higher variations in NADH and NAD$^+$/NADH ratios indicate a more unstable redox state for non-treated BDL rats indicating an increased oxidative stress (Figure 3:25).
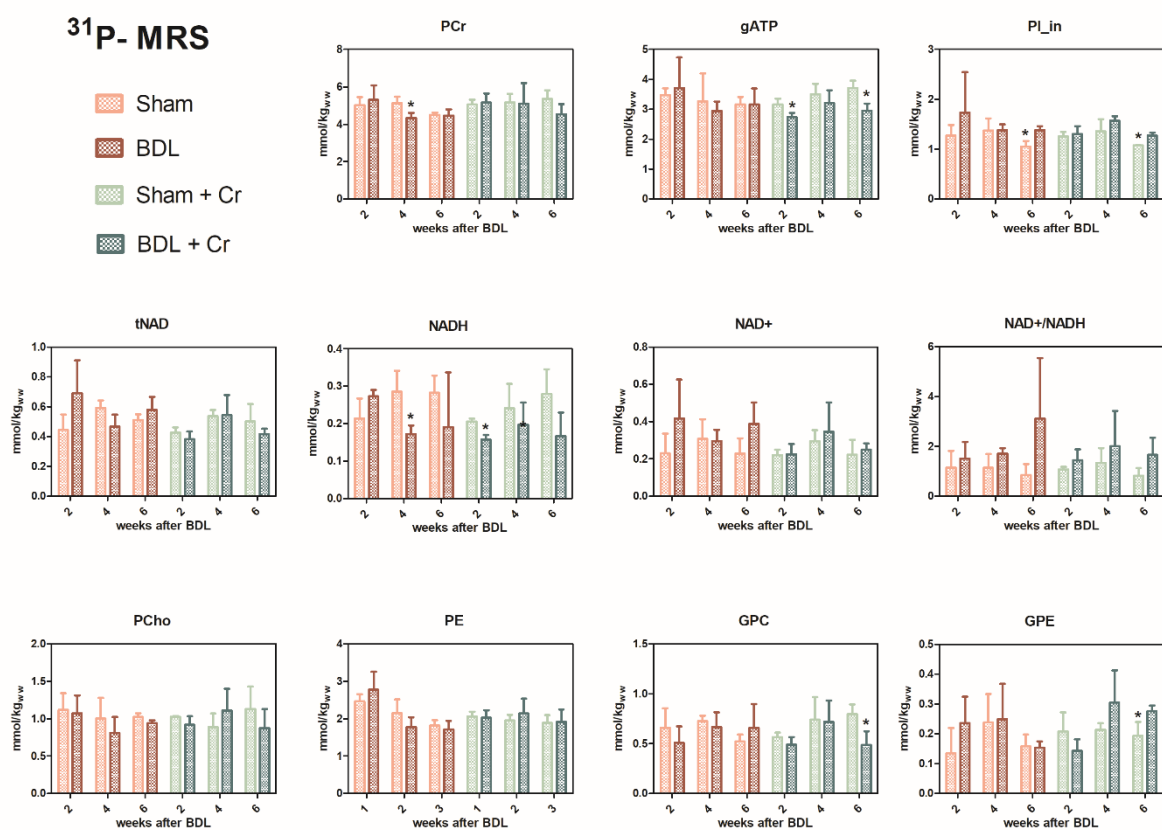
Figure 3:25: Brain metabolic changes measured by ³¹P MRS longitudinally (week 2, week 4 and week 6 post-BDL). Treated rats showed stable PCr at week 4 compared to a decrease in the non-treated animals with no effect on γATP. Variations of tNAD, NADH and NAD⁺/NADH were smaller in treated animals indicating a more balanced redox state. Diseased animals were compared with the corresponding sham operated animals using the unpaired students t-test (*p<0.05, **-p<0.01, ***-p<0.001, ****-p<0.0001).
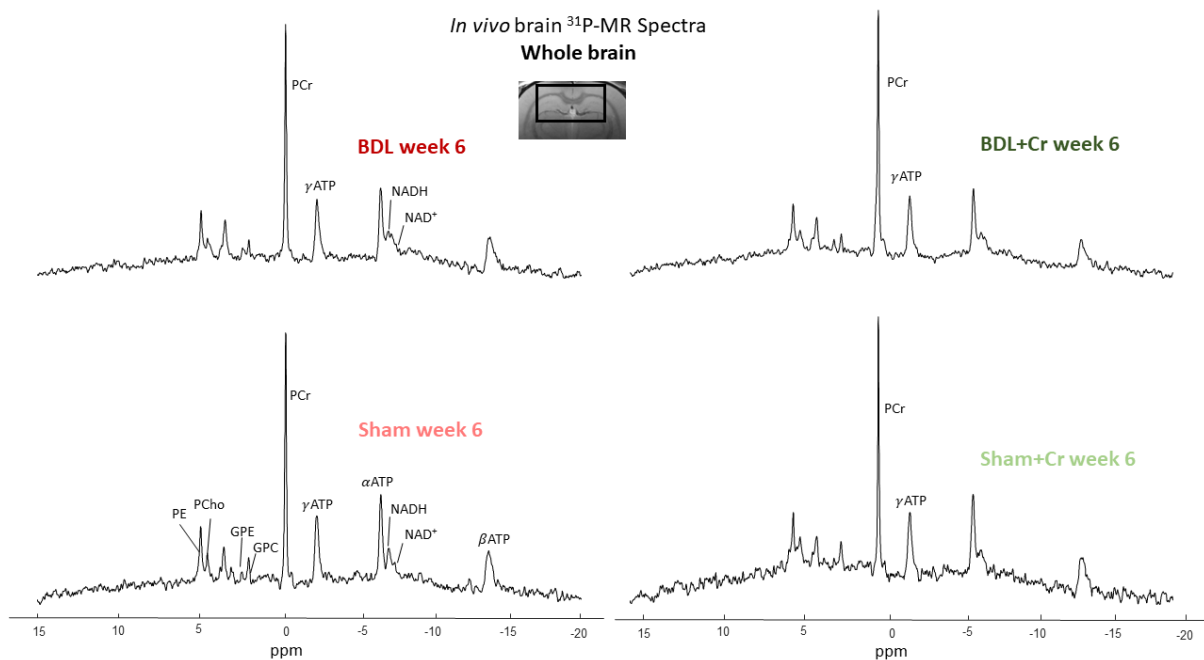
Figure 3:26: In vivo ^{31}P MR spectra from a VOI = 5 x 9 x 9 mm³ comprising an important part of the brain acquired at week 6 after BDL or sham surgery, each spectrum is from one animal.

3.4.4 Conclusion

Our preliminary findings revealed that Cr supplementation improved the neurometabolic profile, emphasizing Cr's antioxidant involvement. We already showed that age affects the susceptibility to CLD-induced HE. In the current study Cr supplementation appeared to validate this distinct vulnerability by leading to difference in response between P15 and P21 BDL rats (Gln, PCr, ATP). The beneficial effects on Asc and other osmolytes suggest that combinatorial treatments in type C HE are required. Additional studies are needed to confirm our findings, as well as to determine whether differences in neurometabolism caused by Cr supplementation translate into different neurological outcomes.

Conclusion

The reported longitudinal metabolic changes in striatum, hippocampus and cerebellum (^{1}H MRS in a BDL rat model) during type C HE led to the conclusion that there is a differential brain regional vulnerability to the disease. Our results emphasize that the observed changes/mechanisms in a single brain region should not be taken as conclusive general disease characteristics. The highest Gln burden and resulting osmolyte release as well as more pronounced Lac, GABA and antioxidants changes were observed in cerebellum. Therefore, we conclude that there is an increased

vulnerability of cerebellum. The increase of Gln was the first observable metabolic change in all the measured regions. STATIS analysis of metabolite data combined with the blood parameters further confirmed that the longitudinal evolution of this metabolite contributes strongly to the data variance (comparable to liver disease marker bilirubin and NH_4^+). Therefore, we conclude that Gln can be considered as first brain metabolic marker of type C HE which could potentially serve to assess HE independently of the results of neuropsychological tests. The histology results showed that the reported neurometabolic changes in combination with previously reported inflammation (neuro and systemic)[1] affected the astrocytes reducing their capacity to remodel processes. Moreover, the observed neuronal alterations suggested there is an interdependence in astrocytic and neuronal morphological changes influencing the overall activity of the neuronal network during disease progression. BDL rats showed an increased CNS and systemic OS when compared with SHAM animals, emphasizing that the increase of OS is more probably a consequence of intra- and extra-cellular ROS than that of reduced antioxidants capacity. The elevated oxidative stress in cerebellum and hippocampus indicated that ROS may play an important role in brain functions disruption, providing a further link between disease progression and cognitive decline in type C HE patients.

The brain regional measurements in the developing brain showed a stronger metabolic stress (e.g. Gln and Lac increase at week 6) when compared to the adult brain confirming the increased vulnerability of the immature CNS. Overall, the three brain regions showed similar tendency of changes in metabolite concentrations with the highest impact on the cerebellar neurometabolic profile. The observed alterations of neurotransmitters in cerebellum during development, because of its role in coordination and learning, may be connected to long term irreversible damage observed in children after liver transplantation.

The preliminary study on the effect of Cr supplementation on the neurometabolic profile of BDL rats in the very early childhood (P15) confirmed the suspected age susceptibility to CLD-induced HE. Some beneficial effects of Cr supplementation are observed on Asc and osmolytes allowing us to conclude that combinatorial treatments in type C HE are required and should be closely investigated.

References

1. Pierzchala, K. *et al.* Central nervous system and systemic oxidative stress interplay with inflammation in a bile duct ligation rat model of type C hepatic encephalopathy. *Free Radic. Biol. Med.* **178**, 295–307 (2022).

2. Moon, A. M., Singal, A. G. & Tapper, E. B. Contemporary Epidemiology of Chronic Liver Disease and Cirrhosis. *Clin. Gastroenterol. Hepatol.* **in press**, (2019).

3. Kronsten, V. T. & Shawcross, D. L. Hepatic encephalopathy and depression in chronic liver disease: is the common link systemic inflammation? *Anal. Biochem.* **636**, 114437 (2022).

4. Weiss, N., Jalan, R. & Thabut, D. Understanding hepatic encephalopathy. *Intensive Care Med.* **44**, 231–234 (2017).

5. Butterworth, R. F. Complications of cirrhosis. III. Hepatic encephalopathy. *J. Hepatol.* (2000) doi:10.1016/s0168-8278(00)80424-9.

6. Rose, C. F. *et al.* Hepatic encephalopathy: Novel insights into classification, pathophysiology and therapy. *J. Hepatol.* **73**, 1526–1547 (2020).

7. Jalan, R. & Kerbert, A. J. C. Recent advances in understanding and managing hepatic encephalopathy in chronic liver disease. *F1000Research* **9**, (2020).

8. DeMorrow, S., Cudalbu, C., Davies, N., Jayakumar, A. R. & Rose, C. F. 2021 ISHEN guidelines on animal models of hepatic encephalopathy. *Liver Int.* **41**, 1474–1488 (2021).

9. Felipo, V. & Butterworth, R. F. Neurobiology of ammonia. *Progress in Neurobiology* (2002) doi:10.1016/S0301-0082(02)00019-9.

10. Bosoi, C. R. & Rose, C. F. Identifying the direct effects of ammonia on the brain. *Metab. Brain Dis.* **24**, 95–102 (2009).

11. Cooper, A. J. L. & Plum, F. Biochemistry and physiology of brain ammonia. *Physiol. Rev.* **67**, 440–519 (1987).

12. Girard, G., Giguère, J. F. & Butterworth, R. F. Region-selective reductions in activities of glutamine synthetase in rat brain following portacaval anastomosis. *Metab. Brain Dis.* **8**, 207–215 (1993).

13. Rackayova, V. *et al.* Longitudinal osmotic and neurometabolic changes in young rats with chronic cholestatic liver disease. *Sci. Rep.* **10**, 7536 (2020).

14. Braissant, O. *et al.* Longitudinal neurometabolic changes in the hippocampus of a rat model of chronic hepatic encephalopathy. *J. Hepatol.* (2019) doi:10.1016/j.jhep.2019.05.022.

15. Kreis, R., Farrow, N. & Ross, B. D. Localized 1H NMR spectroscopy in patients with chronic hepatic encephalopathy. Analysis of changes in cerebral glutamine, choline and inositols. *NMR Biomed* **4**, 109–116 (1991).

16. Häussinger, D. *et al.* Proton magnetic resonance spectroscopy studies on human brain Myo-inositol in hypo-osmolarity and hepatic encephalopathy. *Gastroenterology* **107**, 1475–1480 (1994).

17. Cudalbu, C. & Taylor-Robinson, S. D. Brain Edema in Chronic Hepatic Encephalopathy. *Journal of Clinical and Experimental Hepatology* (2019) doi:10.1016/j.jceh.2019.02.003.

18. Rivera-Mancía, S., Montes, S., Méndez-Armenta, M., Muriel, P. & Ríos, C. Morphological changes of rat astrocytes induced by liver damage but not by manganese chloride exposure. *Metab. Brain Dis.* **24**, 243–255 (2009).

19. Dhanda, S. & Sandhir, R. Blood-Brain Barrier Permeability Is Exacerbated in Experimental Model of Hepatic Encephalopathy via MMP-9 Activation and Downregulation of Tight Junction Proteins. *Mol. Neurobiol.* **55**, 3642–3659 (2018).

20. Jaeger, V., Demorrow, S. & McMillin, M. The direct contribution of astrocytes and microglia to the pathogenesis of hepatic encephalopathy. *J. Clin. Transl. Hepatol.* **7**, 352–361 (2019).

21. Wright, G. *et al.* Endotoxemia produces coma and brain swelling in bile duct ligated rats. *Hepatology* **45**, 1517–1526 (2007).

22. Braissant, O., McLin, V. A. & Cudalbu, C. Ammonia toxicity to the brain. *J. Inherit. Metab. Dis.* **36**, 595–612 (2013).

23. Ochoa-Sanchez, R. & Rose, C. F. Pathogenesis of Hepatic Encephalopathy in Chronic Liver Disease. *J. Clin. Exp. Hepatol.* **8**, 262–271 (2018).

24. Lanz, B., Rackayova, V., Braissant, O. & Cudalbu, C. MRS studies of neuroenergetics and glutamate/glutamine exchange in rats: Extensions to hyperammonemic models. *Anal. Biochem.* (2017) doi:10.1016/j.ab.2016.11.021.

25. Mallet, M. *et al.* Blood ammonia in patients with chronic liver diseases : a better defined role in clinical practice. *Anal. Biochem.*

26. Aldridge, D. R., Tranah, E. J. & Shawcross, D. L. Pathogenesis of hepatic encephalopathy: Role of ammonia and systemic inflammation. *J. Clin. Exp. Hepatol.* **5**, S7–S20 (2015).

27. Rai, R. *et al.* Reversal of low-grade cerebral edema after lactulose/rifaximin therapy in patients with cirrhosis and minimal hepatic encephalopathy. *Clin. Transl. Gastroenterol.* **6**, e111-8 (2015).

28. Jain, L. *et al.* Serum endotoxin, inflammatory mediators, and magnetic resonance spectroscopy before and after treatment in patients with minimal hepatic encephalopathy. *J. Gastroenterol. Hepatol.* **28**, 1187–1193 (2013).

29. Azhari, H. & Swain, M. G. Role of Peripheral Inflammation in Hepatic Encephalopathy. *J. Clin. Exp. Hepatol.* **8**, 281–285 (2018).

30. Capuron, L. & Miller, A. H. Immune system to brain signaling: Neuropsychopharmacological implications. *Pharmacol. Ther.* **130**, 226–238 (2011).

31. DiSabato, D. J., Quan, N. & Godbout, J. P. Neuroinflammation: the devil is in the details. *J. Neurochem.* **139**, 136–153 (2016).

32. Glass, C. K., Saijo, K., Winner, B., Marchetto, M. C. & Gage, F. H. Mechanisms Underlying Inflammation in Neurodegeneration. *Cell* **140**, 918–934 (2010).

33. McCoy, M. K. & Tansey, M. G. TNF signaling inhibition in the CNS: Implications for normal brain function and neurodegenerative disease. *J. Neuroinflammation* **5**, 1–13 (2008).

34. Cagnon, L. & Braissant, O. Hyperammonemia-induced toxicity for the developing central nervous system. *Brain Res. Rev.* **56**, 183–197 (2007).

35. Bosoi, C. R. & Rose, C. F. Oxidative stress: A systemic factor implicated in the pathogenesis of hepatic encephalopathy. *Metab. Brain Dis.* **28**, 175–178 (2013).

36. Mookerjee, R. P. *et al.* Neutrophil dysfunction in alcoholic hepatitis superimposed on cirrhosis is reversible and predicts the outcome. *Hepatology* **46**, 831–840 (2007).

37. Görg, B., Schliess, F. & Häussinger, D. Osmotic and oxidative/nitrosative stress in ammonia toxicity and hepatic encephalopathy. *Arch. Biochem. Biophys.* **536**, 158–163 (2013).

38. Norenberg, M. D., Rama Rao, K. V & Jayakumar, A. R. Signaling factors in the mechanism of ammonia neurotoxicity. *Metab. Brain Dis.* **24**, 103–117 (2009).

39. Shawcross, D. L., Shabbir, S. S., Taylor, N. J. & Hughes, R. D. Ammonia and the neutrophil in the pathogenesis of hepatic encephalopathy in cirrhosis. *Hepatology* **51**, 1062–1069 (2010).

40. Taylor-Robinson, S. D., Sargentoni, J., Marcus, C. D., Morgan, M. Y. & Bryant, D. J. Regional variations in cerebral proton spectroscopy in patients with chronic hepatic encephalopathy. *Metab. Brain Dis.* **9**, 347–359 (1994).

41. Häussinger, D. Low grade cerebral edema and the pathogenesis of hepatic encephalopathy in cirrhosis. *Hepatology* **43**, 1187–1190 (2006).

42. Häussinger, D., Kircheis, G., Fischer, R., Schliess, F. & Dahl, S. Vom. Hepatic encephalopathy in chronic liver disease: A clinical manifestation of astrocyte swelling and low-grade cerebral edema? *J. Hepatol.* **32**, 1035–1038 (2000).

43. Pelle, J. *et al.* Metabolomics in the understanding and management of hepatic encephalopathy. *Anal. Biochem.* **636**, 114477 (2022).

44. Hermann, B., Rudler, M., Galanaud, D., Thabut, D. & Weiss, N. Magnetic resonance spectroscopy: A surrogate marker of hepatic encephalopathy? *J. Hepatol.* **71**, 1055–1057 (2019).

45. Chen, B. *et al.* The Critical Role of Hippocampal Dopamine in the Pathogenesis of Hepatic Encephalopathy. *Physiol. Res.* **70**, 101–110 (2021).

46. García-García, R. *et al.* Learning and Memory Impairments in Patients with Minimal Hepatic Encephalopathy are Associated with Structural and Functional Connectivity Alterations in Hippocampus. *Sci. Rep.* **8**, 1–13 (2018).

47. Khanna, A. *et al.* SIRT1 activation by resveratrol reverses atrophy of apical dendrites of hippocampal CA1 pyramidal neurons and neurobehavioral impairments in moderate grade hepatic encephalopathy rats. *J. Chem. Neuroanat.* **106**, 101797 (2020).

48. Cabrera-Pastor, A. *et al.* Peripheral inflammation induces neuroinflammation that alters neurotransmission and cognitive and motor function in hepatic encephalopathy: Underlying mechanisms and therapeutic implications. *Acta Physiol.* **226**, 1–19 (2019).

49. Stoodley, C. J. The cerebellum and cognition: Evidence from functional imaging studies. *Cerebellum* **11**, 352–365 (2012).

50. García-García, R. *et al.* Reduced resting state connectivity and gray matter volume correlate with cognitive impairment in minimal hepatic encephalopathy. *PLoS One* **12**, 1–17 (2017).

51. Balzano, T. *et al.* The Cerebellum of Patients with Steatohepatitis Shows Lymphocyte Infiltration, Microglial Activation and Loss of Purkinje and Granular Neurons. *Sci. Rep.* **8**, 1–12 (2018).

52. Ahl, B. *et al.* Regional differences in cerebral blood flow and cerebral ammonia metabolism in patients with cirrhosis. *Hepatology* **40**, 73–79 (2004).

53. Balleine, B. W., Delgado, M. R. & Hikosaka, O. The role of the dorsal striatum in reward and decision-making. *J. Neurosci.* **27**, 8161–8165 (2007).

54. Dhanda, S., Sunkaria, A., Halder, A. & Sandhir, R. Mitochondrial dysfunctions contribute to energy deficits in rodent model of hepatic encephalopathy. *Metab. Brain Dis.* **33**, 209–223 (2018).

55. Rackayova, V. *et al.* 1H and 31P magnetic resonance spectroscopy in a rat model of chronic hepatic encephalopathy: in vivo longitudinal measurements of brain energy metabolism. *Metab. Brain Dis.* **31**, 1303–1314 (2016).

56. Butterworth, R. F. *et al.* Experimental models of hepatic encephalopathy: ISHEN guidelines. *Liver Int.* **29**, 783–788 (2009).

57. Tkac, I., Rao, R., Georgieff, M. K. & Gruetter, R. Developmental and regional changes in the neurochemical profile of the rat brain determined by in vivo 1H NMR spectroscopy. *Magn. Reson. Med.* **50**, 24–32 (2003).

58. Račkayová, V. *et al.* Late post-natal neurometabolic development in healthy male rats using 1H and 31P magnetic resonance spectroscopy. *J. Neurochem.* **157**, 508–519 (2021).

59. RStudio Team, Rs. P. RStudio: Integrated Development Environment for R. (2021).

60. Lavit, C., Escoufier, Y. & Sabatier, R. The ACT (STATIS method) J q G G Fl { q K q *. *Comput. Stat. Data Anal.* **18**, 97–119 (1994).

61. Abdi, H., Williams, L. J., Valentin, D. & Bennani-Dosse, M. STATIS and DISTATIS: Optimum multitable principal component analysis and three way metric multidimensional scaling. *Wiley Interdiscip. Rev. Comput. Stat.* **4**, 124–167 (2012).

62. Cudalbu, C. *et al.* Metabolic and transcriptomic profiles of glioblastoma invasion revealed by comparisons between patients and corresponding orthotopic xenografts in mice. *Acta Neuropathol. Commun.* **9**, 1–16 (2021).

63. Lai, M. *et al.* In vivo characterization of brain metabolism by 1 H MRS, 13 C MRS and 18 FDG PET reveals significant glucose oxidation of invasively growing glioma cells. *Int. J. Cancer* **143**, 127–138 (2018).

64. Norenberg, M. D. Distribution of glutamine synthetase in the rat central nervous system. *J. Histochem. Cytochem.* **27**, 756–762 (1979).

65. Haussinger, D., Kircheis, G., Fischer, R., Schliess, F. & vom Dahl, S. Hepatic encephalopathy in chronic liver disease: a clinical manifestation of astrocyte swelling and low-grade cerebral edema? *J. Hepatol.* **32**, 1035–1038 (2000).

66. Brusilow, S. W., Koehler, R. C., Traystman, R. J. & Cooper, A. J. L. Astrocyte Glutamine Synthetase: Importance in Hyperammonemic Syndromes and Potential Target for Therapy. *Neurotherapeutics* **7**, 452–470 (2010).

67. Zwingmann, C. Nuclear magnetic resonance studies of energy metabolism and glutamine shunt in hepatic encephalopathy and hyperammonemia. *J. Neurosci. Res.* **85**, 3429–3442 (2007).

68. Rudler, M. *et al.* Combined diffusion tensor imaging and magnetic resonance spectroscopy to predict neurological outcome before transjugular intrahepatic portosystemic shunt. *Aliment. Pharmacol. Ther.* **48**, 863–874 (2018).

69. Chen, J. R. *et al.* Morphological changes of cortical pyramidal neurons in hepatic encephalopathy. *BMC Neurosci.* **15**, 1–12 (2014).

70. DA, S. Dendritic organization in the neurons of the visual and motor cortices of the cat. *J. Anat.* **87**, 387–406 (1953).

71. Bosoi, C. R. *et al.* Systemic oxidative stress is implicated in the pathogenesis of brain edema in rats with chronic liver failure. *Free Radic. Biol. Med.* **52**, 1228–1235 (2012).

72. Görg, B. *et al.* Oxidative stress markers in the brain of patients with cirrhosis and hepatic encephalopathy. *Hepatology* **52**, 256–265 (2010).

73. Rackayova, V. *et al.* 1H and 31P magnetic resonance spectroscopy in a rat model of chronic hepatic encephalopathy: in vivo longitudinal measurements of brain energy metabolism. *Metab. Brain Dis.* **31**, 1303–1314 (2016).

74. Chiesa, M. & Giamello, E. *Electron Spin Resonance Spectroscopy*. *Encyclopedia of Analytical Chemistry* (2000). doi:10.1002/9780470027318.a6104.pub2.

75. Capani, F. *et al.* Changes in reactive oxygen species (ROS) production in rat brain during global perinatal asphyxia: An ESR study. *Brain Res.* **914**, 204–207 (2001).

76. Arroyo, C. M. *et al.* Spin Trapping of Oxygen and Carbon-centered Free Radicals in Ischemic Canine Myocardium. *Free Radic. Biol. Med.* **3**, 313–315 (1987).

77. Arroyo, C. M., Kramer, J. H., Dickens, B. F. & Weglicki, W. B. Identification of free radicals in myocardial ischemia/reperfusion by spin trapping with nitrone DMPO. *FEBS Lett.* **305**, 166 (1992).

78. Lei, H., Berthet, C., Hirt, L. & Gruetter, R. Evolution of the neurochemical profile after transient focal cerebral ischemia in the mouse brain. *J. Cereb. Blood Flow Metab.* **29**, 811–819 (2009).

79. Braissant, O. *et al.* Ammonium alters creatine transport and synthesis in a 3D culture of developing brain cells, resulting in secondary cerebral creatine deficiency. *Eur. J. Neurosci.* **27**, 1673–1685 (2008).

80. Haris, M., Cai, K., Singh, A., Hariharan, H. & Reddy, R. In vivo mapping of brain myo-inositol. *Neuroimage* **54**, 2079–2085 (2011).

81. Genovese, G. *et al.* Inflammation-driven glial alterations in the cuprizone mouse model probed with diffusion-weighted magnetic resonance spectroscopy at 11.7 T. *NMR Biomed.* **34**, 1–13 (2021).

82. Butterworth, R. F. Taurine in hepatic encephalopathy. *Adv. Exp. Med. Biol.* **403**, 601–606 (1996).

83. Sergeeva, O. A. *et al.* GABAA-receptor modification in taurine transporter knockout mice causes striatal disinhibition. *J. Physiol.* **585**, 539–548 (2007).

84. Hilgier, W. *et al.* Changes in the extracellular profiles of neuroactive amino acids in the rat striatum at the asymptomatic stage of hepatic failure. *J. Neurosci. Res.* **56**, 76–84 (1999).

85. S. H. Zeisel, D. Char, N. F. S. Human and Bovine Milk and Infant Formulas1. *J. Nutr.* 50–58 (1986).

86. Mallet, N., Leblois, A., Maurice, N. & Beurrier, C. Striatal cholinergic interneurons: How to elucidate their function in health and disease. *Front. Pharmacol.* **10**, 1–7 (2019).

87. Bosoi, C. R. *et al.* Increased brain lactate is central to the development of brain edema in rats with chronic liver disease. *J. Hepatol.* **60**, 554–560 (2014).

88. Rama Rao, K. V. & Norenberg, M. D. Brain energy metabolism and mitochondrial dysfunction in acute and chronic hepatic encephalopathy. *Neurochem. Int.* **60**, 697–706 (2012).

89. Jaeger, V., DeMorrow, S. & McMillin, M. The Direct Contribution of Astrocytes and Microglia to the Pathogenesis of Hepatic Encephalopathy. *J. Clin. Transl. Hepatol.* **7**, 1–10 (2019).

90. Korogod, N., Petersen, C. C. H. & Knott, G. W. Ultrastructural analysis of adult mouse neocortex comparing aldehyde perfusion with cryo fixation. *Elife* **4**, e05793 (2015).

91. Sharif, A. & Prevot, V. When Size Matters: How Astrocytic Processes Shape Metabolism. *Cell Metab.* **25**, 995–996 (2017).

92. Zhang, Y., Reichel, J. M., Han, C., Zuniga-Hertz, J. P. & Cai, D. Astrocytic Process Plasticity and IKKβ/NF-κB in Central Control of Blood Glucose, Blood Pressure, and Body Weight. *Cell Metab.* **25**, 1091-1102.e4 (2017).

93. Olude, M. A., Mustapha, O. A., Aderounmu, O. A., Olopade, J. O. & Ihunwo, A. O. Astrocyte morphology, heterogeneity, and density in the developing African giant rat (Cricetomys gambianus). *Front. Neuroanat.* **9**, 1–10 (2015).

94. Kubotera, H. *et al.* Astrocytic endfeet re-cover blood vessels after removal by laser ablation. *Sci. Rep.* **9**, 1–11 (2019).

95. Savchenko, V. L., Nikonenko, I. R., Skibo, G. G. & McKanna, J. A. Distribution of microglia and astrocytes in different regions of the normal adult rat brain. *Neurophysiology* **29**, 343–351 (1997).

96. Bylicky, M. A., Mueller, G. P. & Day, R. M. Mechanisms of endogenous neuroprotective effects of astrocytes in brain injury. *Oxid. Med. Cell. Longev.* **2018**, (2018).

97. Butterworth, R. F. Pathogenesis of hepatic encephalopathy and brain edema in acute liver failure. *J. Clin. Exp. Hepatol.* **5**, S96–S103 (2015).

98. Bélanger, M., Desjardins, P., Chatauret, N. & Butterworth, R. F. Loss of expression of glial fibrillary acidic protein in acute hyperammonemia. *Neurochem. Int.* **41**, 155–160 (2002).

99. Zhou, B., Zuo, Y. X. & Jiang, R. T. Astrocyte morphology: Diversity, plasticity, and role in neurological diseases. *CNS Neurosci. Ther.* **25**, 665–673 (2019).

100. Bordey, A., Lyons, S. A., Hablitz, J. J. & Sontheimer, H. Electrophysiological characteristics of reactive astrocytes in experimental cortical dysplasia. *J. Neurophysiol.* **85**, 1719–1731 (2001).

101. McBean, G. J. Cysteine, glutathione, and thiol redox balance in astrocytes. *Antioxidants* **6**, 1–13 (2017).

102. Chen, J. R. *et al.* Morphological changes of cortical pyramidal neurons in hepatic encephalopathy. *BMC Neurosci.* **15**, (2014).

103. Theodosis, D. T., Poulain, D. A. & Oliet, S. H. R. Activity-dependent structural and functional plasticity of astrocyte-neuron interactions. *Physiol. Rev.* **88**, 983–1008 (2008).

104. Calabrese, B., Wilson, M. S., Halpain, S. & Margaret, S. Development and Regulation of Dendritic Dendritic Spines : What Are They ? *J. Physiol.* 38–47 (2009).

105. Niesmann, K. *et al.* Dendritic spine formation and synaptic function require neurobeachin. *Nat. Commun.* **2**, (2011).

106. Kaufmann, W. E. & Moser, H. W. Dendritic anomalies in disorders associated with mental retardation. *Cereb. Cortex* **10**, 981–991 (2000).

107. Sartorius, A. *et al.* Proton magnetic resonance spectroscopic creatine correlates with creatine transporter protein density in rat brain. *J. Neurosci. Methods* **172**, 215–219 (2008).

108. Malhi, G. S., Valenzuela, M., Wen, W. & Sachdev, P. Magnetic resonance spectroscopy and its applications in psychiatry. *Aust. N. Z. J. Psychiatry* **36**, 31–43 (2002).

109. Ende, G., Demirakca, T. & Tost, H. Chapter 27 The biochemistry of dysfunctional emotions: proton MR spectroscopic findings in major depressive disorder. *Prog. Brain Res.* **156**, 481–501 (2006).

110. Schloss, P., Mayser, wolfgang & Betz, H. The putative rat choline transporter CHOT1 transports creatine and is highly expressed in neural and muscle-rich tissues. *Biochemical and Biophysical Research Communications* vol. 198 637–645 (1994).

111. Lunardi, G. *et al.* The creatine transporter mediates the uptake of creatine by brain tissue, but not the uptake of two creatine-derived compounds. *Neuroscience* **142**, 991–997 (2006).

112. Hadjihambi, A. *et al.* Ammonia mediates cortical hemichannel dysfunction in rodent models of chronic liver disease. *Hepatology* **65**, 1306–1318 (2017).

113. Rose, C. F. Increase brain lactate in hepatic encephalopathy: Cause or consequence? *Neurochem. Int.* **57**, 389–394 (2010).

114. Mosso, J. *et al.* PET CMR glc mapping and 1 H-MRS show altered glucose uptake and neurometabolic profiles in BDL rats. 1–30.

115. Schurr, A. Lactate: The ultimate cerebral oxidative energy substrate? *J. Cereb. Blood Flow Metab.* **26**, 142–152 (2006).

116. Hassan, S. S. *et al.* Cerebellar inhibition in hepatic encephalopathy. *Clin. Neurophysiol.* **130**, 886–892 (2019).

117. Sergeeva, O. A. GABAergic transmission in hepatic encephalopathy. *Arch. Biochem. Biophys.* **536**, 122–130 (2013).

118. Aponso, M., Patti, A., Hearn, M. T. W. & Bennett, L. E. Anxiolytic effects of essential oils may involve anti-oxidant regulation of the pro-oxidant effects of ascorbate in the brain. *Neurochem. Int.* **150**, 105153 (2021).

119. Harrison, F. E. & May, J. M. Vitamin C function in the brain: vital role of the ascorbate transporter SVCT2. *Free Radic. Biol. Med.* **46**, 719–730 (2009).

120. Dwivedi, D., Megha, K., Mishra, R. & Mandal, P. K. Glutathione in Brain: Overview of Its Conformations, Functions, Biochemical Characteristics, Quantitation and Potential Therapeutic Role in Brain Disorders. *Neurochem. Res.* **45**, 1461–1480 (2020).

121. Huang, J. & Philbert, M. A. Distribution of glutathione and glutathione-related enzyme systems in mitochondria and cytosol of cultured cerebellar astrocytes and granule cells. *Brain Res.* **680**, 16–22 (1995).

122. Liu, B., Teschemacher, A. G. & Kasparov, S. Astroglia as a cellular target for neuroprotection and treatment of neuro-psychiatric disorders. *Glia* **65**, 1205–1226 (2017).

123. Knapp, L. T. & Klann, E. Role of reactive oxygen species in hippocampal long-term potentiation: Contributory or inhibitory? *J. Neurosci. Res.* **70**, 1–7 (2002).

124. Auerbach, J. M. & Segal, M. Peroxide modulation of slow onset potentiation in rat hippocampus. *J. Neurosci.* **17**, 8695–8701 (1997).

125. Pellmar, T. C., Hollinden, G. E. & Sarvey, J. M. Free radicals accelerate the decay of long-term potentiation in field CA1 of guinea-pig hippocampus. *Neuroscience* **44**, 353–359 (1991).

126. Bellaver, B., Souza, D. G., Souza, D. O. & Quincozes-Santos, A. Hippocampal Astrocyte Cultures from Adult and Aged Rats Reproduce Changes in Glial Functionality Observed in the Aging Brain. *Mol. Neurobiol.* **54**, 2969–2985 (2017).

127. Ishii, T. *et al.* Endogenous reactive oxygen species cause astrocyte defects and neuronal dysfunctions in the hippocampus: a new model for aging brain. *Aging Cell* **16**, 39–51 (2017).

128. Hacisevki, A. An Overview of Ascorbic Acid Biochemistry. *J. Faculy Pharm.* **38**, 233–255 (2009).

129. Baquer, N. Z., Hothersall, J. S. & McLean, P. *Function and Regulation of the Pentose Phosphate Pathway in Brain*. *Current Topics in Cellular Regulation* vol. 29 (ACADEMIC PRESS, INC., 1988).

130. Bachmann, C. Mechanisms of hyperammonemia. *Clin. Chem. Lab. Med.* **40**, 653–662 (2002).

131. Rodijk, L. H. *et al.* Long-Term Neurodevelopmental Outcomes in Children with Biliary Atresia. *J. Pediatr.* **217**, 118-124.e3. (2020).

132. Caudle, S. E., Katzenstein, J. M., Karpen, S. & McLin, V. Developmental assessment of infants with biliary atresia: differences between boys and girls. *J Pediatr Gastroenterol Nutr* **55**, 384–389 (2012).

133. Caudle, S. E., Katzenstein, J. M., Karpen, S. J. & McLin, V. A. Language and Motor Skills Are Impaired in Infants with Biliary Atresia Before Transplantation. *J. Pediatr.* **156**, (2010).

134. Hirase, T. *et al.* Occludin as a possible determinant of tight junction permeability in endothelial cells. *J. Cell Sci.* **110**, 1603–13 (1997).

135. Ballabh, P., Braun, A. & Nedergaard, M. The blood–brain barrier: an overview. *Neurobiol. Dis.* **16**, 1–13 (2004).

136. Workman, A. D., Charvet, C. J., Clancy, B., Darlington, R. B. & Finlay, B. L. Modeling Transformations of Neurodevelopmental Sequences across Mammalian Species. *J. Neurosci.* **33**, 7368–7383 (2013).

137. Gruetter, R. & Tkáč, I. Field mapping without reference scan using asymmetric echo-planar techniques. *Magn. Reson. Med.* **43**, 319–323 (2000).

138. Beal, M. F. Energetics in the pathogenesis of neurodegenerative diseases. *Trends Neurosci.* **23**, 298–304 (2000).
139. Braissant, O. *et al.* Ammonium-induced impairment of axonal growth is prevented through glial creatine. *J. Neurosci.* **22**, 9810–9820 (2002).
140. Hanna-El-Daher, L., Beard, E., Henry, H., Tenenbaum, L. & Braissant, O. Mild guanidinoacetate increase under partial guanidinoacetate methyltransferase deficiency strongly affects brain cell development. *Neurobiol Dis* **79**, 14–27 (2015).
141. Braissant, O. Ammonia toxicity to the brain: effects on creatine metabolism and transport and protective roles of creatine. *Mol. Genet. Metab.* **100 Suppl**, S53-8 (2010).
142. Beal, M. F. Neuroprotective effects of creatine. *Amino Acids* **40**, 1305–1313 (2011).
143. Bender, A. *et al.* Creatine supplementation in Parkinson disease: a placebo-controlled randomized pilot trial. *Neurology* **67**, 1262–1264 (2006).
144. Ng, V. *et al.* Development and validation of the pediatric liver transplantation quality of life: A disease-specific quality of life measure for pediatric liver transplant recipients. *J. Pediatr.* **165**, 547–555 (2014).
145. Rackayova, V., Braissant, O., Mclin, V. & Cudalbu, C. Chronic hepatic encephalopathy in early developing brain, neurometabolic changes differ depending on the age of disease onset , in vivo longitudinal 1H MRS study. Proc. Intl . Soc. Mag. Reson. Med. 4–7 (2018).
146. Rackayova, V. *et al.* Protective effect of high creatine diet during chronic hepatic encephalopathy in young rats , an in vivo longitudinal 1H and 31P MRS study. Proc. Intl . Soc. Mag. Reson. Med. **4**, 9–12 (2017).
147. Mlynárik, V., Gambarota, G., Frenkel, H. & Gruetter, R. Localized short-echo-time proton MR spectroscopy with full signal-intensity acquisition. *Magn. Reson. Med.* **56**, 965–970 (2006).
148. Rackayová, V. *Brain metabolism during Chronic Hepatic Encephalopathy studied by in vivo 1H and 31P MRS. Epfl-Thesis-8612* (2018).
149. Vanhamme, L. an den Boogaart, A. & Van Huffel, S. Improved Method for Accurate and Efficient Quantification of MRS Data with use of Prior Knowledge. Journal of Magnetic Resonance. **129**, 35–43 (1997).
150. Račkayová, V. *et al.* Late post-natal neurometabolic development in healthy male rats using 1H and 31P MRS. *J. Neurochem.* **submitted**, (2020).
151. Sestili, P. *et al.* Creatine as an antioxidant. *Amino Acids* **40**, 1385–1396 (2011).
152. Bayer, S. M. & McMurray, W. C. The Metabolism of Amino Acids in Developing Rat Brain. *J. Neurochem.* **14**, 695–706 (1967).

Chapter 4   First implementation of FID-MRSI at 14.1T for fast and high-resolution metabolite mapping of the rat brain

Magnetic resonance spectroscopic imaging allows the detection of MR spectra from a multidimensional array of locations providing the characterization of a full object under investigation. Even though the combination of spatial encoding with MRS brings valuable in vivo information for both clinical and biomedical research studies, its use remains limited due to several issues (e.g. low SNR, low spatial resolution, lack of standardized processing and quality assurance tools etc.) However, recent technical advancements have improved MRSI quality and speed, making it a preferred instrument for clinical research. At UHF in the clinical setting pulse-acquire free induction decay (^{1}H FID-MRSI) acquisitions are increasingly used (minimizes the T_2 relaxation, J-evolution chemical shift displacement errors and sensitivity to B_0 inhomogeneities). Moreover, this simple sequence design permits a considerable acquisition time reduction by decreasing the TR while using optimal Ernst's flip angle. While in the human brain, MRSI is increasingly used, in the preclinical setting MRSI is not widely applied mostly because of difficulties related to the small rodent brain, i.e. long acquisition times and low SNR.

The implementation of a novel approach: FID-MRSI on the UHF preclinical scanner (14.1T) is described in this chapter. This method offers a fast (short TR) and robust data acquisition with high spatial resolution resulting in high quality spectroscopic maps in a very short acquisition time providing an increased brain coverage. Our results set the grounds for a wider application of ^{1}H-FID-MRSI in the preclinical setting with a potential for further improvements and acceleration. We tested two noise reduction techniques as a potential step in the postprocessing of preclinical MRSI data. Preliminary assessment of the effect of the Marchenko-Pastur principal component analysis and the low-rank TGV reconstruction on the spectra from preclinical MRSI datasets (FID MRSI and SPECIAL MRSI) and their quantification showed promising results for their future implementation.

My contribution to this chapter is in its entirety (including all the data acquisitions, processing, quantification and statistical analysis as well as drafting the text).

*This Chapter is structured in four sub-chapters. In the first sub chapter titled "**Introduction: challenges of MRSI and its preclinical applications**" (4.1) the challenges of MRSI are briefly described and main sequences used for preclinical MRSI are presented. Moreover, the advantages of FID-MRSI acquisitions at UHF are specified. The second sub-chapter titled "**Calibrations of the FID-MRSI sequence on the 14.1 T Bruker console**" (4.2) provides a detailed description of the first implementation of FID-MRSI sequence (in our laboratory) in the preclinical setting with all the optimization steps, basis set, quantifications and first results in terms of metabolic maps. In the third sub-chapter ("**Effect of noise reduction techniques on preclinical MRSI data: preliminary results**", 4.3) two noise reduction techniques are tested as a potential processing step in the preclinical MRSI post-processing pipeline. Finally, the fourth sub-chapter ("**Conclusion and future perspective**", 4.4) provides an overall conclusion with potential future steps for improvement and acceleration.*

4.1 Introduction: challenges of MRSI and its preclinical application

Magnetic resonance spectroscopic imaging allows the non-invasive detection of MR spectra, simultaneously, from multiple spatial locations in a single slice inside the brain, or in the entire brain if done in 3D. Even though the ability of this technique to map, in vivo, the metabolic regional differences in a slice or the entire brain at a given time point is very valuable for both clinical and biomedical research studies, its routine application remains challenging due to several issues (e.g. low SNR, low spatial resolution, lack of standardized processing and quality assurance tools etc.). However, the availability of ultra-high magnetic fields (UHF), advanced pulse sequences and new encoding methods improved the quality and speed of MRSI, making it a tool of choice in the research community[1–3]. The basic principles of MRSI acquisition and reconstruction were already described in Chapter 1 (sub chapter 1.7).

The advantages of UHF (higher B_0, $\geq$ 7T) that bring benefit to MRSI are the increased sensitivity, SNR and frequency dispersion. Therefore, important new biomarkers like GABA and separated Gln and Glu can be quantified bringing crucial information for diseases like cancer[4], multiple sclerosis[5] and also hepatic encephalopathy[6]. Despite the advantages that UHF brings there are still some remaining challenges in acquisition of good spectral dataset such as B_0 and B_1 inhomogeneities, shorter T_2 relaxation times, stronger chemical shift displacement errors, lipid artifacts, need for a standardized processing and quality assurance tools[7] etc. In addition, in standard MRSI phase encoding (as explained in the sub chapter 1.7) is combined with a localization sequence (e.g. PRESS, STEAM, LASER, see section 1.6.1). Since only one phase encoding step is acquired per repetition time in a traditional MRSI scheme and the number of steps needed increases with the resolution, this leads to long acquisition times. In addition, volume preselection provides spectra only from a selected rectangular volume restricting the access to the border regions of the brain[8]. These are some of the challenges that need to be overcome to successfully implement MRSI and some of them will be tackled in this chapter.

While in the human brain, MRSI is increasingly used, in the preclinical setting MRSI is not yet widely applied mostly because of difficulties related to the small rodent brain[9]. The resulting low SNR comes from a very small nominal voxel size in rodents (e.g. in 32x32 matrix 0.75 x 0.75 x 2mm^3)[10] while in the human brain even at high spatial resolution (128 x 128) the nominal voxel size is fairly big (e.g. 1.7 x 1.7 x 10 mm^3)[11]. While additional challenges inherited from human brain MRSI are still

present in terms of shimming of big volumes with many tissue interfaces, long measurement times (e.g 120 min)[10], water suppression artifacts and lipid contamination[9] etc. Only few studies using SPECIAL[10,12] (pioneered by our group) or PRESS[13] MRSI have been reported in the preclinical settings.

4.1.1   SPECIAL MRSI

SPECIAL MRSI sequence is one of the spectroscopic imaging sequences successfully applied in animals at UHF (9.4T). The advantages of SPECIAL localization scheme[14] (see section 1.6.1.2) in terms of sensitivity combined with MRSI phase encoding allowed for quantitative mapping of the neurometabolic profile consisting of 10 metabolites(Cr, NAA, Glu, Gln, Cho, Tau, Ins, Glc, Lac and Lipids)[15]. In a preclinical setting (rat brain at 9.4T) using a home-built quadrature surface coil for transmit and receive high spatial resolution was achieved (matrix size 32 x 32, FOV = 24 x 24 mm^2) in a rectangular volume of 10 x 2 x 10 mm^3 (coronal orientation, keeping 10 x 11 nominal voxels)[15]. However, even with a very short echo time (TE = 2.8 ms) the TR used was 2-2.5 s for metabolites and 1.5 s for water leading to a total measurement time of 120 -135 min. Thus only few studies were published using this method[15,16].

4.1.2   PRESS-MRSI

One of the first MRSI sequences successfully applied in the preclinical setting (to the rat brain) was PRESS-MRSI[17]. The PRESS localization scheme (see section 1.6.1.2) was further optimized using asymmetric pulses[18] for excitation and refocusing allowing a further shortening of the TE from 15ms to 6ms[17]. The experiment was performed on 4.7T BRUKER in a healthy rat brain where the voxel for the PRESS based MRSI sequence was 10 x 7 x 4 mm^3 (6x9 nominal voxels), showing the feasibility of this sequence however no quantification was presented[17]. More recently, PRESS-MRSI multi slice approach was evaluated in a preclinical model of glioblastoma (following tumor growth)[19]. It was proved that this method is an efficient tool to follow preclinical disease model longitudinally and evaluate their response to therapy[13,20].

4.1.3   FID-MRSI at UHF

At UHF in the clinical setting pulse-acquire free induction decay (^{1}H FID-MRSI)[21,22] acquisitions are increasingly used[2]. It has been shown that T$_2$ relaxation times decrease with the increasing field strength causing a very fast signal decay at UHF[23]. Therefore, very short TEs need to be used. In the FID-MRSI sequence signal is acquired almost immediately after excitation substantially shortening the TE (as low as 1.3ms[22])[8] and therefore minimizing T$_2$ relaxation. Moreover, CSDE increases with

the magnetic field strength (B_0, increased frequency dispersion). CSDE can be decreased using broadband adiabatic RF pulses (as in SPECIAL, see sections 3.1.1 and 1.6.1.2) or by avoiding the refocusing pulses as for the FID acquistion[8]. To sum up, FID-MRSI acquisition minimizes the T_2 relaxation and J-evolution, therefore increasing the SNR. It also reduces the chemical shift displacement errors and sensitivity to B_0 inhomogeneities[2,22,24,25]. Moreover, its simple sequence design permits to reduce considerably the acquisition time by decreasing the TR while using optimal Ernst's flip angle. However, since FID-excitation selects a full slice (or a whole brain in 3D), it requires control of extracranial lipid contamination and proper handling of the macromolecule signals[2]. Therefore, the use of postprocessing and reconstruction techniques that reduce lipid contamination is recommended[2]. Aiming for a shortest possible TR leads to shortening of the WS schemes sometimes resulting in poor WS.

FID-MRSI at UHF (7T) has been successful in investigating glioma (reporting metabolic images of NAA, tCho, tCr, mIns, Gly, Glu and Gln)[26,27], multiple sclerosis[28,29], epilepsy and a number of other neurodegenerative pathologies and psychiatric disorders[8].

4.2   Calibrations of the FID MRSI sequence on the 14.1 T Bruker console

In this sub-chapter, the advantages of pulse-acquire ^{1}H FID-MRSI acquisitions (section 4.1.3) are combined with the UHF of 14.1T to obtain increased SNR and spatial resolution for the first time in the rodent brain. Since this was the first implementation of the FID-MRSI acquisition in our laboratory on the newly obtained 14.1T Bruker console all the tests and acquisition calibrations are described in detail to be used for future implementations.

4.2.1   First tests – Phantom experiment

A phantom made in a 5ml syringe with a mixture of 16 in vivo present metabolites with BSA (Bovine serum albumin) was used for a first test experiment. The exact concentrations in the mixture were: Ala – 1 mM, Asp – 1.5 mM, Cr – 4.8 mM, PCr – 4.4 mM, GABA – 2.1 mM, Gln – 3.4 mM, Glu – 8.8 mM, GSH – 1.8 mM, Ins – 7.3 mM, Lac – 4.2 mM, NAA – 7.5 mM, Tau – 10.4 mM, Glc – 2.2 mM, NAAG – 0.8 mM, PE – 0.7 mM, GPC+PCho – 1.2 mM, Cr+PCr – 9.2 mM and BSA – 2.5 mM.

The single-slice FID-MRSI sequence provided by BRUKER was firstly used. Of note, there were very few acquisition parameters provided in the protocol and they were not adapted to 14.1T. An axial

slice of 2 mm thickness was positioned at the same depth as a previously shimmed volume (9 x 7 x 3 mm, MAPSHIM from BRUKER) in the STEAM sequence (TE=3ms, TM=10ms, TR=4000ms). Only the water signal was acquired with the STEAM sequence to check the water linewidth (shim quality). The parameters used for the FID-MRSI were adjusted to 32 x 32 matrix size, 24 x 24 mm field of view, TE = 1.314ms, TR = 1105ms, 2 averages (weighted averaging mode, total duration 22min 38s). A calculated pulse shape from BRUKER was used with a flip angle of 90° (pulse length = 0.6ms and bandwidth = 7000 Hz). For these first tests, only the water signal was acquired. The resulting map of the significant water signal (provided by the MRSI tool in jMRUI (http: //www.mrui.uab.es/mrui/)) reproduced well the phantom shape leading to the conclusion that the sequence works well in these conditions (phantom experiment, Figure 4:1).
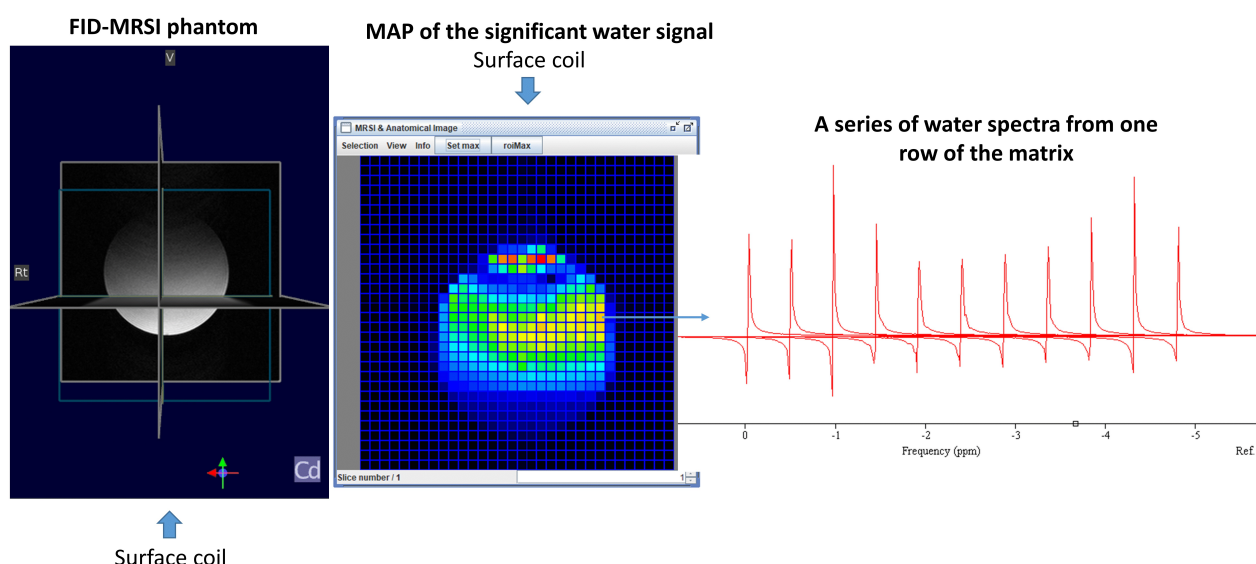

Figure 4:1: FID-MRSI phantom experiment - water spectra. The first FID-MRSI experiment performed on the BRUKER console at 14.1T using a phantom in a 5ml syringe and a home built transmit/receive surface coil. The localizer image is shown on the left with the FID-MRSI slice position in light blue. The resulting water map provided by the jMRUI MRSI tool and the corresponding water spectra (only from one row) are shown in the middle and on the right-hand side.

Further on to evaluate the quality of metabolite signal and WS on a phantom (before the in vivo acquisition), a metabolite spectrum (from the same phantom) was acquired with a STEAM sequence (TE=3ms, TM=10ms, TR=4000ms, 32 averages, VOI =9 x 7 x 3 mm^3) using the default VAPOR water suppression (water suppression pulse BW = 350 Hz and the flip angles 90° and 180°). The obtained spectrum is shown in the Figure 4:2A.

To test the FID-MRSI acquisition of the metabolite spectra, VAPOR water suppression was added before the excitation in the sequence (the default / non-adjusted WS). The metabolite acquisition

was then performed on the same phantom (as for the water map (Figure 4:1) and the metabolite acquisition with the STEAM sequence (Figure 4:2B)). The acquisition parameters and the example spectrum from a nominal voxel ($0.75 \times 0.75 \times 2$ mm^3) are shown in the Figure 4:2B. The spectrum obtained with FID-MRSI matches well to the spectrum obtained with STEAM while a first order phase distortion can be observed due to the acquisition delay of 1.314ms (delay between the excitation pulse and the start of the acquisition). To shorten the total acquisition time we decreased the TR to 820 ms and calculated the corresponding Ernst angle using the average metabolite T_1 relaxation times reported at 14.1T[30]. The new sequence adjustments provided a more uniform water map, significant acquisition time reduction (~6min) and a slightly improved SNR (Figure 4:2C). Note that the big water signal residue observed in all the spectra presented in the Figure 4:2 results from an imperfect (not properly adjusted) VAPOR WS.
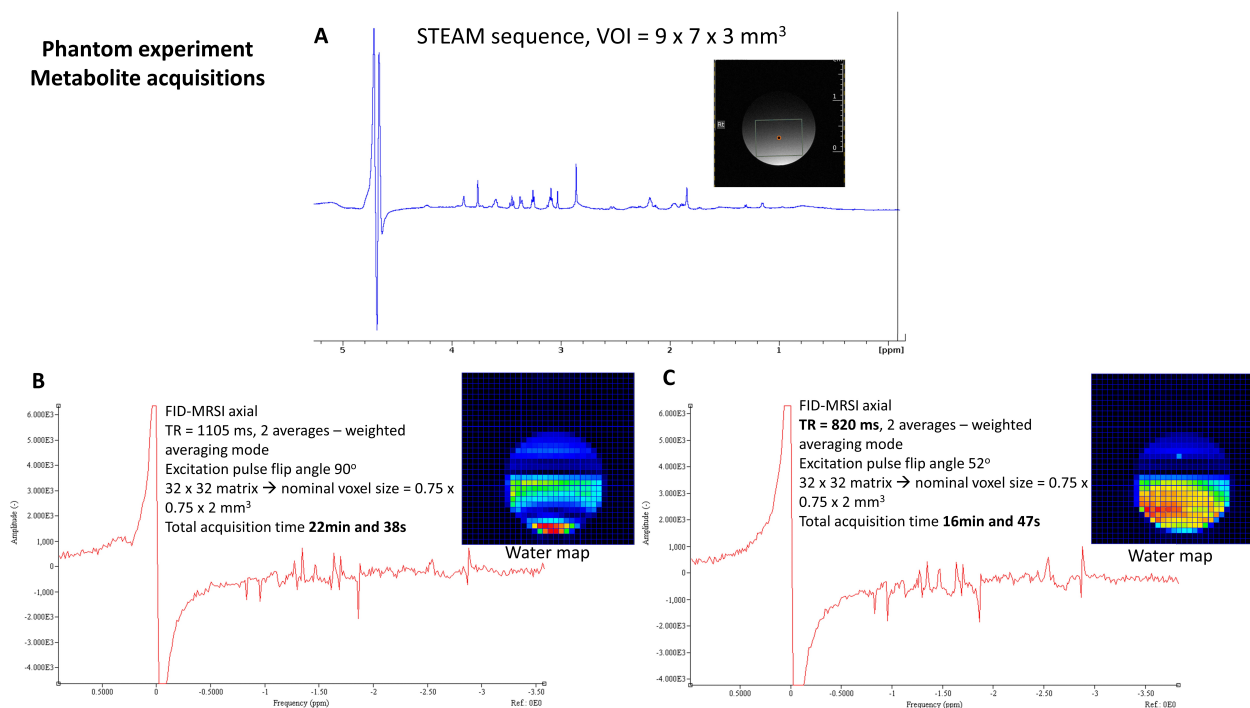

Figure 4:2: FID-MRSI phantom experiment - metabolite spectra. A) Spectrum obtained from a phantom (5 ml syringe with in vivo measurable metabolites) using a STEAM sequence (TE=3ms, TM=10ms, TR=4000ms, 32 averages, VOI =9 x 7 x 3 mm^3), note the poor water suppression; B) FID-MRSI axial acquisition with the addition of the VAPOR water suppression showing a representative metabolite spectrum from the position 11:13; C) FID-MRSI axial acquisition repeated after shortening of the TR and Ernst angle adjustment. The shown spectrum is from the same nominal voxel position as the one displayed in the part (B). Not the poor water suppression also for the FID-MRSI acquisitions.

4.2.2 First in vivo acquisitions – single slice FID-MRSI in the axial direction

4.2.2.1 Water suppression adjustments

The advanced MRSI approaches usually use WET or VAPOR techniques for water suppression (see also section 1.6.2). Even though the VAPOR pulse train is longer and increases the TR compared to the WET technique, in our experimental setting (B_0 = 14.1T and transmit/receive surface coil) VAPOR provides higher efficacy of WS because of its lower sensitivity to B_1^+ variations[31]. However, as can be seen in Figure 4:2 the quality of the WS when using the settings provided by Bruker was poor. Therefore, to achieve efficient WS over the large region of interest for MRSI the VAPOR pulse powers needed to be calibrated correctly[31].

The original VAPOR scheme is described in the section 1.6.2. and it consists of seven pulses with a factor of 1.78 difference in flip angles ($\alpha - \alpha - 1.78\alpha - \alpha - 1.78\alpha - \alpha - 1.78\alpha$). The flip angles were first optimized using a STEAM sequence (default BRUKER sequence, TE=3ms, TM=10ms, TR=4000ms) in a big VOI = 9 x 7 x 3 mm^3, positioned in the axial direction (in vivo in a rat brain at 14.1T, using a transmit/receive home-built quadrature surface coil). The same VOI was used for shimming before the MRSI acquisition (MAPSHIM from BRUKER). An array of experiments was acquired keeping the ratio between the flip angles fixed (1.78) to find the optimal values which provide the best WS (Figure 4:3A). Furthermore, the array of experiments with a smaller flip angle differences was then repeated to pinpoint the values that provide optimal WS (lowest water residual, Figure 4:3B). The inter pulse delays of the VAPOR scheme are set to fixed values (inter-pulse delays (in ms): 150 – 80 – 160 – 80 – 100 – 30 – 26). While it is recommended not to change these preset delays, the last delay (between the last WS pulse and the first excitation pulse) can still be optimized. Therefore, after adjusting the flip angles, another array of experiments was performed (using the optimal flip angles) changing the described last delay (d7, Figure 4:3C).
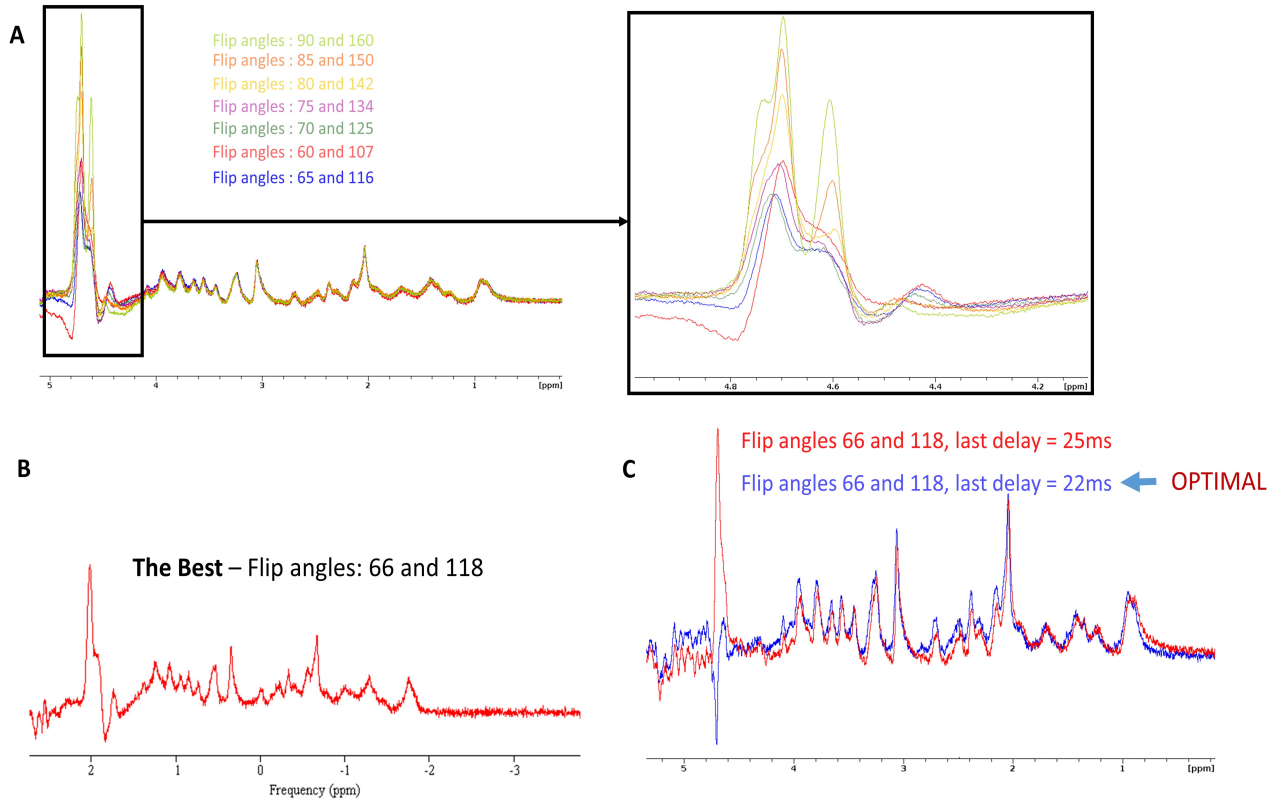
Figure 4:3: VAPOR optimizations. A) A series of experiments with different VAPOR WS flip angles using a STEAM sequence (TE=3ms, TM=10ms, TR=4000ms, in vivo in the rat brain at 14.1T, BRUKER). The zoom on the water residual and how it changes with different flip angles is shown on the right; B) The optimum flip angles found that result in the lowest residual water signal; C) Additional experiments performed with the optimized flip angle value while changing the last delay in VAPOR (between the last WS pulse and the first excitation pulse).

For the FID-MRSI acquisition in addition to the adjusted flip angles and last delay, the WS pulse bandwidth was increased to 600Hz. All these adjustments lead to an improved WS achieved in vivo (see Figure 4:4 compared to Figure 4:2B and C).
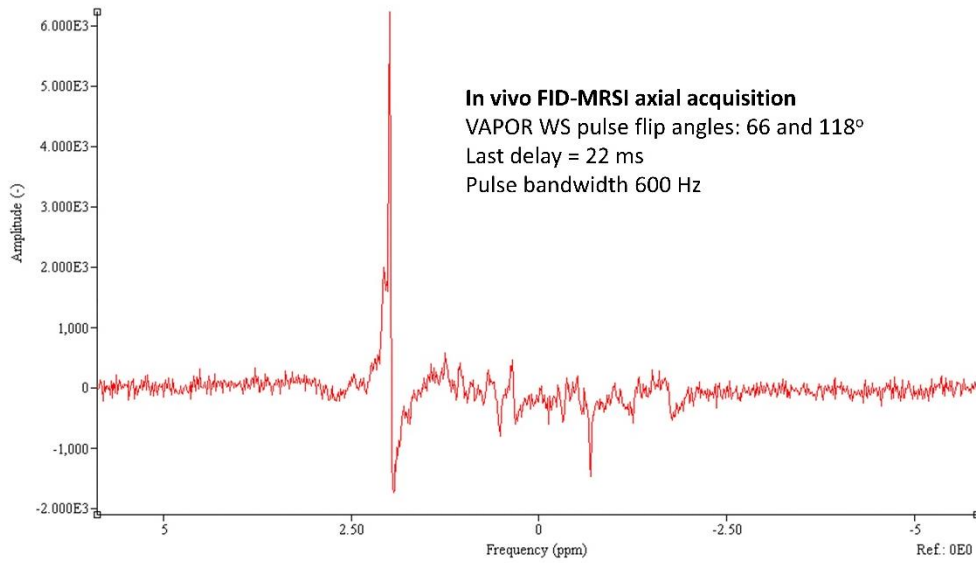
Figure 4:4: FID-MRSI in vivo rat brain spectrum. An example spectrum acquired in vivo in the rat brain at 14.1T using the FID-MRSI axial acquisition (TE=1.3ms, TR=812ms, 32x32 matrix in the FOV=24x24mm^2) with the optimized VAPOR water suppression.

Later improvements in the reference power and WS

The reference power needs to be calibrated at the start of each experiment manually, since we use a quadrature surface coil. A 2mm thick slab is positioned at the same depth in the brain as the slice that will be used for the MRSI acquisition. The power adjustment algorithm is based on a 3-pulse sequence ($\alpha - \frac{TE}{2} - 2\alpha - SE - TM - \alpha - \frac{TE}{2} - STE$, where SE denotes a spin echo, STE a stimulated echo and TM a mixing period for STE formation) with a constant gradient applied during the entire sequence which serves as slice selection, frequency encoding and spoiling gradient. The RF waveform can be changed but the default protocol sets a 0.5 ms blockpulse for the first and third excitation[32]. This protocol was improved for our experimental setting by changing the blockpulse with a gaussian pulse which provided an improved reference power calibration when using home-built surface coils (gaussian pulse performs better in presence of coil related B$_1$ inhomogeneities). The process depicted on the Figure 4:3 for the optimization of WS pulses was repeated with the improved reference power calibration. This resulted in the following optimal values for WS: flip angles 84/150° and d7=26/22ms. These values are reproductible, closer to the original VAPOR sequence and work well for both coronal and axial orientation of the MRSI slice. However, the water suppression RF pulse bandwidth needs to be checked and manually adjusted, if necessary, prior to every experiment (the most used value is 660Hz).

4.2.2.2   Field of view saturation

The first in vivo FID-MRSI experiments were performed with a slightly different parameters when compared to the in vitro experiment (presented in the section 4.2.1). The repetition time was further shortened to TR = 812 ms, the number of averages reduced to one (weighted or standard averaging doesn't play a role anymore) and the matrix size to 31 x 31 (FOV = 24 x 24 mm) leading to the nominal voxel size of 0.774 x 0.774 x 2 mm^3. The matrix size was adjusted following the recommendation from BRUKER saying that it is desirable to sample the center of the k-space which can only be achieved with an odd matrix dimension. This led to a total acquisition time of 12min and 59s. The VAPOR WS was adjusted as described in the section 4.2.2.1 (flip angles of 66° and 118°, last delay of 22ms and pulse bandwidth of 600 Hz).

The influence of field of view saturation was then tested. Six saturation slabs of 10mm thickness were added around the selected slice and positioned around the brain to remove the unwanted signal coming from subcutaneous lipids. The experiment was then repeated without the FOV saturation and the spectra from the same positions (nominal voxels) in the matrix were compared to assess the potential beneficial influence of the FOV saturation (Figure 4:5). It can be observed from the water maps that the saturation bands efficiently nulled the signal coming from the unwanted areas. They reduced the lipid contamination in the full matrix but especially in the locations closer to the edge of the brain (Figure 4:5) and slightly increased the SNR (from 15.4 to 17.5 calculated in jMRUI as the NAA peak height / spectral noise for the position selected in the Figure 4:5). Therefore, the saturation slabs were used in every following experiment.
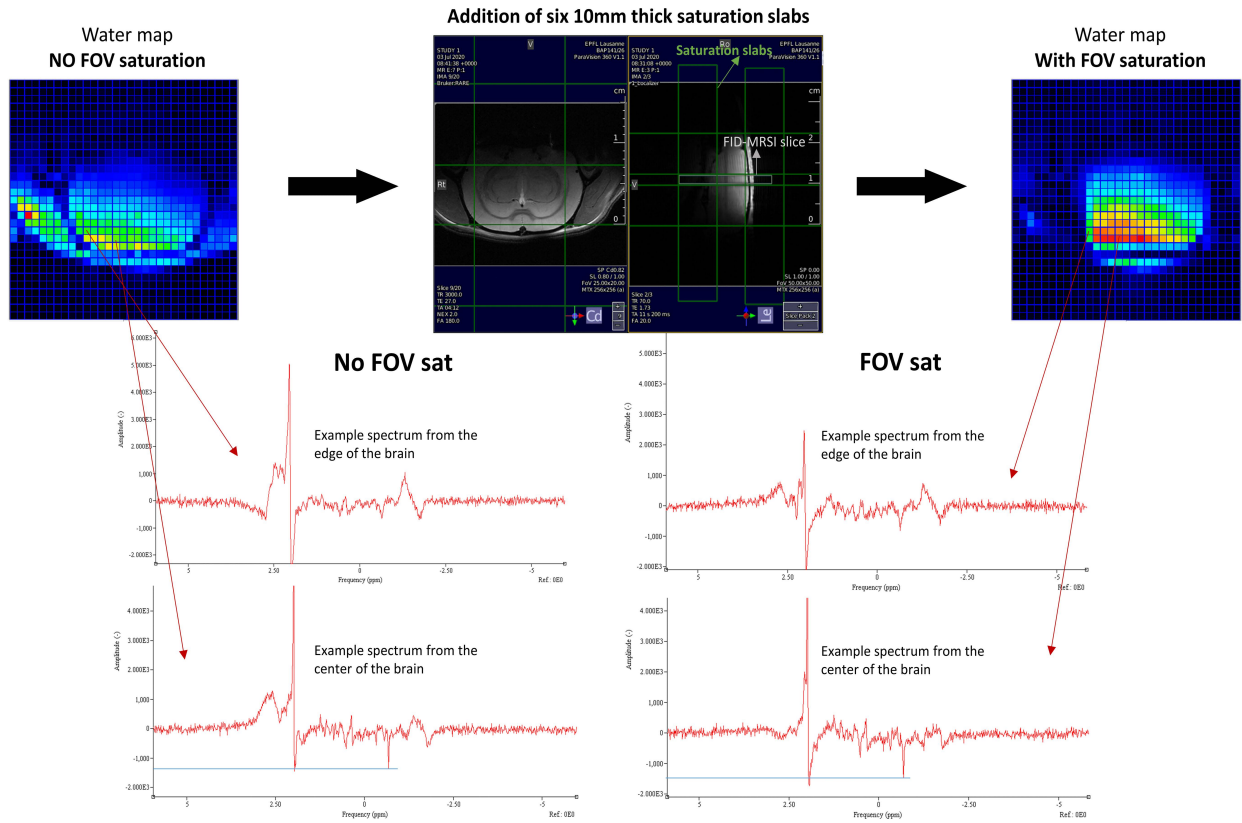
Figure 4:5: FOV saturation test. The water map obtained using FID-MRSI in the axial direction without FOV saturation is shown on the top left. The positioning of six 10mm thick saturation slabs is shown in the top center. The water map obtained using FID-MRSI in the axial direction with FOV saturation is shown on the top right. Two metabolite spectra (FID-MRSI in axial direction with VAPOR WS) from the nominal voxels at the same positions in the matrix are showed (No FOV sat – on the left vs FOV sat – on the right), the chosen positions are in the edge of the brain and in the center of the brain). Note the reduced the lipid contamination especially in the locations closer to the edge of the brain.

4.2.2.3   Comparison with PRESS-MRSI

A more traditional PRESS-MRSI acquisition in the axial direction (sequence provided by BRUKER) was performed just after the FID-MRSI (on the same animal). The FID data (with FOV saturation) were then compared to the PRESS data as a quality assessment. FID-MRSI dataset acquisition parameters are described in detail in the previous section (4.2.2.2).

PRESS-MRSI parameters were set to TE=12.745 ms, TR= 2000 ms, one average, 31 x 31 matrix in a FOV = 24 x 24 mm leading to a total scan time of 32 min and 2 s. The VOI of 9 x 7 x 2 mm^3 was centered in the brain (in the same slice used for FID-MRSI acquisition, see Figure 4:6up). The 90° excitation pulse duration was set to 0.5 ms with 8400 Hz bandwidth and the refocusing 180° pulse length to 0.7 ms and 4857.1 Hz bandwidth. The same flip angles for VAPOR WS RF pulses as

optimized for the FID-MRSI were used (118º and 66º) while WS RF bandwidth was manually adjusted to 450Hz. 1024 points of the FID were acquired in both PRESS- and FID-MRSI.

The water maps provided by the jMRUI MRSI tool resulting from the PRESS and the FID acquisition show an improved brain coverage obtained with the FID-MRSI (Figure 4:6up). Looking more closely we can observe that FID-MRSI still gives a good quality spectrum in the nominal voxels where the PRESS-MRSI doesn't detect any signal (outside of the VOI, Figure 4:6down). For the SNR comparison a sub-matrix (4 x 5 spectra = 20 spectra in total) centered in the PRESS-MRSI VOI was selected. The SNR of the selected 20 spectra was calculated in jMRUI (AMARES) as the NAA peak height / spectral noise. The same sub matrix (20 spectra) was selected from the FID-MRSI dataset and the SNR was calculated in the same way. The average SNR for PRESS-MRSI (20 spectra) was 11.7 $\pm$ 3 and for the FID-MRSI (20 spectra at the same positions) 10.7 $\pm$ 3. We can conclude that both methods lead to a similar spectral quality (see the comparison of two spectra from the same nominal voxel obtained by the PRESS acquisition and FID acquisition in the Figure 4:6down) while the FID-MRSI provides a better brain coverage.
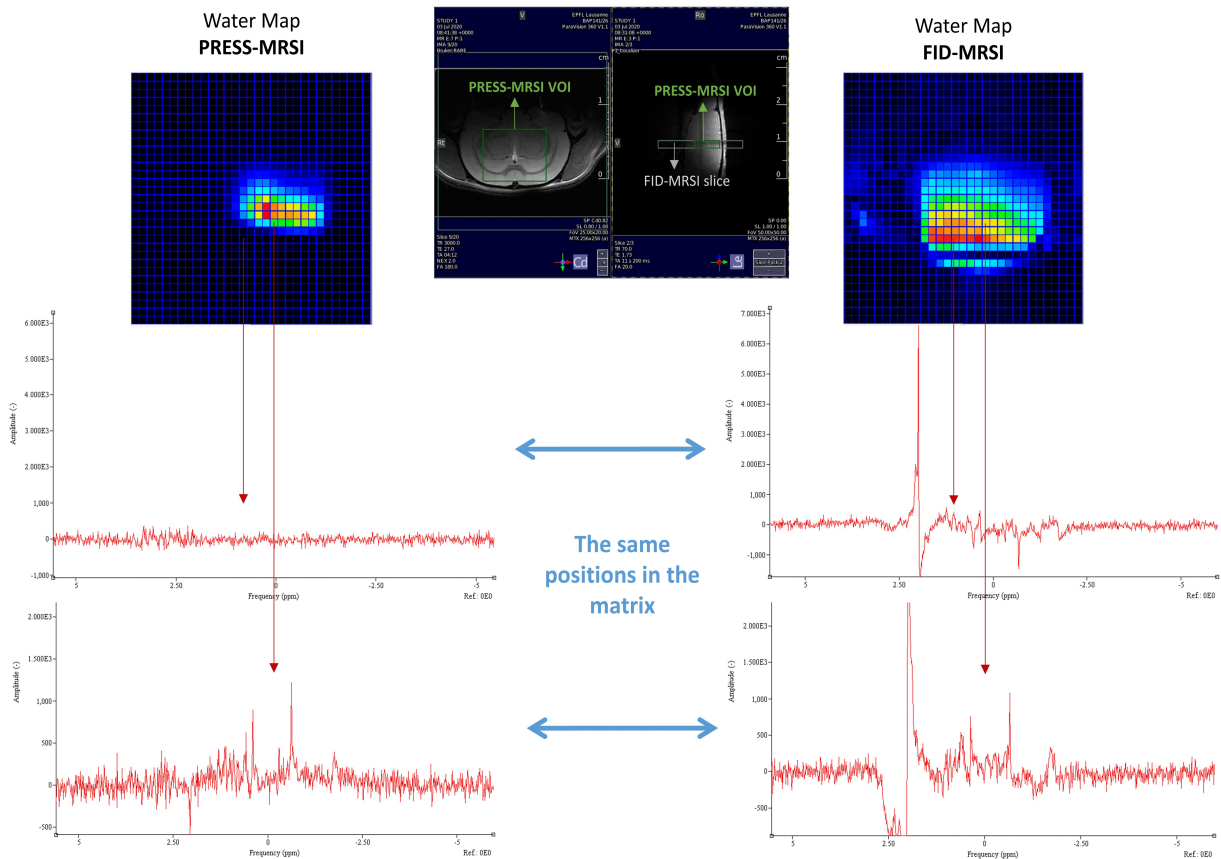

Figure 4:6: PRESS-MRSI vs FID-MRSI in axial direction. (up) The PRESS-MRSI VOI position is highlighted in the middle panel (in green) while the FID-MRSI slice is show in gray. The water map provided by the jMRUI MRSI tool resulting from the PRESS-MRSI acquisition

is shown on the left while the water map resulting from the FID-MRSI acquisition is shown on the right. **(down)** Spectra at two positions in the matrix are highlighted. The first nominal voxel position is chosen outside the PRESS-MRSI FOV to highlight the better brain coverage provided by the FID-MRSI (upper spectra). The second nominal voxel was chosen inside the PRESS-MRSI FOV to compare the spectral appearance (lower spectra). Note that for the lower FID-MRSI spectrum the 1st order phase distortion (due to the delay in acquisition) was partially restored by the AMARES fitting algorithm while performing the SNR calculation.

4.2.2.4   Optimized in vivo FID-MRSI acquisition (axial slice orientation)

After all the adjustments presented in the previous sub chapters (reference power, water suppression and FOV saturation) these are the final parameters used for the FID-MRSI acquisition: TE = 1.3ms, TR = 812 ms, one average, 8 dummy scans, matrix size 31 x 31 (FOV = 24 x 24 mm) leading to the nominal voxel size of 0.774 x 0.774 x 2 mm^3, 1024 points of the FID. The VAPOR WS with the flip angles of 84/150° and the last delay of 26ms. The Figure 4:7 shows the first results obtained using the newly implemented and optimized FID-MRSI sequence at 14.1T with axial slice orientation. As can be seen high quality spectra can be obtained using very short acquisition times (~13min) showing great potential for further implementation and improvements of this sequence.
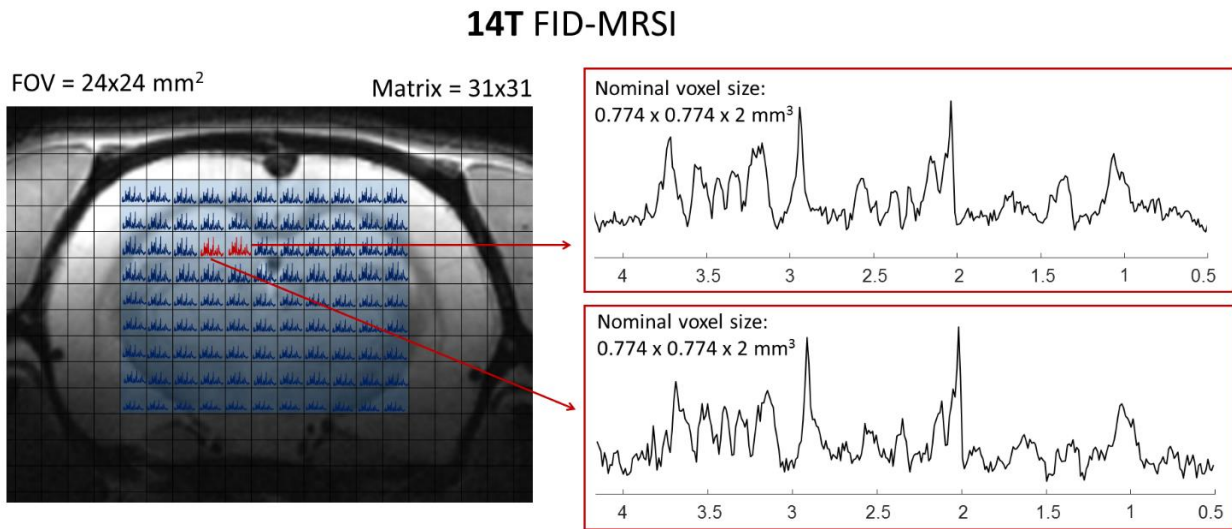
Figure 4:7: Preliminary results for FID-MRSI at 14.1T in the healthy rat brain. Acquisition time 12min and 59s for metabolites, TR=800ms, flip angle 52°.

4.2.3   FID-MRSI coronal slice orientation

4.2.3.1   First experiment and quality assessment

In our experimental setup we use a quadrature surface coil positioned on the top of the rat brain. This results in a substantial loss of SNR in locations further from the coil (deeper in the inside the brain) when an axial slice orientation is used. Therefore, we decided to test the acquisition with a

coronal slice orientation. Figure 4:8 shows the water signal maps provided by the jMRUI MRSI tool (showing from where the significant data comes from) resulting from the axial FID-MRSI acquisition and from the coronal MRSI acquisition. It can be observed that for the coronal slice orientation we have a more uniform excitation resulting in a higher brain coverage (bigger area with the significant spectra locations). Moreover, the spectral quality obtained with the coronal acquisition (sequence parameters were kept the same as optimized for the axial acquisition except that the VOI of 10 x 2 x 10 mm^3 centered on the FID-MRSI slice was shimmed in the STEAM sequence, MAPSHIM from BRUKER) is comparable to the quality of spectra obtained with the axial FID-MRSI acquisition in the locations close to the coil (top of the brain - where the most significant signal comes from, Figure 4:8down).
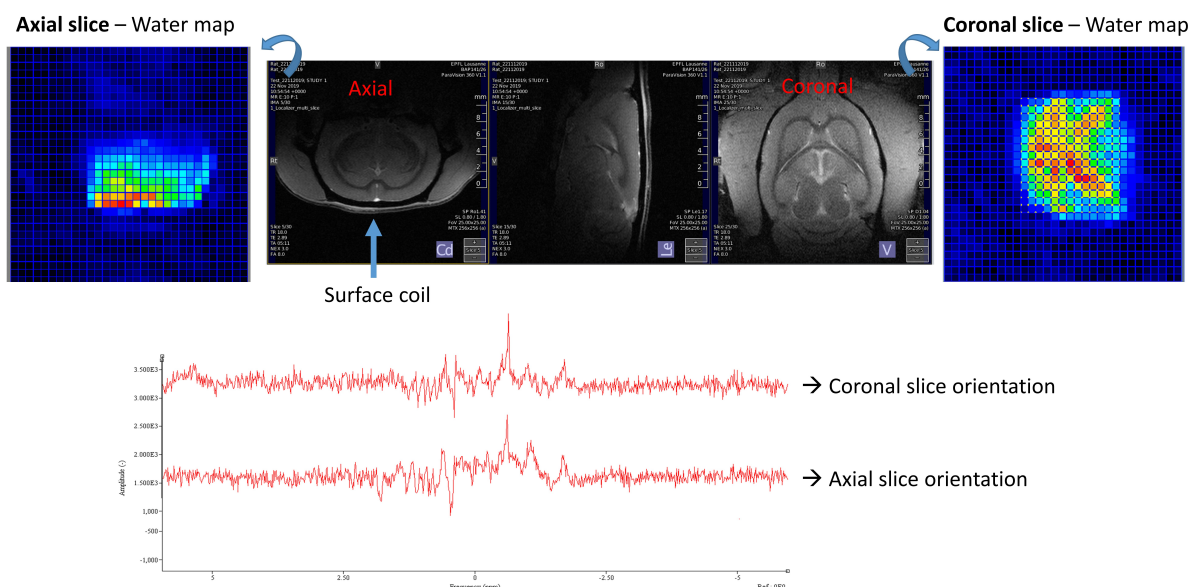

Figure 4:8: Axial vs. coronal slice orientation (up) Comparison of the FID-MRSI acquired with the axial slice orientation and the coronal slice orientation. The water maps (showing the significant spectra locations in color) obtained from the jMRUI MRSI tool show an improved brain coverage and a more uniform excitation for the coronal orientation acquisition. **(down)** Spectrum acquired with FID-MRSI in the axial direction selected from the area close to the coil (top of the brain) and a spectrum acquired with the FID-MRSI in the coronal direction showing a comparable spectral quality between the two. Note that the residual water signal was re-moved from the presented spectra with HLSVD.

An additional experiment was performed using a phantom made in a 5ml syringe containing Cr (8mM) in PBS (phosphate-buffered saline). Coronal slice orientation FID-MRSI and PRESS-MRSI acquisitions were performed to compare the spectral quality and SNR between the two acquisitions.

PRESS-MRSI parameters were set to TE=12.745 ms, TR= 2000 ms, one average, 31 x 31 matrix in a FOV = 24 x 24 mm leading to a total scan time of 32 min and 2 s (same as in the section 4.2.2.3). The VOI of 10 x 2 x 10 mm³ was centered in the phantom (positioned in the same slice used for FID-MRSI).

Parameters used for the FID-MRSI acquisition: TE = 1.3ms, TR = 812 ms, one average, matrix size 31 x 31 in a FOV = 24 x 24 mm (slice positioned so it contains the PRESS VOI) leading to a total acquisition time of 12 min 59s.

Once again for SNR comparison a sub-matrix (4 x 6 spectra = 24 spectra in total) centered in the RESS-MRSI VOI was selected. The SNR of the selected 24spectra was calculated in jMRUI (AMARES) as the higher Cr peak height / spectral noise. The same sub matrix (24 spectra) was selected from the FID-MRSI dataset and the SNR was calculated in the same way. The average SNR for PRESS-MRSI was 17.9 $\pm$ 6 and for the FID-MRSI 16.2 $\pm$ 5. Once again, we can conclude that both methods lead to similar spectral quality (see the comparison of two spectra from the same nominal voxel obtained by the PRESS acquisition and FID acquisition in the Figure 4:9down) while the FID-MRSI provides a better brain coverage also for the coronal slice orientation acquisition and shorter acquisition time.
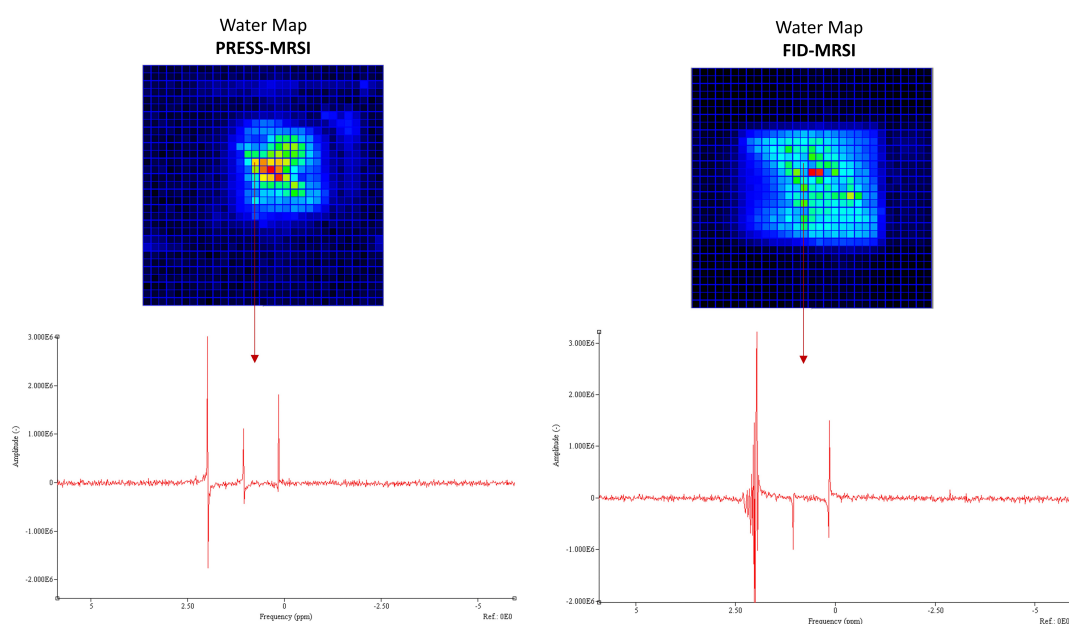
Figure 4:9: PRESS-MRSI vs FID-MRSI with the coronal slice orientation (in vitro – phantom containing only Cr). **(up)** The water map provided by the jMRUI MRSI tool resulting from the PRESS-MRSI acquisition is shown on the left while the water map resulting from the FID-MRSI acquisition is shown on the right. **(down)** Spectra from the same location in the matrix acquired with the two methods (PRESS and FID) are displayed for comparison.

4.2.3.2 Two-compartment phantom

To test the precision of the FID-MRSI sequence and its ability to separate metabolic profiles from different brain regions we built a two-compartment phantom. The phantom consisted of two syringes; a small syringe (5 ml) positioned inside of the big syringe (50 ml). The small syringe was filled with high concentration (50 mM) of Cr with 1 μM/ml gadolinium (Gd) in PBS and the big syringe was filled with high concentration (40 mM) of Glu with 1 μM/ml in PBS (See Figure 4:10up). Both FID and PRESS-MRSI acquisitions were performed with following parameters:

- PRESS-MRSI: TE=12.745 ms, TR= 2000 ms, one average, 31 x 31 matrix in a FOV = 24 x 24 mm leading to a total scan time of 32 min and 2 s. The VOI of 10 x 2 x 10 mm3 was centered in the phantom (positioned in the same slice used for FID-MRSI).
- FID-MRSI: TE = 1.3ms, TR = 812 ms, one average, matrix size 31 x 31 in a FOV = 24 x 24 mm (slice positioned so it contains the PRESS VOI) leading to a total acquisition time of 12 min 59s.

The observed water maps (Figure 4:10up) confirm that a better brain coverage is obtained when the FID-MRSI sequence is used. Moreover, the water maps show that the acquired signal comes from the clearly separated two compartments. Figure 4:10down shows a comparison of spectra from three different positions in the matrix. It can be observed that "pure" Cr spectra are obtained from the nominal voxels located in the Cr compartment, while the spectra from the Glu compartment (on the border with Cr compartment) contain a very minimal Cr contamination. This small Cr signal most probably comes from contamination of the Glu compartment during phantom preparation, rather than from the imperfect localization, supported also by the water maps. We can conclude that FID-MRSI sequence is able to separate metabolic profiles from two closely positioned compartments with different metabolic profiles.
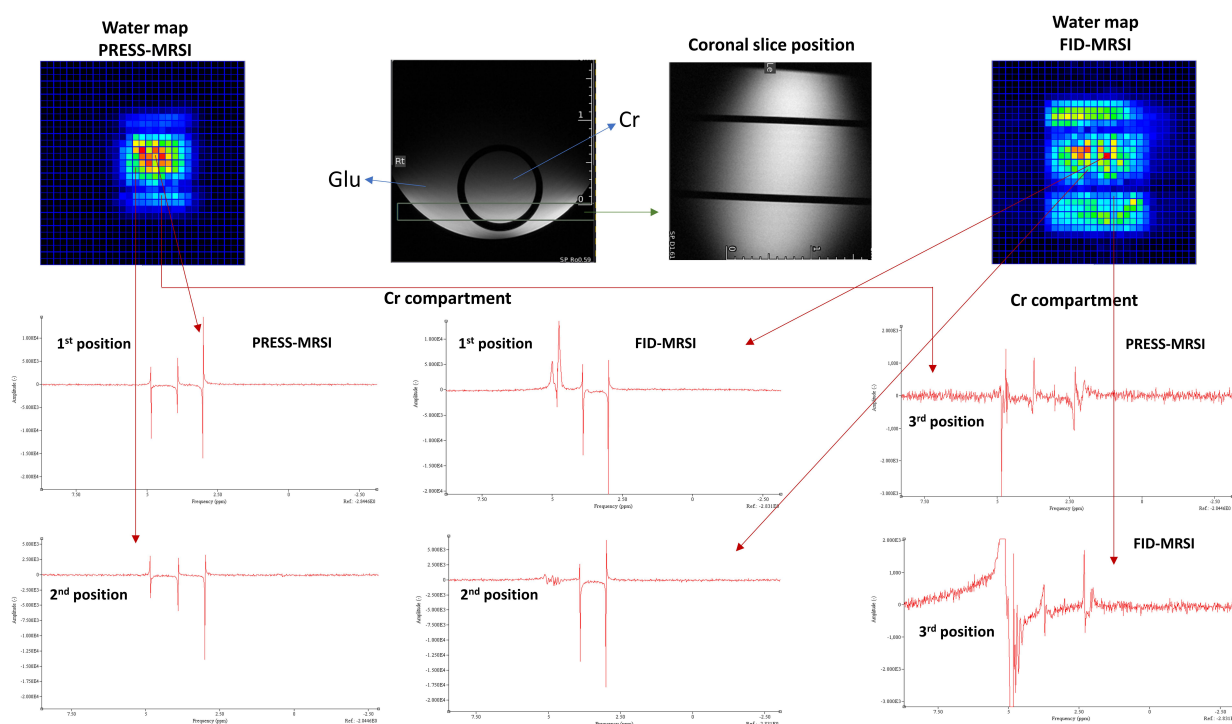
Figure 4:10: Two compartment phantom FID-MRSI vs. PRESS-MRSI. (up) The water map provided by the jMRUI MRSI tool resulting from the PRESS-MRSI acquisition is shown on the left while the water map resulting from the FID-MRSI acquisition is shown on the right. The T_2 -weighted Turbo-RARE images of the phantom in the coronal (centred on the MRSI slice) and axial positions are shown in the middle. **(down)** Spectra from three different positions (locations) in the matrix acquired with the two methods (PRESS and FID) are displayed for comparison (always the identical position for both sequences).

4.2.3.3 Final parameters for coronal FID-MRSI acquisition

The data were acquired in the rat brain (n=3) at 14.1T (Bruker/Magnex Scientific) using a homemade transmit/receive quadrature surface coil. T_2-weighted Turbo-RARE images were acquired in coronal and axial direction to position the MRSI slice for shimming and acquisition (20 slices, TR=3000ms, NA=2, RAREfactor=6).

For the high-resolution two-dimensional fast ^{1}H MRSI a slice selective pulse acquire sequence was used in combination with VAPOR[33] water suppression and 6 saturation slabs to minimize the lipid contamination (FID ^{1}H-MRSI, Figure 4:11).
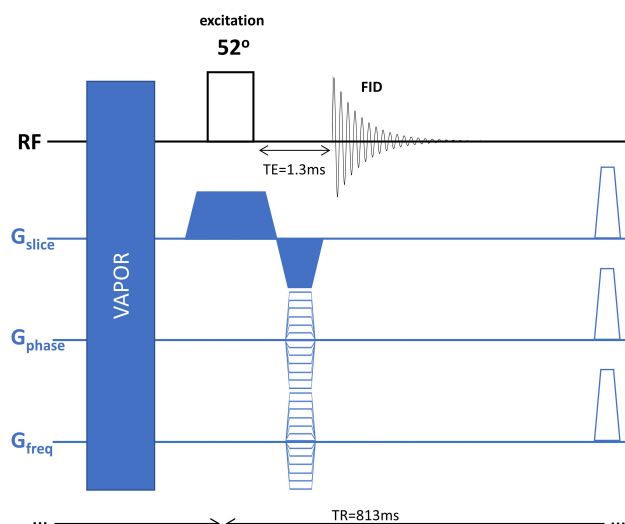
Figure 4:11: A schematic drawing of the ¹H FID-MRSI sequence used for data acquisition.

The MRSI slice was centred on the hippocampus, with 2mm slice thickness and FOV of 24×24mm^2 (Figure 4:12). The matrix size was 31x31 leading to a nominal voxel size of $0.77\times0.77\times2$mm^3 (Figure 4:12). The following acquisition parameters were used: acquisition bandwidth of 7kHz, 1024 spectral data points, Cartesian (linear) k-space sampling, 8 dummy scans, TE=1.3ms, TR=813ms leading to total measurement time of 12min 59s for 1 average. The excitation pulse was adjusted to the Ernst angle of 52° (0.5ms, 8400 Hz, SLR calculated pulse with sharpness 3). First and second order shims were adjusted using MAPSHIM, first in an ellipsoid covering the full brain then in a voxel of $10\times10\times2$mm^3 centered on the MRSI slice. A B_0 map was acquired between each MAPSHIM.
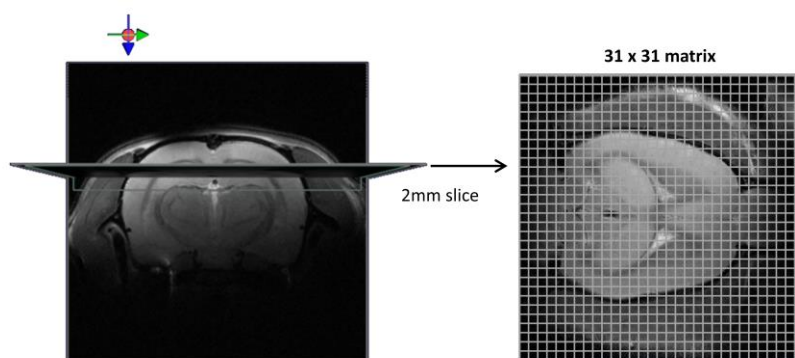
Figure 4:12: The slice position and the spatial resolution used in the FID ¹H MRSI acquisitions in the rat brain at 14.1T

The metabolites for the basis set were simulated using NMRScope-B (18 metabolites) from jMRUI[34], using published values of J-coupling constants and chemical shifts[35,36] and the pulse-acquire sequence with the same parameters as for the in vivo ¹H MRSI metabolite acquisitions (Figure 4:11). The macromolecule (MM) spectrum was acquired using a double inversion recovery STEAM

(TI1=2200ms, TI2=850ms) sequence in the voxel of 10x10x2mm³ centred on the MRSI slice. The metabolite residuals were removed with AMARES[37] following the same procedure elaborately described in the Chapter 2. To match the acquisition delay (1st order phase evolution due to the acquisition delay of 1.3ms) to the one of the metabolites in the basis set the first points of the FID were removed, and this final MM signal was added to the basis set (Figure 4:13).
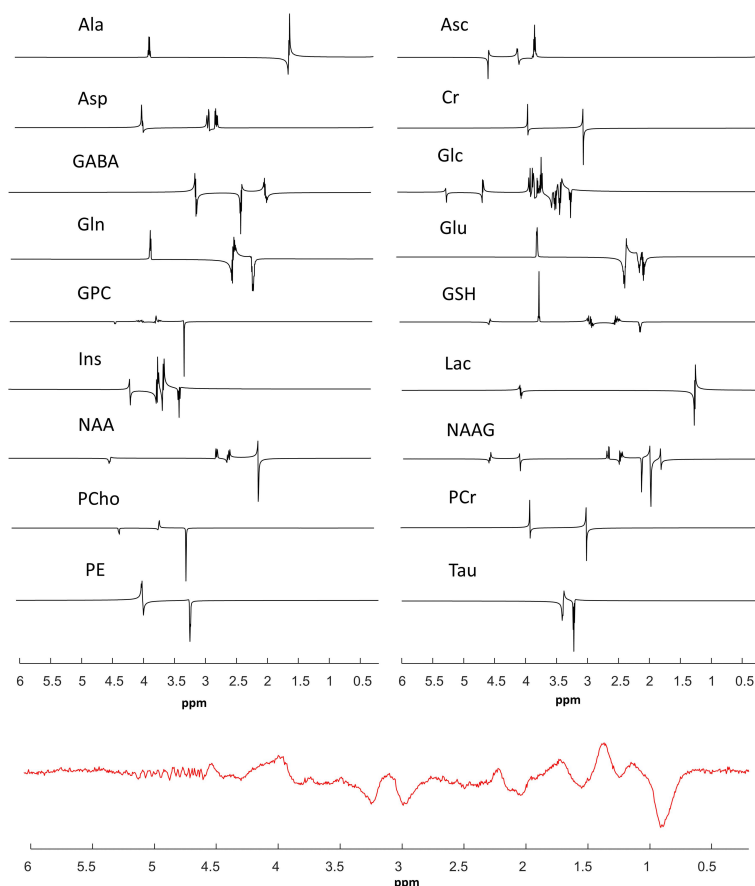
Figure 4:13: The quantification basis set. The metabolites simulated using NMRScope-B (18 metabolites) from jMRUI and the MM included in the basis set. The MM spectrum was acquired with double inversion recovery STEAM and the residual metabolites were removed with AMARES from jMRUI.

The acquired data were read from the BRUKER binary format directly and converted to .raw files named according to their specific position in the matrix using an in house written MATLAB code. The ¹H spectra for quantification were selected automatically from the 31 x 31 matrix using a power map based on the acquired water reference spectra. For every spectrum (in the matrix) the power is calculated by summing the product of every complex point with its complex conjugate. Finally, the selection is performed by subtracting the mean of all the powers (full matrix) from the power at every location in the matrix. The locations having a positive value after the subtraction are the ones

with significant signal and the spectra from these matrix locations are kept for the quantification. This selection is done using an in house written MATLAB code. The quantification is performed using LCModel. To improve the quantification robustness, the water signal was used for phase correction and the metabolite signals were decontaminated from skull lipids using the metabolite-lipid spectral orthogonality approach[38]. The metabolite-lipid orthogonality states that the sum of the products of the only lipid signal and the only metabolite signal equals zero. This means that there are two orthogonal sub spaces that contain metabolite and lipid MR time series. Therefore, the goal is to find a projector matrix which takes the signal acquired in the brain and projects it into the only metabolite space (keeps only the metabolites). To obtain the projector matrix, SVD is performed on the only lipid containing signals (e.g. skull mask). The SVD provides us with a set of singular vectors that characterize the lipid space. To approximate the lipid subspace only a k number of singular vectors is kept. The number k is chosen based on the energy criteria which is given to the algorithm. The energy criteria is the ratio between energy density obtained from only lipid signal (on the mask/skull area) divided by energy density of signal from the brain. Since the lipid space (lipid projector) is orthogonal to the metabolite space (metabolite projector), once the lipid projector is computed the calculation of the metabolite projector is straightforward[38]. Several values for the energy criteria were tested and the value of 0.5 was selected as optimal for the data presented herein. The MATLAB codes and processing pipeline for the phase correction and lipid removal was provided to us by Dr. Antoine Klauser (University of Geneva) and were adapted to our Bruker 14.1T data.

Datasets with both one and two averages were acquired and postprocessed (power map selection, phase correction and lipid removal). The LCModel quantifications, using the above created basis set, provided reliable quality fits for the data obtained with both one and two averages (Figure 4:14).
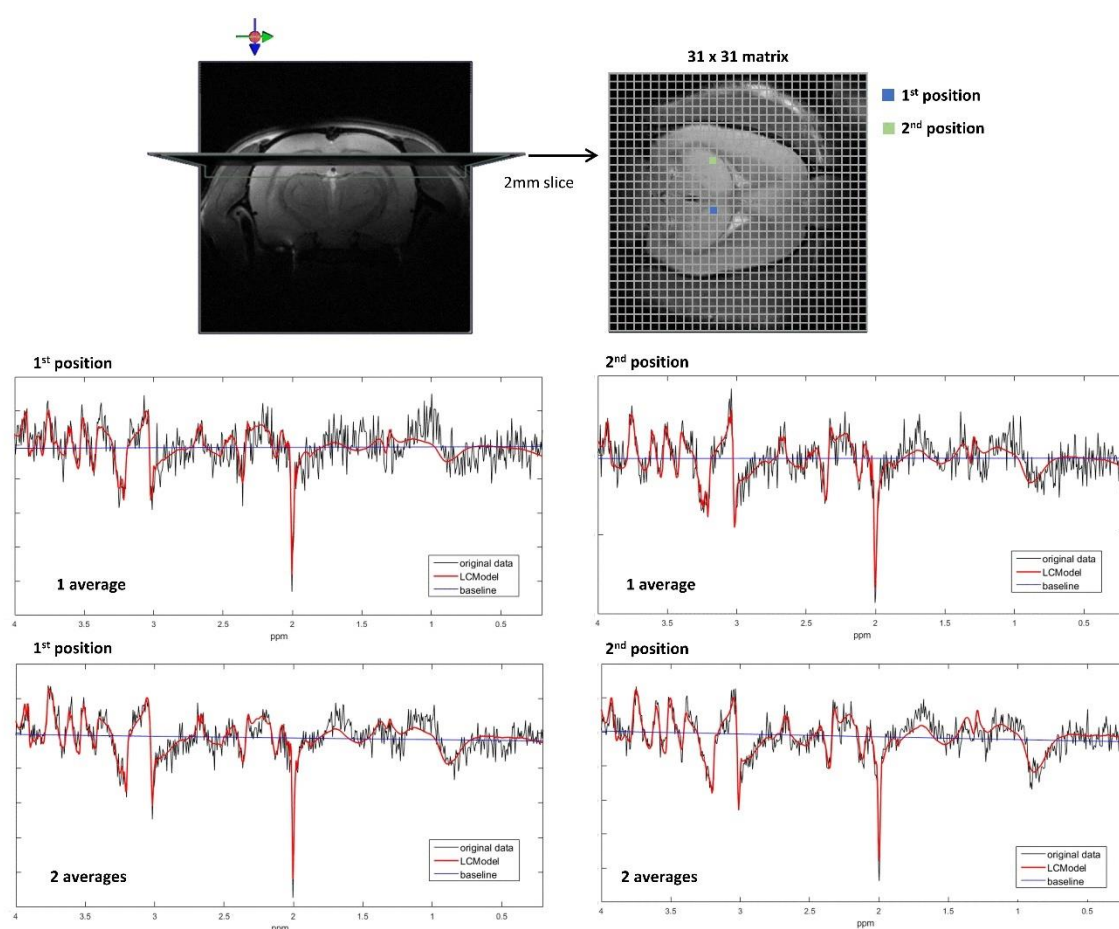
Figure 4:14: The quality of LCModel quantification is shown for spectra from two different positions in the matrix with one and two averages.

4.2.3.4   Metabolic maps resulting from the LCModel quantifications

A manual quality check was performed on the spectra quantified with LCModel (SNR, fit quality and CRB's) to select the spectra and corresponding quantifications further used to build the metabolic maps. The resulting Cramér-Rao lower bounds were sufficiently low (<40%) for the metabolites of interest leading to accurate metabolic maps. The shim adjustments using MAPSHIM proved to be efficient when shimming in large areas, which translated into good quality spectra in a number of nominal voxels in the matrix. Therefore, a large brain coverage was achieved extending also towards the edges of the brain and was not limited to a standard rectangular volume. Metabolic maps overlaid to the corresponding anatomical image for NAA, Glu, GPC+PCho and GABA are shown in Figure 4:15. Although the metabolic maps obtained from the acquisition with two averages provided a better contrast, the maps kept the same pattern when using one average proving that this very fast acquisition leads a satisfactory output.
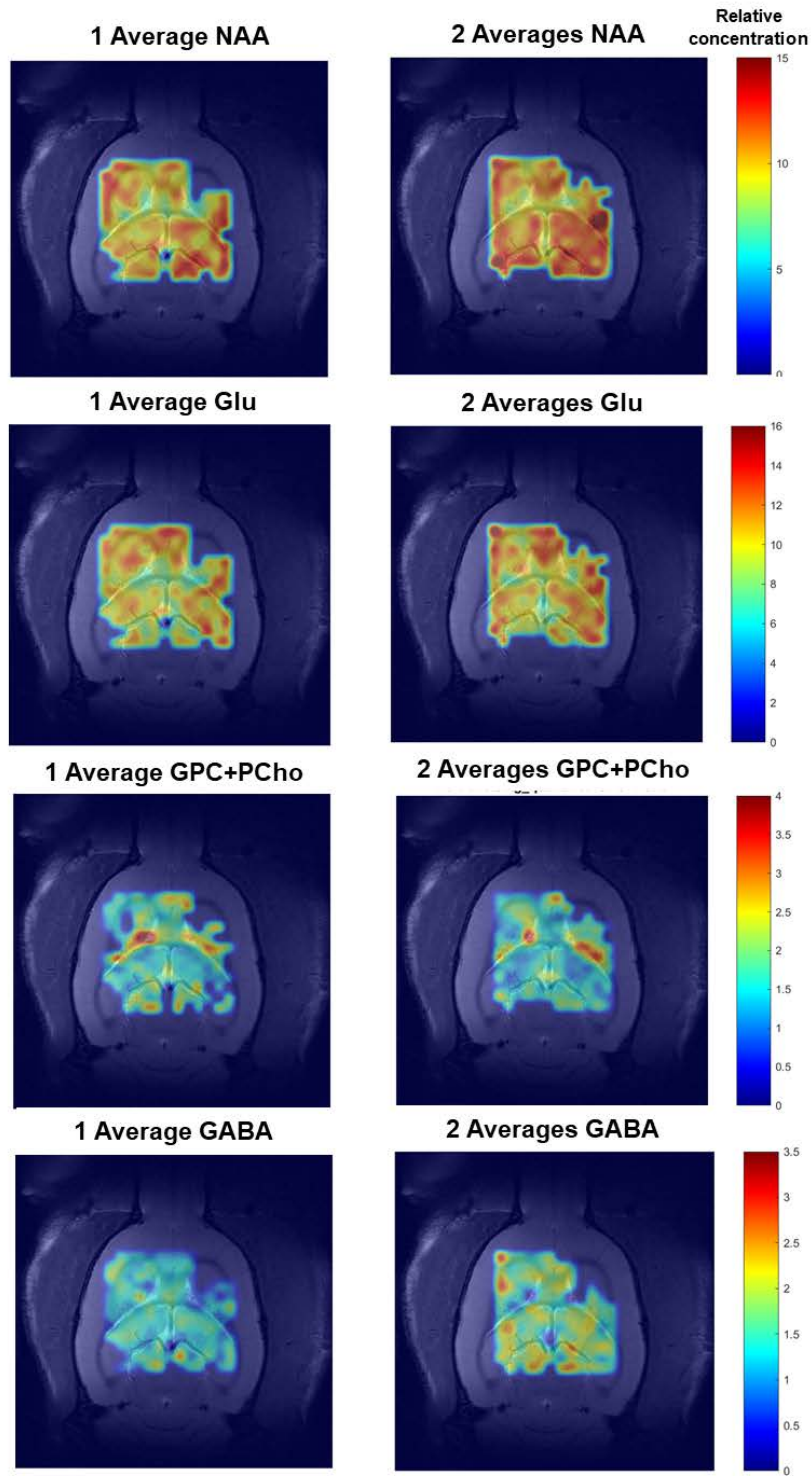
Figure 4:15: Metabolic maps obtained from the LCModel quantification results of the data acquired with one average (on the left) and two averages (on the right). The metabolic maps were superimposed to the corresponding anatomical image using an in house written MATLAB script. The scales correspond to LCModel outputs when referenced to tCr by setting its concentration to 8mmol/kg$_{ww}$.

4.3 Effect of noise reduction techniques on preclinical MRSI data – preliminary results

4.3.1 Introduction

^{1}H MRSI is highly challenging mainly because of the low concentration of metabolites, low signal-to-noise ratio (SNR), long measurement times and advanced pulse sequences and processing methods that need to be implemented[2,3]. The constant appetite for higher spatial resolution leads to an increased search for post-processing methods that aim at minimizing the noise variance in ^{1}H MRSI. The low spectral SNR resulting from an MRSI acquisition is especially enhanced in the preclinical setting because of the small rodent brain leading to very small nominal voxel sizes (e.g 0.75 x 0.75 x 2mm^3 in a rat brain[10] compared to 1.7 x 1.7 x 10 mm^3 in the human brain[11], see sub-chapter 4.1). Several denoising methods have been proposed for ^{1}H MRSI[38–42].

Denoising based on singular value decomposition has been previously used, but the determination of the appropriate thresholds that separate the noise from the signal is problematic leading to possible loss of spatial resolution or the elimination of spectral features that are present in only a small fraction of the voxels. The MP-PCA (based on principal component analysis) technique exploits the fact that noise eigenvalues follow the universal Marchenko-Pastur distribution, a result of the random matrix theory[43]. Thus, this method provides an automatic approach for separation of the noise components from the signal components. It has already shown great performance on diffusion MRI[43], functional MRI and DW-MRS[44] data . The performance of denoising improves with the number of measurements making the MRSI acquisitions suitable as they contain a large number of spectra (i.e high redundancy).

Reconstruction methods based on different low-rank assumptions have been implemented mainly on clinical applications. These methods rely on the linear predictability, the partial separability of spatial-temporal modes, or both to denoise MRSI data[39–41]. In addition, constraints on the spatial distribution of the signal with specific regularization has shown to enhance further the SNR in MRSI reconstruction[38]. In this approach, partial separability is combined with a total generalized variation (TGV) spatial regularization in a reconstruction model. TGV regularization aims to denoise metabolite distribution by penalizing first and second order spatial derivatives. It is known to preserve edges while avoiding stair-casing artifacts present in traditional first order total variation schemes[38].

The aim of the present study was to test the feasibility of two noise reduction techniques on pre-clinical data. The MP-PCA based denoising was tested on 9.4T SPECIAL-MRSI dataset acquired in the healthy rodent brain, while both low-rank TGV reconstruction and MP-PCA denoising were tested on 14.1T fast ^{1}H-FID-MRSI dataset.

Some of the work presented in this sub-chapter (4.3) was done in collaboration with MSc Brayan Alves. Brayan is a new PhD student in our group who is supposed to take over this work and further develop it. As such I was heavily involved in his training since September 2021.

4.3.2 Application of MP-PCA and TGV reconstruction noise reduction techniques on 9.4T SPECIAL MRSI datasets and 14.1T fast ^{1}H-FID-MRSI dataset: preliminary results

4.3.2.1 Methods – SPECIAL-MRSI

The experiments were performed in rat brain on a 9.4T horizontal magnet (Varian Magnex/Scientific). The MRSI data were acquired using an ultra-short echo time SPECIAL spectroscopic imaging sequence (TR=1000 ms, TE=2.8 ms, 34 min per scan)[10,16] with VAPOR WS and OVS around the selected voxel. A matrix size of 32 x 32 nominal voxels with a FOV of 24 x 24 mm^2 was acquired, leading to a nominal voxel size of 0.75 x 0.75 x 2 mm^3. First and second order shims were applied using FASTMAP in a voxel of 6 x 9 x 2 mm^3 centered in the rat brain.

A sub-matrix of 8x15 voxels centered on the region of interest was selected (Figure 4:16), resulting in 120 FIDs used in the further analysis. The complex-valued FIDs were split into real and imaginary parts and organized into a matrix X, where the first dimension contained the time-domain sampling (1024 points) and the second dimension all the spectra from the selected sub-matrix (240 real + imaginary, Figure 4:17). Matrix X was denoised using the MP-PCA approach[43]. Raw and denoised spectra were preprocessed in MATLAB script and quantified with LCModel using an appropriate basis set. All the MATLAB codes for preprocessing and data preparation for LCModel quantifications were written in house and are available for future applications in our laboratory.
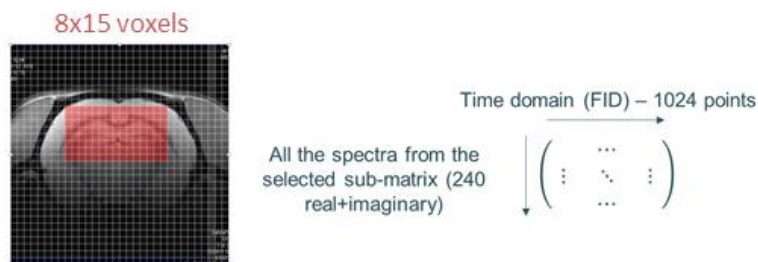
Figure 4:16: MP-PCA data matrix for SPECIAL-MRSI. A selected sub-matrix of 8x15 voxels centered on the region of interest shown in red (**left**). The organization of matrix X which was denoised using MP-PCA approach (**right**).

The effect of denoising was evaluated by comparing standard deviations (SD) of the apparent noise before and after denoising on a selected matrix and assessing the SNR of the spectra as well as the apparent CRLB of the metabolite concentrations. The noise SD-s were calculated on the last 300 points of the FID before and after denoising.

4.3.2.2   Methods – FID-MRSI

The ^{1}H MRSI data were acquired in the rat brain on a 14.1T MRI system (Bruker/Magnex Scientific) using the recently implemented single slice fast ^{1}H FID-MRSI sequence (TE=1.3ms, TR=813ms, 2mm slice thickness centred on the hippocampus, FOV=24x24mm^2, matrix size=31x31, 1 average). For more details on the sequence implementation see section 4.2.3.

The following preprocessing steps were applied prior to application of any of the denoising methods. The data was phase corrected based on the water signal and cleaned from lipid contamination using the metabolite-lipid orthogonality approach as described in[38]. The residual water signal from the metabolite spectra was removed using HLSVD.

The low-rank TGV reconstruction was applied as described in Klauser et.al[38] to the full dataset (31x31 matrix). Dr Antoine Klauser provided us the MATLAB script for performing the TGV reconstruction and trained us on how to use this method. In addition, we adapted the codes to our data and needs. For the MP-PCA a sub-matrix of 12x13 voxels centered in the MRSI slice was selected, resulting in 156 FIDs used in the further analysis. The complex-valued FIDs were split into real and imaginary parts and organized into a matrix X, where the columns contained the time-domain sampling (1024 points) and the rows all the spectra from the selected sub-matrix. Matrix X was denoised using the MP-PCA approach[43].

The resulting spectra: non-denoised, LR-TGV denoised and MP-PCA denoised were quantified with LCModel combined with a simulated basis set using same parameters as in vivo (see section 4.2.3.4). The metabolite maps were created and overlaid to the corresponding MRI image using an in house written Matlab code. The metabolite maps were shaped manually with respect to the SNR of the LCModel quantified spectra and the CRLBs of the given metabolites. The effect of both denoising methods was evaluated by assessing the average apparent SNR of the spectra over the 12x13 voxels sub-matrix and by comparing the distribution of noise SD and the residual difference distribution between denoised and non-denoised spectra on the same sub matrix. The noise SD-s were calculated on 130 points of the spectrum in a signal free region (0 to -1.5 ppm) before and after denoising, for both MP-PCA and LR-TGV denoising.

An additional assessment of the spectral SNR before and after denoising was performed by calculating the SNR in unit time. The maximum value of absolute signal in the time domain (in the range between 0.5 and 4.5 ppm) was divided by the absolute level of noise averaged in the range from 0 to -1.5 ppm. The ratio of this "absolute" SNR value and the square root of the total acquisition time (in seconds) was then computed to obtain the SNR in unit time.

4.3.2.3   Results and discussion

SPECIAL-MRSI

The denoising resulted in accurate fits to the MP distribution and in average 17 principal components were identified (Figure 4:17A). Figure 4:17B shows a clear reduction of the apparent noise SD after denoising (-71%). The noise distribution seemed to be similar among spectra after denoising (Figure 4:17C). The marked effect of the denoising on the spectra in the denoised matrix is visualized in Figure 4:18. An increase in the apparent SNR as quantified by LCModel fitting was observed without any impact on the linewidth or other features of the spectra. The apparent SNR (calculated by LCModel) in the region of interest for quantification ranged from SNR=8 to SNR=20 for the denoised matrix, while it ranged from SNR=3 to SNR=10 in the same region for the original matrix. Note that the LCModel SNR depends not only on the SD of the residuals, but also on the baseline estimate. The average apparent CRLBs over the denoised region (8 x 15 matrix) were overall significantly reduced (i.e. 12% for Tau and 15% for total choline (tCho) – Table 4:1), especially for spectra located on the edges of the region of interest where the apparent SNR is particularly low, which makes

reliable quantification critical. Of note, the resulting apparent CRLB and SNR after denoising should be interpreted with care since they are computed based on the resulting noise after denoising.
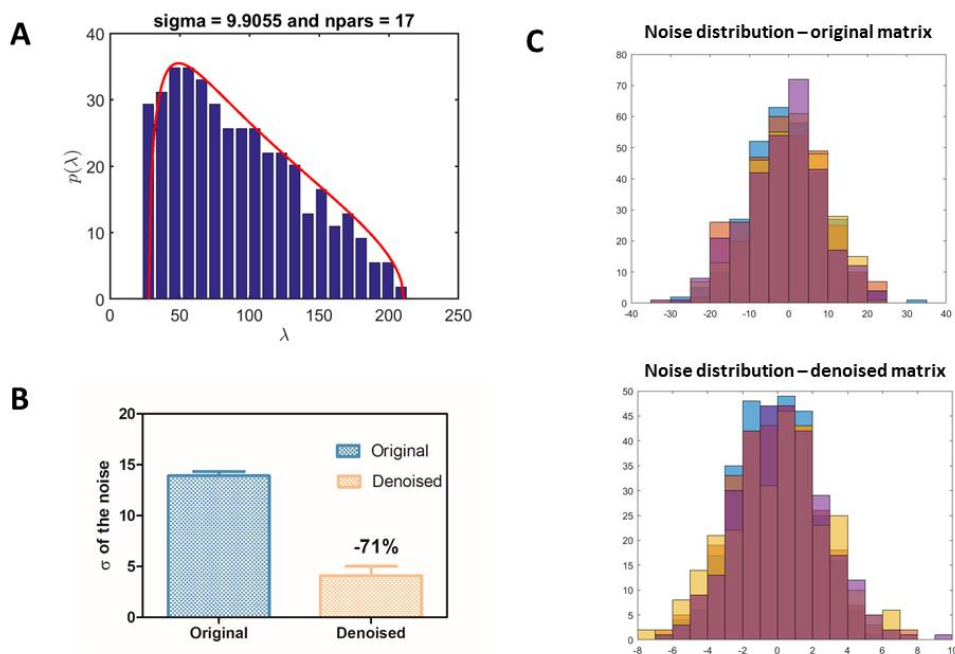

Figure 4:17: MP-PCA results for SPECIAL MRSI (**A**) Fit of MP distribution to the lowest eigenvalues from PCA. (**B**) Mean value of the standard deviation of noise (last 300 points of the FID) from all 120 spectra before and after denoising (upper and lower graphs, respectively). (**C**) The noise distribution of 6 random selected spectra before and after denoising.
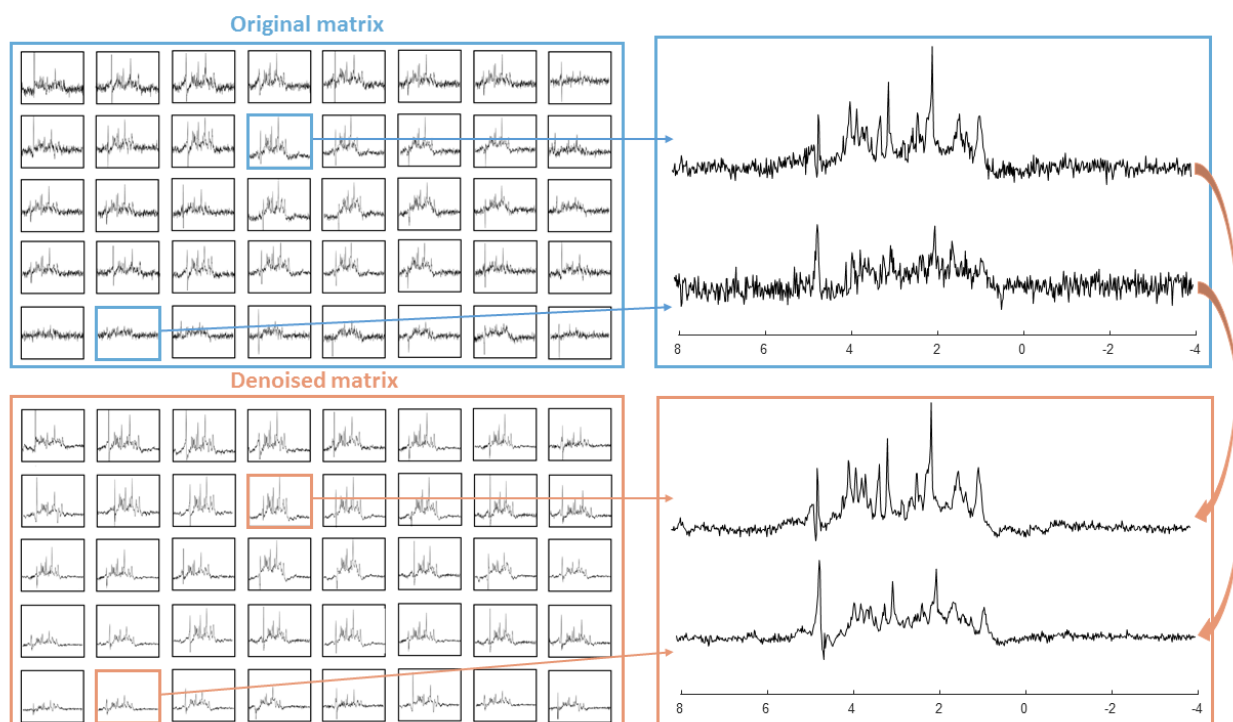
Figure 4:18: Spectra after MP-PCA denoising (SPECIAL-MRSI). A sub-set (5x8) of the full image matrix demonstrates the quality of the spectra before and after denoising with a clear improvement in apparent SNR in spectra located at the edge of the matrix.

Table 4:1: CRLBs comparison of original vs. denoised. Average and SD of the CRLBs obtained from LCModel quantifications of the spectra from the denoised region.

Metabolite	Original		Denoised	
	Mean CRLBs	**STD CRLBs**	**Mean CRLBs**	**STD CRLBs**
Cr	59.00	33.44	28.13	9.32
PCr	33.00	23.65	16.63	4.22
Gln	26.63	6.62	12.81	2.59
Glu	12.56	3.29	6.75	1.57
Ins	10.19	1.52	6.69	1.25
NAA	7.75	1.48	4.69	1.01
Tau	24.19	6.41	12.13	2.75
GPC+Pcho	34.94	15.83	19.13	6.28
NAA+NAAG	7.88	1.71	4.81	0.98
Cr+PCr	8.44	1.41	5.13	1.02
Glu+Gln	10.94	2.24	6.00	1.32

FID-MRSI

An averaged two-fold increase in apparent SNR as quantified by LCModel was observed when using both noise-reduction approaches, without any visual impact on linewidths or other features of the spectra (Figure 4:19). Two important points should be considered when analyzing the SNR computed by LCModel: 1) the baseline estimate has an important contribution in the SNR calculations in addition to the residuals; and 2) the SNR measured from the residual baseline noise is insufficient given the presence of non-uniform variance[41]. Therefore, an additional SNR assessment was performed by calculating the SNR in unit time before and after denoising with MP-PCA and LR-TGV method (Figure 4.20). A substantial SNR increase is observed for MP-PCA and LR-TGV approach when compared to non-denoised data. Moreover, the LR method seems to provide a slightly higher increase in SNR when compared to MP-PCA. However, these results are not conclusive because for example the SNR depends on the number of components kept for signal reconstruction which is different between the two methods (23 and 29 in MP-PCA vs. 20 and 20 in LR-TGV for 1 and two averages respectively) and therefore further assessments need to be made.

Figure 4:21A shows the distribution of the noise SD in the 12x13 voxels sub-matrix and highlights that both methods decrease the range of the noise SD. In addition, the difference in spectra between original and denoised matrix did not provide any visible structure on the residual map for any of the two investigated approaches (Figure 4:21B) suggestive of a certain level of uniformity in noise removal inside the spectrum. Both noise-reduction techniques lead to smother metabolic maps while still preserving regional differences, particularly for spectra located at the edges of the brain (Figure 4:22).

We implemented and showed the potential of two noise-reduction techniques on preclinical 14.1T ^{1}H FID-MRSI and 9.4 T SPECIAL-MRSI datasets. The results are promising offering enormous potential towards novel and fast MRSI developments. Further studies will be performed to quantitatively assess the performance of both denoising techniques on 14.1T ^{1}H-FID-MRSI data and to evaluate if the "apparent" increase in spectral SNR translates in true lower uncertainty in metabolite concentrations.
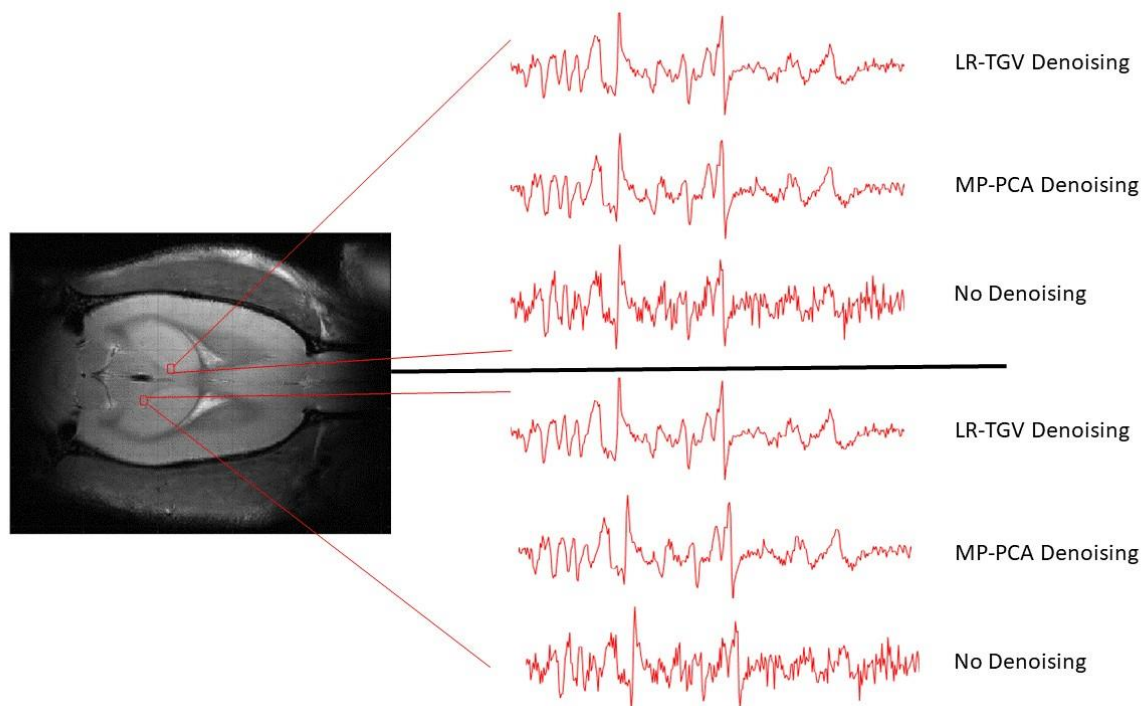
Figure 4:19: Comparison of spectra non-denoised vs. MP-PCA and LR-TGV. Denoised (via MP-PCA and LR-TGV) and non-denoised FID spectra for 2 voxels in the volume of interest. The spectra displayed ranges from 4.2 to 0.2 ppm.
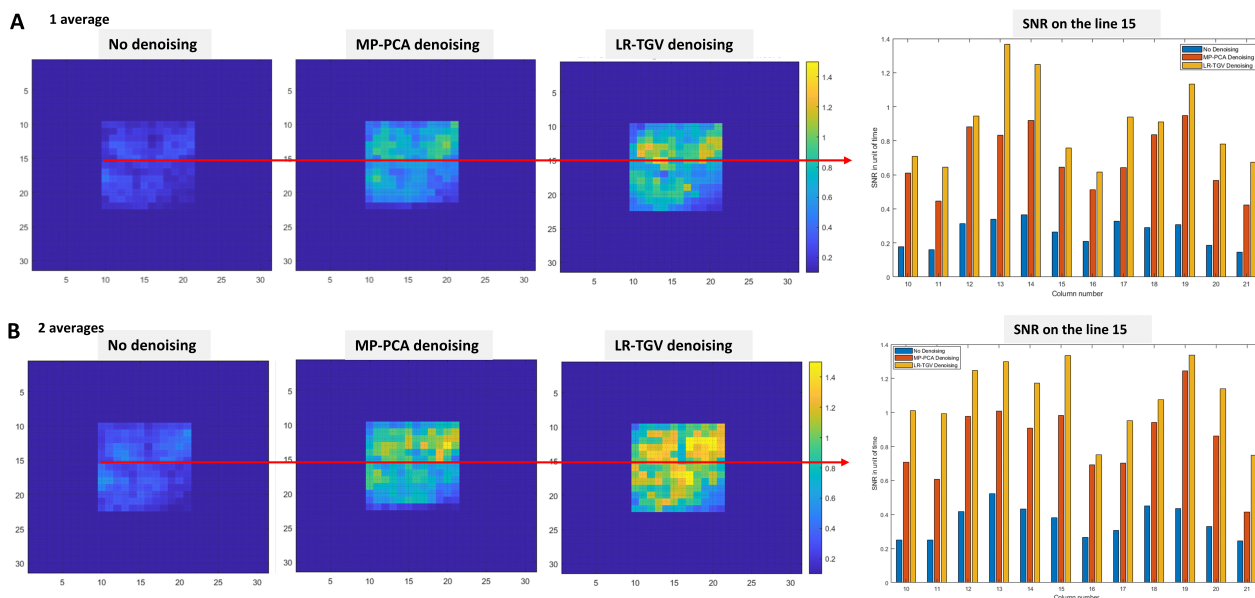
Figure 4:20: Comparison of SNR before and after denoising. Results of the SNR in unit time calculation for 1 average **(A)** and 2 averages **(B)** FID-MRSI data before denoising and after MP-PCA and LR-TGV denoising. The maps present a 12 x 13 sub matrix centered on the brain (area where there is signal). A histogram representation of the SNR calculated for spectra on the line 15 of the matrix is shown on the right.
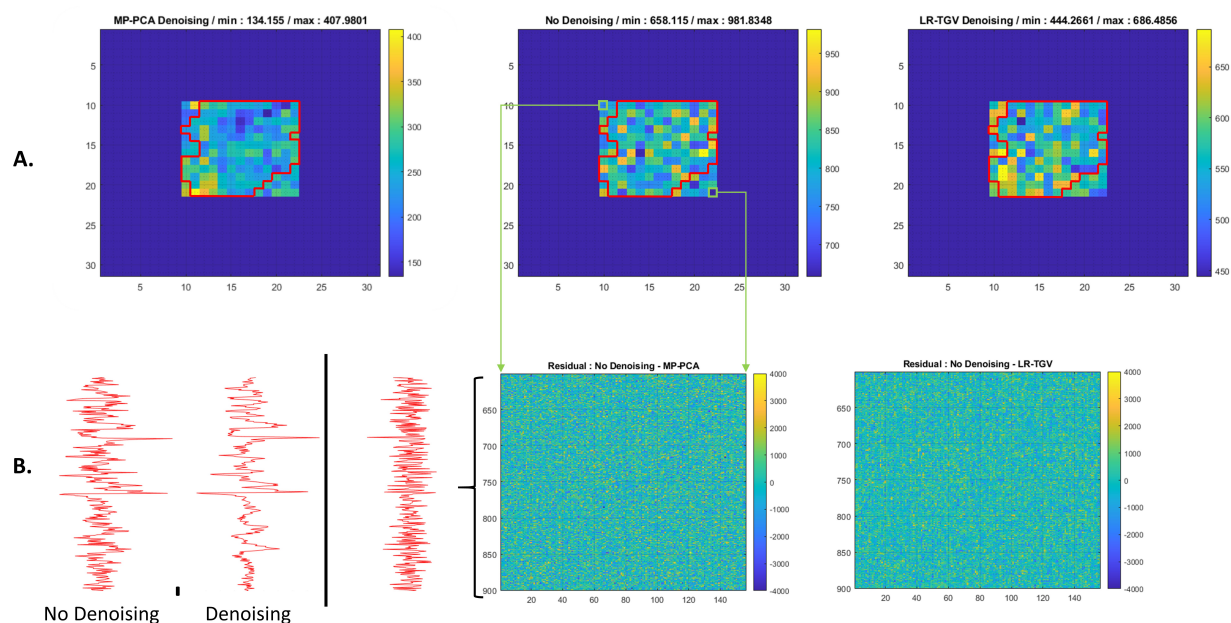
Figure 4:21: Comparison of the noise properties after denoising. (A) Distribution of the noise standard deviation (130 points of the spectra), in the 12x13 voxels sub-matrix. The red border highlights the shape of the metabolic map. The range of each map is set to its respective minimum and maximum value for a better visualization. **(B)** The residual map of the difference between denoised and non-denoised spectra. Each from column represents a difference of spectra, starting from the top left voxel and ending with the bottom right (from top to bottom, then left to right).
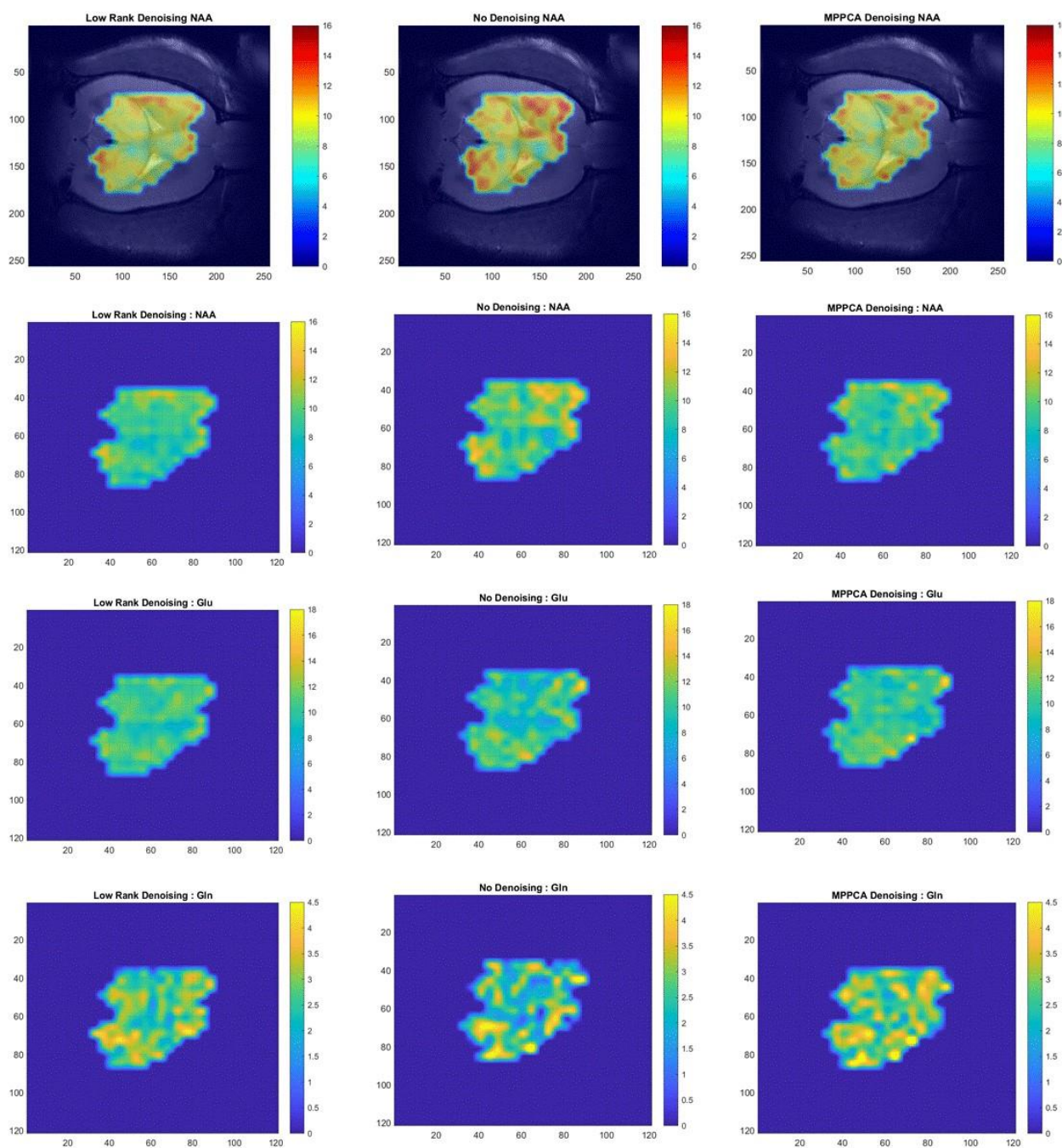
Figure 4:22: Concentration map after denoising. Concentration maps from NAA, Glu and Gln, calculated via the LCModel quantification. From left to right: LR-TGV denoised data, no denoising applied data and MP-PCA denoised data. The top row overlays the concentration map with an anatomical image of the rat brain.

Summary and future perspectives

We presented the first implementation of fast ^{1}H-FID-MRSI in the rat brain at 14.1T which provided an increased brain coverage, reliable and accurate quantification results and metabolic maps in only 13 minutes of acquisition. With this we set the grounds for a wider application of ^{1}H-FID-MRSI in the preclinical setting with a potential for further improvement and acceleration. We tested noise reduction techniques as a potential processing method that could be included in the postprocessing pipeline.

Further improvements will be investigated regarding the efficiency of lipid suppression, improvements in the homogeneity and coverage of the surface coil. In parallel, further reducing TR and implementing a concentric rings encoding would allow for a faster acquisition.

Future steps:

- Post processing of the acquired MM in vivo using an in house programmed double and single inversion recovery module in BRUKER ParaVision 360 and incorporated it into the FID-MRSI sequence. A series of experiments was performed to optimize the inversion time for metabolite nulling and the DIR module with TI1=2200ms and TI2=850ms was chosen as optimal.

- Reduction of the TE from 1.3ms to 0.94ms to reduce the phase evolution. Preliminary data were recently acquired and the processing on these data is ongoing

- More uniform excitation by switching from a quadrature surface coil to an 2x2 array coil or a volume coil as transmit and a surface coil as receive.

- Multi slice acquisition (full brain coverage)

- Switch to non-Cartesian encoding trajectories (spiral or concentric rings encoding) for further acceleration.

- Optimization and automatization of the postprocessing and quality check before quantification using ML techniques as[45,46] .

- Further studies are needed to quantitatively assess the performance of both denoising techniques on 14.1T ^{1}H-FID-MRSI data and to evaluate if the "apparent" increase in spectral SNR translates in true lower uncertainty in metabolite concentrations.

The final goal is to apply the ^{1}H-FID-MRSI technique to the animal model of type C HE (BDL rats). We already shown that UHF scanners in combination with short TE pulse sequences are very advantageous and well suited to study this disease (Chapter 3)[8]. Moreover, differential brain regional

vulnerability to the disease insults and its importance in understanding the pathological outcomes is presented in this thesis using single voxel spectroscopy (Chapter 3, sub-chapter 3.3). Therefore, the ability to follow the metabolic changes in the full brain throughout the disease evolution provided by the ^{1}H-FID-MRSI would be of great importance not only for better understanding the disease pathology but also for evaluation of potential treatment strategies and their brain regional response.

References

1.   de Graaf, R. A. *In Vivo NMR Spectroscopy: Principles and Techniques: 2nd Edition*. *In Vivo NMR Spectroscopy: Principles and Techniques: 2nd Edition* (2007). doi:10.1002/9780470512968.

2.   Maudsley, A. A. *et al.* Advanced magnetic resonance spectroscopic neuroimaging: Experts' consensus recommendations. *NMR Biomed.* **34**, 1–22 (2021).

3.   Bogner, W., Otazo, R. & Henning, A. Accelerated MR spectroscopic imaging—a review of current and emerging techniques. *NMR Biomed.* **34**, (2021).

4.   Obara-Michlewska, M. & Szeliga, M. Targeting glutamine addiction in Gliomas. *Cancers (Basel).* **12**, (2020).

5.   Srinivasan, R., Ratiney, H., Hammond-Rosenbluth, K. E., Pelletier, D. & Nelson, S. J. MR spectroscopic imaging of glutathione in the white and gray matter at 7 T with an application to multiple sclerosis. *Magn. Reson. Imaging* **28**, 163–170 (2010).

6.   Cudalbu, C. & Taylor-Robinson, S. D. Brain Edema in Chronic Hepatic Encephalopathy. *Journal of Clinical and Experimental Hepatology* (2019) doi:10.1016/j.jceh.2019.02.003.

7.   Pedrosa de Barros, N. & Slotboom, J. Quality management in in vivo proton MRS. *Anal. Biochem.* **529**, 98–116 (2017).

8.   Hangel, G. *et al.* Emerging methods and applications of ultra-high field MR spectroscopic imaging in the human brain. *Anal. Biochem.* **638**, 114479 (2022).

9.   Lanz, B. *et al.* Magnetic resonance spectroscopy in the rodent brain: Experts' consensus recommendations. *NMR Biomed.* **34**, 1–20 (2021).

10.   Mlynárik, V. *et al.* Quantitative proton spectroscopic imaging of the neurochemical profile in rat brain with microliter resolution at ultra-short echo times. *Magn. Reson. Med.* **59**, 52–58 (2008).

11.   Hangel, G. *et al.* Ultra-high resolution brain metabolite mapping at 7 T by short-TR Hadamard-encoded FID-MRSI. *Neuroimage* **168**, 199–210 (2018).

12.   Cudalbu, C. In vivo studies of brain metabolism in animal models of Hepatic Encephalopathy using 1H Magnetic Resonance Spectroscopy. *Metab. Brain Dis.* **28**, 167–174 (2013).

13.   Delgado-Goñi, T. *et al.* MRSI-based molecular imaging of therapy response to temozolomide in preclinical glioblastoma using source analysis. *NMR Biomed.* **29**, 732–743 (2016).

14.   Mlynárik, V., Gambarota, G., Frenkel, H. & Gruetter, R. Localized short-echo-time proton MR spectroscopy with full signal-intensity acquisition. *Magn. Reson. Med.* **56**, 965–970 (2006).

15.   Mlynárik, V. *et al.* Quantitative proton spectroscopic imaging of the neurochemical profile in rat brain with microliter resolution at ultra-short echo times. *Magn. Reson. Med.* **59**, 52–58 (2008).

16.   Cudalbu, C. *et al.* Imaging glutamine synthesis rates in the hyperammonemic rat brain. in *ISMRM* 3324 (2010).

17.   Geppert, C., Dreher, W. & Leibfritz, D. PRESS-based proton single-voxel spectroscopy and spectroscopic imaging with very1 short echo times using asymmetric RF pulses. *Magn. Reson. Mater. Physics, Biol. Med.* **16**, 144–148 (2003).

18.   Starčuk, Z., Bartušek, K. & Starčuk, Z. Asymmetric Amplitude-Modulated Radiofrequency Pulses and Their Application to Band-Selective Decoupling. *Journal of Magnetic Resonance, Series A* vol. 104 340–344 (1993).

19.   Arias-Ramos, N. *et al.* Metabolomics of therapy response in preclinical glioblastoma: A multi-slice MRSI-based volumetric analysis for noninvasive assessment of temozolomide treatment. *Metabolites* **7**, 1–29 (2017).

20.   Simões, R. V. *et al.* Improving the classification of brain tumors in mice with perturbation enhanced (PE)-MRSI. *Integr. Biol.* **4**, 183–191 (2012).

21.   Henning, A., Fuchs, A., Murdoch, J. B. & Boesiger, P. Slice-selective FID acquisition, localized by outer volume suppression (FIDLOVS) for 1H-MRSI of the human brain at 7 T with minimal signal loss. *NMR Biomed.* **22**, 683–696 (2009).

22.   Bogner, W., Gruber, S., Trattnig, S. & Chmelik, M. High-resolution mapping of human brain metabolites by free induction decay 1H MRSI at 7T. *NMR Biomed.* **25**, 873–882 (2012).

23.   Tkác, I. *et al.* In vivo 1H NMR spectroscopy of the human brain at 7 T. *Magn. Reson. Med.* **46**, 451–6 (2001).

24.   Henning, A., Fuchs, A., Murdoch, J. B. & Boesiger, P. Slice-selective FID acquisition, localized by outer volume suppression (FIDLOVS) for 1H-MRSI of the human brain at 7 T with minimal signal loss. *NMR Biomed.* **22**, 683–696 (2009).

25.   Nassirpour, S., Chang, P. & Henning, A. High and ultra-high resolution metabolite mapping of the human brain using 1H FID MRSI at 9.4T. *Neuroimage* **168**, 211–221 (2018).

26.   Hangel, G. *et al.* High-resolution metabolic imaging of high-grade gliomas using 7T-CRT-FID-MRSI. *NeuroImage Clin.* **28**, 102433 (2020).

27.   Hangel, G. *et al.* High-resolution metabolic mapping of gliomas via patch-based super-resolution magnetic resonance spectroscopic imaging at 7T. *Neuroimage* **191**, 587–595 (2019).

28.   Heckova, E. *et al.* 7 T Magnetic Resonance Spectroscopic Imaging in Multiple Sclerosis: How Does Spatial Resolution Affect the Detectability of Metabolic Changes in Brain Lesions? *Invest. Radiol.* **54**, 247–254 (2019).

29.   Heckova, E., Dal-bianco, A., Strasser, B. & Hangel, G. J. Extensive Brain Pathologic Alterations Detected with 7 . 0-T MR Spectroscopic Imaging Associated with Disability in Multiple Sclerosis. (2022).

30.   Cudalbu, C., Mlynárik, V., Xin, L. & Gruetter, R. Comparison of T1 relaxation times of the neurochemical profile in rat brain at 9.4 tesla and 14.1 tesla. *Magn. Reson. Med.* **62**, 862–867 (2009).

31.   Tkáč, I. *et al.* Water and lipid suppression techniques for advanced 1H MRS and MRSI of the human brain: Experts' consensus recommendations. *NMR Biomed.* **34**, 1–25 (2021).

32.   BRUKER. ParaVision 360 V1.1 manual●.

33.   Tkáč, I., Starčuk, Z., Choi, I. Y. & Gruetter, R. In vivo 1H NMR spectroscopy of rat brain at 1 ms echo time. *Magn. Reson. Med.*

41, 649–656 (1999).

34.   Starčuk, Z. & Starčuková, J. Quantum-mechanical simulations for in vivo MR spectroscopy: Principles and possibilities demonstrated with the program NMRScopeB. *Anal. Biochem.* **529**, 79–97 (2017).

35.   Govindaraju, V., Young, K. & Maudsley, A. A. Proton NMR chemical shifts and coupling constants for brain metabolites. *NMR Biomed.* **13**, 129–153 (2000).

36.   Govind, V., Young, K. & Maudsley, A. A. Corrigendum to Proton NMR chemical shifts and coupling constants for brain metabolites. [NMR Biomed. 13, (2000), 129-153]. *NMR Biomed.* **28**, 923–924 (2015).

37.   Simicic, D. *et al.* In vivo macromolecule signals in rat brain 1H-MR spectra at 9.4T: Parametrization, spline baseline estimation, and T2 relaxation times. *Magn. Reson. Med.* **86**, 2384–2401 (2021).

38.   Klauser, A. *et al.* Fast high-resolution brain metabolite mapping on a clinical 3T MRI by accelerated 1H-FID-MRSI and low-rank constrained reconstruction. *Magn. Reson. Med.* **81**, 2841–2857 (2019).

39.   Abdoli, A., Stoyanova, R. & Maudsley, A. A. Denoising of MR spectroscopic imaging data using statistical selection of principal components. *Magn. Reson. Mater. Physics, Biol. Med.* **29**, 811–822 (2016).

40.   Nguyen, H. M., Peng, X., Do, M. N. & Liang, Z. P. Denoising MR spectroscopic imaging data with low-rank approximations. *IEEE Trans. Biomed. Eng.* (2013) doi:10.1109/TBME.2012.2223466.

41.   Clarke, W. T. & Chiew, M. Uncertainty in denoising of MRSI using low-rank methods. *Magn. Reson. Med.* **21 Septemb**, (2021).

42.   Simicic, D., Phong, L. T., Heeswijk, R. B. van, Jelescu, I. O. & Cudalbu, C. The impact of Marchenko-Pastur PCA denoising on high resolution MRSI in the rat brain at 9.4T. in *ISMRM* (2021).

43.   Veraart, J. *et al.* Denoising of diffusion MRI using random matrix theory. *Neuroimage* (2016) doi:10.1016/j.neuroimage.2016.08.016.

44.   Jelescu, I. O., Veraart, J. & Cudalbu, C. MP-PCA denoising dramatically improves SNR in large-sized MRS data: an illustration in diffusion weighted MRS.

45.   Pedrosa de Barros, N., McKinley, R., Wiest, R. & Slotboom, J. Improving labeling efficiency in automatic quality control of MRSI data. *Magn. Reson. Med.* **78**, 2399–2405 (2017).

46.   Kyathanahally, S. P. *et al.* Quality of clinical brain tumor MR spectra judged by humans and machine learning tools. *Magn. Reson. Med.* **79**, 2500–2510 (2018).

General Conclusions

In the current thesis novel methodological developments are implemented at UHF together with different applications to study brain regional vulnerability and response to treatment in type C Hepatic Encephalopathy in a rat model.

First this thesis proposed an improved methodological approach for post-processing, fitting and quantification of the MM spectra that can be generally applied. The efficacy of this method was shown by parametrization of MM spectra into 10 individual components and estimation of their apparent T_2 relaxation times in the rat brain at 9.4T. Additionally, the effect of MM model (single MM spectrum or parametrized MM components) and baseline stiffness on metabolite and MM quantification was assessed using both in vivo acquired and Monte Carlo simulated data with a purpose of optimizing the settings for future ^{1}H MRS quantifications. We concluded that a parametrized characterization of the MM contribution to short-echo spectra is feasible and yields reliable quantification results. Moreover, a generally valid degree of baseline stiffness cannot be predicted and it needs to be adapted to the experimental and fitting conditions.

Then the advantages of UHF short TE single voxel spectroscopy, ex-vivo EPR and histology measurements were used in this thesis to describe the regional distribution of metabolites, morphological alterations of neurons and astrocytes and the role of oxidative stress in the adult and developing brain using a well-known rat model of type C HE (the bile duct ligated rat). Three brain regions (hippocampus, striatum and cerebellum) were concomitantly investigated. The reported neurometabolic changes showed that there is a differential brain regional vulnerability to type C HE emphasizing that the mechanisms observed in one brain region cannot be extrapolated as general disease characteristics. The strongest metabolic changes (e.g. highest Gln increase, changes in Lac and antioxidants) were observed in the cerebellum highlighting the increased vulnerability of this brain region. The increase of Gln was the first observed metabolic change in all the regions strongly contributing to the data variance (STATIS analysis). Therefore, we conclude that Gln can be considered as first brain metabolic marker of type C HE which could potentially serve to assess HE independently of the results of neuropsychological tests. In parallel, the histology results lead to the conclusion that there is an interdependence in astrocytic and neuronal morphological changes influencing the overall activity of the neuronal network during disease progression. Moreover, we proved the presence of increased CNS and systemic OS highlighting its important role in the disease pathogenesis. Additionally, the presented results confirmed the increased vulnerability of the developing brain to

CLD induced type C HE. Creatine treatment via creatine supplementation showed a positive effect on the neurometabolic profile of P15 pups (brain in the very early development) suggesting that an appropriate treatment strategy could have a positive impact on the health type C HE patients.

Finally, the successful implementation of fast ^{1}H FID MRSI in the rat brain provided promising results. With this, we have set the basis for a broader use of ^{1}H FID MRSI in the preclinical setting, with the possibility of additional improvements and acceleration.

Future studies

Several studies can be proposed as a continuation of this thesis:

We identified cerebellum as a region which is the most affected by the disease (type C HE) thus future studies should be specifically focused on investigating this brain region. Cerebellum is not easily accessible by ^{1}H MRS in human brain and thus not deeply investigated region, however it offers a great potential for preclinical studies. The disease mechanisms and morphological changes can be further investigated using diffusion weighted spectroscopy and diffusion tensor imaging as well as with ^{31}P MRS and ^{1}H MRSI.

The results presented in this thesis highlight Glutamine as an important disease marker opening possibilities for further treatment strategies that would aim specifically at lowering the concentration of this molecule. Moreover, the observed changes in oxidative stress and its emphasized role in the disease's pathogenesis impose a combinatorial treatment, including molecules specifically targeting reactive oxygen species (antioxidants) together with the already investigated creatine supplemen-tation. Therefore, a study assessing the effect of antioxidant treatment in the BDL rats would be a next logical step.

New methodological developments need to be implemented to further optimize and accelerate the ^{1}H FID MRSI acquisitions. The first step would be to achieve a more uniform excitation by replacing the quadrature surface coil with a volume coil (as transmit). Furthermore, implementing a multi slice acquisition to achieve the full brain coverage and non-Cartesian encoding trajectories (e.g. concentric rings) for further acceleration would increase the potential of this technique.

The final goal would be to apply the ^{1}H FID MRSI to the animal model of type C HE (BDL rats). As the importance of understanding the differential brain regional vulnerability in this disease is shown in this thesis, a study using ^{1}H FID MRSI would allow us to follow the metabolic changes in

the full brain throughout the disease evolution. This would provide a better insight into the disease mech-anisms and improved evaluation of potential treatment strategies.

List of publications

Published

Dunja Simicic, Veronika Rackayova, Lijing Xin, Ivan Tkac, Tamas Borbath, Zenon Starcuk, Jana Starcukova, Bernard Lanz, C. Cudalbu (2021). *In vivo macromolecules in rat brain at ^{1}H MR Spectra at 9.4T: parametrization, spline baseline estimation and T_2 relaxation times*. Magnetic Resonance in Medicine, 86, 2384–2401, doi : 10.1002/mrm.28910

*Veronika Račkayová, *__Dunja Simicic,__ Guillaume Donati, Olivier Braissant, Rolf Gruetter, Valérie A. McLin and Cristina Cudalbu (2021). *Late post-natal neurometabolic development in healthy male rats using ^{1}H and ^{31}P Magnetic Resonance Spectroscopy.* Journal of Neurochem. 157, 508–519, doi: 10.1111/jnc.15294. *Joint first authors

Katarzyna Pierzchala, **Dunja Simicic**, Andrzej Sienkiewicz, Dario Sessa, Stefanita-Octavian Mitrea, Rolf Gruetter, Olivier Braissant, Valerie McLin, and Cristina Cudalbu (2022). *Central nervous system and systemic oxidative stress interplay with inflammation in a bile duct ligation rat model of type C hepatic encephalopathy.* Free Radical Biology and Medicine, 178, 295-307, doi : 10.1016/j.freeradbiomed.2021.12.011

Jessie Mosso, Ting Yin, Carole Poitry-Yamate, **Dunja Simicic**, Mario Lepore, Valerie McLin, Olivier Braissant, Cristina Cudalbu, Bernard Lanz (2022). *PET CMR$_{glc}$ mapping and ^{1}H MRS show altered glucose uptake and neurometabolic profiles in BDL rats.* arXiv:2112.12113 and accepted for publication in the special issue « Brain Biochemistry in Liver Disease » in Analytical Biochemistry.

Under review

Dunja Simicic, Cristina Cudalbu, Katarzyna Pierzchala. *Overview of oxidative stress findings in HE.* **Submitted to** special issue « Brain Biochemistry in Liver Disease » in Analytical Biochemistry.

Anna Hadjihambi, Cristina Cudalbu, Katarzyna Pierzchala, **Dunja Simicic**, Chris Donnelly, Christos Konstantinou, Nathan Davies, Abeba Habtetion, Alexander V Gourine, Rajiv Jalan, Patrick S Hosford. *Ammonia impairs brain oxygenation in an animal model of minimal hepatic encephalopathy*. **Submitted to** Journal of Hepatology Reports.

In preparation

Dunja Simicic*, Katarzyna Pierzchala*, Veronika Rackayova, Olivier Braissant, Valerie McLin and Cristina Cudalbu. *Brain regional vulnerability in type C Hepatic Encephalopathy: in vivo longitudinal ^{1}H MRS and histological results.* *Joint first authors

Dunja Simicic, Bernard Lanz, Ruud B. van Heeswijk, Vladimir Mlynárik, Valerie A. McLin, Olivier Braissant, Cristina Cudalbu. *Brain regional metabolic changes in an hyperammonemic rat brain: an MR spectroscopic imaging study at 9.4T*

Jessie Mosso, **Dunja Simicic,** Cristina Cudalbu*, Ileana O Jelescu*. *MP-PCA denoising for diffusion MRS data: promises and pitfalls.* *Joint last authors

Dunja Simicic, Katarzyna Pierzchala, Veronika Rackayova, Stefanita-Octavian Mitrea, Dario Sessa, Valerie McLin, Olivier Braissant*, Cudalbu Cudalbu*. *Protective role of Creatine in chronic HE in developing brain: in vivo longitudinal ^{1}H and ^{31}P MRS study.* *Joint last authors

Cristina Cudalbu, Guillaume MA Briand, Katarzyna Pierzchala, **Dunja Simicic**, Graham Knott, Stephanie Clerc-Rosset, Bernard Lanz and Ileana Jelescu. *Diffusion of brain metabolites highlights altered brain microstructure in chronic hepatic encephalopathy.*

Conference proceedings

Dunja Simicic, Katarzyna Pierzchala, Veronika Rackayova, Olivier Braissant, Stefanita-Octavian Mitrea, Dario Sessa, Valerie McLin, Cristina Cudalbu. *In vivo longitudinal ^{1}H-MRS study of hippocampal, cereberal and striatal metabolic changes in BDL rats*. Proc. MRS workshop – metabolic imaging, Utrecht 2018 – Oral presentation

Dunja Simicic, Katarzyna Pierzchala, Veronika Rackayova, Olivier Braissant, Stefanita-Octavian Mitrea, Dario Sessa, Valerie McLin, Cristina Cudalbu. *In vivo longitudinal ^{1}H-MRS study of hippocampal, cereberal and striatal metabolic changes in BDL rats*. Proc. SGKC/SSCC annual meeting, Bern, 2018. – Poster presentation

Dunja Simicic, Katarzyna Pierzchala, Veronika Rackayova, Olivier Braissant, Stefanita-Octavian Mitrea, Dario Sessa, Valerie McLin, Cristina Cudalbu. *In vivo longitudinal ^{1}H MRS study of hippocampal, cereberal and striatal metabolic changes in the developing brain using an animal model of Chronic Hepatic Encephalopathy*. Proc. 27th ISMRM annual meeting, Montreal, QC, Canada, May 2019. – Poster presentation

Dunja Simicic, Katarzyna Pierzchala, Veronika Rackayova, Olivier Braissant, Stefanita-Octavian Mitrea, Dario Sessa, Valerie McLin, Cristina Cudalbu. *In vivo longitudinal 1H MRS study of hippo-campal, cereberal and striatal metabolic changes in the adult brain using an animal model of Chronic Hepatic Encephalopathy.* Proc. ISHEN Meeting, Williamsburg, Virginia, US, 2019. – Poster presentation

Dunja Simicic, Veronika Rackayova, Lijing Xin, Bernard Lanz, Cristina Cudalbu. *T_2 relaxation times in rat brain spectra at 9.4T (single inversion recovery + AMARES)* – 1st place trainee poster award. Proc. 28th ISMRM annual meeting, Sydney, Australia, 2020. – Poster presentation

Dunja Simicic, Veronika Rackayova, Cristina Cudalbu. *Influence of parametrized MM and spline baseline in LCModel using in-vivo rat brain ^{1}H-MR spectra and Monte Carlo simulations at 9.4T*. Proc. 28th ISMRM annual meeting, Sydney, Australia, 2020. – Poster presentation

Jessie Mosso, Carole Poitry-Yamate, **Dunja Simicic**, Mario Lepore, Cristina Cudalbu, and Bernard Lanz. *Multimodal assessment of brain energy metabolism in a rat model of hepatic encephalopathy*

using HMRS and F-FDG PET – a pilot study. Proc. 28th ISMRM annual meeting, Sydney, Australia, 2020. – Oral presentation

Cristina Cudalbu[1], Katarzyna Pierzchala, **Dunja Simicic**, Graham Knott, Stephanie Clerc-Rosset, Bernard Lanz and Ileana Jelescu. *Diffusion of brain metabolites highlights altered brain microstructure in chronic hepatic encephalopathy.* Proc. 28th ISMRM annual meeting, Sydney, Australia, 2020. – Oral presentation

Dunja Simicic, Jessie Mosso, Lê Thanh Phong, Ruud B. van Heeswijk, Ileana O. Jelescu, Cristina Cudalbu. *The impact of Marchenko-Pastur MP-PCA denoising on high resolution MRSI in rat brain at 9.4T.* Proc. 29th ISMRM annual meeting, Vancouver, Canada, 2021. – Poster presentation

Dunja Simicic, Katarzyna Pierzchala, Olivier Braissant, Stefanita-Octavian Mitrea, Mitrea, Dario Sessa, Valerie McLin, Cudalbu Cudalbu. *Protective role of Creatine in chronic HE in developing brain: in vivo longitudinal 1H and 31P-MRS study.* Proc. 29th ISMRM annual meeting, Vancouver, Canada, 2021. – Poster presentation

Jessie Mosso, Julien Valette, Katarzyna Pierzchala, **Dunja Simicic**, Ileana Ozana Jelescu, and Cristina Cudalbu. *Diffusion-weighted magnetic resonance spectroscopy in the cerebellum of a rat model of hepatic encephalopathy at 14.1T.* Proc. 29th ISMRM annual meeting, Vancouver, Canada, 2021. – Oral presentation

Curriculum Vitae

CONTACT INFORMATION

Email: dunja.simicic@yahoo.com

PERSONAL INFORMATION

Name: Dunja Šimičić

Date of birth: 25th of April 1994.

Nationality: Croatian

EDUCATION

2000 – 2008	Attended elementary school "Trstenik", Split, Croatia
2008 – 2012	Attended Natural Sciences and Mathematical secondary school in Split, Croatia.
2012 – 2015	Undergraduate studies at the Faculty of science in Engineering Physics, University of Split, Croatia.
2015	Graduated bachelor with thesis "Material Research Using X-ray Diffraction" under the mentorship of Prof. Dr. Sc. Ivica Aviani
2015 –2017	Graduate studies at the Faculty of Science – Biophysics, University of Split, Croatia.
2017	Project for master's thesis at EPFL (École polytechnique fédérale de Lausanne) in the LMPC (Laboratory of Physics of Complex Matter). Project is held under mentorship of Dr. Andrzej Sienkiewicz and direct supervision of Prof. László Forró.
2017	Graduated master with thesis "Mechanistic Insights into Potential Toxicity of Tattoo Inks" under the mentorship of Prof. Dr. Sc. Ivica Aviani, Prof. László Forró and Dr. Andrzej Sienkiewicz
2017–	PhD candidate in physics studies at Laboratory of Functional and Metabolic Imaging, Center for Biomedical Imaging, EPFL (École polytechnique fédérale de Lausanne), Switzerland. PhD supervisors: Prof. Rolf Gruetter and Cristina Cudalbu, PhD.

WORKING EXPERIANCE

2017 –2022	Teaching assistant for 3rd year students in Laboratory exercise in Physics – EPFL

Teaching assistant for 1st year students in General physics: mechanics; Life Sciences Engineering – EPFL

Teaching assistant for 2nd year students in General physics: electrodynamics; Mechanical Engineering – EPFL

Teaching assistant for master students in Fundamentals of Biomedical Imaging – EPFL